UNIVERSITY OF COPENHAGEN
FACULTY OF SCIENCE

Growth of Structure in Theories of Cosmic Acceleration

Cosmological tests and modeling

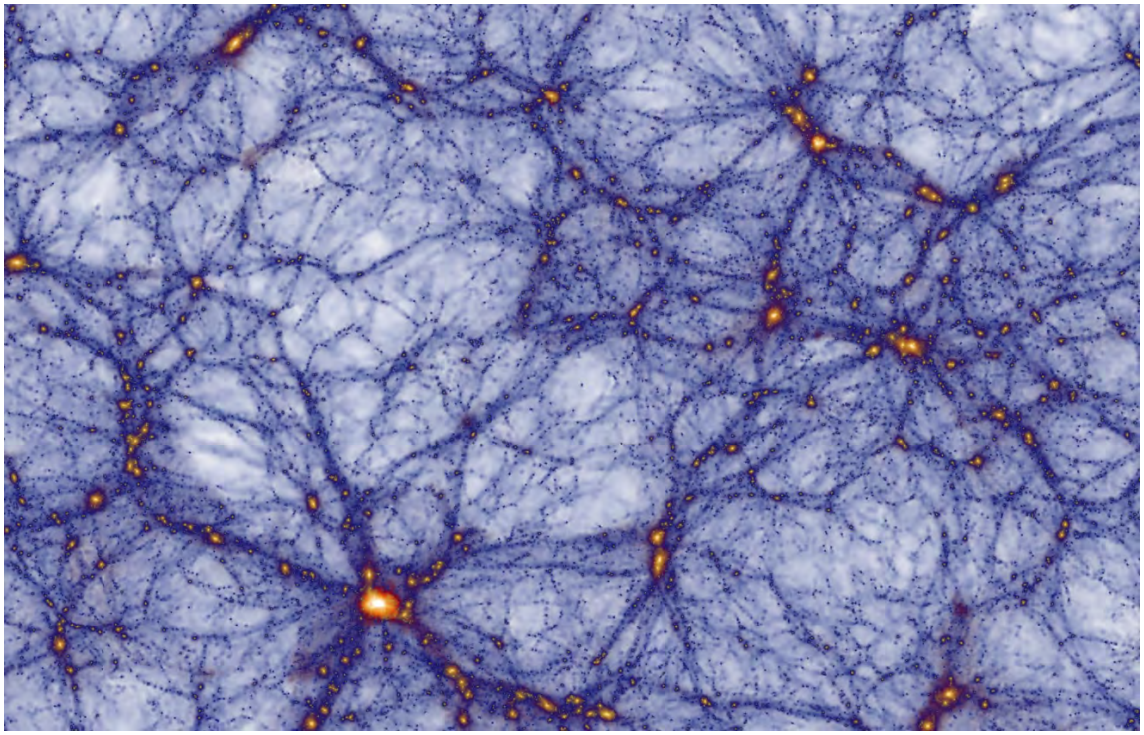

Dissertation submitted for the degree of

Doctor of Philosophy

to the PhD School of The Faculty of Science, University of Copenhagen

on September 19 2016, by

Matteo Cataneo

Supervisor: *Dr. David A. Rapetti*
Co-supervisor: *Prof. Jens Hjorth*

Opponents: *Prof. Luca Amendola*
Prof. Steen H. Hansen
Prof. David Mota

Cover image: "The Millennium-XXL Simulation"

The 'Millennium-XXL', or MXXL, is one of the largest cosmological simulation ever performed and the first multi-hundred billion particle run, surpassing by a factor of 4 in particle number the largest previous simulation of its type. The simulation follows the nonlinear growth of dark matter structures within a cubical region 4.1096 Gpc on a side. This simulated volume is equivalent to that of the whole observable Universe up to redshift 0.72. The particle mass in the MXXL is $m_p = 8.456 \times 10^9\, M_\odot$. This mass resolution is sufficient to identify the dark matter halos hosting galaxies with stellar masses of $\approx 1.5 \times 10^{10}\, M_\odot$ (considerably smaller than the Milky Way), and also to predict robustly the internal properties of the halos corresponding to very massive clusters, which are represented by more than 10^5 dark matter particles.

Credits: Max-Planck-Institute for Astrophysics and Virgo consortium. Image obtained with the Millennium XXL Browser.

Ai miei genitori

Acknowledgements

Firstly, I would like to express my sincere gratitude to my supervisor Dr. David Rapetti for believing in me, and for realizing the dream of a little boy that wanted to make sense of the wonders of the universe. I really enjoyed our long, long discussions, engaging at the point we both risked starvation in more than one occasion. I have learned a lot in these years, and the precious freedom you gave me contributed immensely in shaping my future as a scientist.

I am also very grateful to the Niels Bohr Institute and Dark Cosmology Centre for the fantastic opportunities I was presented in all these years. My current network of collaborators and friends from all over the world, and with that this thesis, would have not been possible without their support. In particular, I would like to thank Simon Foreman for his infinite patience with my unsatisfactory understanding of the true theory of the universe, Marco Scalisi for his sacred mate ritual and Hideki Perrier for singing along the limitless loops of 'Petit Poney'.

A big thanks goes to Claudio and Daniele, who despite their busy lives did their best to improve the clarity of this thesis and to limit unavoidable typos. Well, Daniele also deserves a special mention for his *Cataneo Support Committee*, whose declared mission was to cheer me up during the writing process. Thanks for your white T-shirts, devastated cakes and questionable pictures!

This has been a tremendous journey, and being a long one I had many travel buddies. Thanks to the entire extended Italian crew, Adriano, Alberto, Anna, Arianna, Chiara, Claudio, Daniele, Ia, Mario, Martina, Matteo, Nicolò, Stefania and Stefano. During these years you made my time in and outside DARK more enjoyable. And those of you that were unfortunate enough to be around during the writing of this thesis, I would like to let you know that you did a remarkable job at managing my irascible temperament in the final rush. Thanks for keeping me sane!

Of course, my mystagogue holds a special place in my heart and mind. He has been a source of unlimited knowledge, thought-provoking discussions, fun and inspiration for future unconventional careers, to say the least.

Breaks would have not been the same without my fellow foosball addicts: Carlos, Chiara, Jonatan, Johannes, Mario, Mikkel, Nick and Peter. Thanks for all the improbable trajectories challenging the laws of physics.

A gargantuan thanks goes to Verdiana. She literally took care of everything, including myself, in times of big changes. Needless to say that this thesis would not be a real thing without her. Thanks for always being there for me.

Last but not the least, I would like to thank my parents for supporting me throughout all my education, and for teaching me devotion, hard work and that no obstacle is unsurmountable with the power of determination. This thesis is dedicated to you.

Abstract

Various astrophysical data sets support the current standard model of cosmology, in which our universe is well-described on large scales by a cosmological constant (Λ) and cold dark matter (CDM). The ΛCDM paradigm rests on two assumptions: (i) the cosmological principle; and that (ii) Einstein's General Relativity is the correct theory of gravity in the classical limit. The former implies that regardless of our location in the universe, its properties look the same if smoothed on large enough scales. The latter dictates how the universe as a whole and the structures within it evolve, gravitation being the dominant force at large distances. Under these premises, to explain the observed late-time accelerated expansion of the universe we need an exotic form of energy with large negative pressure, named dark energy. Λ is the simplest candidate for this obscure ingredient, and is currently associated with the energy density of the vacuum. Cold dark matter is the second most abundant constituent of the universe, even though it has not been detected yet. This slowly moving collection of particles forms the scaffolding of the stunning, luminous structures we see with our telescopes. Although both dark components are so far in the realm of speculation, a cosmological constant suffers from important theoretical shortcomings.

An alternative is to question the validity of General Relativity on cosmological scales. In fact, cosmic acceleration could stem from gravity behaving differently on the largest scales, eliminating the need for dark energy. Moreover, modifications to General Relativity lead to changes in the formation of structures compared to standard gravity. In particular, the accretion history of collapsed objects, as well as their abundance as a function of mass and time are key probes for such departures. Most of this thesis is devoted to testing gravity on cosmological scales with massive galaxy clusters.

Chapter 1 starts with a discussion on the motivations for considering a cosmological constant. It continues with the general relativistic approach to the homogeneous and isotropic universe, followed by a description of the growth of matter density inhomogeneities at late times. Alternative theories of gravity are also discussed, along with their effects on structure formation. It concludes with a brief description of the main cosmological observables employed in measurements of the growth of structure.

In chapter 2, consistency tests of General Relativity are investigated by means of a popular parametrization of the linear growth rate. X-ray selected galaxy clusters detected in the

ROSAT All-Sky Survey, in combination with robust weak gravitational lensing data, are used to improve cosmological constraints from measurements of the cluster mass function and its evolution. Chapter 3 employs the same cluster number count data to place an upper bound on deviations from General Relativity in the context of chameleon $f(R)$ gravity. The high quality of the cluster growth data analysis reduces the allowed region of parameter space by a factor of ten compared to previous similar studies. However, the theoretical mass function adopted is overly conservative, in that deviations from standard gravity are systematically underestimated. Tighter constraints on the additional scalar degree of freedom of the theory are possible with a more accurate modeling of our predictions. Chapter 4 addresses this topic with a discussion on the refinement of the mass and environment dependent spherical collapse model of chameleon $f(R)$ gravity. This approach is based on the calibration of a phenomenological correction inspired by the parameterized post-Friedmann framework against high-resolution N-body simulations. This method provides predictions for the fractional enhancement of the $f(R)$ halo abundance with respect to that of General Relativity within a precision of $\lesssim 5\%$ from the results obtained in the simulations. These results suggest that upper bounds competitive with current Solar System tests are within reach of cluster number count analyses from ongoing and upcoming surveys at much larger scales.

Nowadays, N-body simulations of the dark matter fluid with impressive mass resolution and box sizes are routinely performed. They give us valuable information on the distribution of matter, covering scales separated by several orders of magnitude, from the whole universe to galactic halos. The complex nonlinear dynamics on small distances makes them an essential tool for the study of structure formation and evolution. Nonetheless, they are extremely time consuming, with a considerable fraction of their computations dedicated to scales in the perturbative regime. This can be avoided on the condition that an accurate analytical treatment of dark matter clustering down to quasi-linear scales is available. The Effective Field Theory of Large-Scale Structure (EFTofLSS) has been developed with this purpose in mind. Within this framework, large-scale structure observables are obtained with arbitrary precision on scales only a factor of a few the size of the largest virialized objects. This comes at the price of including free coefficients that encode the analytically inaccessible information from short distance physics. From a different perspective, however, measuring these quantities as a function of the cosmological parameters could reveal relevant properties of dark matter, such as its sound speed and viscosity. The last chapter presents the rationale of two public codes I developed, which accurately and efficiently explore the cosmology-dependence of the EFTofLSS parameters within the ΛCDM model.

Resumé på Dansk

Forskellige astrofysiske datasæt bekræfter den kosmologiske standardmodel, i hvilken vores univers er beskrevet, på stor skala, af en koslomologisk konstand (Λ) og koldt mørkt stof (CDM). ΛCDM-paradigmet hviler på to antagelser: (i) det kosmologiske princip; og at (ii) Einsteins generelle relativitetsteori er den korrekte teori til beskrivelse af tyndekraft i den klassiske grænse. Det kosmologiske princip betyder, at uanset vores placering i universet, vil dets egenskaber se ens ud, hvis de bliver målt over tilpas stor skala. Einsteins generelle relativitetsteori styrer hvordan universet som helhed, samt de strukturer der udgør det, udvikler sig henover tid, da tyngdekraft er den dominerede kraft over store afstande. Hvis disse to antagelser er korrekte, skal man for at forklare den fundne accelerationen af universet, indføre en eksotisk form for energi, der udøver et negativt tryk, kaldet mørk energi. Λ er den simpleste kandidat til denne mystiske ingrediens, og er forbundet til energitætheden af vacuum. Koldt mørkt stof er den næstmest forekommende bestandel af universet, på trods af at det stadig ikke er set direkte. Denne langsommelige samling partikler former det stillads som understøtter de slående, lysende strukturer vi ser med vores teleskoper. Selvom begge de mørke komponenter stadig ikke er set direkte, så lider den kosmologiske konstant af vigtige teoretiske mangler.

Som alternativ til behovet for den kosmologiske konstant, kan man undersøge om den generelle relativitetsteori gælder på de største skalaer. Faktisk kan den kosmiske acceleration fremkomme hvis tyngdekraften opfører sig anderledes på meget stor skala, hvorved man eliminere behovet for den mørke energi. ændringer i den generelle relativitetsteori vil ændre måden hvorpå strukturer bliver formet, sammenlignet med den klassiske beskrivelse. Specifikt, vil massetilvæksthistorien af kollapsende objekter samt deres forekomst som funktion af masse og tid, være essentielle værktøjer til at undersøge disse afvigelser. Størstedelen af denne afhandling er dedikeret til at teste tyngdekraften på kosmologiske skalaer, ved brug af galaksehobe.

Kapitel 1 starter med en diskussion af motivationen for at overveje en kosmologisk konstant. Det forsætter med den generelt relativistiske tilgang til et homogent og isotropisk univers, efterfulgt af en beskrivelse af hvordan inhomogeniteter i massetætheden vokser, sent i universets udvikling. Alternative tyngdeteorier bliver diskuteret, såvel som deres påvirkning

på hvordan strukturer bliver dannet. Kapitlet bliver afsluttet med en kort beskrivelse af de centrale observable der bliver brugt til målinger af strukturformationen.

I kapitel 2 bliver konsistenstests af den generelle relativitetsteori undersøgt ved hjælp af den populære parametrisation af den lineære vækstrate. Röntgen-udvalgte galaksehobe, fundet ROSAT All-Sky Survey, er sammen med robuste data fra den svage lenseeffekt, brugt til at forbedre de kosmologiske parameterafgrænsninger fra målinger af massefunktionen af galaksehobe og dens udvikling. Kapitel 3 bruger de samme data til at sætte en øvre grænse på afvigelserne fra den generelle relativitetsteori i konteksten af $f(R)$ kameleon tyngdekraft. Den høje kvalitet af hobvækst data-analysen reducerer det tilladte parameterrum med en faktor 10, sammenlignet med hvad tidligere, lignende studier har fundet. Den antagede teoretiske massefunktion er for konservativ, i og med at afvigelserne fra den generelle relativitetsteori, er systematisk underestimerede. Tættere bånd på den tilføjede skalare frihedsgrad bliver mulig med en mere præcis modellering af vores forudsigelser. Kapitel 4 adresserer dette tema med en diskussion af forbedringen af det masse- og omgivelsesafhængige sfæriske kollaps af $f(R)$ kameleon tyngdekraft. Denne tilgang er baseret på kalibreringen af den fænomenologiske korrektion, der er inspireret af den parametriserede post-Friedmann ramme, mod højopløsnings N-body-simuleringer. Denne metode giver forudsigelser på den fraktionelle forbedring af $f(R)$ halo forekomsten med hensyn til den generelle relativitetsteori med $\lesssim 5\%$ fra de resultater der er obnået med simuleringerne. Disse resultater viser at den øvre grænser opnået er konkurrencedygtige med solsystemstests og inden for vores rækkevidde med de nuværende og fremtidige tælletal af galaksehobe i meget større skala.

Nutildags er N-body-simuleringer af mørkt stof med imponerede massopløsning og boksstørrelse en rutineoperation. De giver os vigtig information om fordelingen af stof, hvor flere skalaer kan dækkes samtidig, fra hele universet til enkelte haloer. De komplekse ikke-lineære dynamikker der virker på korte afstande, gør dem til essentielle værktøjer i studiet af strukturformation og udvikling. Ikke desto mindre, er de ekstremt tidskrævende, med en væsentlig del af deres udregninger dedikeret til udregninger i det pertubative regime. Dette kan blive undgået på den betingelse at en præcis analytisk behandling af sammenklumpningen af mørkt stof, ned til den kvasi-lineære grænse er tilgængelig. Den effektive feltteori for storskala struktur (EFTofLSS) er blevet udviklet til netop dette formål. Inden for denne ramme, kan de observable af storskalastrukturen, opnåes med arbitrær præcision, på skalaer kun et par størrelsesklasser over de største visualisede objekter. Dette kommer på bekostning af frie koefficienter der indeholder den analytisk utilgængelige information fra den fysik der virker på kort afstand. Fra et andet perspektiv kan målingen af disse størrelser som funktion af de kosmologiske parametre, vise sig at indeholde vigtig information of mørkt stof, som lydens hastighed i mørkt stof og dets viskositet. Det sidste kapitel præsenterer to offentligt tilgængelige koder jeg har udviklet. Disse koder kan præcist og effektivt udforske kosmologiafhængigheden af EFTofLSS parametrene, inden for ΛCDM-modellen.

Table of contents

Chapter 1

Introduction

This chapter serves as a common thread to guide the reader through the core content of this thesis, presented in chapters 2–5. Sec. 1.1 briefly reviews the observational evidence for dark energy coming from a variety of independent data sets. Sec. 1.2 provides the basic mathematical framework for understanding the phenomenology of dark energy and unfolding the information encoded in cosmological data. Sec. 1.3 focuses on a specific class of theories that attempts to explain the mysterious dark energy by invoking modifications of the law of gravity on cosmic scales. Finally, sec. 1.4 summarizes the cosmological observables modeled or employed in the following chapters to measure the growth of structure in our universe.

1.1 Why do we need dark energy?

In 1998, two teams of astronomers investigating the relationship between distance and luminosity of type Ia supernovae (SNe Ia) independently reported that the universe is expanding at an accelerated rate (Riess et al. 1998; Perlmutter et al. 1999). For most of the scientific community this came as an absolute surprise. Since the discovery of the cosmic expansion (Hubble 1929), cosmologists had expected to observe a gradual slow down of this expansion due to the gravitational pull of all the matter in the universe. The discovery of cosmic acceleration is unanimously considered a major breakthrough in modern cosmology, with developments capable of shaking our current understanding of nature's clockwork.

Despite the tremendous amount of clever ideas aimed at explaining the physical origin of cosmic acceleration (for reviews see e.g., Copeland, Sami, and Tsujikawa 2006; Clifton, Ferreira, et al. 2012), to date none of them seems compelling enough. For lack of a better understanding, all these theories have been grouped under the name of *dark energy*, the simplest of which is the cosmological constant Λ (Weinberg 1989b) – a new smooth form of energy with constant density in time. In the Λ Cold Dark Matter (ΛCDM) paradigm, Einstein's theory of General Relativity (GR) (Einstein 1916) describes gravity at all scales,

and Λ provides the large negative pressure that leads to the observed accelerated expansion by contributing to 70% of the present energy density of the universe. The remaining 30% is shared between dark matter (25%), and ordinary (or baryonic) matter (5%). Dark matter is still to be identified and does not interact with light. It is a necessary ingredient to the formation of structures, from the smallest galaxies up to the clusters, filaments, sheets and walls forming the cosmic web.

Since 1998, a growing body of observational evidence has confirmed that dark energy is a fundamental component of our universe, affirming the ΛCDM model as the new standard model of cosmology. In fact, this model has shown remarkable consistency across several independent data sets:

- **Type Ia supernovae.** These exploding stars provide bright, standardizable candles, which means they can be observed up to large distances and the amount of light they give off is approximately the same independently of their location in time and space. These properties are ideal to measure the cosmic expansion and its late-time acceleration. In the years following the pioneering works of Riess et al. (1998) and Perlmutter et al. (1999), the quality and quantity of distant supernovae data had benefited from space-based and ground-based surveys (see Fig. 1.1) (Conley et al. 2011; Suzuki et al. 2012; Betoule et al. 2014; Rest et al. 2014). Together with an improved modeling of systematic uncertainties, this strengthened the evidence for acceleration and dispelled all doubts about the first supernova results.

- **Cosmic microwave background.** Anisotropies of the cosmic microwave background (CMB) provide a window on the early universe, when it was about 380,000 years old (see top panel in Fig. 1.2) (e.g., see Hu and Dodelson 2002). The auto- and cross-power spectra of CMB temperature and polarization anisotropies are characterized by acoustic peaks associated with gravity-driven sound waves in the photon-baryon fluid (see bottom panel in Fig. 1.2). The amplitudes and positions of these peaks tell us a great deal about the universe's constituents and expansion history, and they are fully consistent with dark energy in the form of a cosmological constant taking up 70% of the present energy budget (see e.g., Keisler et al. 2011; Hinshaw et al. 2013; Story et al. 2013; Das et al. 2014; Ade et al. 2015a). Moreover, the bending of CMB photons' trajectories, caused by the intervening mass of the large scale structure between us and the surface of last scattering, provides additional information in agreement with Λ (Reichardt et al. 2012; Engelen et al. 2012; Das et al. 2014; Ade et al. 2015b). A dark energy component is also required to explain the large-angle anisotropy of the CMB related to the late-time integrated Sachs-Wolfe (ISW) effect – a secondary anisotropy caused by the differential redshifts of CMB photons as they cross the evolving gravitational potential wells in the large-scale structure (Ade et al. 2015c).

- **Clustering of galaxies.** Galaxies are not randomly distributed in space. Due to gravity, they clump into massive structures called clusters, flowing through filaments and sheets of dark matter that form the so-called cosmic web, while leaving empty regions of space referred to as voids (see top panel in Fig. 1.3). The clustering of galaxies is a dynamical process, and its evolution in time depends sensibly on the relative balance between dark matter and dark energy. The presence of a cosmological constant leads to larger voids and higher density contrasts between overdense and underdense regions compared to a universe filled only with dark and ordinary matter. In practice, the distribution of galaxies in the universe can be described by n-point correlations functions. The first statistically meaningful quantity used to study the clustering of matter on large scales is the two-point correlation function (see right panel in Fig. 1.4), or equivalently its Fourier transform, the power spectrum (see bottom panel in Fig. 1.3). The observed clustering of galaxies provides further evidence for the existence of dark energy in the form of a cosmological constant.

- **Baryon acoustic oscillations.** The baryon acoustic oscillations (BAO) generating the peaks in the CMB anisotropy leave also a small imprint in the galaxy two-point correlation function at later times (see left panel in Fig. 1.4). This can be used as a standard ruler with a characteristic length scale of $\sim 100\,h^{-1}$ Mpc[1] (see right panel in Fig. 1.4). Measurements of the BAO scale at different epochs are complementary to other probes and are consistent with a late-time accelerated expansion driven by a cosmological constant (see e.g., Eisenstein et al. 2005; Blake et al. 2011a; Beutler et al. 2011; Padmanabhan, Xu, et al. 2012; Anderson et al. 2014b; Anderson et al. 2014a; Kazin et al. 2014; Ross, Samushia, et al. 2015).

- **Weak gravitational lensing.** Similarly to CMB photons, the incoming light from distant galaxies passes through the structures forming the cosmic web before reaching us (see top panel in Fig. 1.3). The net effect is a small, correlated distortion of the original galaxy shapes due to the gravitational lensing of the large scale structure shown in the left panel of Fig. 1.5 (see e.g., Munshi, Valageas, et al. 2008). Therefore, this cosmic shear carries information on the clustering of dark matter and indirectly on the presence of dark energy, that suppresses the growth of structure on cosmological scales by means of the accelerated expansion. This data further supports a universe dominated by Λ (see right panel in Fig. 1.5) (Kilbinger et al. 2013; Abbott et al. 2016).

- **Galaxy clusters.** These are the largest collapsed objects in the universe, and their number, clustering and composition are tightly connected to the expansion history of the universe and the growth of structure within it. As such, they can be used to

[1] Mpc stands for megaparsec, which is equivalent to 3.09×10^{19} km. The h factor is a rescaling that accounts for the current size of the universe (see sec. 1.2.1 for details).

test dark energy. One possible avenue consists in measuring the X-ray fluxes and temperatures associated with the hot emitting gas confined in dynamically relaxed clusters. Deconvolution of these two quantities gives the cluster gas mass (baryons) and its total mass (baryons+dark matter). The predicted fraction of total mass residing in gas, $f_{\rm gas}$, is a constant approximately given by the ratio of the background density of baryons to the background density of all matter, namely $f_{\rm gas} \approx \Omega_{\rm b}/\Omega_{\rm m}$ (see right panel in Fig. 1.6). This expectation follows from the fact that both quantities scale as the inverse of the volume of the universe, and when galaxy clusters form the relative abundance of these two types of matter reflects that of the background at any given epoch. Results from gas mass fractions are aligned to those from other methods, with ΛCDM being a very good fit to the data and ruling out with a high confidence level models of the universe without dark energy (Allen, Schmidt, and Fabian 2002; Allen, Schmidt, Ebeling, et al. 2004; Allen, Rapetti, et al. 2008; Mantz et al. 2014).

Thanks to cosmological N-body simulations, the number density of galaxy clusters in the universe, each associated to a dark matter halo, can be accurately predicted as a function of redshift (i.e. time) and mass (see right panel in Fig. 1.6). The comparison of these expectations to cluster number counts from deep, large-area cluster surveys provides strong support for Λ (A. Mantz, S. W. Allen, et al. 2008; Vikhlinin et al. 2009; Mantz, Allen, Rapetti, and Ebeling 2010; Mantz et al. 2015). The strength of this probe is the capability of probing simultaneously the expansion history (survey volume) and the late-time growth of structure (cluster formation).

- **Age of the universe.** From measurements of the matter-energy content of the universe, and how this is distributed among the different species, we can infer how long the universe has been expanding. Independent age estimators must give consistent results, a fact that can be used to investigate dark energy. One example is to compare the age of the universe from cosmological probes with the ages of the oldest stars in globular clusters. Once more, a universe without dark energy cannot accommodate both measurements simultaneously (Krauss and Chaboyer 2003).

In spite of these remarkable successes, a cosmological constant poses serious problems from the viewpoint of particle physics. In this context, Λ is mathematically equivalent to the energy density of empty space, the vacuum. However, theoretical expectations for the vacuum energy density are at least 60 orders of magnitude larger than the observed cosmological value, arguably the worst prediction in the history of physics known as the "cosmological constant problem" (Weinberg 1989b). Although different strategies to alleviate this discrepancy have been put forward in the years, none of them can make sense of the smallness of the measured cosmological constant without incurring ad hoc unsatisfactory fine-tuning or unpredictability (see e.g., Padilla 2015 and references therein).

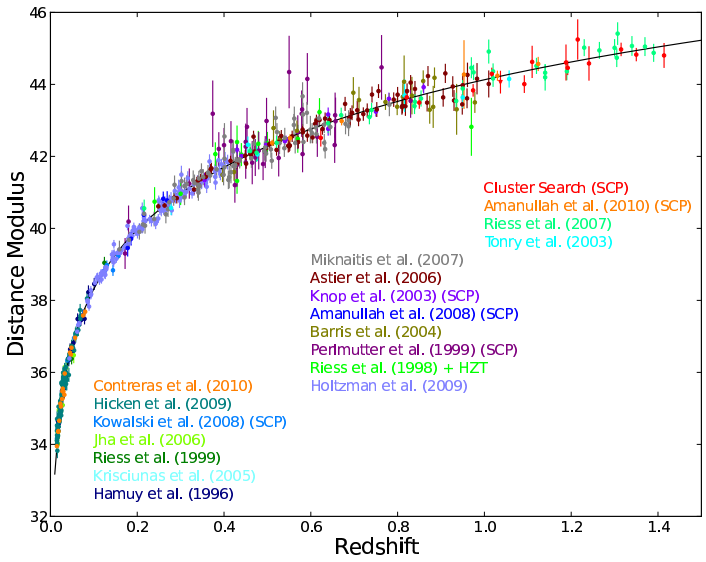

Fig. 1.1 Hubble diagram for the Union2.1 compilation of Type Ia supernovae showing distance modulus (the difference between apparent and absolute magnitudes) versus redshift (caused by the expansion of the universe) measurements. The solid line illustrates the prediction for a universe filled at 70% with a cosmological constant and at 30% with ordinary and dark matter. Figure taken form Suzuki et al. (2012).

Another unsolved conundrum is the so-called "coincidence problem". If the cosmological constant is responsible for the late-time accelerated expansion, the similarity between its observed value and the current matter density might look somewhat unlikely. As the universe expands their relative abundance rapidly changes, with matter dominating at early epochs and dark energy prevailing in the future. There is only a brief window (in cosmological terms) in which the two energy densities are comparable, and we are living right through it. Many possible solutions to this problem have been formulated, but this apparent coincidence still remains an open question.

In light of the above considerations, it seems worth exploring theoretical alternatives to the cosmological constant, regardless of its triumphs. Under the assumption of isotropy and homogeneity on large scales, the observed phenomenology of dark energy can be reproduced in two ways: (i) as a modification of the matter-energy content of the universe (see e.g., Copeland, Sami, and Tsujikawa 2006; Amendola and Tsujikawa 2010); (ii) as a modification of the laws of gravity, i.e. of General Relativity (see e.g., Clifton, Ferreira, et al. 2012). Part of this thesis will focus on searching for departures from GR in cosmological data, in particular using the abundance of galaxy clusters as a probe of gravity.

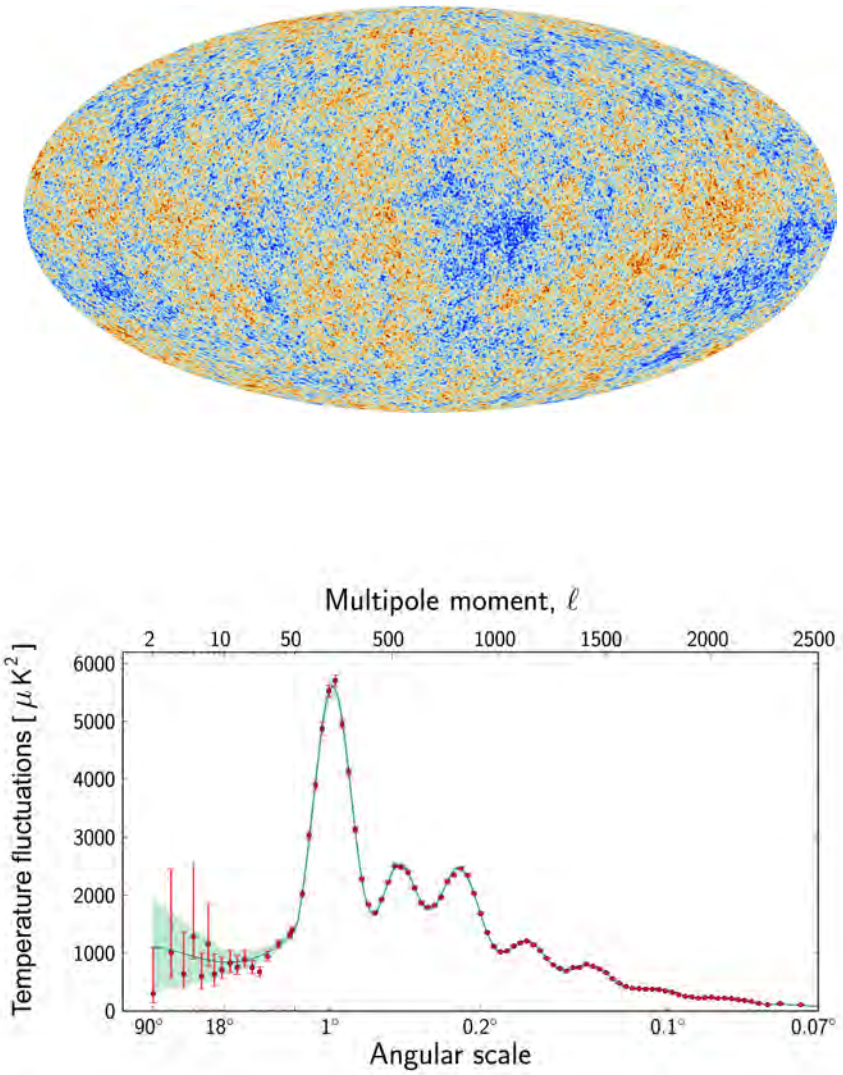

Fig. 1.2 *Top:* all-sky picture of the primordial universe as seen by the Planck satellite. The temperature fluctuations of the cosmic microwave background are shown as color differences. They are the seeds that through gravitational instability will evolve into the stars and galaxies of today. *Bottom:* angular power spectrum of the cosmic microwave background anisotropies shown in the top panel. Data points corresponding to measurements from *Planck* are overlapped to the best-fit ΛCDM cosmology (green curve). (Copyright: ESA and the Planck Collaboration)

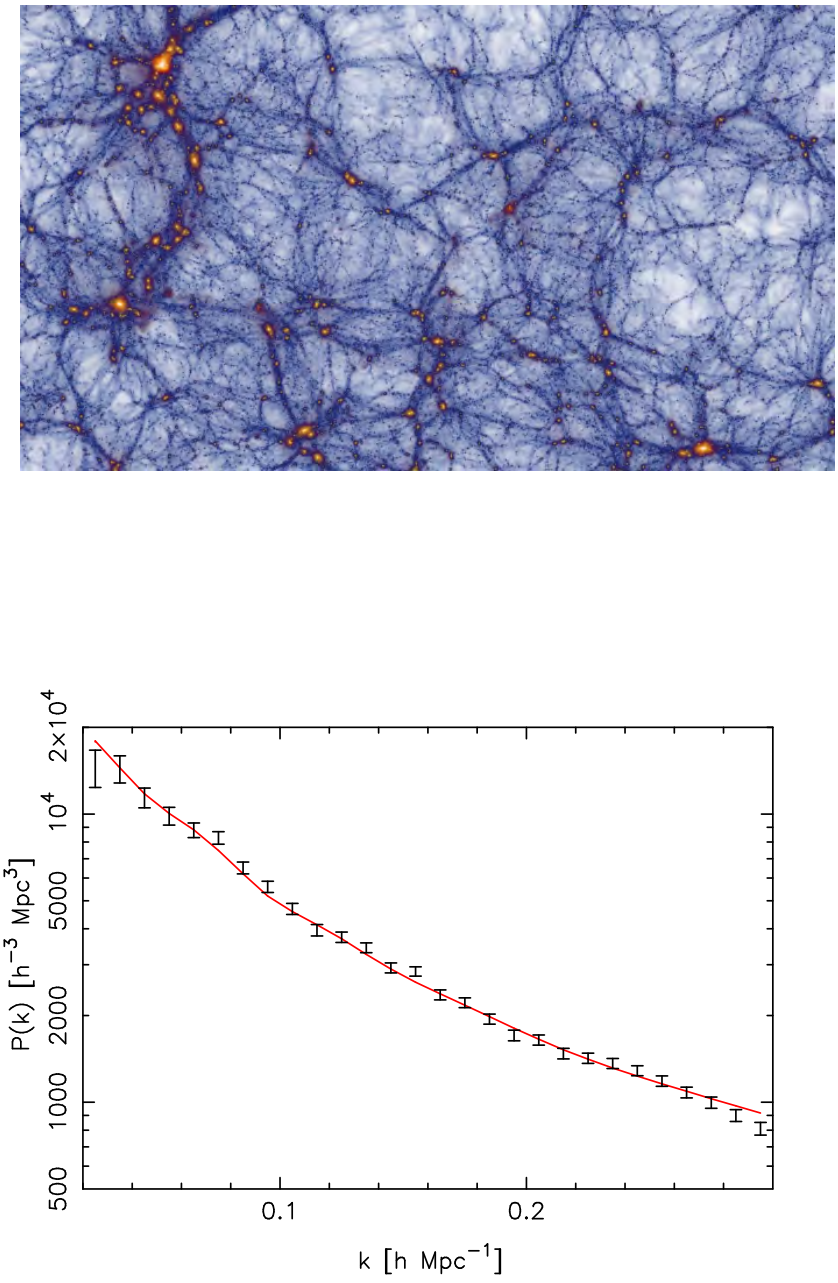

Fig. 1.3 *Top:* dark matter distribution in the Millenium XXL cosmological simulation. The dark blue web-like structure represents overdense regions (clusters, filaments and sheets) delimiting large underdense volumes (voids). Dark matter halos hosting galaxies and clusters of galaxies are shown in yellow/orange tone. (Credits: the Millenium XXL browser) *Bottom:* comparison of the galaxy power spectrum prediction in ΛCDM (red curve) to the WiggleZ Dark Energy Survey measurements (black). (Taken from Blake, James, and Poole 2014)

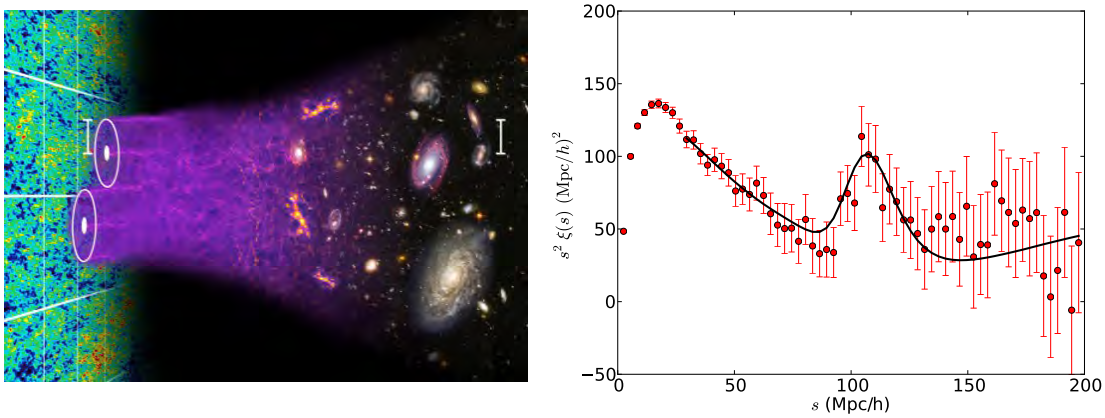

Fig. 1.4 *Left:* artist's impression of the baryon acoustic oscillations concept. These features are imprinted in the cosmic microwave background (bottom panel in Fig. 1.2) and can still be seen today in the large-scale distribution of galaxies, which makes them an ideal standard ruler to measure the expansion history of the universe. (Credits: the Sloan Digital Sky Survey III website, with courtesy of Chris Blake and Sam Moorfield). *Right:* baryon acoustic peak detection in the two-point galaxy correlation function of the luminous red galaxies sample in the Sloan Digital Sky Survey Data Release 7 (red points). The black curve represents the best-fit prediction for the ΛCDM cosmology with about 70% of the total energy in the universe in the form of a cosmological constant. Figure taken from Padmanabhan, Xu, et al. (2012).

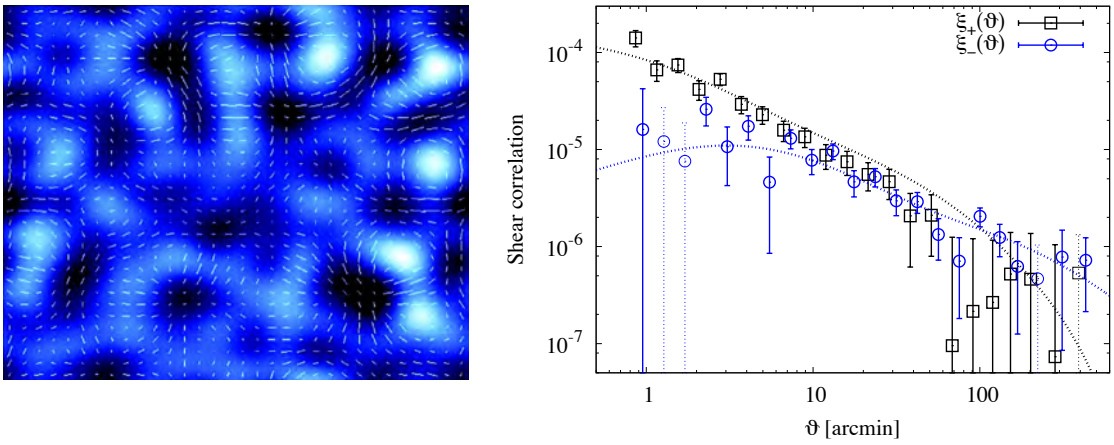

Fig. 1.5 *Left:* Illustration of weak gravitational lensing from a cosmological N-body simulation. The projected mass distribution of dark matter is shown in blue tones, with bright regions indicating overdensities. The cosmic shear field (white tick marks) corresponds to the average shapes and orientations of distant faint galaxies (assumed statistically to be round in shape) viewed through the intervening dark matter. Where the dark matter clumps, the background galaxies align tangentially around the structure; around voids, on the other hand, the galaxies align radially. This correlation of the shear field with the foreground mass distribution allows us to investigate the clustering properties of the (invisible) dark matter (taken from Ellis 2010). *Right:* two-point correlation functions of the cosmic shear field measured by the Canada-France Hawaii Telescope Lensing Survey. ξ_+ (black squares) and ξ_- (blue circles) correspond to a conveniently chosen decomposition of the correlation function. The dotted lines represent the predictions for the best-fit ΛCDM cosmology resulting from the analysis of independent CMB data.

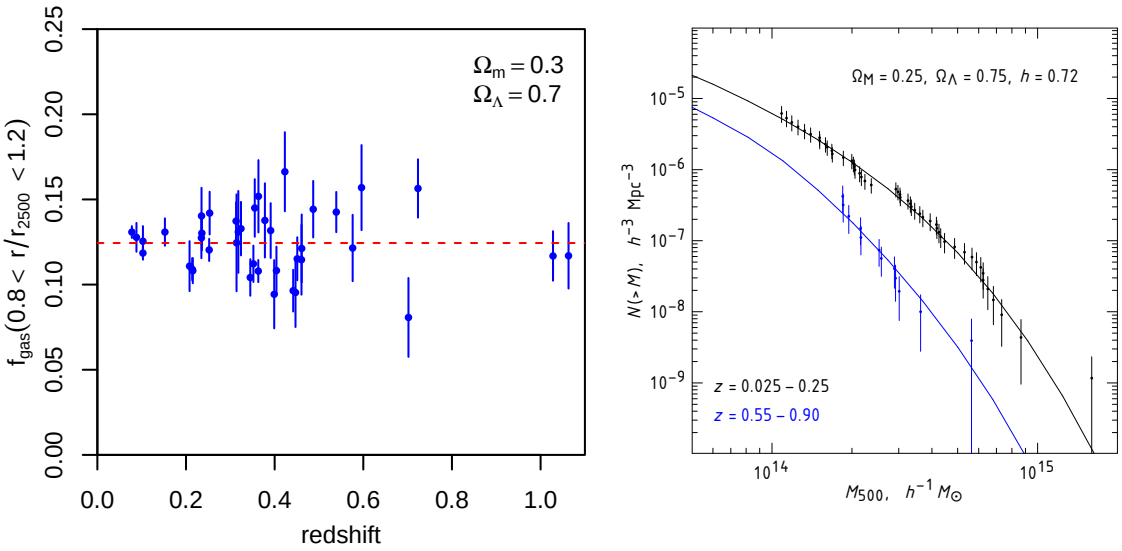

Fig. 1.6 *Left:* Gas mass fractions versus redshift measurements for a ΛCDM cosmology with a cosmological constant taking up 70% of the full energy budget in the universe (blue points). The constant red dashed line shows that the data is consistent with the expectation of no evolution (taken from Mantz et al. 2014). *Right:* the measured number densities of galaxy clusters as a function of mass at low (black bars) and high redshifts (blue bars) are in very good agreement with predictions for the ΛCDM model (solid lines), making a strong case for the presence of dark energy (figure taken from Vikhlinin et al. 2009).

1.2 The concordance model

The growing observational evidence in favor of the ΛCDM cosmology has earned it the name of *concordance model*. This model is based on the assumptions that the universe is homogenous and isotropic on large scales ($\gtrsim 100\,\mathrm{Mpc}$), and that GR is the correct theory of gravity. Given a set of boundary conditions, the evolution of the universe can then be derived from the action

$$S_{\Lambda\mathrm{CDM}} = \frac{1}{16\pi G}\int \mathrm{d}^4x\sqrt{-g}(R - 2\Lambda) + S_{\mathrm{matter}}(g_{\mu\nu}, \psi_{\mathrm{m}}^{(i)}), \tag{1.1}$$

where G is Newton's gravitational constant, and here and throughout we adopt natural units $c = \hbar = 1$ and metric signature $(-,+,+,+)$. In Eq. (1.1) the integral is performed in the 4-dimensional spacetime, $g_{\mu\nu}$ is the metric tensor[2] describing the spacetime structure at each point, g is the metric determinant, R is the Ricci scalar constructed from the metric, which carries information on the intrinsic curvature of spacetime. The fields $\psi_{\mathrm{m}}^{(i)}$ represent all standard particles (i.e. photons, electrons, protons, neutrons, neutrinos etc.) and dark matter. At late times, most of the ordinary non-relativistic matter (generically called baryons) is in the form of hydrogen, deuterium, helium, but also free protons and electrons. Contrary to dark

[2]Greek indices run from 0 to 3.

matter, baryons can interact with photons, and on small scales ($\lesssim 1\,\mathrm{Mpc}$) the electromagnetic interaction impacts significantly on their dynamics. On cosmological scales, however, gravity is the dominant force shaping the universe implying that baryonic and dark matter behave similarly. Cosmologists simply group them under the name of *matter*. In what follows, we will stick to this convention and make the distinction only when appropriate.

Einstein's field equations are obtained requiring stationarity of the action Eq. (1.1) under variations of $g^{\mu\nu}$, i.e. $\delta S_{\Lambda\mathrm{CDM}}/\delta g^{\mu\nu} = 0$, which gives (see, e.g., Amendola and Tsujikawa 2010)

$$R_{\mu\nu} - \frac{1}{2} g_{\mu\nu} R + \Lambda g_{\mu\nu} = 8\pi G T_{\mu\nu}, \tag{1.2}$$

where $R_{\mu\nu}$ is the Ricci tensor that contracted gives[3] $R = g^{\mu\nu} R_{\mu\nu}$, and

$$T_{\mu\nu} \equiv -\frac{2}{\sqrt{-g}} \frac{\delta S_{\mathrm{matter}}}{\delta g^{\mu\nu}} \tag{1.3}$$

is the energy-momentum tensor describing the energy and momentum of all matter fields. By defining $T^{(\Lambda)}_{\mu\nu} \equiv -\Lambda g_{\mu\nu}/8\pi G$ and $\hat{T}_{\mu\nu} \equiv T_{\mu\nu} + T^{(\Lambda)}_{\mu\nu}$, Eq. (1.2) can be rewritten as

$$G^{\mu}_{\nu} \equiv R^{\mu}_{\nu} - \frac{1}{2} \delta^{\mu}_{\nu} R = 8\pi G \hat{T}^{\mu}_{\nu}, \tag{1.4}$$

where G^{μ}_{ν} is the Einstein tensor, δ^{μ}_{ν} is Kronecker's delta, and indices have been raised with the metric. The Bianchi identities ensure the total energy-momentum tensor conservation (see e.g., Carroll 2004)

$$\nabla_{\mu} \hat{T}^{\mu}_{\nu} = 0, \tag{1.5}$$

a result that will prove very useful to study the expansion of the universe and the formation of its large-scale structure. In Eq. (1.5) the differential operator ∇_{μ} denotes the covariant derivative constructed from the metric tensor and its derivatives,

$$\nabla_{\mu} \hat{T}^{\mu}_{\nu} = \partial_{\mu} \hat{T}^{\mu}_{\nu} + \hat{T}^{\alpha}_{\nu} \Gamma^{\mu}_{\alpha\mu} - \hat{T}^{\mu}_{\alpha} \Gamma^{\alpha}_{\nu\mu}, \tag{1.6}$$

where $\partial_{\mu} \equiv \partial/\partial x^{\mu}$ and the Christoffel symbols are

$$\Gamma^{\mu}_{\nu\alpha} = \frac{1}{2} g^{\mu\rho} (\partial_{\alpha} g_{\rho\nu} + \partial_{\nu} g_{\rho\alpha} - \partial_{\rho} g_{\nu\alpha}), \tag{1.7}$$

which also define the Ricci tensor above as

$$R_{\mu\nu} = \partial_{\alpha} \Gamma^{\alpha}_{\mu\nu} - \partial_{\nu} \Gamma^{\alpha}_{\mu\alpha} - \Gamma^{\alpha}_{\mu\nu} \Gamma^{\beta}_{\alpha\beta} - \Gamma^{\alpha}_{\mu\beta} \Gamma^{\beta}_{\alpha\nu}. \tag{1.8}$$

[3] According to Einstein summation notation repeated indices are implicitly summed over.

1.2.1 Background expansion

Observations of the large-scale distribution of galaxies and the near-uniformity of the CMB temperature ($\delta T_{\rm CMB}/T_{\rm CMB} \sim 10^{-5}$) strongly suggest that our universe is nearly homogeneous and isotropic on cosmic scales. Homogeneity implies that observers at different locations measure the same average distribution of matter on the largest scales. Isotropy, instead, means that what we observe from any given place in the universe is independent of the direction we look in. These are the two pillars of the *cosmological principle*. Homogeneity and isotropy are properties mathematically equivalent to the invariance of space under translations and rotations, respectively. Time is clearly not involved. In fact, after Hubble (1929) first observed that distant galaxies are receding from us, it soon was realized that the universe is not static, but changing with time. It follows that an adequate description of the universe on scales $\gtrsim 100\,$Mpc is provided by the Friedmann-Lemaître-Robertson-Walker (FLRW) spacetime. In the language of general relativity, the distance between two infinitesimally close events in spacetime is given by the line-element

$$\mathrm{d}s^2 = g_{\mu\nu}\mathrm{d}x^\mu \mathrm{d}x^\nu = -\mathrm{d}t^2 + a^2(t)\mathrm{d}\Sigma^2, \tag{1.9}$$

where $a(t)$ is the scale factor describing the evolution of space as a function of cosmic time t, and

$$\mathrm{d}\Sigma^2 = \gamma_{ij}\mathrm{d}x^i\mathrm{d}x^j = \frac{\mathrm{d}r^2}{1-Kr^2} + r^2(\mathrm{d}\theta^2 + \sin^2\theta\mathrm{d}\phi^2) \tag{1.10}$$

is the line-element associated with the time-independent maximally symmetric metric γ_{ij} of the 3-dimensional space. The curvature of space K can take three values: $K = 0$ corresponds to a spatially flat, Euclidean universe, $K = +1$ to a closed universe (three-sphere), and $K = -1$ to an open universe (saddle). In Eq. (1.10) $(x^1, x^2, x^3) = (r, \theta, \phi)$ are comoving polar coordinates, and the Latin indices i and j run from 1 to 3.

In the FLRW spacetime the only allowed form of the energy-momentum tensor is that of a perfect fluid, that is

$$\hat{T}^\mu_\nu = \sum_I \mathrm{diag}(-\bar{\rho}_I, \bar{P}_I, \bar{P}_I, \bar{P}_I), \tag{1.11}$$

where $\bar{\rho}_I$ and $\bar{P}_I$ are the background (homogeneous) energy density and pressure of the matter field I, including also the cosmological constant Λ. More generally, the energy-momentum tensor for each fluid can be written in the following, explicitly covariant, form

$$T^\mu_\nu = (\bar{\rho} + \bar{P})U^\mu U_\nu + \bar{P}\delta^\mu_\nu, \tag{1.12}$$

where U^μ is the relative 4-velocity between the fluid and the observer. Of course, we recover Eq. (1.11) for $U^\mu = (-1, 0, 0, 0)$, i.e. in the rest-frame of the fluid. Taking the (00) and (ii) components of Einstein equations (1.4), and using Eqs. (1.9)–(1.11), gives the Friedmann

equations

$$H^2 = \frac{8\pi G}{3}\sum_i \bar{\rho}_i - \frac{K}{a^2}, \tag{1.13a}$$

$$\frac{\ddot{a}}{a} = -\frac{4\pi G}{3}\sum_i (\bar{\rho}_i + 3\bar{P}_i), \tag{1.13b}$$

where $H \equiv \dot{a}/a$ is the Hubble parameter and characterizes the rate of expansion of the universe. The value of the Hubble parameter at the present epoch is called the Hubble constant, H_0, which is often parametrized as

$$H_0 = 100\ h\,\mathrm{kms}^{-1}\mathrm{Mpc}^{-1}, \tag{1.14}$$

with $h \approx 0.7$ from recent measurements. Cosmological scales are typically compared to the Hubble length

$$d_H = c/H_0 \approx 3 \times 10^3\, h^{-1}\ \mathrm{Mpc}, \tag{1.15}$$

and Hubble time

$$t_H = 1/H_0 \approx 9.8 \times 10^9\, h^{-1}\ \mathrm{yr}, \tag{1.16}$$

where for clarity we have temporarily reintroduced the speed of light c. In addition, we define the critical density $\bar{\rho}_{\mathrm{crit}} \equiv 3H^2/8\pi G$, as the total energy density of a flat universe. Eq (1.13b) is also known as the acceleration equation, and tells us if the expansion is slowing down ($\ddot{a} < 0$), accelerating ($\ddot{a} > 0$) or constant ($\ddot{a} = 0$) in relation to the components filling the universe.

Another important piece of information comes from the conservation of the energy-momentum tensor. In particular, the time component of Eq. (1.5) yields the continuity equation

$$\dot{\bar{\rho}}_i + 3H\bar{\rho}_i(1 + w_i) = 0, \tag{1.17}$$

where each fluid is separately conserved, and we have defined the equation-of-state parameter $w_i \equiv \bar{P}_i/\bar{\rho}_i$. Hence, introducing the dimensionless density parameters $\Omega_i(t) \equiv \bar{\rho}_i/\bar{\rho}_{\mathrm{crit}}$, Eq. (1.13) can be recast as

$$\sum_i \Omega_i(t) - 1 = \frac{K}{(aH)^2}, \tag{1.18a}$$

$$\frac{\ddot{a}}{a} = -\frac{4\pi G}{3}\sum_i \bar{\rho}_i(1 + 3w_i). \tag{1.18b}$$

The evolution of the energy density derives directly from solving Eq. (4.5), which gives

$$\bar{\rho}_i \propto a^{-3(1+w_i)}. \tag{1.19}$$

For non-relativistic matter, which includes both dark matter and baryons, $w_\mathrm{m} \approx 0$; for radiation, i.e. relativistic particles, $w_\mathrm{r} = 1/3$; for a cosmological constant, $P_\Lambda = -\rho_\Lambda = -\Lambda/8\pi G$, thus $w_\Lambda = -1$ (see, e.g., Amendola and Tsujikawa 2010 for a detailed derivation). In the single fluid approximation (i.e. one cosmological fluid dominates the energy-momentum tensor describing the matter content of the universe) Eq. (1.18b) informs us that an accelerated expansion ($\ddot{a} > 0$) occurs for an equation of state $w < -1/3$. The only candidate among the fluids discussed above is the cosmological constant.

From Eq. (1.19), the energy densities of the different cosmological fluids evolve as

$$\bar{\rho}_\mathrm{m} \propto a^{-3},\ \bar{\rho}_\mathrm{r} \propto a^{-4},\ \rho_\Lambda \propto a^{0}. \tag{1.20}$$

The expansion of the universe ($a(t_1) < a(t_2)$ for $t_1 < t_2$) dilutes each fluid differently, with radiation rapidly falling off below non-relativistic matter first, and Λ later. In this thesis, we are mainly interested in the late-time evolution of the universe, when dark matter and dark energy dominate over radiation, and in what follows we will neglect any contribution from relativistic particles. We will make a further simplification based on the fact that observations indicate that our universe is very close to a Euclidean geometry, i.e. $|\sum_i \Omega_i(t) - 1| \approx 0$ (Ade et al. 2015a). Hence, hereafter we will set $K = 0$, with the two free parameters Ω_m and H_0 fully describing the late-time background universe.

Distances in cosmology

In order to measure the cosmological parameters that define our universe, we need to introduce the concept of distance in an expanding background. From observations, we can infer the distance from an object in a number of ways, e.g. through a comparison of its apparent brightness to its intrinsic luminosity, or its apparent angular size to its physical extent. The light emitted by some source becomes red-shifted due to the expansion of space, and this fact is used to describe the evolution of the universe. The change in the wavelength λ can be quantified by the redshift z as

$$1 + z = \frac{\lambda_0}{\lambda} \equiv \frac{a_0}{a}, \tag{1.21}$$

where the subscript zero denotes the quantities given at the present epoch, and we will follow the common convention of setting the scale factor $a_0 = 1$.

The first important distance definition is the so-called comoving distance, which remains unchanged during the evolution. This is opposed to the physical distance, that instead scales proportionally to the scale factor. From Eq. (1.9), the light traveling along the radial direction satisfies the geodesic equation $\mathrm{d}s^2 = -\mathrm{d}t^2 + a^2(t)\mathrm{d}r^2 = 0$. For photons emitted at time $t = t_1$ with $r = r_1$ (redshift z) that reach an observer at time $t = t_0$ with $r = 0$ ($z = 0$),

the comoving distance can be obtained by integration of the geodesic equation and reads

$$\chi \equiv r_1 = \int_0^{r_1} \mathrm{d}r = -\int_{t_0}^{t_1} \frac{\mathrm{d}t}{a(t)} = \frac{1}{H_0}\int_0^z \frac{\mathrm{d}z'}{E(z)}, \tag{1.22}$$

where $E(z) \equiv H(z)/H_0$, and in the last equality we have used Eq. (1.21) and the definition of the Hubble parameter.

For an object of intrinsic luminosity L, we can employ the inverse-square law to infer the luminosity distance d_L to the object from the measured energy flux F. The luminosity distance is related to the comoving distance through (see e.g., Copeland, Sami, and Tsujikawa 2006)

$$d_L(z) \equiv \sqrt{\frac{L}{4\pi F}} = (1+z)\chi(z). \tag{1.23}$$

This distance is very useful, e.g., in observations of Type Ia supernovae, where the luminosity of the exploding star provides a mean to measure the expansion rate of the universe.

For observations of characteristic length scales (e.g. BAO), it is more appropriate to employ the angular-diameter distance d_A. This can be derived from the geodesic equation of a light ray traveling across a region of space of physical size Δx oriented orthogonally to the line of sight, i.e. $r = \text{const.}$, and located at redshift z (or $t = t_1$). The observer can conveniently choose a coordinate system such that $\phi = \text{const.}$, which upon integration gives

$$\Delta x = a(t_1)\chi\Delta\theta, \tag{1.24}$$

where $\Delta\theta$ is the apparent angular size of the region. In practice, the angular-diameter distance is defined by $d_A \equiv \Delta x/\Delta\theta$, a quick comparison to Eq. (1.25) yields

$$d_A(z) = a(t_1)\chi(z) = \frac{\chi(z)}{1+z} = \frac{d_L(z)}{(1+z)^2}. \tag{1.25}$$

Note that all distances defined above have a different form for curved universes (see e.g., Amendola and Tsujikawa 2010).

1.2.2 Linear growth of structure

As a matter of fact, the universe we live in is not perfectly homogeneous. The infant universe experienced a period of rapid accelerated expansion known as *inflation*, in which quantum fluctuations of the inflaton field stretched to cosmic scales, planting the seeds of all structures we see today.

To understand the formation and evolution of the large-scale structure, we need to extend the simplified FLRW treatment. Specifically, we will split all quantities into homogeneous background values, that depend only on time, and spatially dependent perturbations (for a

comprehensive treatment, see e.g., Weinberg (2008) and references therein). For the metric this means that we write

$$g_{\mu\nu} = \bar{g}_{\mu\nu}(t) + \delta g_{\mu\nu}(t, \boldsymbol{x}), \tag{1.26}$$

while density and pressure fluctuations in the fluid are defined as

$$\rho = \bar{\rho}(t) + \delta\rho(t, \boldsymbol{x}), \tag{1.27}$$

$$P = \bar{P}(t) + \delta P(t, \boldsymbol{x}). \tag{1.28}$$

This leads to perturbations in the Einstein tensor and the energy-momentum tensor

$$G^{\mu}_{\nu} = \bar{G}^{\mu}_{\nu}(t) + \delta G^{\mu}_{\nu}(t, \boldsymbol{x}), \tag{1.29}$$

$$T^{\mu}_{\nu} = \bar{T}^{\mu}_{\nu}(t) + \delta T^{\mu}_{\nu}(t, \boldsymbol{x}), \tag{1.30}$$

where to avoid cumbersome notation we have defined $T^{\mu}_{\nu} \equiv \hat{T}^{\mu}_{\nu}$, also including the vacuum energy component. We derived the equations for the background quantities in sec. 1.2.1,

$$\bar{G}^{\mu}_{\nu} = 8\pi G \bar{T}^{\mu}_{\nu}. \tag{1.31}$$

Here, instead, we are interested in the Einstein equations for the perturbations

$$\delta G^{\mu}_{\nu} = 8\pi G \delta T^{\mu}_{\nu}. \tag{1.32}$$

The early phase of accelerated expansion smoothed out any initially large primordial fluctuation. Therefore, after the end of inflation fluctuations are small and we can simply expand the Einstein equations to linear order in perturbations.

The most general linear perturbation around the background metric Eq. (1.9) reads

$$\mathrm{d}s^2 = a^2(\tau)\left\{-(1+2\Psi)\mathrm{d}\tau^2 - 2B_i \mathrm{d}x^i \mathrm{d}\tau + \left[(1-2\Phi)\delta_{ij} + 2E_{ij}\right]\mathrm{d}x^i \mathrm{d}x^j\right\}, \tag{1.33}$$

where τ is the conformal time defined by $\mathrm{d}\tau \equiv \mathrm{d}t/a(t)$, $\Psi(\tau, \boldsymbol{x})$ is a 3-scalar called the *lapse*, $B_i(\tau, \boldsymbol{x})$ is a 3-vector called the *shift*, $\Phi(\tau, \boldsymbol{x})$ is the 3-scalar spatial *curvature* perturbation, and $E_{ij}(\tau, \boldsymbol{x})$ is the symmetric and traceless[4] spatial *shear* 3-tensor. Note that an analogous decomposition to Eq. (1.33) can be performed for any rank-2 tensor, e.g. the energy-momentum tensor. Below, we will see that a convenient choice of coordinates allows us to set some of the metric perturbations to zero, greatly simplifying Eq. (1.33) for practical applications.

[4]The trace-free condition corresponds to asking $E^i_i = \delta^{ij}E_{ij} = 0$. We shall adopt the useful convention that Latin indices on spatial vectors and tensors are raised and lowered with δ_{ij}.

The Einstein equations (1.32) provide the link between the metric perturbations and the energy-momentum perturbations. In general, these are coupled nonlinear and second-order partial differential equations. However, throughout most of the history of the universe perturbations are small, meaning that we can drop all nonlinear terms (i.e. terms originating from the product of two or more perturbations). The remaining equations contain exclusively first-order terms (i.e. allow only for exactly one power of the perturbed quantities). The linearization of the perturbed equations comes with two important advantages:

- Scalars, vectors and tensors perturbations do not mix.
- Fourier modes decouple.

Scalar-Vector-Tensor decomposition

The spatial symmetries of the FLRW background spacetime allow us to decouple the scalar, vector and tensor components of the perturbations. First, we notice that vectors and tensors can be conveniently decomposed in simpler parts. Specifically, by virtue of the Helmholtz theorem, the 3-vector B_i can be written as

$$B_i = B_i^{\parallel} + B_i^{\perp}, \tag{1.34}$$

where $\boldsymbol{B}^{\parallel}$ is the longitudinal part (i.e. curl-free, $\nabla \times \boldsymbol{B}^{\parallel} = 0$) and $\boldsymbol{B}^{\perp}$ is the transverse part (i.e. divergence-free, $\nabla \cdot \boldsymbol{B}^{\perp} = 0$). This terminology follows from their behavior in Fourier space. By construction, $\boldsymbol{B}^{\parallel} = \nabla B$ for some scalar potential B, implying that the decomposition Eq. (1.34) is equivalent to a separation in scalar and pure vector components. Similarly, for symmetric, trace-free 3-tensors the decomposition in scalar, vector and tensor parts can be written as

$$E_{ij} = E_{ij}^{\parallel} + E_{ij}^{\perp} + E_{ij}^{T}, \tag{1.35}$$

where

$$E_{ij}^{\parallel} \equiv \left(\partial_i\partial_j - \frac{1}{3}\delta_{ij}\nabla^2\right) E, \tag{1.36}$$

$$E_{ij}^{\perp} \equiv \frac{1}{2}\left(\partial_i E_j + \partial_j E_i\right), \tag{1.37}$$

for some scalar E and vector E_i. Both the vector and tensor parts are transverse[5], i.e. $\partial^i E_i = \partial^i\partial^j E_{ij}^T = 0$.

Rotational invariance of the background guarantees that the scalar, vector and tensor modes of the linearized Einstein equations evolve independently (see e.g., Hu 2004). Scalar

[5]Recall that we are working in flat space at first-order in the perturbations. In general, though, partial derivatives should be replaced by covariant derivatives.

terms describe clumping of matter (i.e. growth of structure). Vector modes are associated with vorticity and are not present in the primordial universe if the initial fluctuations were produced by inflation, and even if they were they would rapidly decay as the universe expands. Tensor perturbations represent gravitational waves, and are generated by inflation in the early stages of the primordial universe. Scalar perturbations play a central role for the entire history of the universe, and are of particular interest at late times to study the formation of structure and the impact of dark energy. Therefore, we will focus on scalar modes and neglect the other types of perturbations in the rest of this thesis.

Fourier modes

Fourier space is the perfect arena to analyze the linear evolution of the Einstein equations (1.32). In fact, we can write a generic real space perturbation $f(\tau, \boldsymbol{x})$ in terms of its Fourier components $f_{\boldsymbol{k}}(\tau)$ as

$$f(\tau, \boldsymbol{x}) = \int \frac{\mathrm{d}^3 k}{(2\pi)^{3/2}} f_{\boldsymbol{k}}(\tau) e^{i\boldsymbol{k}\cdot\boldsymbol{x}}. \tag{1.38}$$

This transformation implies that partial differential equations in real space become ordinary differential equations in Fourier space. In addition, thanks to translational invariance, different Fourier modes (i.e. different wave numbers k) evolve independently (see e.g., Weinberg 2008). The following correspondences between real space gradients and comoving wavenumbers in Fourier space hold: $\partial_j \mapsto ik_j$ and $\nabla^2 \equiv \delta^{ij}\partial_i\partial_j \mapsto -k^2$. Hereafter, we will always work in Fourier space and drop the momentum labels for all perturbed quantities, i.e. $f_{\boldsymbol{k}} = f(\boldsymbol{k}) = f$.

Gauge fixing

In the study of cosmological perturbations the separation into background quantities and their perturbations is not unique, that is it depends on the choice of coordinates or the *gauge* choice (see e.g., Bardeen 1980). This is a direct consequence of the covariance of Einstein equations. For the background universe we introduced coordinates t and x^i (equivalently τ and x^i) to define the FLRW metric. In that case, the 3-surfaces of constant time corresponded to a homogenous universe. Moreover, comoving observers ($x^i = const.$) are free-falling. Hence, they see zero momentum density at their location and a universe expanding isotropically. These features made our coordinate choice so peculiar that we needed not consider other coordinates (in which homogeneity and isotropy would not be manifest). However, when considering an inhomogeneous spacetime there is no preferred choice of coordinates. By fixing the gauge we define the 3-surfaces of constant time and the comoving observers of the spacetime, which in turn also specifies the perturbations. We can use this gauge freedom to further simplify the form of our equations.

The conformal Newtonian gauge (also known as the longitudinal gauge) is a particularly simple gauge to use for the scalar mode of metric perturbations (Mukhanov, Feldman, and Brandenberger 1992) where $B = E = 0$, that is

$$\mathrm{d}s^2 = a^2(\tau)\left[-(1+2\Psi)\mathrm{d}\tau^2 + (1-2\Phi)\delta_{ij}\mathrm{d}x^i\mathrm{d}x^j\right]. \tag{1.39}$$

In this gauge the physics is rather intuitive and reduces easily to the Newtonian case. In fact, comoving observers see that non-relativistic particles interacting only through gravity move towards high-density regions, and Ψ plays the role of the gravitational potential in the Newtonian limit. The difference between the two potentials Ψ and Φ is sourced by a non-vanishing anisotropic stress in the energy-momentum tensor δT^μ_ν.

Energy-momentum tensor perturbations

Before deriving the linearized Einstein equations, we need to specify the energy-momentum tensor in a perturbed universe. Now, the energy density ρ, the pressure P, and the 4-velocity U^μ can be functions of position. Moreover, contributions from viscosity and heat conduction are possible. We write the energy-momentum tensor of this imperfect fluid as

$$T^\mu_\nu = (\bar{\rho} + \bar{P})U^\mu U_\nu + \bar{P}\delta^\mu_\nu + q^\mu U_\nu + q_\nu U^\mu + \Pi^\mu_\nu, \tag{1.40}$$

where Π^μ_ν is the traceless anisotropic stress tensor with Π^i_j as the only non-vanishing components, and q^μ is the heat flux vector. In practice, anisotropic stress and heat conduction will always be negligible for our purposes. Using the perturbed metric Eq. (1.39) we find the energy-momentum tensor perturbations at linear order

$$\delta T^0_0 = -\delta\rho, \tag{1.41a}$$

$$\delta T^0_i = (1+w)\bar{\rho}v_i = -\delta T^i_0, \tag{1.41b}$$

$$\delta T^i_j = \delta P \delta^i_j, \tag{1.41c}$$

where $v_i \equiv \mathrm{d}x_i/\mathrm{d}\tau$ is the fluid peculiar velocity with respect to the general expansion. For convenience, we also define the divergence of the fluid velocity $\theta \equiv ik^i v_i$. Note that for multiple fluids (e.g. photons, baryons, dark matter, neutrinos, etc.) contributions are simply added, i.e. $\delta T_{\mu\nu} = \sum_I \delta T^I_{\mu\nu}$.

Table 1.1 Analytical limits of the solutions for the potential Φ (see Eq. (1.47)) and the matter density contrast δ_m (see Eq. (1.46)) in the radiation dominated (RD) and matter dominated (MD) universe. Modes are categorized on the basis of the time of horizon crossing (before/after a_eq). Baryons have been neglected, i.e. $\delta_\mathrm{c} = \delta_\mathrm{m}$.

Mode		RD		MD	
		Φ	δ_m	Φ	δ_m
$k \gg k_\mathrm{eq}$	super-horizon	*const.*	*const.*	–	–
	sub-horizon	a^{-2}	$\ln a$	*const.*	a
$k \ll k_\mathrm{eq}$	super-horizon	*const.*	*const.*	*const.*	*const.*
	sub-horizon	–	–	*const.*	a

Linearized Einstein equations

Finally, the first-order perturbed Einstein equations (1.32) give

$$k^2\Phi + 3\mathcal{H}\left(\dot{\Phi} + \mathcal{H}\Psi\right) = -4\pi G a^2 \delta\rho, \tag{1.42a}$$

$$k^2\left(\dot{\Phi} + \mathcal{H}\Psi\right) = 4\pi G a^2 (1+w)\bar{\rho}\theta, \tag{1.42b}$$

$$\ddot{\Phi} + \mathcal{H}\left(\dot{\Psi} + 2\dot{\Phi}\right) + \left(2\dot{\mathcal{H}} - \mathcal{H}^2\right)\Psi = 4\pi G a^2 \delta P, \tag{1.42c}$$

$$\Phi = \Psi, \tag{1.42d}$$

where $\mathcal{H} = aH = a^{-1}\mathrm{d}a/\mathrm{d}\tau$ is the conformal Hubble parameter, and overdots denote derivative with respect to conformal time. From the energy-momentum conservation Eq. (1.5) we obtain

$$\dot{\delta} = -(1+w)\left(\theta - 3\dot{\Phi}\right) - 3\mathcal{H}\left(c_s^2 - w\right)\delta, \tag{1.43a}$$

$$\dot{\theta} = -\mathcal{H}(1-3w)\theta - \frac{\dot{w}}{1+w}\theta + \frac{c_s^2}{1+w}k^2\delta + k^2\Psi. \tag{1.43b}$$

Here, we have defined the fractional density contrast $\delta \equiv \delta\rho/\bar{\rho}$ and the sound speed $c_s^2 \equiv \delta P/\delta\rho$. In this thesis, we will assume adiabatic initial conditions set by inflation (see, e.g., Weinberg 2008) for a mixture of barotopic fluids, i.e. $P = P(\rho)$, which will remain so even when perturbed. Then, $c_s^2 = \mathrm{d}P/\mathrm{d}\rho$. Also, both c_s^2 and w multiply first-order quantities in Eqs. (1.42) and (1.43), which means we can keep only their background values in the linearized equations, namely

$$c_s^2 \mapsto \frac{\dot{\bar{P}}}{\dot{\bar{\rho}}} = w - \frac{\dot{w}}{3\mathcal{H}(1+w)} \quad \text{and} \quad w \mapsto \frac{\bar{P}}{\bar{\rho}}. \tag{1.44}$$

In particular, for a constant equation of state $c_s^2 = w = \textit{constant}$. This is valid for both non-relativistic matter and radiation.

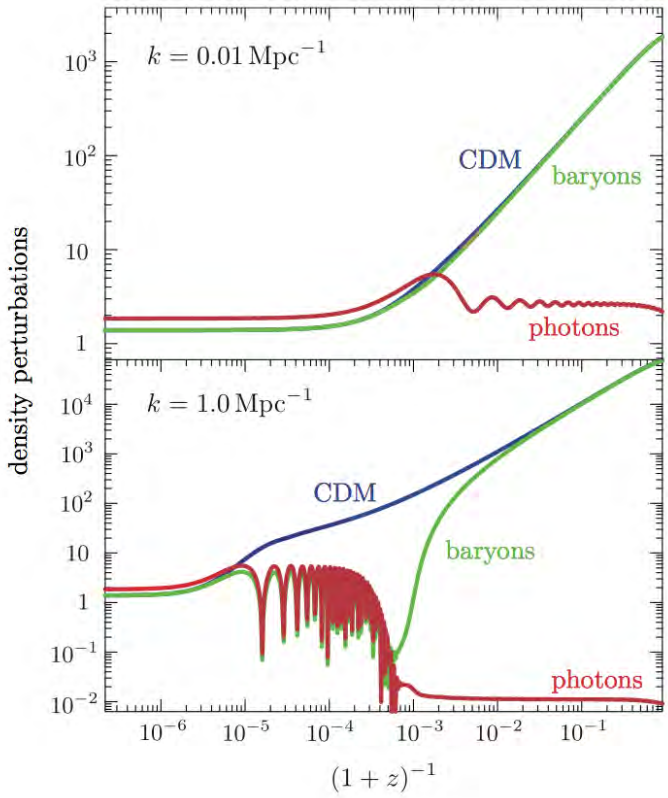

Fig. 1.7 Exact numerical evolution of cold dark matter (CDM), baryons and photons density contrasts for long-wavelength (top) and short-wavelength (bottom) perturbation modes. At early times and small scales, baryons and photons are tightly coupled evolving as a single fluid due to Thomson scattering. Pressure support produces acoustic oscillations that will be later on imprinted on the observed large-scale distribution of matter. Before decoupling $\delta_c \gg \delta_b$. After recombination, baryons fall into the dark matter potential wells and $\delta_b \to \delta_c$. This happens earlier for long-wavelength perturbations. Note that, at late times, density perturbation in the photon fluid are much smaller than those in the non-relativistic matter, thus they can be safely neglected in the study of structure formation. (Figure taken from Daniel Baumann's *Cosmology* lecture notes).

Eqs. (1.43) are valid for a single uncoupled fluid, or for the mass-averaged $\delta_{\rm tot}$ and $\theta_{\rm tot}$ for all fluids defined by

$$\delta_{\rm tot} \equiv \frac{\sum_I \bar{\rho}_I \delta\rho_I}{\sum_I \bar{\rho}_I}, \tag{1.45a}$$

$$\theta_{\rm tot} \equiv \frac{1}{1+w_{\rm tot}} \frac{\sum_I (1+w_I)\bar{\rho}_I \theta_I}{\sum_I \bar{\rho}_I}, \tag{1.45b}$$

where $w_{\rm tot} = \sum_I w_I \bar{\rho}_I / \sum_I \bar{\rho}_I$. Note that they need to be modified for individual components if additional interactions are present. The baryonic fluid falls in this category as it couples to the photons before recombination via Thomson scattering. However, after decoupling baryons rapidly fall into the dark matter potential wells, and $\delta_{\rm b} \approx \delta_{\rm c} \approx \delta_{\rm m}$ as we will show below (see also Fig. 1.7).

Since dark matter couples only gravitationally (i.e. through the metric) to the other matter species, its evolution equations are relatively simple. Combining the conservation equations (1.43) gives a single equation for the dark matter density contrast

$$\ddot{\delta}_{\rm c} + \mathcal{H}\dot{\delta}_{\rm c} = 3\ddot{\Phi} + 3\mathcal{H}\dot{\Phi} - k^2\Phi, \tag{1.46}$$

where the gravitational potential is sourced by the total matter perturbations $\delta\rho$ and δP. For adiabatic perturbations the Einstein equations (1.42a) and (1.42c) give a closed-form equation for the gravitational potential, which for fluids with $c_s^2 = w = \textit{constant}$ becomes

$$\ddot{\Phi} + 3(1+c_s^2)\mathcal{H}\dot{\Phi} + c_s^2 k^2 \Phi = 0. \tag{1.47}$$

This is the differential equation for a generic damped harmonic oscillator, with oscillation frequency and viscosity depending on background evolution (through $\mathcal{H}$), fluid properties (through c_s^2) and perturbation wavelength (through k). Even within the assumption of no additional interaction between fluids apart from gravity, an analytic solution valid on all scales and all times cannot be derived. A detailed derivation of an approximate solution can be found in, e.g., Dodelson (2003). Here, we summarize the evolution of Φ in Table 1.1 for super- and sub-horizon modes[6], as well as for a radiation dominated and a matter dominated universe. The epoch of matter-radiation equality $a_{\rm eq}$ marks the transition between two very different evolutionary phases. It is derived from the equality $\bar{\rho}_{\rm m}(a_{\rm eq}) = \bar{\rho}_{\rm r}(a_{\rm eq})$ as

$$a_{\rm eq} = \frac{\bar{\rho}_{\rm r}(a=1)}{\bar{\rho}_{\rm m}(a=1)} = \frac{\Omega_{\rm r}}{\Omega_{\rm m}}. \tag{1.48}$$

[6]The conformal (or comoving) Hubble radius $\mathcal{H}^{-1}$ sets the length and time scales relevant for cosmological evolution. Although this quantity is not a proper horizon, cosmologists often refer to it as such for its fundamental role in cosmological perturbation theory. In particular, modes with comoving wavelength $\lambda_{\rm c} = 2\pi/k$ well inside the Hubble radius, i.e. $k \gg \mathcal{H}$, are called sub-horizon modes. Super-horizon modes satisfy the opposite inequality, i.e. $k \ll \mathcal{H}$.

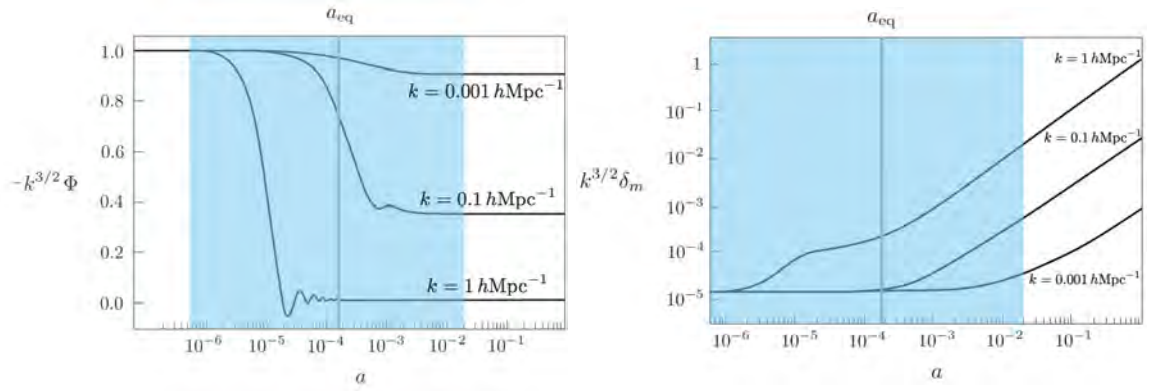

Fig. 1.8 Numerical solutions for the gravitational potential Φ (left) and the matter density contrast $\delta_{\rm m}$ (right) for $k = 10^{-3}, 10^{-1}, 1\,h\,\mathrm{Mpc}^{-1}$ bracketing the relevant regime of cosmological structure formation at late times. The blue shaded area covers the time interval that goes from the horizon crossing of the shortest mode of interest to the end of the radiation-matter transition ($a = a_{\rm late}$), when the longest mode enters the horizon. Deep in the era of matter domination all modes evolve identically. (Figures adapted from Daniel Baumann's *Cosmology* lecture notes).

Before moving forward with a phenomenological understanding of Eq (1.47), let us introduce an important quantity that is conserved on super-horizon scales for adiabatic, scalar fluctuations regardless the fluid's specific equation of state: the *comoving curvature perturbation*. It corresponds to the perturbation of the intrinsic curvature scalar of comoving hypersurfaces, namely those 3-surfaces of constant time defined by observers comoving with the total fluid. Its relevance derives from the fact that we can directly match the primordial perturbations from inflation to those at later time, in the radiation dominated universe. The comoving curvature perturbation in the conformal Newtonian gauge is defined by (see e.g., Weinberg 2008)

$$\mathcal{R} \equiv -\Phi + \mathcal{H}v, \tag{1.49}$$

where $v_i = \partial_i v$. After using Eq. (1.42b) to eliminate the velocity potential we have

$$\mathcal{R} = -\Phi - \frac{\mathcal{H}(\dot{\Phi} + \mathcal{H}\Phi)}{4\pi G a^2 \bar{\rho}(1+w)}. \tag{1.50}$$

On scales larger than the horizon ($k \ll \mathcal{H}$), a constant gravitational potential is a solution to Eq. (1.47), i.e. $\dot{\Phi} = 0$. This information, combined with the Friedmann equation (1.13a), gives the important result

$$\mathcal{R} = -\frac{5+3w}{3+3w}\Phi, \tag{1.51}$$

that will allow us to link the primordial initial conditions set up by inflation to the late time growth of structure.

After inflation, perturbation modes re-enter the horizon only once, either in the radiation dominated era or in the matter dominated era. We can predict when this happens for a

particular mode by comparing its wavenumber k with that of the mode crossing the horizon at matter-radiation equality, $k_{\rm eq} \equiv \mathcal{H}(a_{\rm eq})$. With this in mind, we can qualitatively analyze Eq. (1.47) to grasp the evolution of the gravitational potential through the different stages of cosmic history:

1. Early on, since all modes are outside the horizon ($k \ll \mathcal{H}$), the last term in Eq. (1.47) can be neglected. Thus, a constant solution describes the potential in this regime.

2. The subsequent evolution of Φ depends on whether $k \ll k_{\rm eq}$ or $k \gg k_{\rm eq}$. For modes that cross the horizon during radiation domination ($a \ll a_{\rm eq}$), Eq. (1.47) describes the evolution of a damped harmonic oscillator with a rapidly decaying envelope and oscillation frequency depending on the wavelength of the perturbation. On the other hand, for modes that cross the horizon during matter domination ($a \gg a_{\rm eq}$), the last term in Eq. (1.47) is identically zero ($c^2_{s,\rm m} = 0$) and a constant potential is again a solution, although different from that of the early universe. However, they are not independent. The conservation of comoving curvature perturbations on super-horizon scales Eq. (1.51) implies that the two solutions are related by $\Phi_{\rm MD} = \frac{9}{10}\Phi_{\rm RD}$. Modes with $k \sim k_{\rm eq}$ have a somewhat more complex behavior influenced by the radiation-matter transition.

3. At late times (before Λ domination), all modes of interest are inside the horizon and the gravitational potential does not evolve, with values matching the solutions at the end of the radiation-matter transition ($a_{\rm late} \sim 0.02$).

The left panel of Fig. 1.8 shows the exact numerical evolution of the gravitational potential for three representative modes, with the shortest and longest wavelengths delimiting the range of interest for cosmological structure formation.

Now that we have the source term of Eq. (1.46), we can solve for the dark matter density contrast $\delta_{\rm c}$ or, neglecting baryons, for the total matter density contrast $\delta_{\rm m}$. Approximate analytical limits are given in Tab. (1.1) for modes inside and outside the horizon, crossing the Hubble radius either in the radiation dominated or in the matter dominated epochs. Exact numerical solutions not including baryons are shown in the right panel of Fig. 1.8 for long-, intermediate- and short-wavelength modes.

Late time evolution of matter perturbations in the Newtonian limit

Gravitational instabilities are predominantly effective at late epochs, when non-relativistic matter dominates the evolution of the universe. In this regime, Eq. (1.46) can be simplified on sub-horizon scales as

$$\ddot{\delta}_{\rm c} + \mathcal{H}\dot{\delta}_{\rm c} = -k^2\Phi, \tag{1.52}$$

where Φ is sourced by the total matter perturbations through the Poisson equation

$$k^2\Phi = -4\pi G a^2 \delta\rho, \tag{1.53}$$

which results from the combination of Eq. (1.42a) and Eq. (1.42b) on sub-horizon scales. At late times, radiation can be safely neglected and vacuum energy contribution is limited to the background evolution. Therefore, the total density perturbation receives contributions only from baryons and dark matter, i.e. $\bar{\rho}_\mathrm{m}\delta_\mathrm{m} = \bar{\rho}_\mathrm{c}\delta_\mathrm{c} + \bar{\rho}_\mathrm{b}\delta_\mathrm{b}$. The combination of Eq. (1.52) with Eq. (1.53) provides a system of coupled differential equations describing the dynamics of the baryonic and dark matter fluids

$$\ddot{\delta}_\mathrm{c} + \mathcal{H}\dot{\delta}_\mathrm{c} = 4\pi G a^2(\bar{\rho}_\mathrm{c}\delta_\mathrm{c} + \bar{\rho}_\mathrm{b}\delta_\mathrm{b}), \tag{1.54a}$$

$$\ddot{\delta}_\mathrm{b} + \mathcal{H}\dot{\delta}_\mathrm{b} = 4\pi G a^2(\bar{\rho}_\mathrm{c}\delta_\mathrm{c} + \bar{\rho}_\mathrm{b}\delta_\mathrm{b}). \tag{1.54b}$$

We can decouple these equations by defining $\delta_\mathrm{bc} \equiv \delta_\mathrm{b} - \delta_\mathrm{c}$. In addition, during the matter dominated era, the Friedmann equation (1.13) implies $a \propto \tau^2$ and $\mathcal{H} = 2/\tau$, which gives the following growing modes for the total matter density contrast and the differential density contrast

$$\delta_\mathrm{bc} \propto \text{const.} \quad \text{and} \quad \delta_\mathrm{m} \propto a \propto \tau^2. \tag{1.55}$$

We can express the ratio between the baryonic and dark matter components as

$$\frac{\delta_\mathrm{b}}{\delta_\mathrm{c}} = \frac{\bar{\rho}_\mathrm{m}\delta_\mathrm{m} + \bar{\rho}_\mathrm{b}\delta_\mathrm{bc}}{\bar{\rho}_\mathrm{m}\delta_\mathrm{m} - \bar{\rho}_\mathrm{c}\delta_\mathrm{bc}}, \tag{1.56}$$

and using Eq. (1.55) we see that δ_b approaches δ_c during matter domination (see Fig. 1.7). The evolution equation for the total matter density contrast on sub-horizon scales then reads

$$\ddot{\delta}_\mathrm{m} + \mathcal{H}\dot{\delta}_\mathrm{m} - 4\pi G a^2 \bar{\rho}_\mathrm{m}\delta_\mathrm{m} = 0, \tag{1.57}$$

which is valid in both the matter dominated and the Λ dominated eras. Inserting the solution for δ_m given in Eq. (1.55) into the Poisson equation (1.53), we see that $\Phi \propto a^2\bar{\rho}_\mathrm{m}\delta_\mathrm{m} \propto a^2 a^{-3} a \propto a^0$. This is an additional cross-check showing that the gravitational potential remains constant during the pure matter dominated epoch.

Assuming that the evolution of the matter density contrast up to some late time $a_\mathrm{late} \sim 0.02$ deep in the matter dominated era is known, we can write

$$\delta_\mathrm{m}(a, \boldsymbol{k}) = \frac{D_+(a)}{a_\mathrm{late}}\delta_\mathrm{m}(a_\mathrm{late}, \boldsymbol{k}) \quad \text{for} \quad a > a_\mathrm{late}, \tag{1.58}$$

where $D_+(a)$ is called the *linear growth factor*, and $\delta_\mathrm{m}(a_\mathrm{late}, \boldsymbol{k})$ represents the matter density contrast evolved from the initial conditions set by inflation to late times, after the epochs of

horizon crossing and radiation-matter transition. Plugging this expression into Eq. (1.57) and using a in place of τ as time variable, we obtain the solution

$$D_+(a) = \frac{5}{2}\mathcal{H}_0^2\Omega_{\rm m}\frac{\mathcal{H}}{a}\int_0^a \frac{{\rm d}a'}{\mathcal{H}^3(a')}, \tag{1.59}$$

with $\Omega_{\rm m} \equiv \bar{\rho}_{\rm m}(a=1)/\bar{\rho}_{\rm crit}(a=1)$. From this equation it can be readily checked that $D_+(a) = a$ in the matter dominated universe. Cosmologists often work with the *growth rate* f, a quantity derived from the growth factor as (cfr. Eq. (2.13))

$$f \equiv \frac{{\rm d}\ln\delta_{\rm m}}{{\rm d}\ln a}, \tag{1.60}$$

which will play a central role in chapter 2 for consistency tests of the concordance model with growth data.

The post-processing of primordial perturbations due to the epochs of horizon crossing and radiation-matter transition can be incorporated in the so-called *transfer function*, while the growth factor describes the k-independent growth at late times. The interesting regime for cosmological structure formation is on scales $10^{-3} \lesssim k\,(h^{-1}\ {\rm Mpc}) \lesssim 1$, which are all well within the horizon for $a \gtrsim 0.02$, deep in the matter dominated era. Using Eq. (1.53) together with the relation $\Phi(a_{\rm late}, \boldsymbol{k}) = -\frac{3}{5}\mathcal{R}(a_{\rm late}, \boldsymbol{k})$ (see Eq. (1.50)), we have

$$\delta_{\rm m}(a_{\rm late}, \boldsymbol{k}) = \frac{2}{5}\left(\frac{k}{\mathcal{H}}\right)^2 \mathcal{R}(a_{\rm late}, \boldsymbol{k}). \tag{1.61}$$

The comoving curvature at late times is related to the primordial curvature $\mathcal{R}(0, \boldsymbol{k})$ by the transfer function $T(k)$. Hence, Eq. (1.58) becomes

$$\delta_{\rm m}(a, \boldsymbol{k}) = \frac{2}{5}\left(\frac{k}{\mathcal{H}}\right)^2 T(k)\mathcal{R}(0, \boldsymbol{k})\frac{D_+(a)}{a_{\rm late}}, \tag{1.62}$$

with the normalization $T(k \ll k_{\rm eq}) \to 1$. The late effects of dark energy on the large-scale structure only enter through $D_+(a)$. For a cosmological constant all modes keep evolving identically and the gravitational potential Φ starts decaying once $\bar{\rho}_{\rm m} \approx \bar{\rho}_\Lambda$, preventing the formation of ever larger structures. In sec. 1.3 we will see that modified gravity models predict a richer dynamics that also depends on the scale of the perturbation.

One final word concerns the peculiar velocity field θ. This can be easily derived from the matter density contrast Eq. (1.62). Indeed, in the sub-horizon limit and for non-relativistic fluids Eq. (1.43a) gives

$$\theta = -\mathcal{H}f\delta_{\rm m}, \quad \text{or} \quad v^i = i\mathcal{H}f\delta_{\rm m}\frac{k^i}{k^2}, \tag{1.63}$$

where we also used Eq. (1.60). As expected, the divergence field displays a negative sign associated with the flows of matter out of underdense region into regions of high density contrast.

1.2.3 Beyond the linear regime of structure formation

Linear perturbation theory fails to capture the dynamics of large enough fluctuations, starting at $\delta_{\rm m} \sim 1$. At this stage perturbations enter the quasi-linear regime, a process that happened for scales $k \gtrsim 0.1\,h\,{\rm Mpc}^{-1}$ by now. Such perturbations evolve to become fully nonlinear, leading to their rapid collapse and eventual formation of gravitationally bound structures, e.g. clusters of galaxies, with velocity dispersion preventing further contraction.

Before the gravitational instability reaches a regime of non-linearity there is an intermediate regime in which the growth of structure is still entirely governed by gravity and effects beyond linearity become measurable. This regime lies between linear perturbation theory and the full nonlinear dynamics that can be studied only with N-body simulations or with simplified models for the formation of single objects.

The Effective Field Theory of Large-Scale Structure

Density fluctuations grow under the effect of gravitational instability and eventually depart from the simple linear regime. A perturbative approach on all scales and times capturing the complex nonlinear dynamics is therefore impossible. Despite the fact that fluctuations on small scales are large (i.e. strongly nonlinear in nature), over long distances they remain relatively small (i.e. $\delta \sim 1$ [7]). If we are interested in an analytical description of the matter distribution on cosmological scales (i.e. $k \lesssim 1\,h\,{\rm Mpc}^{-1}$), then it should be possible to treat modes in the mildly nonlinear regime perturbatively, where they are only weakly coupled. However, nonlinearities also generate coupling between large scale fluctuations (long modes) and small scale fluctuations (short modes), which will impact on the long distance dynamics we aim to describe. Thus, we would also like to incorporate the feedback of small scale physics into our predictions for the evolution of the large-scale structure. An effective field theory (EFT) approach provides proper tools to consistently study this physical system (Baumann, Nicolis, et al. 2012; Carrasco, Hertzberg, and Senatore 2012). It captures all relevant degrees of freedom required to describe the universe on scales larger than the nonlinear scale[8],

[7] Throughout this section $\delta_{\rm m} = \delta_{\rm c} \equiv \delta$. See sec. 1.2.2 for a discussion.

[8] We lack a precise estimate of the nonlinear scale at which the effective theory description breaks down. Nevertheless, on purely empirical grounds and based on the size of the largest virialized structures in the universe we expect the present-day nonlinear scale to be $k_{\rm NL} \lesssim 1\,h\,{\rm Mpc}^{-1}$, growing with redshift. Note that this estimate is not related to the baryonic feedback on large scales, but simply to gravitational nonlinearities. In fact, while dark matter and baryons are on an equal footing in this thesis, the effect of baryonic physics on cosmological scales can be consistently included in the EFT of large-scale structure (Lewandowski, Senatore, et al. 2015). Also, the $k_{\rm NL}$ we refer to here is different from the estimate used to define the breakdown of

$k_{\rm NL} \sim 1\,h\,{\rm Mpc}^{-1}$, and accounts for the effect of short scales on long modes through a series of terms in the equations of motion for the long modes. In essence, small-scale dynamics is systematically integrated out and parametrized in a set of coefficients encoding the unknown nonlinear physics. These include speed of sound and viscosity of the fluid and are determined by matching the EFT predictions to the full nonlinear output from N-body simulations, or directly to observational data.

Well after matter-radiation equality and on sub-horizon scales, the Newtonian approximation in an expanding background faithfully describes the gravitational interaction of non-relativistic matter (see sec. 1.2.2). We will first consider the matter fluid as a gas of collisionless point particles. The state of the system is defined by a set of $2N \gg 1$ vectors which identify the comoving position $\boldsymbol{x}_n$ and peculiar velocity $\boldsymbol{v}_n$ of the n-th particle. We define the single-particle phase space density $f_n(\boldsymbol{x},\boldsymbol{p})$ as the probability of particle n occupying an infinitesimal phase space volume element. For a point particle, the phase space density reads

$$f_n(\boldsymbol{x},\boldsymbol{p}) = \delta_D^{(3)}(\boldsymbol{x}-\boldsymbol{x}_n)\delta_D^{(3)}(\boldsymbol{p}-ma\boldsymbol{v}_n), \tag{1.64}$$

where the coordinates $\boldsymbol{x}$ and momentum $\boldsymbol{p}$ are both comoving. Summation over n gives the total phase space density f, and taking its moments we find the physical mass density scalar field ρ, the momentum density vector field π^i, and the kinetic tensor field σ^{ij} as

$$f(\boldsymbol{x},\boldsymbol{p}) = \sum_n \delta_D^{(3)}(\boldsymbol{x}-\boldsymbol{x}_n)\,\delta_D^{(3)}(\boldsymbol{p}-ma\boldsymbol{v}_n), \tag{1.65}$$

$$\rho(\boldsymbol{x}) = ma^{-3}\int {\rm d}^3\boldsymbol{p}\, f(\boldsymbol{x},\boldsymbol{p}) = \sum_n ma^{-3}\delta_D^{(3)}(\boldsymbol{x}-\boldsymbol{x}_n), \tag{1.66}$$

$$\pi^i(\boldsymbol{x}) = a^{-4}\int {\rm d}^3\boldsymbol{p}\, p^i f(\boldsymbol{x},\boldsymbol{p}) = \sum_n ma^{-3}v_n^i\delta_D^{(3)}(\boldsymbol{x}-\boldsymbol{x}_n), \tag{1.67}$$

$$\sigma^{ij}(\boldsymbol{x}) = m^{-1}a^{-5}\int {\rm d}^3\boldsymbol{p}\, p^i p^j f(\boldsymbol{x},\boldsymbol{p}) = \sum_n ma^{-3}v_n^i v_n^j\delta_D^{(3)}(\boldsymbol{x}-\boldsymbol{x}_n). \tag{1.68}$$

where $\delta_D^{(3)}$ denotes the three-dimensional Dirac delta. In an infinite homogeneous universe the Newtonian potential presents an infrared quadratic divergence. To regularize it we introduce an exponential infrared cutoff ν and will take $\nu \to 0$ at the end of our derivation (Rindler 1977). The solutions for the single-particle and total Newtonian potentials are

$$\Phi_n(\boldsymbol{x}) = -Ga^2\int {\rm d}^3\boldsymbol{x}'\,\frac{\rho_n(\boldsymbol{x}')}{|\boldsymbol{x}-\boldsymbol{x}'|}e^{-\nu|\boldsymbol{x}-\boldsymbol{x}'|} = -\frac{Gm}{a|\boldsymbol{x}-\boldsymbol{x}_n|}e^{-\nu|\boldsymbol{x}-\boldsymbol{x}_n|}, \tag{1.69}$$

$$\Phi(\boldsymbol{x}) = -Ga^2\int {\rm d}^3\boldsymbol{x}'\,\frac{\rho(\boldsymbol{x}')-\bar\rho}{|\boldsymbol{x}-\boldsymbol{x}'|}e^{-\nu|\boldsymbol{x}-\boldsymbol{x}'|} = \sum_n \Phi_n + \frac{4\pi G a^2\bar\rho}{\nu^2}. \tag{1.70}$$

linear theory, which is $\sim 0.1\ h\,{\rm Mpc}^{-1}$. This value is based on a specific definition that does not necessarily coincide with the definition in the context of the EFT of large-scale structure.

Note that the total Newtonian potential Φ is infrared divergent for an infinite universe, which results from the breaking of the Newtonian approximation. Regularization, however, ensures that only the physically meaningful gradients survive.

Phase space conservation is described by the collisionless Boltzmann equation (or Vlasov equation)

$$0 = \frac{Df}{D\tau} = \frac{\partial f}{\partial \tau} + \frac{\boldsymbol{p}}{ma} \cdot \frac{\partial f}{\partial \boldsymbol{x}} - ma \sum_{n,\bar{n};\bar{n}\neq n} \frac{\partial \Phi_{\bar{n}}}{\partial \boldsymbol{x}} \cdot \frac{\partial f_n}{\partial \boldsymbol{p}}, \tag{1.71}$$

where we have removed the self-force contribution in the sum. We are interested in the theory at scales much larger that the nonlinear scale $k_{\rm NL}$. The effective long-wavelength theory is obtained by integrating out short-wavelength modes below a scale[9] $\Lambda \ll k_{\rm NL}$. In real space, this corresponds to a convolution of all fields with a window function[10] $W_\Lambda(\boldsymbol{x})$ normalized such that $\int \mathrm{d}^3\boldsymbol{x} W_\Lambda(\boldsymbol{x}) = 1$. The final product are averages of the fields over domain of size Λ^{-1}. Thus, given a field $\mathcal{X}$, we will define the smoothed value by the convolution

$$\mathcal{X}_\ell(\boldsymbol{x}) = [\mathcal{X}]_\Lambda(\boldsymbol{x}) \equiv \int \mathrm{d}^3\boldsymbol{x}'\, W_\Lambda(|\boldsymbol{x}-\boldsymbol{x}'|)\mathcal{X}(\boldsymbol{x}'), \tag{1.72}$$

or, equivalently, in Fourier space

$$\mathcal{X}_\ell(\boldsymbol{k}) = W_\Lambda(\boldsymbol{k})\mathcal{X}(\boldsymbol{k}). \tag{1.73}$$

We can split each field into long and short modes

$$\mathcal{X} = \mathcal{X}_\ell + \mathcal{X}_s, \tag{1.74}$$

where the short-wavelength fluctuations are defined in Fourier space by

$$\mathcal{X}_s(\boldsymbol{k}) = F_\Lambda(\boldsymbol{k})\mathcal{X}(\boldsymbol{k}), \tag{1.75}$$

with $F_\Lambda(\boldsymbol{k}) \equiv 1 - W_\Lambda(\boldsymbol{k})$. The smoothed version of Eq. (1.71) becomes

$$0 = \left[\frac{Df}{D\tau}\right]_\Lambda = \frac{\partial f_\ell}{\partial \tau} + \frac{\boldsymbol{p}}{ma} \cdot \frac{\partial f_\ell}{\partial \boldsymbol{x}} - ma \sum_{n,\bar{n};n\neq\bar{n}} \int \mathrm{d}^3\boldsymbol{x}'\, W_\Lambda(\boldsymbol{x}-\boldsymbol{x}') \frac{\partial \Phi_{\bar{n}}}{\partial \boldsymbol{x}'} \cdot \frac{\partial f_n}{\partial \boldsymbol{p}}, \tag{1.76}$$

where couplings between short-wavelength modes and the large-scale dynamics are encapsulated in the integral term. This is a nonlinear integro-differential equation with seven variables, extremely difficult to solve and does not admit a full analytical solution. Even so, we can break it in an infinite hierarchy of more tractable equations for the long-wavelength

[9] Here, we adopt the conventional symbol Λ for the cutoff scale, not to be confused with the cosmological constant Λ. Its meaning should be clear from the context.

[10] Typical shapes include Gaussian filters and top-hats, although the entire treatment and final results do not depend on the details of W_Λ.

fields. In practice, we proceed by taking moments of Eq. (1.76),

$$0 = \int \mathrm{d}^3\boldsymbol{p}\, p^{i_1} \cdots p^{i_m} \left[\frac{Df}{D\tau}\right]_\Lambda . \tag{1.77}$$

In this way, each moment of the smoothed total phase space distribution will be related to the subsequent one by an equation of motion. The zeroth and first moments give the continuity and Euler equations,

$$\dot{\rho}_\ell + 3\mathcal{H}\rho_\ell + \partial_i(\rho_\ell\, v_\ell^i) = 0, \tag{1.78a}$$

$$\dot{v}_\ell^i + \mathcal{H}v_\ell^i + v_\ell^j\partial_j v_\ell^i + \partial_i\Phi_\ell = -\frac{1}{\rho_\ell}\partial_j\left[\tau^{ij}\right]_\Lambda , \tag{1.78b}$$

where we introduced the velocity field[11]

$$v_\ell^i(\boldsymbol{x}) \equiv \frac{\pi_\ell^i(\boldsymbol{x})}{\rho_\ell(\boldsymbol{x})}. \tag{1.79}$$

By virtue of Helmholtz's theorem, we can completely characterise the velocity field with its divergence $\theta_\ell \equiv \partial_i v_\ell^i$ and curl $\omega^i = \epsilon_{ijk}\partial^j v_\ell^k$ (also known as *vorticity*). For our purposes, we will neglect vorticity in the remainder of this section, and will resort to either the divergence θ_ℓ or the rescaled velocity potential $\partial^2\Phi_{v,\ell} = -(\mathcal{H}f)^{-1}\theta_\ell$ to describe the velocity field[12].

Eqs. (1.78a) and (1.78b) express the conservation of mass and momentum, respectively. The right hand side of the Euler equation contains the smoothed effective stress tensor $[\tau^{ij}]_\Lambda$ sourced by the short modes, which we can write as (Carrasco, Hertzberg, and Senatore 2012)

$$[\tau^{ij}]_\Lambda = \kappa_\ell^{ij} + \Phi_\ell^{ij}. \tag{1.80}$$

Here, κ_ℓ^{ij} gives a kinetic contribution and Φ_ℓ^{ij} includes only terms related to the gravitational potential, namely

$$\kappa_\ell^{ij} = \sigma_\ell^{ij} - \rho_\ell v_\ell^i v_\ell^j, \tag{1.81}$$

$$\Phi_\ell^{ij} = -\frac{w_\ell^{kk}\delta^{ij} - 2w_\ell^{ij}}{8\pi G a^2} + \frac{\partial_k\Phi_\ell\partial_k\Phi_\ell\delta^{ij} - 2\partial^i\Phi_\ell\partial^j\Phi_\ell}{8\pi G a^2}, \tag{1.82}$$

[11] Strictly speaking, the velocity field defined in Eq. (1.79) is not a purely long-wavelength quantity, but rather a "composite operator", in the sense that $[\pi^i/\rho]_\Lambda \neq \pi_\ell^i/\rho_\ell$. However, for correlators involving only the smoothed density field this subtlety is irrelevant (Carrasco, Foreman, et al. 2014b), and our results in chapter 5 remain valid even with this definition.

[12] In the linear regime vorticity decays with time as a^{-1}. Therefore, any primordial contribution can be safely neglected at late times, when structures form. On the other hand, nonlinearities act as a source for ω_ℓ^i through the effective stress tensor (simply consider the curl of Eq. (1.78b)). However, Carrasco, Foreman, et al. (2014b) and Mercolli and Pajer (2014) showed that this contribution is small at the order in perturbation theory relevant for this thesis.

where

$$w_\ell^{ij}(\boldsymbol{x}) = \int \mathrm{d}^3\boldsymbol{x}'\, W_\Lambda(\boldsymbol{x}-\boldsymbol{x}') \left[\partial^i\Phi(\boldsymbol{x}')\partial^j\Phi(\boldsymbol{x}') - \sum_n \partial^i\Phi_n(\boldsymbol{x}')\partial^j\Phi_n(\boldsymbol{x}')\right]. \tag{1.83}$$

Note that we removed the self-term in w_ℓ^{ij}, and used $\nabla^2\Phi = 4\pi G a^2(\rho-\bar\rho)$ and $\nabla^2\Phi_\ell = 4\pi G a^2(\rho_\ell-\bar\rho)$ to express Φ_ℓ in terms of Φ and Φ_ℓ. In the limit in which there are no short modes, κ_ℓ^{ij} and Φ_ℓ^{ij} vanish identically (see Appendix A in Carrasco, Hertzberg, and Senatore 2012). The continuity and Euler equations are sufficient to study the dynamics of the long-wavelength effective fluid. In fact, Baumann, Nicolis, et al. (2012) showed that higher moments of the total phase distribution are systematically suppressed for scales $k \ll k_{\rm NL}$.

Since the effective stress tensor is explicitly dependent on the large and strongly coupled short-wavelength fluctuations, it is not possible to derive it within the effective theory. Nonetheless, the evolution of short modes responds to long-wavelength perturbations through tidal forces (i.e. $\partial^i\partial^j\Phi_\ell$) and shears (i.e. $\partial^i\partial^j\Phi_{v,\ell}$), which are both locally measurable quantities[13]. Intuitively, long-wavelength modes change the particle geodesics on small-scales, leading to modifications in the stress tensor associated with short-wavelength modes. We can then employ an effective approach, and describe the stress tensor as a derivative expansion of the long-wavelength fields in powers of $k^2/k_{\rm NL}^2$,

$$[\tau^{ij}]_\Lambda = \bar\rho\left[c_1^{(m)}\left(\frac{\partial^2}{k_{\rm NL}^2}\right)_{ij} + \cdots\right]\{\Phi_\ell, \Phi_{v,\ell}\} + \cdots, \tag{1.84}$$

where the ellipsis inside square brackets denote higher-order derivatives, and those outside refer to higher-order terms in the fields. The double index $_{ij}$ indicates combinations of the derivative operators[14] $\partial_i\partial_j$ and $\delta_{ij}\partial^2$, and the index m runs over the fields in the vector between curly brackets. Finally, we include the symmetrized expansion Eq. (1.84) into the equations of motion (1.78) and parametrise our ignorance of the short distance physics through the coefficients c_i multiplying each derivative.

At leading order in the derivatives and at first order in the fields, Eq. (1.84) assumes the more familiar form of the stress tensor for an imperfect fluid[15] (Landau and Lifshitz 1959;

[13] The Equivalence Principle ensures that the uniform acceleration produced by long-wavelength perturbations (i.e. $\partial^i\Phi_\ell$) on short scales is locally unobservable (see, e.g., Baldauf, Mercolli, Mirbabayi, et al. 2015; Abolhasani, Mirbabayi, and Pajer 2016).

[14] $\partial^2 = \partial_i\partial^i = \nabla^2$. In Fourier space, $\partial^2 \to -k^2$.

[15] In the following discussion we will always omit the stochastic contribution $\Delta\tau^{ij}$. This term accounts for the statistical deviation of the effective stress tensor from the ensemble average, with recent estimates revealing its importance only for predictions at order higher than those included here (Foreman, Perrier, and Senatore 2016).

Weinberg 1972)

$$[\tau^{ij}]_\Lambda = \delta^{ij}\bar{P} + \bar{\rho}\left[c_s^2\delta^{ij}\delta_\ell - \frac{c_{bv}^2}{\mathcal{H}}\delta^{ij}\partial_k v_\ell^k - \frac{3}{4}\frac{c_{sv}^2}{\mathcal{H}}\left(\partial^j v_\ell^i + \partial^i v_\ell^j - \frac{2}{3}\delta^{ij}\partial_k v_\ell^k\right)\right], \tag{1.85}$$

where we used the Poisson equation $\nabla^2\Phi_\ell = 4\pi G a^2\bar{\rho}\delta_\ell$ to replace Φ_ℓ with $\delta_\ell = (\rho_\ell - \bar{\rho})/\bar{\rho}$. Here, $\bar{P}$ is the background pressure generated by small scale fluctuations even in the absence of long modes[16], c_s is the sound speed, and c_{sv}, c_{bv} are viscosity coefficients with units of speed. These coefficients are related to pressure perturbations δp, shear viscosity η, and bulk viscosity ζ by

$$\delta p = c_s^2\bar{\rho}\delta_\ell, \quad \eta = \frac{3\bar{\rho}c_{sv}^2}{4\mathcal{H}}, \quad \zeta = \frac{\bar{\rho}c_{bv}^2}{\mathcal{H}}. \tag{1.86}$$

We will see below that the equation of motion for the velocity divergence field is sourced by a double divergence of the effective stress tensor. This induces a degeneracy between the dissipative coefficients and the speed of sound, that we parametrise in the combined speed of sound $c_{s(1)}^2$ (Carrasco, Hertzberg, and Senatore 2012). Clearly, this coefficient and those associated with higher-order corrections exhibit a dependence on the cutoff scale Λ, i.e. $c_{s(1)}^2 = c_{s(1)}^2(\Lambda)$. Fortunately, the form of the different pieces included in the effective stress tensor expansion exactly balance the cutoff dependence of the various integrals involved in standard perturbation theory. This perturbative scheme corresponds to the EFT limit in which the effective stress tensor vanishes and the matter fluid is pressureless. Therefore, large fluctuations on small scales will also be treated perturbatively, introducing significant inaccuracies in the predictions. Within the EFT framework, we can identify these errors with the non-zero finite coefficients in Eq. (1.85) derived in the limit $\Lambda \to \infty$. For this, terms in the effective stress tensor will be often referred to as *counterterms*.

[16] Although virialized objects do not contribute to the effective pressure, non-virialized scales give corrections to the background of the order of the velocity dispersion, i.e. $w_{\rm eff} \sim v^2 \sim 10^{-5}$ (Baumann, Nicolis, et al. 2012). However, these are too small to have a measurable effect on the background expansion.

After taking the divergence of (1.78b) and moving to Fourier space[17], the equations of motion for the long-wavelength fluid read

$$\dot{\delta}(a,\boldsymbol{k}) + \theta(a,\boldsymbol{k}) = -\int \frac{\mathrm{d}^3\boldsymbol{q}}{(2\pi)^3}\alpha(\boldsymbol{q},\boldsymbol{k}-\boldsymbol{q})\delta(a,\boldsymbol{k}-\boldsymbol{q})\theta(a,\boldsymbol{q}), \tag{1.88a}$$

$$\dot{\theta}(a,\boldsymbol{k}) + \mathcal{H}\theta(a,\boldsymbol{k}) + \frac{3}{2}\mathcal{H}^2\Omega_{\mathrm{m}}(a)\delta(a,\boldsymbol{k}) = -\int \frac{\mathrm{d}^3\boldsymbol{q}}{(2\pi)^3}\beta(\boldsymbol{q},\boldsymbol{k}-\boldsymbol{q})\theta(a,\boldsymbol{k}-\boldsymbol{q})\theta(a,\boldsymbol{q}) - ik_i(\partial\tau)_{\rho_\ell}{}^i(\boldsymbol{k}), \tag{1.88b}$$

where we suppressed all subscripts ℓ defining long-wavelength fields, and the functions

$$\alpha(\boldsymbol{k},\boldsymbol{q}) = \frac{(\boldsymbol{k}+\boldsymbol{q})\cdot\boldsymbol{k}}{k^2}, \qquad \beta(\boldsymbol{k},\boldsymbol{q}) = \frac{(\boldsymbol{k}+\boldsymbol{q})^2\,\boldsymbol{k}\cdot\boldsymbol{q}}{2q^2k^2}, \tag{1.89}$$

embody the coupling between long modes. The last term in Eq. (1.88b) is simply defined as

$$(\partial\tau)_{\rho_\ell}{}^i \equiv \frac{1}{\rho_\ell}\partial_j[\tau^{ij}]_\Lambda. \tag{1.90}$$

The fluid equations above are then solved perturbatively around the linear solutions for $\delta_\ell(a,\boldsymbol{k})$ and $\theta_\ell(a,\boldsymbol{k})$, with the n-th-order solutions $\delta_\ell^{(n)}$ and $\theta_\ell^{(n)}$ expressed as integrals over the linear solution $\delta^{(1)}$ (see sec. 1.2.2). Our aim is to obtain an efficient prescription to derive two-point correlation functions of the density field, i.e. $\langle\delta_\ell^{(a)}\delta_\ell^{(b)}\rangle$, with angle brackets denoting the ensemble average. These will be calculated in sec. 1.4.1 and used in chapter 5, and beyond the linear regime (i.e. tree level) will involve integrations over momenta (i.e. loop corrections) that can be organised in terms of Feynman diagrams.

In chapter 5 we will be interested in two-loop corrections (i.e. integration over two momenta) to the two-point correlation function accurate to sub-percent level. This calls for an extension of the expansion Eq. (1.85) to second order in the fields and next-to-leading order in derivatives, where the relevant counterterms are

$$(\partial\tau)_{\rho_\ell}{}^i \subset \{\partial^i\delta, \partial^i\delta^2, \partial^2\partial^i\delta\}. \tag{1.91}$$

The evaluation of these counterterms requires however particular attention. Before reaching virialization, short modes evolve on a time scale comparable to that of the long modes, namely $\mathcal{H}^{-1}$. As a result, counterterms are generally non-local in time because short distance physics

[17] Differently from sec. 1.2.2, here and in sec. 1.4.1 we adopt the non-unitary Fourier transform convention

$$A(\boldsymbol{k}) = \int \mathrm{d}^3\boldsymbol{x}A(\boldsymbol{x})e^{-i\boldsymbol{k}\cdot\boldsymbol{x}}, \quad A(\boldsymbol{x}) = \int \frac{\mathrm{d}^3\boldsymbol{k}}{(2\pi)^3}A(\boldsymbol{k})e^{i\boldsymbol{k}\cdot\boldsymbol{x}}. \tag{1.87}$$

displays long-range time correlations. In this sense, the behaviour of the long-wavelength fields along the trajectory of fluid elements should impact on its own dynamics. Thus, we can express each term in $(\partial\tau)_{\rho_\ell}{}^i$ as a convolution with some (unknown) time-dependent kernel K_m, namely

$$\begin{aligned}(\partial\tau)_{\rho_\ell}{}^i = &\int \mathrm{d}\tau' K_1(\tau,\tau')\partial^i\delta(\tau',\boldsymbol{x}_{\mathrm{fl}}) \\ &+ \int \mathrm{d}\tau' K_2(\tau,\tau')\partial^i\delta^2(\tau',\boldsymbol{x}_{\mathrm{fl}}) \\ &+ \int \mathrm{d}\tau' K_3(\tau,\tau')\partial^2\partial^i\delta(\tau',\boldsymbol{x}_{\mathrm{fl}}).\end{aligned} \tag{1.92}$$

Here, derivatives are with respect to $\boldsymbol{x}$, while the field is evaluated along the path $\boldsymbol{x}_{\mathrm{fl}}[\tau,\tau']$ of a fluid element, defined recursively by

$$\boldsymbol{x}_{\mathrm{fl}}[\tau,\tau'] = \boldsymbol{x} - \int_{\tau'}^{\tau} \mathrm{d}\tau'' \boldsymbol{v}(\tau'',\boldsymbol{x}_{\mathrm{fl}}[\tau,\tau'']). \tag{1.93}$$

The specific form of $\boldsymbol{x}_{\mathrm{fl}}$ ensures that the equations of motion satisfy generalized Galilean invariance, where the trasformations are defined by $\boldsymbol{v}(\boldsymbol{x},\tau) \to \boldsymbol{v}(\boldsymbol{x}',\tau) - \dot{\boldsymbol{n}}(\tau)$ and $\Phi(\boldsymbol{x},\tau) \to \Phi(\boldsymbol{x}',\tau) + (\mathcal{H}\dot{\boldsymbol{n}}(\tau) + \ddot{\boldsymbol{n}}(\tau))\cdot\boldsymbol{x}'$, with $\boldsymbol{x} \to \boldsymbol{x}' + \boldsymbol{n}(\tau)$ (see, e.g., Baldauf, Mercolli, Mirbabayi, et al. 2015). However, we need not worry about the details of the entire fluid trajectory $\boldsymbol{x}_{\mathrm{fl}}$ if we are interested in perturbative solutions up to a certain finite order. In fact, Baldauf, Mercolli, Mirbabayi, et al. (2015) found that at any given order in perturbation theory, the counterterms in Eq. (1.92) can always be written as finite set of operators evaluated at the same point in time. In addition, Foreman and Senatore (2016) explicitly showed that including non-locality in time does not improve significantly the performance of the theory. Thus, we can assume locality in time from the start, i.e. $K_m \propto \delta_D(a-a')$, and incorporate all memory effects in the time-dependent fluid parameters of $(\partial\tau)_{\rho_\ell}{}^i$ (see also Angulo, Foreman, et al. 2015). Inserting the local approximation of Eq. (1.92) into the equation of motion for the long-wavelength velocity field gives

$$\begin{aligned}a\mathcal{H}\theta' + \mathcal{H}\theta + \frac{3}{2}\mathcal{H}^2\Omega_{\mathrm{m}}(a)\delta = &-\int \frac{\mathrm{d}^3q}{(2\pi)^3}\beta(\boldsymbol{q},\boldsymbol{k}-\boldsymbol{q})\theta(a,\boldsymbol{k}-\boldsymbol{q})\theta(a,\boldsymbol{q}) \\ &+ \epsilon_s(2\pi)\bar{c}^2_{s(1)}(a)\frac{k^2}{k^2_{\mathrm{NL}}}\delta(a,\boldsymbol{k}) \\ &+ \epsilon_1(2\pi)\bar{c}_1(a)\frac{k^2}{k^2_{\mathrm{NL}}}\left[\delta(a,\boldsymbol{k}) * \delta(a,\boldsymbol{k})\right] \\ &+ \epsilon_4(2\pi)^2\bar{c}_4(a)\frac{k^4}{k^4_{\mathrm{NL}}}\delta(a,\boldsymbol{k}),\end{aligned} \tag{1.94}$$

where primes represent derivatives with respect to the scale factor a, $\sqcup * \sqcup$ denotes the convolution operation, and the ϵ_α's are factors used to organize the order of the perturbative

solution, i.e. ϵ_α^0 corresponds to the standard solution, and higher powers are associated with the related EFT corrections with unknown coefficients $\bar{c}_\alpha$. To further simplify the algebra involved we employ the approximation

$$f(a) \approx \Omega_{\rm m}(a)^{1/2}, \tag{1.95}$$

which captures remarkably well the evolution of the linear growth factor in ΛCDM (Bernardeau, Colombi, et al. 2002). Without loss of generality, we also extract part of the time-dependence of the EFT coefficients as

$$\begin{aligned} \bar{c}^2_{s(1)}(a) &= c^2_{s(1)}(a)\left(\mu D_1(a)^\zeta \mathcal{H}^2 f^2\right), \\ \bar{c}_1(a) &= c_1(a)\left(\nu D_1(a)^\xi \mathcal{H}^2 f^2\right), \\ \bar{c}_4(a) &= c_4(a)\left(\sigma D_1(a)^\chi \mathcal{H}^2 f^2\right). \end{aligned} \tag{1.96}$$

Here, $D_1(a) \equiv D_+(a)/D_+(1)$ is the normalized linear growth factor, μ, ν and σ are constants that we can set to any convenient value, and ζ, ξ and χ allow for a time-dependence of the EFT perturbative solutions that is not fully captured by the standard ansatz in powers of the growth factor (see Eq. (1.97) below).

It can be shown that the following ansatz for the time-dependence of the long-wavelength fields provides solutions entirely in terms of the linear density field (Angulo, Foreman, et al. 2015; Foreman and Senatore 2016)

$$\begin{aligned} \delta(a,\boldsymbol{k}) = &\sum_{n=1}^{\infty}[D_1(a)]^n \delta^{(n)}(\boldsymbol{k}) + \epsilon_s \sum_{n=1}^{\infty}[D_1(a)]^{n+\zeta}\tilde{\delta}^{(n)}(\boldsymbol{k}) + \epsilon_s^2 \sum_{n=1}^{\infty}[D_1(a)]^{n+2\zeta}\hat{\delta}^{(n)}(\boldsymbol{k}) \\ &+ \epsilon_1 \sum_{n=1}^{\infty}[D_1(a)]^{n+\xi}\check{\delta}^{(n)}(\boldsymbol{k}) + \epsilon_4 \sum_{n=1}^{\infty}[D_1(a)]^{n+\chi}\bar{\delta}^{(n)}(\boldsymbol{k}), \end{aligned} \tag{1.97a}$$

$$\begin{aligned} \theta(a,\boldsymbol{k}) = -\mathcal{H}(a)f(a)\Bigg\{ &\sum_{n=1}^{\infty}[D_1(a)]^n \theta^{(n)}(\boldsymbol{k}) + \epsilon_s \sum_{n=1}^{\infty}[D_1(a)]^{n+\zeta}\tilde{\theta}^{(n)}(\boldsymbol{k}) \\ &+ \epsilon_s^2 \sum_{n=1}^{\infty}[D_1(a)]^{n+2\zeta}\hat{\theta}^{(n)}(\boldsymbol{k}) + \epsilon_1 \sum_{n=1}^{\infty}[D_1(a)]^{n+\xi}\check{\theta}^{(n)}(\boldsymbol{k}) \\ &+ \epsilon_4 \sum_{n=1}^{\infty}[D_1(a)]^{n+\chi}\bar{\theta}^{(n)}(\boldsymbol{k})\Bigg\}, \end{aligned} \tag{1.97b}$$

where $\delta^{(n)}(\boldsymbol{k})$ and $\theta^{(n)}(\boldsymbol{k})$ are the solutions in standard perturbation theory, and the remaining analogous terms are corrections introduced by the counterterms in Eq. (1.94). By plugging Eq. (1.97) in the equations of motion (1.88a) and (1.94), and separately collecting terms of order ϵ_α^0 we can find the standard solutions for the long-wavelength fields in terms of

symmetrized kernels $F_n^{(s)}$ and $G_n^{(s)}$ as[18]

$$\delta^{(n)}(\boldsymbol{k}) = \int_{\boldsymbol{q}_1} \cdots \int_{\boldsymbol{q}_n} (2\pi)^3 \delta_{\mathrm{D}}(\boldsymbol{k} - \boldsymbol{q}_{1\cdots n}) F_n^{(s)}(\boldsymbol{q}_1, \ldots, \boldsymbol{q}_n) \delta^{(1)}(\boldsymbol{q}_1) \cdots \delta^{(1)}(\boldsymbol{q}_n), \tag{1.100}$$

$$\theta^{(n)}(\boldsymbol{k}) = \int_{\boldsymbol{q}_1} \cdots \int_{\boldsymbol{q}_n} (2\pi)^3 \delta_{\mathrm{D}}(\boldsymbol{k} - \boldsymbol{q}_{1\cdots n}) G_n^{(s)}(\boldsymbol{q}_1, \ldots, \boldsymbol{q}_n) \delta^{(1)}(\boldsymbol{q}_1) \cdots \delta^{(1)}(\boldsymbol{q}_n), \tag{1.101}$$

where $\boldsymbol{q}_{1\cdots n} = \boldsymbol{q}_1 + \cdots + \boldsymbol{q}_n$, and we have used the shorthand notation

$$\int_{\boldsymbol{q}} \equiv \int \frac{\mathrm{d}^3\boldsymbol{q}}{(2\pi)^3}. \tag{1.102}$$

Grouping terms with powers ϵ_s^1 and ϵ_s^2, we obtain the new solutions $\tilde{\delta}^{(n)}(\boldsymbol{k})$, $\tilde{\theta}^{(n)}(\boldsymbol{k})$, $\hat{\delta}^{(n)}(\boldsymbol{k})$ and $\hat{\theta}^{(n)}(\boldsymbol{k})$, which have similar forms in terms of $\tilde{F}_n^{(s)}$, $\tilde{G}_n^{(s)}$, $\hat{F}_n^{(s)}$ and $\hat{G}_n^{(s)}$, respectively[19]. Likewise, we can collect terms with powers ϵ_1^1 and ϵ_4^1 that give the solutions corresponding to c_1 and c_4 counterterms. Once all kernels are specified, n-point correlation functions of δ or θ can be calculated up to a desired loop order (see sec. 1.4.1 for details on the two-point correlation function).

Full nonlinear regime

As we mentioned in the previous section, the amplification of density fluctuations due to gravity eventually reaches a stage in which a perturbative analysis is no longer applicable. The EFT technique is suitable for a coarse-grained universe, to investigate the overall distribution of matter on cosmological distances. We now shift our focus on smaller scales, deep in the nonlinear regime, where collapsed objects such as clusters of galaxies form. This is a topic of extreme interest. In fact, the abundance of clusters in the observable universe is strongly dependent on its constituents and on the nature of dark energy. Cluster number counts data thus provide an invaluable source of information for comprehending the cosmos. To consistently interpret the available observations we need a method capable of predicting the

[18] $F_n^{(s)}$ and $G_n^{(s)}$ are symmetric homogeneous functions of the wave vectors $\boldsymbol{q}_1, \ldots, \boldsymbol{q}_n$ with degree zero. They can be derived from the recurrence relations for F_n and G_n given in, e.g., Bernardeau, Colombi, et al. (2002) as

$$F_n^{(s)}(\boldsymbol{q}_1, \ldots, \boldsymbol{q}_n) = \frac{1}{n!} \sum_{\pi} F_n(\boldsymbol{q}_{\pi(1)}, \ldots, \boldsymbol{q}_{\pi(n)}), \tag{1.98}$$

$$G_n^{(s)}(\boldsymbol{q}_1, \ldots, \boldsymbol{q}_n) = \frac{1}{n!} \sum_{\pi} G_n(\boldsymbol{q}_{\pi(1)}, \ldots, \boldsymbol{q}_{\pi(n)}), \tag{1.99}$$

where the sum runs over all possible permutations π of the set $\{1, \ldots, n\}$. The complexity of the symmetrized kernels increases rapidly with n. For instance, the number of terms in $F_3^{(s)}$ and $G_3^{(s)}$ is 134, and considering $n = 4$, instead, already gives 8523 terms. This is a critical point if we are to include higher-order corrections to the linear solutions. A method to reduce the effect of this feature is discussed in chapter 5.

[19] Explicit expressions for the recursion relations $\tilde{F}_n$, $\tilde{G}_n$, $\hat{F}_n$ and $\hat{G}_n$ can be found in Angulo, Foreman, et al. (2015) and Foreman and Senatore (2016).

formation of these virialized structures. Despite its limitations, the spherical collapse model is a simple physical system that takes us one step closer to the answer.

Let us consider a spherical, uniform and small density perturbation of the non-relativistic matter fluid in an otherwise homogeneous universe. To describe its evolution we can combine the nonlinear continuity and Euler equations (1.78) for a pressureless perfect fluid and no smoothing, i.e. $(\partial\tau)_{\rho_\ell}{}^i = 0$. Together with the Poisson equation they give

$$\ddot{\delta}_\mathrm{m} + 2H\dot{\delta}_\mathrm{m} - \frac{(1+\delta_\mathrm{m})}{a^2}\partial_i\partial_j v^i v^j = 4\pi G\bar{\rho}_\mathrm{m}\delta_\mathrm{m}(1+\delta_\mathrm{m}), \tag{1.103}$$

where time derivatives and peculiar velocities are taken with respect to cosmic time t. For the velocity field, we enforce the top-hat profile throughout the evolution. Hence, the interior velocity field is constrained to be $\boldsymbol{v} = A(\tau)\boldsymbol{r}$, where $\boldsymbol{r}$ is the comoving radial coordinate. The continuity equation gives its amplitude in terms of the top-hat density perturbation as

$$\dot{\delta}_\mathrm{m} + \frac{3}{a}(1+\delta_\mathrm{m})A = 0, \tag{1.104}$$

which gives the relation[20]

$$\partial_i\partial_j v^i v^j = 12A^2 = \frac{4}{3}a^2\frac{\dot{\delta}_\mathrm{m}^2}{(1+\delta_\mathrm{m})^2}, \tag{1.105}$$

for the velocity term in Eq. (1.103). Accordingly, the evolution of a top-hat overdensity is governed by the following nonlinear second-order differential equation

$$\ddot{\delta}_\mathrm{m} + 2H\dot{\delta}_\mathrm{m} - \frac{4}{3}\frac{\dot{\delta}_\mathrm{m}^2}{(1+\delta_\mathrm{m})} = 4\pi G\bar{\rho}_\mathrm{m}\delta_\mathrm{m}(1+\delta_\mathrm{m}). \tag{1.106}$$

To study the evolution of the top-hat radius we resort to mass conservation, i.e.

$$M = (4\pi/3)r^3\bar{\rho}_\mathrm{m}(1+\delta_\mathrm{m}) = \text{const.}, \tag{1.107}$$

which upon differentiation relates r and δ as

$$\frac{\ddot{r}}{r} = H^2 + \dot{H} - \frac{1}{3(1+\delta_\mathrm{m})}(\ddot{\delta}_\mathrm{m} + 2\dot{\delta}_\mathrm{m}H - \frac{4}{3}\frac{\dot{\delta}_\mathrm{m}^2}{1+\delta_\mathrm{m}}). \tag{1.108}$$

[20] This can be derived using $\boldsymbol{v} = Ar\hat{\boldsymbol{r}}$. The unit vector in cartesian coordinates reads

$$\hat{r}^i = \frac{x^i}{(x_i x^i)^{1/2}},$$

with $r^2 = x_i x^i$. These give $v^i = Ax^i$, which plugged in the second derivative of Eq. (1.105) justifies the first equality.

Eqs. (1.106) and (1.108) can be combined to obtain

$$\frac{\ddot{r}}{r} = -\frac{4\pi G}{3}[\bar{\rho}_{\rm m} - 2\bar{\rho}_\Lambda] - \frac{4\pi G}{3}\delta\rho_{\rm m}, \tag{1.109}$$

where we have employed the Friedmann equation (1.13a) to replace the Hubble parameter in favour of the background densities.

Expressing time derivatives as $' = d/d\ln a$, and defining $y \equiv [r - r_i a/a_i]/r_i$, we have

$$y'' + \frac{H'}{H}y' = -\frac{1}{2}\frac{\Omega_{\rm m}a^{-3} - 2\Omega_\Lambda}{\Omega_{\rm m}a^{-3} + \Omega_\Lambda}y - \frac{1}{2}\frac{\Omega_{\rm m}a^{-3}}{\Omega_{\rm m}a^{-3} + \Omega_\Lambda}\left(\frac{a}{a_i} + y\right)\delta_{\rm m}, \tag{1.110}$$

with

$$\delta_{\rm m} = \left(\frac{1}{ya_i/a + 1}\right)^3 (1 + \delta_{{\rm m},i}) - 1 \tag{1.111}$$

and $\delta_{{\rm m},i}$ is the initial density perturbation at a_i. The initial conditions are set during matter domination (i.e. $\Omega_{\rm m}(a_i) \approx 1$) when $\delta_{\rm m} \ll 1$ and $\delta_{\rm m} \propto a$ (see Eq. (1.55)). Therefore, at $a = a_i$ we have $y = 0$ and $y' = -\delta_{{\rm m},i}/3$.

We will solve numerically Eq. (1.110), and its extensions to alternative theories of gravity, in chapters 3 and 4. Here, we discuss in broad terms the formation of a collapsed object embedded in an expanding universe. At early times, $a \approx a_i$, the overdensity evolves according to the predictions of the linear perturbation theory developed in sec. 1.2.2. As time passes, the perturbation grows and leaves the linear regime, eventually reaching a maximum radius and halting the expansion. This stage is called *turnaround* and defines the epoch of complete decoupling from the background expansion. After that, contraction starts. For the simple system at hand, with ideal spherical symmetry and a pressureless perfect fluid, the perturbation would collapse to a singularity, thus ending in an infinite dense state. However, perfect spherical symmetry never occurs in the universe, and dark matter behaves as an imperfect fluid on small scales (e.g., see the introductory section on the EFT of large-scale structure). Rather, the perturbation undergoes extreme shell crossing and finally results in a virialized object with finite size commonly known as *halo*. It is typically assumed that the time of virialization corresponds to the epoch of singular collapse of the spherical top-hat perturbation. Interestingly, this result has been corroborated by numerical simulations of collapsing halos (see, e.g., Mo, van den Bosch, and White 2010). We can relate the real dynamics to the spherical collapse equation (1.110) using that turnaround occurs when $r' = 0$ or $y' = -a/a_i$, and collapse happens when $r = 0$ or $y = -a/a_i$.

A very useful quantity within the theory of structure formation is the linear overdensity extrapolated to the collapse epoch $a_{\rm collapse}$. This is simply obtained applying Eq. (1.58) to

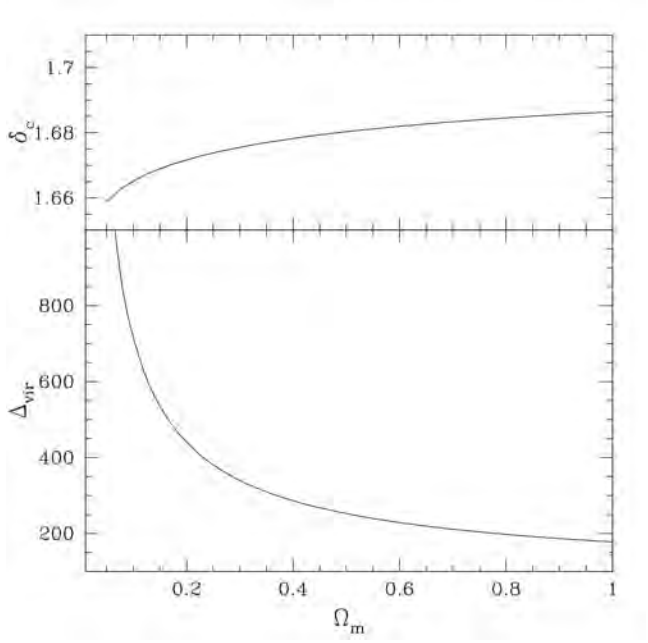

Fig. 1.9 Present-day spherical collapse parameters for the flat ΛCDM model as a function of $\Omega_{\rm m}$. The top panel shows the linear overdensity extrapolated to the epoch of collapse, δ_c. The bottom panel illustrates the overdensity reached at the time of virialization, $\Delta_{\rm v}$. Figure adapted from Schmidt, Lima, et al. (2009).

the initial density perturbation as

$$\delta_c \equiv \delta_{\rm m}(a_{\rm collapse}) = \frac{D_+(a_{\rm collapse})}{a_i}\delta_{\rm m,i}. \tag{1.112}$$

Note that for this cosmological model, δ_c is completely independent of the size (or mass) of the initial overdensity. This is not generally the case for modified gravity theories, as we shall see in chapter 4. For reference, collapse during matter domination gives $\delta_c = 1.686$, and with $\Omega_{\rm m} = 0.3$, $\delta_c = 1.679$ for objects forming today. In Fig. 1.9 (top panel), we show the threshold for collapse at $a = 1$ as a function of $\Omega_{\rm m}$.

To relate spherical collapse with virialized halos we need the virial theorem. The potential energy of a self-gravitating top-hat matter overdensity of mass M and radius r is (see, e.g., Binney and Tremaine 2008)

$$W = -\frac{3}{5}\frac{GM^2}{r}. \tag{1.113}$$

During matter domination the virial theorem reads $W = -2T$, where T is the kinetic energy. At turnaround $T = 0$, and we can use the virial theorem together with total energy conservation to link the turnaround radius to the final radius at virialization, that is

$$W(r_{\rm max}) = W(r_{\rm vir}) + T(r_{\rm vir}) = W(r_{\rm vir})/2, \tag{1.114}$$

implying $r_{\rm vir} = r_{\rm max}/2$. The virial overdensity $\Delta_{\rm vir}$ is defined by

$$\Delta_{\rm vir} \equiv \delta_{\rm vir} + 1 = \frac{\rho_{\rm m}(r_{\rm vir})}{\bar{\rho}_{\rm m}(r=0)}, \tag{1.115}$$

where $\rho_{\rm m}(r_{\rm vir})$ is the density of the top-hat perturbation when $r = r_{\rm vir}$ during collapse, and $\bar{\rho}_{\rm m}(r=0)$ represents the average density of matter in the universe at $a = a_{\rm collapse}$. For collapse in the matter dominated regime $\Delta_{\rm vir} \approx 178$.

At low redshifts, these relations change under the effect of cosmic acceleration. A cosmological constant contributes with a potential energy per unit mass $w_\Lambda = -4\pi G\bar{\rho}_\Lambda r^2/3$ (Lahav, Lilje, et al. 1991), and upon integration over the top-hat profile we get $W_\Lambda = -(4\pi G\bar{\rho}_\Lambda/5)Mr^2$. The virial theorem then becomes

$$T = -\frac{1}{2}W + W_\Lambda, \tag{1.116}$$

which relates the radius at turnaround to the virial radius as

$$\frac{1}{2}W(r_{\rm vir}) + 2W_\Lambda(r_{\rm vir}) = W(r_{\rm max}) + W_\Lambda(r_{\rm max}). \tag{1.117}$$

By defining the ratio $s \equiv r_{\rm v}/r_{\rm max}$ and the quantity

$$\eta \equiv \frac{2\bar{\rho}_\Lambda}{\rho_{\rm m}(r_{\rm max})} = \frac{2\Omega_\Lambda}{\Omega_{\rm m}a^{-3}(1+\delta_{\rm m})} \tag{1.118}$$

at turnaround, we can find the relationship between the two radii from inverting

$$\eta = \frac{2s-1}{2s^3-s}, \tag{1.119}$$

with $s \to 1/2$ for $\eta \to 0$, as expected. In Fig. 1.9 (lower panel), we show the virial overdensity for collapse at $z = 0$ as a function of $\Omega_{\rm m}$. For a ΛCDM cosmology with $\Omega_{\rm m} = 0.3$ this amounts to $\Delta_{\rm vir} \approx 380$.

1.3 Infrared challenge to General Relativity

The concordance cosmology has shown remarkable consistency across a number of observations despite its simple framework (see sec. 1.1). We would be content with this picture of the universe, were it not for the stark discrepancy between the predicted and the observed values of the cosmological constant.

From the present-day Hubble parameter[21], $H_0 = 2.13h \times 10^{-42}$ GeV, the energy density associated with the cosmological constant is

$$\rho_\Lambda = \frac{\Lambda}{8\pi G} \sim M_{\rm pl}^2 H_0^2 \sim 10^{-48}\ \text{GeV}^4. \tag{1.120}$$

From a theoretical viewpoint, we expect a contribution to the cosmological constant in the form of vacuum energy[22] (Weinberg 1989a)

$$\langle T_{\mu\nu} \rangle \sim -\langle \rho \rangle g_{\mu\nu}, \tag{1.121}$$

produced by quantum-mechanical processes involving Standard Model fields. An approximate estimate of its value can be derived by modeling these fields as a collection of independent harmonic oscillators at each point in space. A sum over their zero-point energies gives

$$\langle \rho \rangle \sim \int_0^{\Lambda_{\rm UV}} \frac{{\rm d}^3 k}{(2\pi)^3} E_k \sim \int_0^{\Lambda_{\rm UV}} {\rm d}k\ k^2 \sqrt{k^2 + m^2} \sim \Lambda_{\rm UV}^4, \tag{1.122}$$

where $\Lambda_{\rm UV}$ is a cutoff that represents the maximum energy scale up to which our predictions can be trusted. We can conservatively set $\Lambda_{\rm UV} \sim 1$ TeV, which corresponds to the energies around the weak scale, where we know the Standard Model works very well. For this value, the theoretical expectation for the cosmological constant is

$$\langle \rho \rangle \sim (1\,\text{TeV})^4 \sim\ 10^{12}\ \text{GeV}^4, \tag{1.123}$$

which is 60 orders of magnitude larger than what is required for the late-time cosmic acceleration! We could add a classical contribution to the cosmological constant and through extreme fine-tuning obtain the observed value. However, such tuning is unstable under quantum corrections (see, e.g., Padilla 2015). This is the so-called *cosmological constant problem*. Also, if the source of the accelerating expansion is a cosmological constant, it is somewhat unexpected for $\Omega_{\rm m}$ and Ω_Λ to be similar today. This is known as the *coincidence problem*.

A possible solution might come from reconsidering the assumptions underlying the ΛCDM model, namely (i) the statistical homogeneity and isotropy on large scales, and (ii) the description of gravity with GR on all scales. We will hold on to the first pillar, and examine the consequences of possible modifications to GR. This is motivated by the huge extrapolation

[21] Here, we briefly align to the language of particle physics, where quantities are defined in natural units $c = \hbar = 1$. Mass and energy are expressed in electronvolts (eV) or its multiples (e.g. 10^9 eV = 1 GeV); lengths and times are in units of eV^{-1}. The reduced Planck mass then becomes $M_{\rm pl} = 1/\sqrt{8\pi G} \approx 2.4 \times 10^{18}$ GeV.

[22] This may be deduced from Lorentz invariance in flat space, which requires $\langle T_{\mu\nu} \rangle \propto \eta_{\mu\nu}$. The equivalence principle allows then the mapping $\eta_{\mu\nu} \mapsto g_{\mu\nu}$.

we make from Solar System scales ($\ll 1$ pc), where GR has been extremely well tested, up to the Hubble scale and beyond ($\gtrsim 1$ Gpc).

Our freedom to apply modifications to the GR machinery is hampered by the Lovelock's theorem (Lovelock 1971; Lovelock 1972). It states that in a four dimensional space, Einstein's equations are the only possible second-order local equations of motion for a metric. It suggests that, in order to construct extension of GR, we must do one or more of the following:

- Include other fields, beyond the metric tensor.
- Allow for higher than second derivatives of the metric in the field equations.
- Work in a higher dimensional spacetime.
- Accept non-locality.

In recent years, theorists have worked tirelessly to find viable alternatives to GR that could lead to a solution to the cosmological constant problem and explain the late-time acceleration of the Universe (see, e.g., Clifton, Ferreira, et al. 2012). In this thesis, we will consider models of a class of modified gravity theories with an extra degree of freedom in the form of a scalar field. These particular extensions belong to the family of *scalar-tensor theories* (Bergmann 1968; Nordtvedt 1970; Wagoner 1970), and generally present three regimes:

- At the background level, gravity is modified to accommodate the late-time acceleration.
- In the linear regime the scalar field mediates an additional fifth force with a range inversely proportional to its mass.
- On small scales the non-linear interactions of the scalar field restore GR, which is essential to ensure that we have a viable theory that satisfies local constraints.

In chapters 3 and 4 we will be interested in testing and modeling the growth of structure in the linear and nonlinear regimes of $f(R)$ gravity[23]. The allowed range of theory parameters will be chosen to closely match the effect of a cosmological constant on the background expansion, effectively making it indistinguishable from a ΛCDM cosmology using SNIa or BAO data alone.

1.3.1 Scalar-tensor theories

Although in GR gravity is mediated only by the metric tensor field $g_{\mu\nu}$, it is plausible to consider other fields in the equations describing the gravitational dynamics, with the simplest

[23]In its first formulations $f(R)$ gravity was laid out as a higher-derivative extension of GR (see, e.g., Sotiriou and Faraoni 2010 and references therein). However, several authors later showed that, under a suitable transformation, these theories are dynamically equivalent to a subclass of scalar-tensor theories (see, e.g., Chiba 2003; Flanagan 2004; Sotiriou 2006). More on this topic below.

scenario being the addition of an extra scalar field. As mentioned above, the effect of this new field needs to be suppressed on laboratory or Solar System scales, where GR is known to be an accurate description of gravity. This is usually achieved via a screening mechanism.

Scalar-tensor theories are popular and well studied alternatives to GR, and arise naturally as effective field theories at low energies of higher dimensional theories, such as string models (Taylor and Veneziano 1988; Maeda 1988; Damour and Polyakov 1994; Damour, Piazza, and Veneziano 2002a; Damour, Piazza, and Veneziano 2002b). The action for a general scalar-tensor theory that contains up to first derivatives of the scalar field ϕ can be written as (Dicke 1962)

$$S = \frac{1}{2\kappa^2}\int \mathrm{d}^4x\sqrt{-g}\left[\phi R - \frac{\omega(\phi)}{\phi}\nabla_\mu\phi\nabla^\mu\phi - 2\Lambda(\phi)\right] + S_\mathrm{m}[g_{\mu\nu}, \psi_\mathrm{m}^{(i)}], \tag{1.124}$$

where $\kappa^2 \equiv 8\pi G$, $\omega(\phi)$ is an arbitrary function, often referred to as the *coupling parameter*, and $\Lambda(\phi)$ is a generalization of the cosmological constant. This theory reduces to GR with a cosmological constant in the limit $\omega \to \infty$, $\omega'/\omega^2 \to 0$ and $\Lambda \to$ constant (see Eq. (1.1)). The formulation of scalar-tensor theories in the form of Eq. (1.124) is referred to as the Jordan frame. In this frame, the scalar field is minimally-coupled to the matter fields, and test particles follow the geodesics of the metric $g_{\mu\nu}$.

The variation of the action with respect to $g^{\mu\nu}$ gives the field equations

$$\phi G_{\mu\nu} + \left[\Box\phi + \frac{1}{2}\frac{\omega}{\phi}(\nabla\phi)^2 + \Lambda\right]g_{\mu\nu} - \nabla_\mu\nabla_\nu\phi - \frac{\omega}{\phi}\nabla_\mu\phi\nabla_\nu\phi = \kappa^2 T_{\mu\nu}. \tag{1.125}$$

Since these theories contain an additional degree of freedom, we must find the equation of motion describing its dynamics. By varying the action Eq. (1.124) with respect to ϕ and eliminating R with the trace of Eq. (1.125), we obtain

$$(2\omega + 3)\Box\phi + \omega'(\nabla\phi)^2 + 4\Lambda - 2\phi\Lambda' = \kappa^2 T, \tag{1.126}$$

where primes here denote derivatives with respect to ϕ, and $T \equiv g^{\mu\nu}T_{\mu\nu}$ is the trace of the energy-momentum tensor. These field equations completely characterize scalar-tensor theories.

We can rephrase the scalar-tensor theory action Eq. (1.124) in more familiar terms. In fact, these theories are *conformally equivalent* to GR, in that the metric $\tilde{g}_{\mu\nu}$ defined by

$$g_{\mu\nu} = A(\phi)^2\tilde{g}_{\mu\nu} \tag{1.127}$$

evolves according to the usual Einstein equations, with the scalar field contributing as a matter field[24]. However, in this formulation, known as Einstein frame, the scalar field is

[24] A conformal transformation of the metric is a transformation that alters scales, but preserves local angles.

non-minimally coupled to the non-relativistic matter fields and the weak equivalence principle is not satisfied. In other words, all massive particles in this frame are pulled away from the geodesics of $\tilde{g}_{\mu\nu}$ by a new force mediated by the scalar field, the so-called *fifth force*.

The transformation Eq. (1.127), along with the definitions $\sqrt{12+8A^2\omega} \equiv \partial\varphi/\partial \ln A$ and $V(\varphi) \equiv 2A^4\Lambda$ for the scalar φ and its potential $V(\varphi)$, map the Jordan frame action Eq. (1.124) to the following Einstein frame action

$$S = \int \mathrm{d}^4x\sqrt{-\tilde{g}}\left[\frac{\tilde{R}}{2\kappa^2} - \frac{1}{2}\tilde{\nabla}_\mu\varphi\tilde{\nabla}^\mu\varphi - V(\varphi)\right] + S_\mathrm{m}[A^2(\varphi)\tilde{g}_{\mu\nu}, \psi_\mathrm{m}^{(i)}], \tag{1.128}$$

where all quantities with a tilde are derived from the Einstein frame metric $\tilde{g}_{\mu\nu}$. Taking the coupling parameter ω as constant, the scalar fields ϕ and φ are therefore related by

$$\ln\phi = -\sqrt{\frac{2\kappa^2}{3+2\omega}}\varphi. \tag{1.129}$$

We can obtain the Einstein frame field equations by extremising the action Eq. (1.128) with respect to $\tilde{g}_{\mu\nu}$ and φ, which now read

$$\tilde{G}_{\mu\nu} = \kappa^2\left[\tilde{T}_{\mu\nu} + \tilde{\nabla}_\mu\varphi\tilde{\nabla}_\nu\varphi - \left(\frac{1}{2}\tilde{\nabla}_\sigma\varphi\tilde{\nabla}^\sigma\varphi + V\right)\tilde{g}_{\mu\nu}\right] \tag{1.130}$$

and

$$\tilde{\Box}\varphi - \frac{\mathrm{d}V}{\mathrm{d}\varphi} = -\frac{\mathrm{d}\ln A}{\mathrm{d}\varphi}\tilde{T}. \tag{1.131}$$

Note that since the Jordan frame metric couples minimally to matter, the associated energy-momentum tensor is conserved, $\nabla_\mu T^{\mu\nu} = 0$. On the other hand, because of the coupling with the scalar field, its counterpart in the Einstein frame is not,

$$\tilde{\nabla}_\mu\tilde{T}^{\mu\nu} = \tilde{T}\frac{\mathrm{d}\ln A}{\mathrm{d}\varphi}\tilde{\nabla}^\nu\varphi. \tag{1.132}$$

A modification to gravity that has sparked interest is the so-called $f(R)$ gravity (see, e.g., Sotiriou and Faraoni 2010 for a review). In these models, the gravitational part of the action Eq. (1.1) is extended to include a nonlinear function of the Ricci scalar, replacing the cosmological constant term. Thus, in the Jordan frame the action takes the form

$$S = \frac{1}{2\kappa^2}\int \mathrm{d}^4x\sqrt{-g}\big[R + f(R)\big] + S_\mathrm{m}[g_{\mu\nu}, \psi^{(i)}]. \tag{1.133}$$

In fact, this theory is classically equivalent to a particular scalar-tensor theory with the action given by Eq. (1.128) (Chiba 2003; Nunez and Solganik 2004). We can show this starting

from the alternative action

$$S = \frac{1}{2\kappa^2}\int \mathrm{d}^4x\sqrt{-g}\left[R + f(\Xi) + \frac{\mathrm{d}f}{\mathrm{d}\Xi}(R-\Xi)\right] + S_{\mathrm{m}}[g_{\mu\nu},\psi^{(i)}]\ , \tag{1.134}$$

which gives the field equations (Song, Hu, and Sawicki 2007; Hu and Sawicki 2007; Silvestri and Trodden 2009)[25]

$$(1+f_R)R_{\mu\nu} - \frac{1}{2}\left(R + f - 2\Box f_R\right)g_{\mu\nu} - \nabla_\mu\nabla_\nu f_R = \kappa^2 T_{\mu\nu}, \tag{1.135}$$

$$\Xi = R, \tag{1.136}$$

where $f_R \equiv \mathrm{d}f/\mathrm{d}R = \mathrm{d}f/\mathrm{d}\Xi$. From Eq. (1.136), we see that Ξ is a non-dynamical degree of freedom (its equation of motion does not involve time derivatives of Ξ). We can therefore use this equation to eliminate Ξ from the action and obtain the $f(R)$ action Eq. (1.133). The trace of Eq. (1.135) produces an equation for the scalar degree of freedom f_R,

$$\Box f_R = \frac{1}{3}\left(R + 2f - f_R R + \kappa^2 T\right) \equiv \frac{\mathrm{d}V_{\mathrm{eff}}(f_R)}{\mathrm{d}f_R}, \tag{1.137}$$

where $V_{\mathrm{eff}}(f_R)$ is an effective potential. A further differentiation gives the effective mass of the scalar f_R

$$m_{f_R}^2 = \frac{1}{3}\left(\frac{1+f_R}{f_{RR}} - R\right), \tag{1.138}$$

where $f_{RR} = \mathrm{d}^2 f/\mathrm{d}R^2$. Now, with the following conformal transformation and a field redefinition

$$\tilde{g}_{\mu\nu} = \left(1 + \frac{\mathrm{d}f}{\mathrm{d}\Xi}\right)g_{\mu\nu}, \qquad \varphi = -\sqrt{\frac{3}{2}}\kappa \ln\left(1 + \frac{\mathrm{d}f}{\mathrm{d}\Xi}\right), \tag{1.139}$$

the action Eq. (1.134) takes the form of Eq. (1.128), with

$$A^2(\varphi) = e^{\sqrt{2/3}\kappa\varphi}, \quad \text{and} \quad V(\varphi) = \frac{1}{2\kappa^2}\frac{\left(\varphi\frac{\mathrm{d}f}{\mathrm{d}\varphi} - f(\varphi)\right)}{\left(1 + \frac{\mathrm{d}f}{\mathrm{d}\varphi}\right)^2}. \tag{1.140}$$

Note that the relation between the fields in the two frames can be deduced from Eq. (1.129) for $\omega = 0$. Importantly, the potential for the scalar field depends on the function f, and viable functions must generate a screening mechanism to suppress modifications of gravity in high-density regions, such as our Solar System. A more extensive discussion on $f(R)$ gravity is provided in chapters 3 and 4.

[25] Note that we have assumed $f_{,\Xi\Xi} \neq 0$ in the Ξ equation of motion.

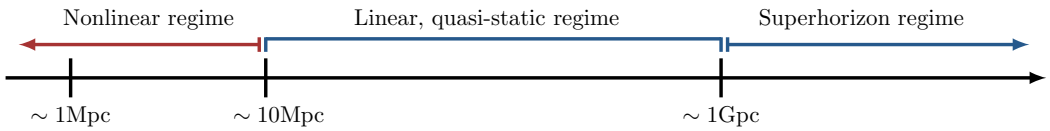

Fig. 1.10 Outside the horizon ($k \ll \mathcal{H}$) perturbations closely follow Eq. (1.141). Between ∼10–500 Mpc, linear perturbation theory robustly describes the evolution of fluctuations and time derivatives can be neglected. For scales $\lesssim 10$ Mpc, nonlinear gravitational effects become significant and need to be included for a correct description of structure formation. The fully nonlinear scale ∼1 Mpc roughly corresponds to the virial radius of a massive galaxy cluster. Figure taken from Joyce, Jain, et al. (2015).

1.3.2 Modified growth of structure

Intuitively, the presence of a fifth force in modified gravity theories will typically change the formation of structures compared to GR (see, e.g., Clifton, Ferreira, et al. 2012 for a comprehensive review). The evolution of perturbations follows the same qualitative classification discussed in sec. 1.2, which we recall here in Fig. 1.10 for easy reference. While it is relatively simple to incorporate model-independent modifications of gravity in the quasi-static Newtonian regime, the nonlinear regime demands more attention. In addition to the mode coupling already present in standard gravity, the purely nonlinear screening mechanism acts to suppress deviations from GR on small scales. This effect is inherently model-dependent, and an accurate description in this regime can only be satisfactory if carried out case-by-case.

Superhorizon scales

Assuming energy-momentum conservation, Bertschinger (2006) showed that metric fluctuations above the horizon obey a universal evolution equation in any metric theory of gravity. This fundamental constraint follows from the conservation of the gauge-invariant curvature perturbations $\mathcal{R}$ for adiabatic initial conditions. In conformal Newtonian gauge, the conservation of Eq. (1.49), combined with the momentum conservation Eq. (1.43b) for non-relativistic matter, gives

$$\Phi'' - \frac{H''}{H'}\Phi' + H\Psi' + \left(2H' - \frac{HH''}{H'}\right)\Psi = 0, \tag{1.141}$$

where primes represent differentiation with respect to cosmic time. Given the background evolution for H, and a function of time specifying the relation between Φ and Ψ, Eq. (1.141) determines the superhorizon evolution of the metric perturbations.

Subhorizon scales

On subhorizon scales, the conservation equations (1.43) remain unchanged in the Jordan frame. As in GR, their combination gives the second-order differential equation that describes the evolution of density perturbations, which for a non-relativistic fluid reads

$$\ddot{\delta} + \mathcal{H}\dot{\delta} = -k^2\Psi. \tag{1.142}$$

Note that differently from Eq. (1.52), we now can have $\Psi \neq \Phi$. We can express the relation between the two potentials through a general function of time and scale,

$$\gamma(a,k) \equiv \frac{\Phi}{\Psi}, \tag{1.143}$$

where $\gamma = 1$ in GR. The Poisson equation for the curvature potential can be obtained directly from Eq. (1.42a) as

$$k^2\Phi = -4\pi G a^2 \bar{\rho}\delta. \tag{1.144}$$

The gravitational effects of the scalar field on the non-relativistic matter can be parameterized by an effective time- and scale-dependent gravitational constant $G_{\rm eff}(a,k)$, that enters the Poisson equation for the Newtonian potential as

$$k^2\Psi = -4\pi G_{\rm eff}(a,k) a^2 \bar{\rho}\delta. \tag{1.145}$$

We can define the dimensionless quantity

$$\mu(a,k) \equiv \frac{G_{\rm eff}(a,k)}{G}, \tag{1.146}$$

so that Eq. (1.142) becomes

$$\ddot{\delta} + \mathcal{H}\dot{\delta} - 4\pi G\mu(a,k) a^2 \bar{\rho}\delta = 0. \tag{1.147}$$

For $\delta(a,k) = D_1(a,k)\delta(a_{\rm late},k)$, this equation tells us that the linear growth factor includes now a scale dependence.

Silvestri, Pogosian, and Buniy (2013) showed that for local, four-dimensional scalar-tensor theories, and under the quasi-static approximation, $\mu(a,k)$ and $\gamma(a,k)$ reduce to rational functions of k^2. If we further assume that the equations for Φ and Ψ have no higher than

second-order derivatives, we can write

$$\gamma = \frac{p_1(a) + p_2(a)k^2}{1 + p_3(a)k^2}, \tag{1.148}$$

$$\mu = \frac{1 + p_3(a)k^2}{p_4(a) + p_5(a)k^2}, \tag{1.149}$$

where the p_i's are functions of time only that can be either constrained by data or assume specific forms related to the model under consideration. For example, in $f(R)$ gravity

$$\gamma = \frac{2 + \bar{m}^2_{f_R} a^2/k^2}{4 + \bar{m}^2_{f_R} a^2/k^2}, \tag{1.150}$$

$$\mu = \frac{4 + \bar{m}^2_{f_R} a^2/k^2}{3 + \bar{m}^2_{f_R} a^2/k^2}, \tag{1.151}$$

which for a light background scalar field ($\bar{m}^2_{f_R} a^2 \ll k$) reduce to $\mu = 4/3$ and $\gamma = 1/2$. Eqs. (1.150) and (1.151) will be extensively used in chapter 3 to calculate the linear growth of structure in these modified theories of gravity.

Nonlinear regime

The evolution of nonlinear structure formation in viable modified gravity theories is further complicated by their screening mechanisms. For scalar-tensor theories in the form of Eq. (1.128), this implies that the linear parameterization of Eqs. (1.148) and (1.149) cannot correctly describe the suppression of the fifth force in high-density regions, where GR has been well tested. As a result, cosmological constraints on modified gravity from nonlinear scales are typically model-dependent.

In the Einstein frame, for non-relativistic matter we can define the energy density $\varrho \equiv -A^{-1}\tilde{\rho}$, such that the background continuity equation derived from Eq. (1.132) becomes

$$\dot{\varrho} + 3\mathcal{H}\varrho = 0. \tag{1.152}$$

This density is conserved in the Einstein frame since it decouples from the scalar field. The equation of motion (1.131) for the scalar now takes the simple form

$$\tilde{\Box}\varphi = V_{\text{eff},\varphi}(\varphi), \tag{1.153}$$

where

$$V_{\text{eff}}(\varphi) = V(\varphi) + A(\varphi)\varrho \tag{1.154}$$

is an effective potential that explicitly depends on the density ϱ. Therefore, suitable combinations of the bare potential $V(\varphi)$ and coupling $A(\varphi)$ can lead to a screening of the scalar field mediated force in regions of high density.

The general class of theories described by the action Eq. (1.128) exhibits screening mechanisms that activate in regions where the Newtonian potential exceeds some threshold value, $|\Psi_{\rm N}| \gtrsim C\kappa|\bar{\varphi}|$ (see, e.g., Joyce, Jain, et al. 2015), where C is a model-dependent constant of order unity and $\bar{\varphi}$ is the background field value. Equivalently, in deep potential wells φ is locally suppressed with respect to $\bar{\varphi}$ and departures from GR become unobservable. By reversing this condition, we can estimate the value of the background scalar field required to pass Solar System tests, i.e. $C\kappa|\bar{\varphi}| \lesssim 10^{-6}$. This constrains the background field mass to be $\bar{m}_\varphi \gg H$ (Wang, Hui, and Khoury 2012), which in turn implicates that viable scalar-tensor theories only influence structure formation on scales $\lesssim 30$ Mpc.

The near-universality of halo density profiles (see, e.g., Taylor 2011) allows a well-defined mapping between the potential and the mass of the halo. This means that the screening criterion above selects a characteristic threshold halo mass, $M_{\rm scr}(\bar{\varphi})$, such that for halos with $M > M_{\rm scr}(\bar{\varphi})$ fifth force effects are hidden, while halos with $M < M_{\rm scr}(\bar{\varphi})$ are unscreened. Accordingly, the formation and dynamics of virialized objects will now depend on their mass, a fact that we must account for in the spherical collapse model discussed in sec. 1.2.3. In chapter 4, we will include suitable modifications to this model in the context of $f(R)$ gravity, in which the scalar field develops a density-dependent mass through the effective potential as

$$m^2_{\rm eff}(\varphi_0) = \left.\frac{{\rm d}^2 V_{\rm eff}}{{\rm d}\varphi^2}\right|_{\varphi_0} = \left.\frac{{\rm d}^2 V}{{\rm d}\varphi^2}\right|_{\varphi_0} + \left.\frac{{\rm d}^2 A}{{\rm d}\varphi^2}\right|_{\varphi_0} \varrho, \tag{1.155}$$

where the bare potential and the coupling to matter are given by Eq. (1.140), and φ_0 denotes the minimum of the effective potential. This is known as the *chameleon* mechanism.

1.4 Measuring the cosmic growth

This section introduces two important cosmological observables employed in tests of cosmological models: the matter power spectrum and the abundance of massive halos. These are sensitive probes of gravity and dark energy on large scales, and as such can be used to effectively discriminate alternative cosmological models from ΛCDM. However, it is important to keep in mind that to avoid biased constraints that might point to new physics, we need accurate theoretical predictions of these observables. Undoubtedly, a non-trivial task even in the standard scenario.

1.4.1 The matter power spectrum

The observed large-scale structure originates from the gravitational amplification of initial, small perturbations in an otherwise homogenous universe. Despite the impressive progress in observational cosmology, our knowledge of the initial conditions is fundamentally limited by the quantum nature of the fluctuations generated during inflation (see, e.g., Baumann 2011). For this, the resulting classical fluctuations in the matter density field at later times are inherently stochastic, and our universe is treated as a realization drawn from an infinite ensemble of alternatives. Thus, testing our expectations for the matter distribution on cosmological scales is only possible in a statistical sense.

To completely characterize a random field $\delta(\boldsymbol{x})$ at any give time, all we need to know is its probability distribution function $\mathcal{D}$. Let us partition the universe in N infinitesimal cells centered at positions $\boldsymbol{x}_1$, $\boldsymbol{x}_2$, ..., $\boldsymbol{x}_N$. Then, the probability that the random field takes values in the range $[\delta_i, \delta_i + \mathrm{d}\delta_i]$ at positions $\boldsymbol{x}_i$ is given by

$$\mathcal{D}(\delta_1, \delta_2, \ldots, \delta_N)\mathrm{d}\delta_1\mathrm{d}\delta_2 \ldots \mathrm{d}\delta_N. \tag{1.156}$$

The moments of the distribution are defined by

$$\left\langle \delta_1^{\ell_1}\delta_2^{\ell_2}\cdots\delta_N^{\ell_N} \right\rangle \equiv \int \delta_1^{\ell_1}\delta_2^{\ell_2}\cdots\delta_N^{\ell_N}\mathcal{D}(\delta_1, \delta_2, \ldots, \delta_N)\mathrm{d}\delta_1\mathrm{d}\delta_2 \ldots \mathrm{d}\delta_N, \tag{1.157}$$

with ℓ_i being non-negative integers. The cosmological principle implies that the probability distribution function must be invariant under translations and spatial rotations. In this sense, the cosmic field is statistically homogeneous and isotropic. It follows that the same symmetries are satisfied by all moments of Eq. (1.157). For the linear density perturbation field, by definition we have that the first moment vanishes identically, i.e. $\left\langle \delta^{(1)}(\boldsymbol{x}) \right\rangle = 0$.

The generalized second moment for two locations $\boldsymbol{x}_1 = \boldsymbol{x}$ and $\boldsymbol{x}_2 = \boldsymbol{x} + \boldsymbol{r}$ is

$$\xi(r) \equiv \langle \delta(\boldsymbol{x})\delta(\boldsymbol{x} + \boldsymbol{r}) \rangle \,, \tag{1.158}$$

which is called the two-point correlation function, and due to statistical homogeneity and isotropy depends only on the norm of the distance, r. The physical interpretation of this statistics is that it measures the clustering of matter under the effect of gravity, with $\xi = 0$ being equivalent to a random (Poisson) distribution.

Equivalently, we can consider the Fourier transform of the density field, and compute the joint ensemble average for two different modes, $\langle \delta(\boldsymbol{k})\delta(\boldsymbol{k}') \rangle$. Since $\delta(\boldsymbol{x})$ is real, we must have $\delta(\boldsymbol{k}) = \delta^*(-\boldsymbol{k})$, and we only need modes with $\boldsymbol{k}$ in the upper half of Fourier space to completely determine $\delta(\boldsymbol{x})$. From Eq. (1.158) and using the inverse Fourier transform defined

in Eq. (1.87) we obtain

$$\langle \delta(\boldsymbol{k})\delta(\boldsymbol{k}')\rangle = (2\pi)^3\delta_D(\boldsymbol{k}+\boldsymbol{k}')\int \mathrm{d}^3\boldsymbol{r}\xi(\boldsymbol{r})e^{i\boldsymbol{k}\cdot\boldsymbol{r}} \equiv (2\pi)^3\delta_D(\boldsymbol{k}+\boldsymbol{k}')P(k), \tag{1.159}$$

where the matter power spectrum $P(k)$ is defined as the Fourier transform of the two-point correlation function, and it is expressed in units of $(h^{-1}\ \mathrm{Mpc})^3$. The rotational invariance of the correlation function reduces the Fourier transform to a one-dimensional integral, that is

$$P(k) = 4\pi\int_0^\infty \xi(r)\frac{\sin kr}{kr}r^2\mathrm{d}r. \tag{1.160}$$

For the linearized density field $\delta^{(1)}(\boldsymbol{k})$ the corresponding power spectrum can be found from the combination of Eq. (1.159) with Eq. (1.62). Thus, the dimensionless linear power spectrum $\Delta^2(k)$ reads[26]

$$\Delta^2(k,a) \equiv \frac{k^3P_{\rm lin}(k,a)}{2\pi^2} = \frac{4}{25}\left(\frac{k}{\mathcal{H}}\right)^4 T^2(k)\Delta^2_{\mathcal{R}}(k)D_1^2(a), \tag{1.161}$$

where we have explicitly reintroduced the dependence on time. In simple models of inflation, the power spectrum of primordial curvature perturbations takes a power-law form (e.g., Peiris et al. 2003)

$$\Delta^2_{\mathcal{R}}(k) = A_s(k_0)\left(\frac{k}{k_0}\right)^{n_s-1}, \tag{1.162}$$

with A_s and n_s denoting the amplitude and spectral index of scalar fluctuations, respectively, and k_0 is the pivot scale, which typically takes the values $0.05\,\mathrm{Mpc}^{-1}$ or $0.002\,\mathrm{Mpc}^{-1}$. Theoretical predictions set $n_s \sim 1$, a result that has been confirmed to exquisite precision by recent observations (Ade et al. 2015a). The transfer function $T(k)$ is evaluated numerically with Boltzmann codes, such as CLASS (Blas, Lesgourgues, and Tram 2011) and CAMB (Lewis, Challinor, and Lasenby 2000), to include the information on the physical processes occurring at early times (e.g., the baryon acoustic oscillations). In Fig. 1.11 the linear power spectrum $P_{\rm lin}$ is compared to the output from N-body simulations, indicating that for $k \gtrsim 0.1\,h\,\mathrm{Mpc}^{-1}$ linear predictions fail to capture the full nonlinear dynamics due to mode-coupling and non-perturbative effects.

We will assume that the primordial fluctuations follow a Gaussian distribution, which is a prediction of the simplest model of inflation and a very good approximation to the statistics of more sophisticated models (e.g., Bartolo, Komatsu, et al. 2004). Their Gaussianity persists throughout the linear regime, but is lost at the onset of nonlinear structure formation. For a

[26] In general, modified theories of gravity introduce a scale-dependence in the linear growth function, i.e. $D_1(a) \mapsto D_1(k,a)$ (see sec. 1.3). We will employ this correction in chapter 3 to calculate the linear power spectrum in $f(R)$ gravity.

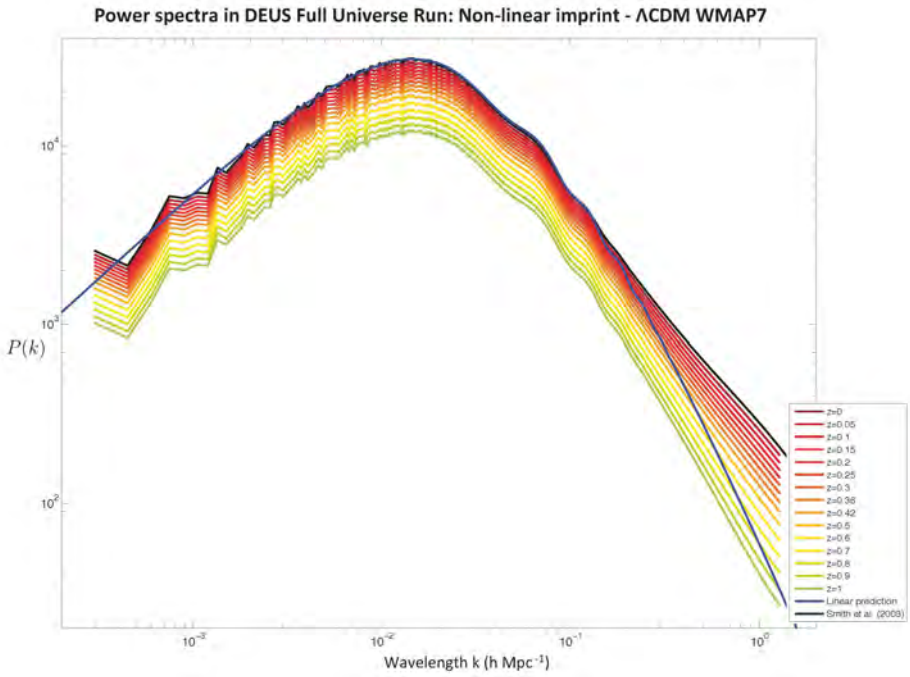

Fig. 1.11 Matter power spectrum for the WMAP 7-year best-fit ΛCDM cosmology (Komatsu et al. 2011). Lines within the color gradient represent the output of cosmological N-body simulations from $z = 1$ (bottom line) to $z = 0$ (top line). The result from linear predictions at $z = 0$ is shown for comparison (blue). Nonlinear effects become important for $k \gtrsim 0.1\,h\,\mathrm{Mpc}^{-1}$. The visible wiggly features in the range $0.05 \lesssim k\,h^{-1}$ Mpc $\lesssim 0.3$ are the imprints of baryon acoustic oscillations that took place before photon decoupling. (Copyright: DEUS consortium)

Gaussian random field the multipoint distribution function takes the form

$$\mathcal{D}(\delta_1, \delta_2, \ldots, \delta_N) = \frac{1}{\sqrt{(2\pi)^N \det(\mathcal{M})}} e^{-\frac{1}{2}\sum_{ij} \delta_i (\mathcal{M}^{-1})_{ij} \delta_j}, \tag{1.163}$$

where $\mathcal{M} \equiv \langle \delta_i \delta_j \rangle$ is the covariance matrix. Statistical isotropy and homogeneity implies that the distribution is completely characterized by the two-point correlation function Eq. (1.158). Since the Fourier modes $\delta(\boldsymbol{k})$ are a linear combination of Gaussian fields, they are also Gaussian. Then, by virtue of Wick's (or Isserlis') theorem, the ensemble average of any product of fields can be expressed as the product of ensemble averages from all possible full contractions of the fields, that is

$$\langle \delta(\boldsymbol{k}_1) \cdots \delta(\boldsymbol{k}_n) \rangle = 0 \quad \text{for } n \text{ odd} \tag{1.164}$$

$$\langle \delta(\boldsymbol{k}_1) \cdots \delta(\boldsymbol{k}_n) \rangle = \sum_{\mathcal{J} \in \mathcal{C}} \prod_{p_{ij} \in \mathcal{J}} \langle \delta(\boldsymbol{k}_i) \delta(\boldsymbol{k}_j) \rangle \quad \text{for } n \text{ even}, \tag{1.165}$$

where $\mathcal{S}$ is the set of all possible full contractions, $\mathcal{J}$ is a particular full contraction, and p_{ij} denotes a specific pairs of fields $\{\delta(\boldsymbol{k}_i), \delta(\boldsymbol{k}_j)\}$ that has been contracted within $\mathcal{J}$. For the linear overdensity field this means that we can simply use Eq. (1.161) to calculate any moment $\left\langle \delta^{(1)}(\boldsymbol{k}_1) \cdots \delta^{(1)}(\boldsymbol{k}_n) \right\rangle$ in Fourier space, which is essential to obtain analytical higher-order corrections to the matter power spectrum in the weakly non-linear regime.

In standard perturbation theory, the power spectrum definition Eq. (1.159), with the perturbative expansion for the density field Eq. (1.97a)[27] and its solution Eq. (1.100), lead to a collection of terms that can be organized in terms of Feynman diagrams (Scoccimarro and Frieman 1996). More specifically, each group of diagrams will contribute to a given order in the matter power spectrum, with the leading-order being tree-diagrams, the next-to-leading-order 1-loop diagrams and so on. In each diagram, external lines are associated with the spectral components of the density field involved in the inital correlators (e.g. $\delta(\boldsymbol{k}, a)$). Internal lines result from the full expansion of the perturbative solution Eq. (1.100). They represent a linear power spectrum $P_{\rm lin}(q, a)$, which is integrated over the wave-vector $\boldsymbol{q}$. Fig. 1.12 shows the correspondence between diagrams and quantities contained in the correlations.

It follows from Wick's theorem that the only surviving contributions to the matter power spectrum must have an even number of components of the linear density field:

$$\begin{aligned}\langle \delta\delta \rangle = &\left\langle \delta^{(1)}\delta^{(1)} \right\rangle + 2\left\langle \delta^{(1)}\delta^{(3)} \right\rangle + \left\langle \delta^{(2)}\delta^{(2)} \right\rangle \\ &+ 2\left\langle \delta^{(1)}\delta^{(5)} \right\rangle + 2\left\langle \delta^{(2)}\delta^{(4)} \right\rangle + \left\langle \delta^{(3)}\delta^{(3)} \right\rangle + \mathcal{O}((\delta^{(1)})^8),\end{aligned} \tag{1.166}$$

[27] We keep only terms proportional to ϵ_α^0 there.

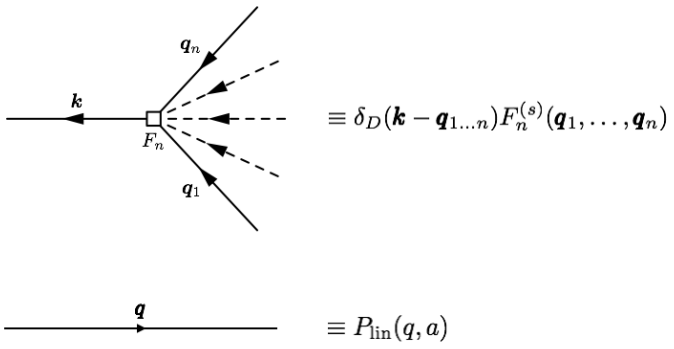

Fig. 1.12 Standard perturbation theory diagrammatic rules for vertices and internal lines.

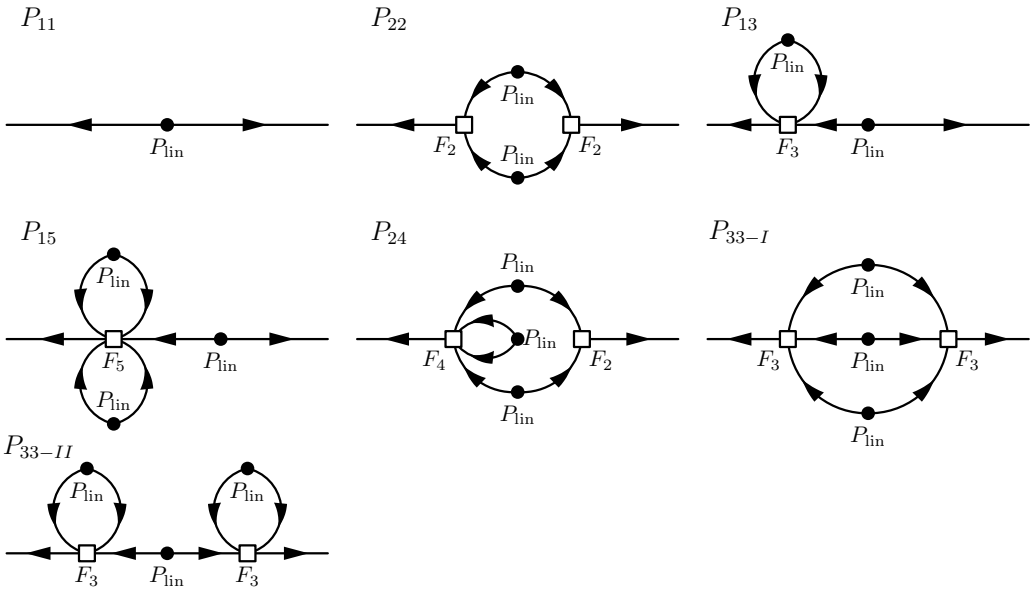

Fig. 1.13 Diagrams for the tree-level, 1- and 2-loop terms of the standard perturbation theory matter power spectrum. Figure taken from Baldauf, Mercolli, and Zaldarriaga (2015).

where we have momentarily dropped the dependence on wavenumber and time, and the factor of 2 multiplying terms $\left\langle \delta^{(n)} \delta^{(m)} \right\rangle$ for $n \neq m$ derives from the equality $\left\langle \delta^{(n)} \delta^{(m)} \right\rangle = \left\langle \delta^{(m)} \delta^{(n)} \right\rangle$. Using Eq. (1.159), we can rewrite the expression above in the more compact form

$$P_{\delta\delta} = \underbrace{P_{11}}_{\text{tree-level}} + \underbrace{2P_{13} + P_{22}}_{\text{1-loop}} + \underbrace{2P_{15} + 2P_{24} + P_{33\text{-I}} + P_{33\text{-II}}}_{\text{2-loop}}, \tag{1.167}$$

where terms are collected based on the order they belong to, as shown by the corresponding diagrams in Fig. 1.13.

The n-th-order pertubation of Eq. (1.100) can be expressed as an n-fold convolution of the linear density field, filtered by the symmetrized kernel $F_n^{(s)}$,

$$\delta^{(n)} = F_n^{(s)} \delta^{(1)} * \cdots * \delta^{(1)}, \tag{1.168}$$

which is particularly useful to see the connections between diagrams, contractions and loop integrals. We will only consider terms contributing at 1-loop, and refer the reader to, e.g., Schmittfull and Vlah (2016) for 2-loop expressions. From the $\left\langle \delta^{(2)} \delta^{(2)} \right\rangle$ average we obtain

$$\begin{aligned} P_{22}(k) &= 2 \left\langle \overbrace{F_2 \, \delta^{(1)} * \delta^{(1)}}^{} \underbrace{F_2 \, \delta^{(1)} * \delta^{(1)}}_{} \right\rangle \\ &= 2 \int_{\boldsymbol{q}} F_2^2(\boldsymbol{q}, \boldsymbol{k} - \boldsymbol{q}) P_{\rm lin}(q) P_{\rm lin}(|\boldsymbol{k} - \boldsymbol{q}|), \end{aligned} \tag{1.169}$$

and the $\left\langle \delta^{(1)} \delta^{(3)} \right\rangle$ correlator instead gives

$$\begin{aligned} P_{13}(k) &= 3 \left\langle \overbrace{\delta^{(1)} F_3^{(s)} \, \delta^{(1)}}^{} * \overbrace{\delta^{(1)} * \delta^{(1)}}^{} \right\rangle \\ &= 3 P_{\rm lin}(k) \int_{\boldsymbol{q}} F_3(\boldsymbol{k}, \boldsymbol{q}, -\boldsymbol{q}) P_{\rm lin}(q). \end{aligned} \tag{1.170}$$

The factors of 2 and 3 before the integrals account for the number of permutations of the linear fields ($\delta^{(1)}$'s) that leave the diagram unchanged.

As discussed in sec. 1.2.3, the EFT of large-scale structure contains additional terms in the perturbative expansion of Eq. (1.97a) to include the effects of short wavelength modes on long distances. In turn, this produces further correlators that will play the role of counterterms in Eq. (1.167). Obviously, it admits a diagrammatic representation similar to the one described above, although with vertices replaced by the corresponding kernels $\tilde{F}_n^{(s)}$, $\hat{F}_n^{(s)}$, $\bar{F}_n^{(s)}$ and $\check{F}_n^{(s)}$. These carry the information of small-scale nonlinear physics through the unkown coefficients $c^2_{s(1)}$, c_1 and c_4. For example, the leading order correction comes from the tree-level correlator $\left\langle \delta^{(1)} \tilde{\delta}^{(1)} \right\rangle$, which is related to the diagram in Fig. 1.14. From the fluid equations (1.88a) and (1.94), together with the ansatz Eq. (1.100), it can be shown that (Foreman and Senatore 2016)

$$\tilde{\delta}^{(1)}(\boldsymbol{k}) = -(2\pi) c^2_{s(1)} \frac{k^2}{k^2_{\rm NL}} \delta^{(1)}(\boldsymbol{k}). \tag{1.171}$$

Thus, the leading order correction to the $P_{\text{1-loop}}$ contribution from standard perturbation theory takes the form

$$P^{(c_s)}_{\rm tree}(k) = -2(2\pi) c^2_{s(1)} \frac{k^2}{k^2_{\rm NL}} P_{11}(k). \tag{1.172}$$

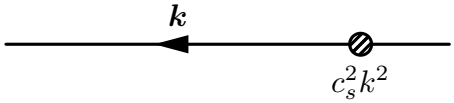

Fig. 1.14 Leading order counterterm in the EFT of large-scale structure. Figure taken from Baldauf, Mercolli, Mirbabayi, et al. (2015).

Next-to-leading-order counterterms and even higher-order corrections can be derived following similar steps, collecting higher powers of ϵ_s or considering terms including ϵ_1 and ϵ_4 in Eq. (1.100) (e.g., Carrasco, Foreman, et al. 2014b; Foreman and Senatore 2016; Foreman, Perrier, and Senatore 2016). These will be used extensively in chapter 5 to study the cosmology and time dependence of the unknown parameters of the theory.

1.4.2 Halo counts

The spherical collapse model discussed in sec. 1.2.3 provides a method to determine if an isolated overdensity with a specific geometry will eventually form a virialized object, i.e. a halo. The real universe, however, is a realization of the initial Gaussian[28] overdensity field $\delta_{\rm ini}(\boldsymbol{x})$, with different values at different locations. To link this field to the halos hosting galaxies and clusters of galaxies, we need a prescription to select portions of the continuous matter distribution from which collapsed objects will form. We will assume that the linear density field $\delta(\boldsymbol{x})$ at some early time deep in the matter-dominated era can be separated into a set of disjoint regions, each of which will generate a single collapsed object at some later time.

The mapping between the overdensity field and masses is realized by smoothing the field with a spherically symmetric window function $W(r)$ of characteristic comoving radius R, enclosing a mass $M \propto \bar{\rho}_{\rm m} R^3$. In practice, we define the smoothed density field as

$$\delta_M(\boldsymbol{x}, t) = \int \mathrm{d}x'^3 \delta(\boldsymbol{x} - \boldsymbol{x'}, t) W(|\boldsymbol{x'}|, M), \tag{1.173}$$

where the window function is normalized for any mass M [29], i.e. $\int W(|\boldsymbol{x}|, M)\mathrm{d}x^3 = 1$. A frequent choice for the window function is the top-hat filter

$$W(r, R) = \begin{cases} 3/(4\pi R^3) & \text{if } r \leq R, \\ 0 & \text{if } r > R, \end{cases} \tag{1.174}$$

[28] Note that theoretical models allow for primordial non-Gaussianities in the initial density field (e.g., Renaux-Petel 2015). For the purpose of this thesis, we will restrict our discussion to the simple Gaussian statistics, which we also employed in sec. 1.4.1.

[29] We will be using masses and radii interchangeably, both as characteristic scales and as arguments of the window function.

which in Fourier space becomes

$$W(k,R) = \frac{3}{(kR)^3}\left[\sin(kR) - kR\cos(kR)\right]. \tag{1.175}$$

To completely describe a Gaussian random field we only need its first two statistical moments. The statistics of the smoothed *linear* overdensity field follows directly from that of $\delta^{(1)}$, and for the first moment we obtain

$$\langle \delta_M(\boldsymbol{x},t)\rangle = \int \mathrm{d}x'^3 \left\langle \delta^{(1)}(\boldsymbol{x}-\boldsymbol{x'},t)\right\rangle W(|\boldsymbol{x'}|,M) \equiv 0. \tag{1.176}$$

The second moment can be derived from the linear power spectrum of Eq. (1.161) as

$$\sigma_M^2(t) \equiv \left\langle \delta_M^2(\boldsymbol{x},t)\right\rangle = \langle \delta_M(\boldsymbol{x},t)\delta_M^*(\boldsymbol{x},t)\rangle = \frac{1}{2\pi^2}\int_0^\infty \mathrm{d}k\; k^2 P_{11}(k,t)|W(k,M)|^2, \tag{1.177}$$

where we have used the Fourier transform of the linear overdensity field, the definition of the linear power spectrum Eq. (1.159), and the rotational invariance of the window function.

According to the spherical collapse model, regions with $\delta(\boldsymbol{x},t) > \delta_\mathrm{c}$ will have collapsed to form a halo. We will apply this result to estimate the comoving number density of halos in the universe at a given time[30], denoted by $n(M,z)$. The basic idea was proposed by Press and Schechter (1974), and goes by the name of *Press-Schechter formalism*. Essentially, they identified the probability that $\delta_M(\boldsymbol{x},t) > \delta_\mathrm{c}$ with the fraction of mass elements that a time t are contained in halos with mass larger than M. Since $\delta_M(\boldsymbol{x},t) \to 0$ for $M \to \infty$, a mass $M_\mathrm{h} > M$ such that $\delta_{M_\mathrm{h}}(\boldsymbol{x},t) = \delta_\mathrm{c}$ always exists, and will correspond to the mass of the halo at the position $\boldsymbol{x}$. Using Eqs. (1.176) and (1.177), the probability that at a random position δ_M exceeds the threshold δ_c is

$$\mathcal{P}[>\delta_\mathrm{c}] = \frac{1}{\sqrt{2\pi}\sigma_M}\int_{\delta_\mathrm{c}}^\infty \exp\left(-\frac{\delta_M^2}{2\sigma_M^2}\right)\mathrm{d}\delta_M = \frac{1}{2}\mathrm{erfc}\left(\frac{\nu}{\sqrt{2}}\right), \tag{1.178}$$

where $\nu \equiv \delta_\mathrm{c}/\sigma_M$ is called the *peak height*. However, for our universe Eq. (1.177) has the limit $\sigma_M \to \infty$ for $M \to 0$, which in turn gives $\mathcal{P}[>\delta_\mathrm{c}] \to 1/2$. If the probability Eq. (1.178) is equal to $F(>M)$, the mass fraction of halos with mass larger than M, then only half of the mass in the universe is contained in collapsed objects of any mass. This is a natural consequence of linear theory, which implies that only initially overdense regions can form halos. Nevertheless, underdense regions can reside in extended overdense regions, allowing for the possibility of finding them in a final larger collapsed object. Press and Schechter (1974) postulated that the mass elements in initially underdense regions will eventually fall into

[30] We will often use the redshift z as time variable instead of cosmic time t. This gives a closer link to observations, for which only redshifts are directly measurable.

collapsed objects, or equivalently, $F(>M) = 2\mathcal{P}[>\delta_{\rm c}]$ [31]. The comoving number density of halos with masses in the range $[M, M+\mathrm{d}M]$ is then given by

$$\begin{aligned}\frac{\mathrm{d}n}{\mathrm{d}M}\mathrm{d}M &= \frac{\bar{\rho}_{\rm m}}{M}\frac{\mathrm{d}F(>M)}{\mathrm{d}M}\mathrm{d}M = 2\frac{\bar{\rho}_{\rm m}}{M}\frac{\mathrm{d}\mathcal{P}[>\delta_{\rm c}]}{\mathrm{d}\sigma_M}\left|\frac{\mathrm{d}\sigma_M}{\mathrm{d}M}\right|\mathrm{d}M \\ &= \sqrt{\frac{2}{\pi}}\frac{\bar{\rho}_{\rm m}}{M^2}\frac{\delta_{\rm c}}{\sigma_M}\exp\left(-\frac{\delta_{\rm c}^2}{2\sigma_M^2}\right)\left|\frac{\mathrm{d}\sigma_M}{\mathrm{d}M}\right|\mathrm{d}M, \end{aligned} \tag{1.179}$$

which is also known as the Press & Schechter halo mass function. It can be rewritten in a more compact form using the peak height variable, that is

$$\frac{\mathrm{d}n}{\mathrm{d}\ln M} = \frac{\bar{\rho}_{\rm m}}{M}\nu f_{\rm PS}(\nu)\left|\frac{\mathrm{d}\ln\nu}{\mathrm{d}\ln M}\right|, \tag{1.180}$$

where

$$\nu f_{\rm PS}(\nu) = \sqrt{\frac{2}{\pi}\nu^2}\exp\left[\nu^2/2\right] \tag{1.181}$$

is the multiplicity function giving the fraction of the mass in halos in a unit range of $\ln\nu$.

From the exponential cutoff in Eqs. (1.179) and (1.181) we can see that only halos with mass M such that $\sigma(M,z) \gtrsim \delta_{\rm c}$ are present in significant number. By implicitly defining a characteristic mass M^* as

$$\sigma(M^*, z) = D_1(z)\sigma(M^*, z=0) = \delta_{\rm c}, \tag{1.182}$$

we obtain that the abundance of halos with $M \gtrsim M^*$ is suppressed at redshift z. Given that $D_1(z)$ increases with time, and that $\sigma(M^*, z=0)$ decreases with mass, together with the weak evolution of $\delta_{\rm c}$ we deduce that M^* grows with time. Therefore, as time goes by, massive halos become more abundant.

The heuristic Press-Schechter approach is based on simplistic assumptions that reduce its utility for precision cosmology. In particular, the collapse of overdensities is generically ellipsoidal rather than spherical. This more realistic scenario introduces important changes in the halo mass function, and brings the theoretical predictions in better agreement with N-body simulations (Sheth, Mo, and Tormen 2001). The resulting improved mass function is obtained from the following Sheth-Tormen multiplicity function

$$\nu f_{\rm ST}(\nu) = A\sqrt{\frac{2}{\pi}a\nu^2}\left[1 + (a\nu^2)^{-p}\right]\exp\left[a\nu^2/2\right], \tag{1.183}$$

where A, a and p are additional free parameters derived from simulations (see chapters 3 and 4 for further details). Recently, considerable effort has gone into simulation calibrated

[31] The appearance of the "fudge factor" of 2 is more rigorously motivated by the excursion set formalism (Bond, Cole, et al. 1991).

formulas or fitting formulas derived from simulations (e.g., Sheth and Tormen 1999; Jenkins, Frenk, et al. 2001; Sheth, Mo, and Tormen 2001; Warren, Abazajian, et al. 2006; Tinker, Kravtsov, et al. 2008; Pillepich, Porciani, and Hahn 2010; Reed, Smith, et al. 2013). The left panel of Fig. 1.15 shows the difference between the Press-Schechter mass function and the fits from Pillepich, Porciani, and Hahn (2010) at two different epochs. Notably, for ΛCDM cosmologies and for redshifts $z \lesssim 1$, fitting formulas are now available with a precision of a few percent in the mass range of interest for cluster cosmology studies (e.g., Tinker, Kravtsov, et al. 2008; Pillepich, Porciani, and Hahn 2010). However, systematic uncertainties in the halo mass function come from the various halo definitions used in simulations (see, e.g., Knebe et al. 2013), and also from effects associated with baryonic physics (e.g., Stanek, Rudd, and Evrard 2009; Cui, Borgani, et al. 2012; Balaguera-Antolinez and Porciani 2013; Bocquet, Saro, et al. 2016). Both these contributions can impact significantly on the accuracy of the mass functions fits based on pure dark matter simulations.

Modifications to GR introduce important changes in the shape and evolution of the halo mass function. In particular, the formation of collapsed objects is a highly nonlinear process, and the activation of screening mechanisms in viable theories of gravity needs to be consistently included. The right panel of Fig 1.15 illustrates the fractional enhancement of the halo abundance with respect to ΛCDM in chameleon $f(R)$ gravity. One important fact is that the overabundance of halos depends on the present-day background amplitude of the scalar, f_{R0}, or equivalently its mass, $\bar{m}^0_{f_R}$. For values $|f_{R0}|$ much larger than the Newtonian potential associated with massive clusters ($|\Psi_{\rm N}| \sim 10^{-5}$), the screening mass[32] $M_{\rm scr} \gg M^*$ and the fifth force increases accretion and merger rates of the entire halo population. The opposite is true for $|f_{R0}| \ll 10^{-5}$, in which case only masses $M < M_{\rm scr}$ experience the fifth force, whereas for larger masses modifications are suppressed. Accurate halo mass function predictions calibrated with high-resolution N-body simulations for $f(R)$ gravity are discussed in chapter 4.

Cluster surveys provide data in the form of angular positions, redshifts, and observed signals (or mass proxy), $\mathcal{S}$. Let us assume a survey with a perfect mass proxy, $\mathcal{S} = M$, and exact redshift measurements, $z_{\rm est} = z$. We can organise the observations in mass bins $\Delta M_\alpha = M_{\alpha+1} - M_\alpha$ and redshift bins $\Delta z_i = z_{i+1} - z_i$ with solid angle $\Delta\Omega_i$. Then, the expected number of halos, $\overline{N}_{\alpha i}$, in a cell labeled by the mass M_α and redshift z_i, is

$$\overline{N}(M_\alpha, z_i) \equiv \overline{N}_{\alpha i} = \frac{\Delta\Omega_i}{4\pi} \int_{z_i}^{z_{i+1}} \mathrm{d}z \frac{\mathrm{d}V}{\mathrm{d}z} \int_{\ln M_\alpha}^{\ln M_{\alpha+1}} \mathrm{d}\ln M \frac{\mathrm{d}n}{\mathrm{d}\ln M}. \tag{1.184}$$

As mentioned in sec. 1.1, cluster abundance is sensitive to dark energy/modified gravity effects. It measures the expansion history through the evolution of the comoving volume

[32] See sec. 1.3.2 for a discussion.

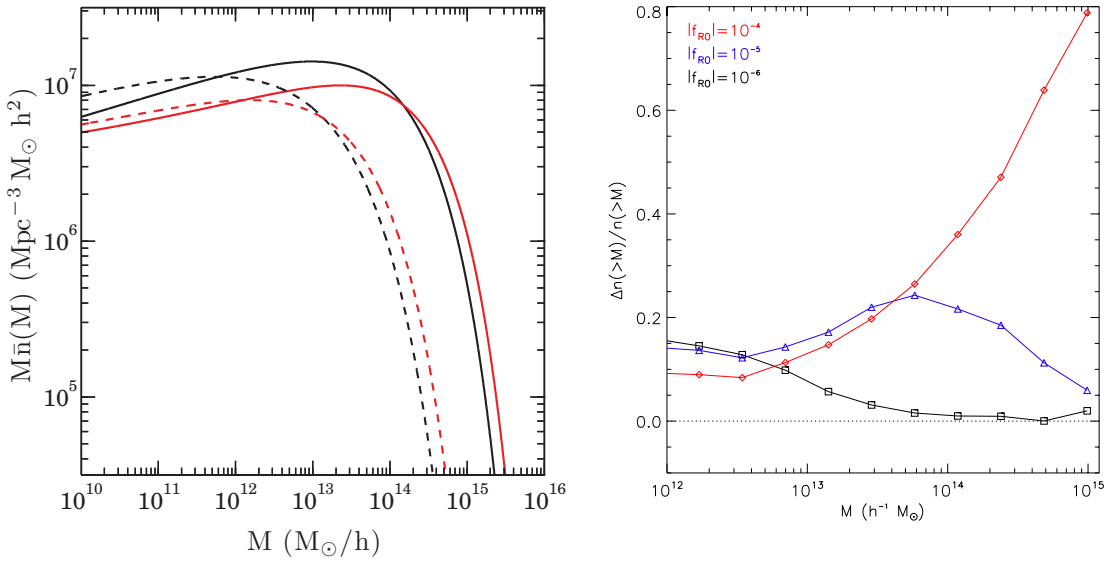

Fig. 1.15 *Left:* halo mass density $\rho_{\rm h}(M,z) = Mn(M,z)$ for two different redshifts in a ΛCDM cosmology. The black lines represent the Press-Schechter mass function (1.179) and the red lines are obtained from the fitting formula of Pillepich, Porciani, and Hahn (2010). Solid lines correspond to $z = 0$ and dashed lines to $z = 1$. Figure taken from Knobel (2012). *Right:* present-day fractional deviations of the halo mass function with respect to a ΛCDM cosmology from $f(R)$ gravity simulations. Here, the expansion history is identical for all models. Lines corresponds to three different values of the background scalar amplitude $|f_{R0}|$, and show the activation of the chameleon screening mechanism for massive halos. Figure taken from Joyce, Jain, et al. (2015).

within a solid angle $\mathrm{d}\Omega$,

$$\frac{\mathrm{d}^2 V}{\mathrm{d}z\mathrm{d}\Omega} = \frac{\chi^2(z)}{H(z)}, \tag{1.185}$$

with $\chi(z)$ given by Eq. (1.22), and the growth of structure via the mass function. Of course, no mass proxy can perfectly trace cluster masses, and any survey presents some degree of incompleteness (missed sources) as well as impurity (false sources). Robust statistical analyses of large cluster surveys must properly account for these uncertainties when evaluating Eq. (1.184), as we will do in chapters 2 and 3 (for details, see sec. 2.3.3). Note that, for spectroscopic surveys, uncertainties in redshift measurements are much smaller than the bin size, and we can set $\mathcal{P}(z_{\rm est}|z) = \delta_D(z - z_{\rm est})$.

Chapter 2

Cluster abundance as a probe of gravity: GR consistency tests

This chapter is an adaptation of the following article:

"Weighing the Giants IV: Cosmology and Neutrino Mass"

Published in *Mon. Not. Roy. Astron. Soc., 446, 2205-2225 (2015).*

Authors:

A. B. Mantz, A. von der Linden, S. W. Allen, D. E. Applegate, P. L. Kelly, R. G. Morris, D. A. Rapetti, R. W. Schmidt, S. Adhikari, M. T. Allen, P. R. Burchat, D. L. Burke, M. Cataneo, D. Donovan, H. Ebeling, S. Shandera, A. Wright

We employ robust weak gravitational lensing measurements to improve cosmological constraints from measurements of the galaxy cluster mass function and its evolution, using X-ray selected clusters detected in the ROSAT All-Sky Survey. Our lensing analysis constrains the absolute mass scale of such clusters at the 8 per cent level, including both statistical and systematic uncertainties. Combining it with the survey data and X-ray follow-up observations, we find improved constraints on modifications of gravity with respect to previous work, primarily due to the reduced systematic uncertainty in the absolute mass calibration provided by the lensing analysis.

2.1 Introduction

Great strides have been made in recent years in the use of galaxy cluster surveys as probes of the halo mass function, and thereby of cosmology and fundamental physics (for a review, see Allen, Evrard, and Mantz 2011). Cluster surveys covering the entire extragalactic sky, or a significant fraction of it, now exist at X-ray (Truemper 1993; Ebeling, Edge, Bohringer, et al. 1998; Ebeling, Edge, Mantz, et al. 2010; Boehringer et al. 2004), optical/IR (e.g. Koester et al. 2007; Rykoff et al. 2014) and millimeter (Reichardt et al. 2013; Hasselfield et al. 2013; Ade et al. 2014e) wavelengths, and a number of independent groups have published cosmological constraints in broad agreement with one another based on these data (e.g. Eke, Cole, et al. 1998; Donahue and Voit 1999; Henry 2000; Henry 2004; Borgani, Rosati, et al. 2001; Reiprich and Boehringer 2002; Seljak 2002; Viana, Nichol, and Liddle 2002; Allen, Fabian, et al. 2003; Pierpaoli, Borgani, et al. 2003; Schuecker, Bohringer, et al. 2003; Vikhlinin et al. 2003; Vikhlinin et al. 2009; Voevodkin and Vikhlinin 2004; Dahle 2006; A. Mantz, S. W. Allen, et al. 2008; Mantz, Allen, Rapetti, and Ebeling 2010; Henry, Evrard, et al. 2009; Rozo et al. 2010; Sehgal et al. 2011; Benson et al. 2013; Ade et al. 2014d).

These cluster survey data have provided highly competitive constraints on dark energy and modifications of gravity (e.g. Vikhlinin et al. 2009; Mantz, Allen, Rapetti, and Ebeling 2010; Schmidt, Vikhlinin, and Hu 2009; Rapetti, Blake, et al. 2013), as well as measurements of the late-time normalization of the matter power spectrum (σ_8, defined by Equation 2.1, below). Constraints on σ_8 are a key complement to measurements of the amplitude of the power spectrum at high redshift from the CMB in many cosmological models of interest, particularly those where the dark energy equation of state or neutrino masses are free parameters. Since cosmological data currently provide our best limits on the species-summed neutrino mass (Mantz, Allen, and Rapetti 2010; Reid, Verde, et al. 2010), improving constraints on σ_8 is a priority.

Previous constraints on σ_8 from clusters have been systematically limited due to fundamental uncertainties regarding the absolute calibration of cluster mass measurements (for a discussion, see Linden et al. 2014a). The most widespread observational techniques used to estimate masses, based on X-ray data or optical spectroscopy, assume that the measured thermal/kinetic energies accurately reflect the underlying gravitating mass, and are thus subject to a theoretically uncertain bias. Recently, measurements of the gravitational lensing of background galaxies due to clusters have emerged as a potential avenue for providing a more accurate absolute mass calibration, since weak-lensing mass measurements are expected to be nearly unbiased when the analysis is restricted to the appropriate radial range (e.g. Becker and Kravtsov 2011) and systematic effects in the shear measurements and photometric redshifts can be accounted for (Applegate, Linden, et al. 2014). Thanks to the availability of wide field-of-view imagers with superb image quality, such as SuprimeCam at the Sub-

aru telescope and MegaCam/MegaPrime at the Canada-France-Hawaii Telescope (CFHT), unbiased weak lensing measurements for large samples of clusters are now within reach.

The *Weighing the Giants* project was conceived in order to provide just such an accurate and precise calibration of cluster masses for studies of cosmology, and for the closely related analysis of cluster scaling relations. The project involves 51 massive clusters that have previously been used in cosmological studies (Allen, Rapetti, et al. 2008; Mantz, Allen, Rapetti, and Ebeling 2010; Mantz, Allen, Ebeling, et al. 2010, hereafter M10a,b). Details of the lensing data and their analysis appear in Papers I–III of this series (Linden et al. 2014b; Kelly et al. 2014; Applegate, Linden, et al. 2014), which we collectively refer to as WtG below. The WtG lensing analysis has already been used to calibrate mass estimates based on X-ray observations that assume hydrostatic equilibrium (Linden et al. 2014a; Applegate et al. 2016), particularly in the context of the cosmological constraints available from gas mass fraction ($f_{\rm gas}$) measurements in relaxed clusters (Mantz et al. 2014). Here we apply the lensing data to cosmological tests based on the cluster mass function (also referred to as cluster counts), specifically by incorporating the WtG data into the M10a,b analysis of X-ray cluster survey and follow-up data. A companion paper (A. B. Mantz, S. W. Allen, et al. 2016) explores the astrophysical consequences of our mass calibration for cluster scaling relations, which are necessarily constrained simultaneously with cosmological parameters in our analysis.

Given both the widespread expectation that the "correct" answers for cosmological parameters will be consistent with those determined from CMB data for a spatially flat, cosmological-constant model, and the potential of galaxy cluster surveys to provide high-precision cosmological constraints, minimizing the possibility of observer bias is paramount in such work. The WtG lensing analysis employed a procedure whereby those working on it were blind in all comparisons to independent mass estimates, in particular (but not limited to) those from X-ray observations and from lensing results in the literature, until the lensing analysis was finalized (see Applegate, Linden, et al. 2014 for a full discussion). This entire lensing analysis was completed before the cosmological analysis presented here had begun. Although we did not explicitly blind cosmological parameter results in this work, the constraints reported here are simply those that follow from incorporating the WtG lensing data into an already mature analysis pipeline (M10a), which is a simple and straightforward addition (Section 2.3.3).

This paper is organized as follows. Section 2.2 describes our cluster data and the external cosmological probes with which we combine them, while Section 2.3 outlines the analysis procedure and the models fitted to the data. Our results are presented in Section 2.4. Section 2.5 considers the importance of the lensing and X-ray follow-up data to the analysis, and the potential gains from obtaining an expanded lensing data set and combining surveys at different wavelengths. We conclude in Section 2.6. Best-fitting parameter values reported here

always correspond to modes of the marginalized posterior distributions, and uncertainties correspond to 68.3 per cent confidence maximum-likelihood intervals, unless otherwise specified. We make occasional use of a reference cosmological model, which has Hubble parameter $h = H_0/100\,\mathrm{km\,s^{-1}\,Mpc^{-1}} = 0.7$, mean matter density in units of the critical density $\Omega_\mathrm{m} = 0.3$, and cosmological constant energy density $\Omega_\Lambda = 0.7$. We use the standard definition of cluster masses and characteristic radii in terms of a spherical overdensity, Δ, with respect to the critical density at the cluster's redshift: $M_\Delta = (4\pi/3)\Delta\rho_\mathrm{cr}(z)r_\Delta^3$.

2.2 Data

The data set employed here consists of three X-ray flux-limited samples of clusters (i.e. redshifts and fluxes, along with the associated selection functions), as well as deeper follow-up X-ray data and/or high-quality optical imaging for a subset of the detected clusters. As in M10a,b, the cluster samples used here are based on the BCS (Ebeling, Edge, Bohringer, et al. 1998), REFLEX (Boehringer et al. 2004), and Bright MACS (Ebeling, Edge, Mantz, et al. 2010) catalogs, themselves compiled from the ROSAT All-Sky Survey (RASS; Truemper 1993). In the cases of BCS and REFLEX (covering redshifts $z < 0.3$), we use only clusters with 0.1–2.4 keV luminosities $> 2.5 \times 10^{44}\,\mathrm{erg\,s^{-1}}$ (as estimated for our reference cosmology) to eliminate low-mass clusters and groups; this cut has no impact on the Bright MACS sample ($0.3 < z < 0.5$). We depart slightly from M10a,b by using a higher flux limit of $5 \times 10^{-12}\,\mathrm{erg\,s^{-1}\,cm^{-2}}$ in the 0.1–2.4 keV band when selecting clusters from the BCS in order to avoid incompleteness that affects the lowest fluxes in BCS at all redshifts (see Ebeling, Edge, Bohringer, et al. 1998).[1] We have also expanded the allowance for overall incompleteness/impurity for Bright MACS to ±10 per cent from the ±5 per cent previously assumed for MACS and other surveys in M10a, reflecting the greater challenges affecting the MACS survey construction. Finally, we have removed Abell 2318, RX J0250.2−2129 and RX J1050.6−2405 from the data set, as these appear consistent with their X-ray emission being dominated by active galactic nuclei (AGN) rather than the intracluster medium (A. Edge, private communication; other deletions from the published catalogs are listed in M10b). However, these changes to the data set are not significant enough to affect any of our cosmological results, as we have verified by explicitly comparing constraints using the old and new samples. The new sample contains a total of 224 clusters.

X-ray luminosities and gas masses were derived from ROSAT and/or *Chandra* data for 94 clusters in M10b. We employ these measurements again in the present work, in addition to

[1] For the REFLEX and Bright MACS catalogs, we respectively use flux limits of 3 and $2 \times 10^{-12}\,\mathrm{erg\,s^{-1}\,cm^{-2}}$, as in M10a,b.

the survey data, to improve constraints on the cluster scaling relations and refine the mass information available for individual clusters (see Sections 2.3.2 and 2.5.1).[2]

The new data that are central to this work are the measurements of weak gravitational lensing for 50 massive clusters,[3] which are used to calibrate the absolute cluster mass scale. These data and their analysis are described in WtG. Specifically, we use the shear profiles derived from the simpler "color-cut" method of that work, which are available for the entire data set, rather than those from the "$p(z)$" method, which are available for just over half of the sample.[4] Of the 50 WtG clusters, 27 belong to the flux-limited sample identified above, and are straightforward to incorporate into the likelihood function for cosmology and scaling relations described in M10a and reviewed in Section 2.3.3. The remaining 23 cannot be used to constrain the X-ray luminosity–mass relation because, even though they are X-ray selected, we do not have a robustly quantified selection function for them with which to account for selection biases. However, they can still be used to calibrate the relation linking gas and total mass, to the extent that the correlation of intrinsic scatters in luminosity and gas mass at fixed total mass is small (e.g. Allen, Evrard, and Mantz 2011). We have verified empirically that including these additional lensing data in this way (see Section 2.3.3) does not bias our cosmological results.

In addition to the measurements of redshift, X-ray luminosity, gas mass and total mass (integrated over radii $\lesssim r_{500}$), we take advantage of the cosmological information available from X-ray measurements of the gas mass fraction, $f_{\rm gas}$, at $\sim r_{2500}$ for relaxed clusters (Mantz et al. 2014, hereafter M14).[5] More precisely, these $f_{\rm gas}$ measurements are made in a spherical shell spanning 0.8–1.2 r_{2500}, where theoretical and observational uncertainties due to various astrophysical effects (e.g. AGN feedback, gas cooling and clumping, etc.) are minimized and where X-ray spectroscopy permits precise total mass estimates. These data provide additional constraints on dark energy parameters and, when combined with external priors on the cosmic mean baryon density ($\Omega_{\rm b}$), produce tight constraints on $\Omega_{\rm m}$. These

[2]Since the analysis of M10b, the model for the contaminant affecting the *Chandra* ACIS detectors (including its time dependence) has been modified slightly. An overall bias in gas masses or luminosities from follow-up observations would have no effect on the cosmological analysis in this work, since gas mass is used only as an empirically calibrated mass proxy, and luminosities from follow-up data are cross-calibrated to the ROSAT survey luminosities (see M10a). Nevertheless, we note that directly comparing luminosities and gas mass profiles for 59 clusters in common between the M10b and Mantz et al. (2014) generations of analysis (not all of which were published in each paper), shows agreement at the per cent level.

[3]While the full WtG analysis employs 51 clusters, we omit Abell 370 from this work, since it has fundamentally different selection properties from our data set (i.e. it is not X-ray selected).

[4]The more robust $p(z)$ masses have been used to characterize the bias and scatter of the color-cut method (Applegate, Linden, et al. 2014), and this information is fed into the analysis presented here (specifically it factors into the width of the lensing-to-true mass normalization; see Section 2.3.2). The larger number of clusters for which we can do a color-cut analysis makes this cross-calibration approach preferable to relying exclusively on $p(z)$ clusters.

[5]We use the term $f_{\rm gas}$ generically to refer to the M14 data set in this paper, or $f_{\rm gas}(0.8\text{–}1.2\,r_{2500})$ when necessary for clarity. The integrated gas mass fraction that is constrained at radii $\sim r_{500}$ from the X-ray and lensing follow-up observations that form part of the cluster counts data set will be referred to as $f_{\rm gas}(r_{500})$.

$f_{\rm gas}(0.8\text{–}1.2\,r_{2500})$ data do not constrain σ_8, although their constraint on $\Omega_{\rm m}$ is useful for breaking the degeneracy between the two parameters in cluster counts data.

Our baseline cluster analysis uses all the data described above, the RASS cluster catalogs, mass proxies from X-ray follow-up data, lensing data and $f_{\rm gas}$ measurements, and also incorporates Gaussian priors on the Hubble parameter ($h = 0.738 \pm 0.024$; Riess, Macri, et al. 2011) and the cosmic baryon density ($100\,\Omega_{\rm b}h^2 = 2.202 \pm 0.045$; Cooke, Pettini, et al. 2014). (Note that these external priors are not required or used when the cluster data are combined with CMB data.) In Section 2.4, we present results from these cluster data, and compare and combine our results with those from independent cosmological probes. Specifically, we use all-sky CMB data from the *Wilkinson Microwave Anisotropy Probe* (WMAP 9-year release; Bennett et al. 2013; Hinshaw et al. 2013) and the *Planck* satellite (1-year release, including WMAP polarization data, called *Planck*+WP below; Ade et al. 2014a), as well as high-multipole data from the Atacama Cosmology Telescope (ACT; Das et al. 2014) and the South Pole Telescope (SPT; Keisler et al. 2011; Reichardt et al. 2012; Story et al. 2013). We also include the Union 2.1 compilation of type Ia supernovae (Suzuki et al. 2012) and baryon acoustic oscillation (BAO) data from the combination of results from the 6-degree Field Galaxy Survey (6dF; $z = 0.106$; Beutler et al. 2011) and the Sloan Digital Sky Survey (SDSS, $z = 0.35$ and 0.57; Padmanabhan, Xu, et al. 2012; Anderson et al. 2014b). Technical details of our use of these non-cluster data can be found in M14.

2.3 Model and Analysis Methods

M10a provide a detailed description of the analysis procedure for the cluster survey and X-ray follow-up data, including models for the cosmological background, halo abundance and measurement process employed in this work. Here we review the most relevant aspects of the analysis and describe the additions necessary to include the new gravitational lensing data. For details of the analysis of the $f_{\rm gas}$ data, see M14.

2.3.1 Cosmological Model

As in M10a and M14, we consider cosmological models with a flat Friedmann-Robertson-Walker metric, containing radiation, baryons, neutrinos, cold dark matter (CDM), and dark energy. For the cluster data, the key parameters describing the average universe are the Hubble parameter (h), the cosmic densities of baryons ($\Omega_{\rm b}$), neutrinos (parametrized by their species-summed mass, $\sum m_\nu$), matter (in total, $\Omega_{\rm m}$) and dark energy ($\Omega_{\rm DE}$, or Ω_Λ in the case of a cosmological constant).

The variance of the linearly evolved density field, smoothed by a spherical top-hat window of comoving radius R, enclosing mass $M = 4\pi\rho R^3/3$, is

$$\sigma^2(R,z) = \frac{1}{2\pi^2}\int_0^\infty k^2 P(k,z)|W_R(k)|^2 dk, \tag{2.1}$$

where $P(k,z)$ is the linear power spectrum evolved to redshift z and $W_R(k)$ is the Fourier transform of the window function. The matter power spectrum is parametrized by an amplitude, conventionally $\sigma_8 = \sigma(R = 8h^{-1}\,\mathrm{Mpc}, z = 0)$, and the scalar spectral index, n_s. We express the halo mass function, the expected number density as a function of redshift and mass, in the standard way:

$$\left\langle \frac{dn(M,z)}{dM} \right\rangle = \frac{\rho}{M}\frac{d\ln\sigma^{-1}}{dM} f(\sigma,z). \tag{2.2}$$

As in M10a, we use the Tinker, Kravtsov, et al. (2008) parametrization of $f(\sigma,z)$, including its explicit redshift dependence. To account for systematic uncertainties in the mass function, including for models other than ΛCDM, the effects of baryons, etc., we marginalize over priors at the 10 per cent level both in the baseline function, $f(\sigma, z = 0)$, and in the redshift dependent terms from Tinker, Kravtsov, et al. (2008, see details in M10a).

In Equation 2.2, as well as in the correspondence of mass and scale (i.e. $M \propto \rho R^3$) entering $W_R(k)$, ρ refers to the sum of baryon and CDM densities. Note that Section 2.4.1 introduces modifications to the evolution of the power spectrum in order to investigate departures from General Relativity (GR). These are outlined in the respective section.

2.3.2 Cluster Scaling Relations

Connecting the predicted mass function to a flux-limited survey requires a scaling relation – a stochastic function consisting of a mean relation and a model for intrinsic scatter – linking mass and X-ray luminosity. Additional observables that have a smaller intrinsic scatter at fixed mass (i.e. better mass proxies, namely gas mass and temperature in the case of X-ray follow-up observations) can improve cosmological constraints by refining the information available for individual clusters (e.g. Wu, Rozo, and Wechsler 2010; see also Section 2.5.1). It is therefore advantageous to define joint scaling relations, describing the trends and joint scatter of several observables as a function of mass, as we do below. Due to the ubiquity of selection biases in cosmological samples and the steepness of the mass function, accurate constraints on scaling relations (and cosmology) can only be obtained from a simultaneous cosmology+scaling relation analysis that properly accounts for the influence of the mass function and the survey selection function on the observed data (see Section 2.3.3, M10a,b and Allen, Evrard, and Mantz 2011).

Our model for the cluster scaling relations is that of M10a,b, expanded to include the new weak lensing observations. We describe the scaling of each observable cluster property with mass as a power law, and the joint intrinsic scatter as a multi-dimensional log-normal distribution. For this purpose, we define the logarithmic total mass within r_{500} as[6]

$$m = \ln\left(\frac{E(z)M_{500}}{10^{15}\,M_\odot}\right), \tag{2.3}$$

with $E(z) = H(z)/H_0$. The corresponding definitions for observables – luminosity (0.1–2.4 keV band), center-excised temperature, gas mass and lensing mass – are

$$\begin{aligned}
\ell &= \ln\left(\frac{L_{500}}{E(z)10^{44}\,\mathrm{erg\,s^{-1}}}\right), \\
t &= \ln\left(\frac{kT_{500}}{\mathrm{keV}}\right), \\
m_{\mathrm{gas}} &= \ln\left(\frac{E(z)M_{\mathrm{gas},500}}{10^{15}\,M_\odot}\right), \\
m_{\mathrm{lens}} &= \ln\left(\frac{E(z)M_{\mathrm{lens},500}}{10^{15}\,M_\odot}\right).
\end{aligned} \tag{2.4}$$

The quantities in Equation 2.4 represent intrinsic properties of a given cluster, as distinct from measured values (to which they are related by a model for measurement scatter); along with m, they are free parameters of the model.[7] With these definitions, power-law scaling relations become linear relations between $\boldsymbol{y} \equiv (\ell, t, m_{\mathrm{gas}}, m_{\mathrm{lens}})$ and m. For a given cluster, the expectation value of $\boldsymbol{y}$ is $\boldsymbol{\beta_0} + \boldsymbol{\beta_1} m$, and we assume a multivariate Gaussian intrinsic scatter in $\boldsymbol{y}$ at fixed m; i.e.

$$P(\boldsymbol{y}|m) \propto |\boldsymbol{\Sigma}|^{-1/2} \exp\left(-\frac{1}{2}\boldsymbol{\eta}^{\mathrm{t}}\boldsymbol{\Sigma}^{-1}\boldsymbol{\eta}\right), \tag{2.5}$$

where $\boldsymbol{\Sigma}$ is a covariance matrix and $\boldsymbol{\eta} = \boldsymbol{y} - (\boldsymbol{\beta_0} + \boldsymbol{\beta_1} m)$. The normalizations ($\boldsymbol{\beta_0}$), slopes ($\boldsymbol{\beta_1}$) and diagonal elements of $\boldsymbol{\Sigma}$ are in general free parameters that we allow the data to fit (though see below). Following M10b, we also fit the off-diagonal covariance between ℓ and t (which turns out to be consistent with zero; M10b). For simplicity, and because there is no particular expectation for a non-zero covariance, we fix the off-diagonal covariance terms involving m_{lens} and m_{gas} to zero (see details in A. B. Mantz, S. W. Allen, et al. 2016).

[6] To simplify interpretation of the intrinsic scatter terms, we use natural logarithms in the scaling relation model, a change of notation with respect to M10a,b.

[7] Note that, while m represents true mass, the quantities in Equation 2.4 need not be identically the true luminosity, average temperature, etc. for a cluster (although they do correspond to the measured quantities generally described as such). For example, asphericity might result in a departure of m_{gas} from the true gas mass within r_{500}, an effect that contributes to the intrinsic scatter of the m_{gas}–m relation. Similarly, m_{lens} refers to the spherical mass that would be reconstructed from an ideal shear profile (i.e. without statistical error), which is in general different from the true mass due to projected structure.

For the $m_{\rm lens}$–m relation, we assume a slope of unity and place priors on the normalization and intrinsic scatter. Specifically, we adopt a Gaussian prior on the normalization, $\beta_{0,m_{\rm lens}} = 0.99 \pm 0.07$, encoding the expected bias (and its uncertainty) of weak lensing masses due to triaxiality, line-of-sight structure, the assumption of a Navarro, Frenk, and White (1997, hereafter NFW) mass profile, systematic biases affecting shear measurements, photometric redshift errors, and the statistical uncertainty accrued in cross-calibrating $p(z)$ (5-filter) and color-cut (3-filter) lensing data. (Full details can be found in Applegate, Linden, et al. 2014.) We constrain the scatter between $m_{\rm lens}$ and m with a wide Gaussian prior, 20 ± 10 per cent, where the central value is motivated by the simulations of Becker and Kravtsov (2011).[8]

The $m_{\rm gas}$–m relation deserves some additional consideration, since the value and evolution of its normalization, $\beta_{0,m_{\rm gas}} = \ln f_{\rm gas}(r_{500})$, carry additional cosmological information (Sasaki 1996; Pen 1997; Allen, Schmidt, and Fabian 2002; Allen, Schmidt, Ebeling, et al. 2004; Allen, Rapetti, et al. 2008; Allen, Evrard, and Mantz 2011; Ettori, Tozzi, and Rosati 2003; Ettori, Morandi, et al. 2009; Battaglia, Bond, et al. 2013; Planelles, Borgani, et al. 2013; M14). In principle, this information could be used in tandem with the more precise $f_{\rm gas}(0.8\text{–}1.2\,r_{2500})$ measurements of M14, given a suitable model for their covariance. In practice, the low precision of our mass constraints at r_{500} for individual clusters (due to the scatter in $m_{\rm lens}|m$) significantly limits the information available from the $m_{\rm gas}$–m relation. In addition, the measurement correlation between the two $f_{\rm gas}$ values is negligible, since the total masses are estimated independently from different data (lensing vs. X-ray) and the gas mass measured in the $0.8\text{–}1.2\,r_{2500}$ shell is a small fraction of that integrated within r_{500}. We therefore simplify the analysis by keeping the model for $f_{\rm gas}(0.8\text{–}1.2\,r_{2500})$, used for the M14 data, independent of the parameters of the $m_{\rm gas}$–m relation. In addition to allowing the normalization, mass dependence and intrinsic scatter of the $m_{\rm gas}$–m relation to vary, we marginalize over a ± 5 per cent uniform prior on the evolution of the normalization, of the form $f_{\rm gas}(r_{500}, z) = f_{\rm gas}(r_{500}, z = 0)(1 + \alpha_f z)$. This form, and the prior itself, are identical to those used to describe the evolution in $f_{\rm gas}(0.8\text{–}1.2\,r_{2500})$ in M14, but α_f is varied independently of the corresponding parameter at r_{2500}. We constrain the intrinsic scatter in $m_{\rm gas}|m$ with a uniform prior spanning 0.0–0.10, where 0.10 corresponds to the high end of the confidence interval for the fractional intrinsic scatter of $f_{\rm gas}(r_{500})$, measured from the M14 data (A. B. Mantz, S. W. Allen, et al. 2016).

[8]Comparing the scatter in two mass bins, both lower in mass than the clusters in our lensing sample, these simulations imply that the intrinsic scatter decreases as a function of mass. We have tested whether a power-law dependence of the scatter on mass would change our results, marginalizing over indices in the range ± 0.35, and find that this has a negligible effect on our cosmological constraints. This is due to the small range in mass covered by our lensing data, and the fact that, when X-ray mass proxy information is also included in the analysis, the data are able to directly constrain the intrinsic scatter at the pivot mass of the lensing sample. Note that the width of our prior on the intrinsic scatter, significantly greater than the uncertainties reported by Becker and Kravtsov (2011), partly reflects differences between their analysis and ours, such as our use of a fixed NFW concentration parameter (Section 2.3.3).

2.3.3 Likelihood Function

The complete likelihood of the X-ray and lensing data set takes the same form as in M10a,

$$\mathcal{L} \propto e^{-\langle N_{\rm det}\rangle} \prod_{i=1}^{N_{\rm det}} \langle \tilde{n}_{{\rm det},i}\rangle \,. \tag{2.6}$$

Here $\langle N_{\rm det}\rangle$ is the expected number of cluster detections in the survey data for a given set of model parameters, accounting for the selection function. The product runs over the $N_{\rm det}$ detected clusters, and accounts for their redshifts, survey fluxes and any follow-up measurements. Following M10a, we use an abbreviated notation where $\boldsymbol{x}$ stands for the true values of z and m; $\boldsymbol{y}$ stands for the intrinsic values of ℓ, t, $m_{\rm gas}$ and $m_{\rm lens}$ (as above); and $\hat{\boldsymbol{y}}$ stands for the measured values of $\boldsymbol{y}$, plus the X-ray survey flux, $\hat{F}$. Similarly, $\hat{\boldsymbol{x}}$ indicates measured values of $\boldsymbol{x}$, although in practice we model any mass estimates as response variables of the scaling relations (i.e. components of $\hat{\boldsymbol{y}}$). The per-cluster likelihood term can then be expressed as

$$\langle \tilde{n}_{{\rm det},i}\rangle = \int d\boldsymbol{x} \int d\boldsymbol{y} \left\langle \frac{dN}{d\boldsymbol{x}} \right\rangle P(\boldsymbol{y}|\boldsymbol{x})\, P(\hat{\boldsymbol{x}}_{\boldsymbol{i}}, \hat{\boldsymbol{y}}_{\boldsymbol{i}}|\boldsymbol{x},\boldsymbol{y}) \times P(I|\boldsymbol{x},\boldsymbol{y},\hat{\boldsymbol{x}}_{\boldsymbol{i}},\hat{\boldsymbol{y}}_{\boldsymbol{i}}). \tag{2.7}$$

Here, $\langle dN/d\boldsymbol{x}\rangle = \langle d^2N/dzdm\rangle$ can be calculated from the mass function and cosmic expansion history,

$$\left\langle \frac{d^2N}{dzdm} \right\rangle = M\,\frac{dV}{dz} \left\langle \frac{dn(M,z)}{dM} \right\rangle, \tag{2.8}$$

where V is the comoving volume as a function of redshift. The likelihood associated with the scaling relations is simply the function $P(\boldsymbol{y}|\boldsymbol{x})$ given in Equation 2.5. The remaining factors are respectively the likelihoods associated with the measurements, $P(\hat{\boldsymbol{x}}_{\boldsymbol{i}}, \hat{\boldsymbol{y}}_{\boldsymbol{i}}|\boldsymbol{x},\boldsymbol{y})$, and selection function (the probability to be Included in the data set), $P(I|\boldsymbol{x},\boldsymbol{y},\hat{\boldsymbol{x}}_{\boldsymbol{i}},\hat{\boldsymbol{y}}_{\boldsymbol{i}})$, for a particular cluster. These are written in a general form in Equation 2.7 and can be simplified for our purposes, as we detail below.

In the case of a cluster with a precisely determined redshift (i.e. measured spectroscopically, which is the case for all our clusters), the integral $d\boldsymbol{x} = dz\,dm$ can be replaced by an integral over mass only (dm) at fixed z.[9] For a given parent cluster sample, our selection function is simply a function of redshift and detected X-ray survey flux; hence, the final term reduces to $P(I|z,\hat{F})$, a function that is tabulated for each of the BCS, REFLEX and Bright MACS samples (Ebeling, Edge, Bohringer, et al. 1998; Ebeling, Edge, Mantz, et al. 2010; Boehringer et al. 2004). Note that, as in M10a, we marginalize over separate allowances for the overall completeness/purity of each cluster sample. The measurement term can be factored into

[9] This is equivalent to factoring the term associated with the redshift measurement, $P(\hat{z}_i|z)$, out of $P(\hat{\boldsymbol{x}}_{\boldsymbol{i}}, \hat{\boldsymbol{y}}_{\boldsymbol{i}}|\boldsymbol{x},\boldsymbol{y})$, and approximating it as a delta function.

survey, X-ray follow-up and lensing parts, since these three observations are independent; to be explicit,

$$P(\hat{\boldsymbol{x}}_{\boldsymbol{i}}, \hat{\boldsymbol{y}}_{\boldsymbol{i}}|\boldsymbol{x}, \boldsymbol{y}) = P(\hat{F}|z, \ell, t)\, P(\hat{\ell}, \hat{t}, \hat{m}_{\rm gas}|z, m, \ell, t, m_{\rm gas}) \times P(\hat{m}_{\rm lens}|z, m_{\rm lens}). \tag{2.9}$$

The X-ray measurement models we employ are identical to those in M10a, and we refer the interested reader there for full details. In brief, the survey flux model straightforwardly follows from the intrinsic cluster luminosity, temperature and redshift, with the appropriate K-correction, and accounts for Poisson scaling of the measurement uncertainties with true flux. The model for X-ray follow-up measurements of mass proxies accounts not only for the straightforward statistical uncertainties in each measurement and their covariance (due to being measured from the same data), but also for their aperture dependence (i.e. the difference between the aperture used in the measurement and the true value of r_{500} according to m and the cosmological model).

To evaluate the likelihood associated with the lensing data for a cluster, we compare the shear profile measured by WtG[10] (specifically, using the color-cut method) to the shear profile predicted from an NFW profile with mass given by $m_{\rm lens}$ and concentration parameter $c = 4$ (consistent with the mean concentration measured in WtG and the mean population concentration in N-body simulations; Neto, Gao, et al. 2007). The profiles are measured in annuli about the X-ray center in the radial range 750 kpc to 3 Mpc (in our reference cosmological model),[11] where the annuli are chosen to contain approximately equal numbers of galaxies (at least 300). We write

$$\ln P(\hat{m}_{\rm lens}|z, m_{\rm lens}) = -\frac{1}{2}\sum_j \left[\frac{\hat{g}_j - g_j(z, m_{\rm lens}, c = 4)}{\sigma_{g,j}}\right]^2, \tag{2.10}$$

where $\hat{g}_j$ is the azimuthally averaged tangential shear measured in annulus j, and $\sigma_{g,j}$ is its uncertainty, determined by bootstrapping the galaxy population in each annulus.[12] The predicted shear at projected radius θ_j is evaluated as

$$g_j(z, m_{\rm lens}, c) = \frac{\langle\beta_{\rm s}\rangle\, \gamma_{{\rm t},\infty}(\theta_j; m_{\rm lens}, c)}{1 - \frac{\langle\beta_{\rm s}^2\rangle}{\langle\beta_{\rm s}\rangle}\kappa_\infty(\theta_j; m_{\rm lens}, c)}, \tag{2.11}$$

where $\gamma_{{\rm t},\infty}$ and κ_∞ are respectively the tangential shear and convergence of a source at infinite redshift due to a lens at redshift z with an NFW mass distribution given by $m_{\rm lens}$

[10] Hence, the term $\hat{m}_{\rm lens}$ in our equations should be interpreted as shorthand for the measured shear profile of a cluster.

[11] This radial range is chosen to minimize sensitivity to the assumed concentration, avoid high values of shear and cluster galaxy contamination in cluster centers, and reduce the effect of possible mis-centering, as discussed in detail by Applegate, Linden, et al. (2014).

[12] As described in WtG, corrections for shear calibration are applied on a per-galaxy basis, whereas corrections for contamination by cluster member galaxies are applied to the average shear measured in each annulus.

and c (Wright and Brainerd 2000). β_s encodes the dependence on the redshift of the cluster and the lensed sources,

$$\beta_s = \frac{D_{LS} D_{O\infty}}{D_{OS} D_{L\infty}}, \tag{2.12}$$

where the terms on the right hand side are variously the angular diameter distances separating the lens (L), source (S), observer (O), and a fictitious source at infinite redshift (∞). Note that these terms introduce a cosmology dependence to the predicted shear. The averages of β_s and β_s^2 that appear in Equation 2.11 are evaluated using the distribution of galaxy redshifts in the COSMOS field, after replicating the same catalog selection cuts applied to each cluster field, such as the removal of the cluster red sequence. More details can be found in Applegate, Linden, et al. (2014).

2.4 Cosmological Results

Our results are produced using COSMOMC[13] (Lewis and Bridle 2002; October 2013 version), appropriately modified to evaluate the likelihoods of the f_{gas}[14] and cluster counts data. Cosmological calculations were performed using the CAMB[15] package of Lewis, Challinor, and Lasenby (2000).

When analyzing cluster data alone, we incorporate Gaussian priors on the Hubble parameter, $h = 0.738 \pm 0.024$ (Riess, Macri, et al. 2011), and mean baryon density, $100\,\Omega_b h^2 = 2.202 \pm 0.045$ (Cooke, Pettini, et al. 2014); we additionally fix the scalar spectral index of density perturbations to $n_s = 0.95$ in this case.[16] When CMB data are included in the fit, these three parameters are allowed to vary freely, along with the optical depth to reionization. We assume the standard effective number of relativistic species, $N_{eff} = 3.046$.

2.4.1 Constraints on Modifications of Gravity

While dark energy (in the form of a cosmological constant) has been a mainstay of the standard cosmological model since the discovery that the expansion of the Universe is accelerating, other explanations for acceleration are possible. In particular, various modifications to GR in the large-scale/weak-field limit have been proposed (for recent reviews see, e.g., Frieman, Turner, and Huterer 2008; Clifton, Ferreira, et al. 2012; Joyce, Jain, et al. 2015). Being sensitive to the action of gravity in this regime, the growth of cosmic structure has the

[13] http://cosmologist.info/cosmomc/
[14] http://www.slac.stanford.edu/~amantz/work/fgas14/
[15] http://www.camb.info/
[16] Since the cluster data probe the amplitude of the power spectrum over a very limited range of scales, there is a degeneracy between n_s and σ_8 constraints from clusters alone. However, varying n_s within the range allowed by CMB data ($\Delta n_s \sim 0.03$) would result in a sub-per-cent shift in our clusters-only value of σ_8 (M10a).

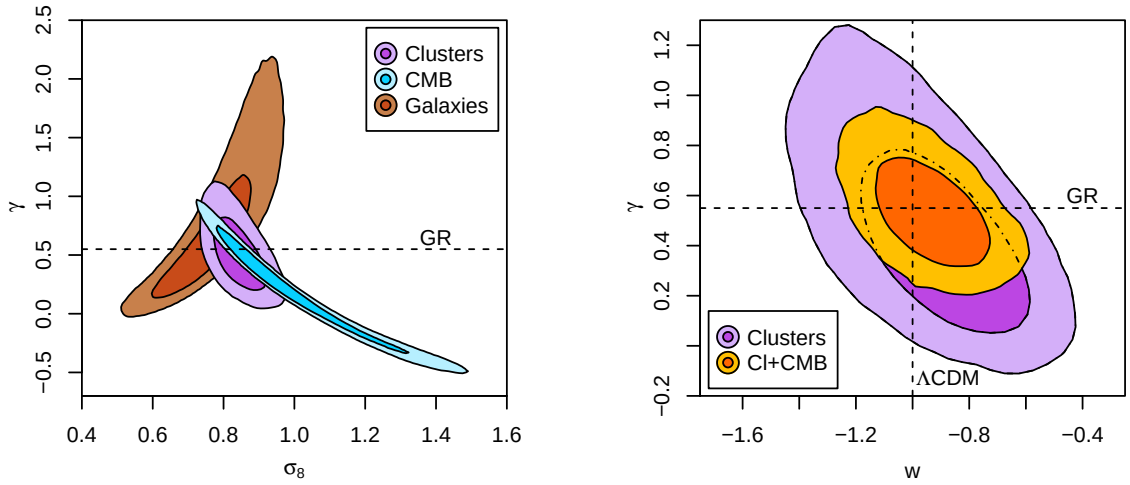

Fig. 2.1 Constraints on models where the growth index of cosmic structure formation, γ, is a free parameter. Dark and light shading respectively indicate the 68.3 and 95.4 per cent confidence regions, accounting for systematic uncertainties. Left: Constraints from clusters, the CMB, and galaxy survey data individually, marginalizing over the standard flat ΛCDM parametrization of the cosmic expansion history. Note that the treatment of the galaxy survey data uses a multivariate Gaussian approximation to constraints from RSD and the AP effect (see also Rapetti, Blake, et al. 2013). GR corresponds approximately to $\gamma = 0.55$ (dashed line). Right: Constraints from clusters and the combination of clusters and the CMB for models where w is allowed to be free in the parametrization of the expansion history (this parameter does not directly affect the growth history in this model). Here the horizontal and vertical dashed lines respectively correspond to the standard models for the growth of cosmic structure (GR) and the expansion of the Universe (ΛCDM). In these figures, 'CMB' refers to the combination of ACT, SPT and WMAP data; see Appendix A for the corresponding figures using *Planck*+WP instead of WMAP data.

potential to distinguish between dark energy and modified gravity theories that predict identical expansion histories.

A simple and entirely phenomenological approach involves modifying the growth rate of density perturbations at late times, when the growth is approximately scale-independent. We adopt the simple parametrization in terms of the growth index, γ (e.g. Linder 2005),

$$f(a) = \frac{d\ln\,\delta}{d\ln\,a} = \Omega_{\rm m}(a)^{\gamma}, \tag{2.13}$$

where δ is the linear density contrast in synchronous gauge (at any scale), and where $\gamma = 0.55$ approximately corresponds to GR for a wide range of expansion histories compatible with current data (Polarski and Gannouji 2008). Note that constraints on the growth index serve only as a useful consistency check of GR, rather than directly testing GR against alternative models of gravity. Constraints on γ from earlier versions of our cluster analysis (in conjunction with contemporaneous cosmological data) are presented by Rapetti, Allen, et al. (2009); Rapetti, Allen, et al. (2010); Rapetti, Blake, et al. (2013). Independent constraints from other

Table 2.1 Marginalized best-fitting values and 68.3 per cent maximum-likelihood confidence intervals for the growth index (γ), σ_8, and w from clusters (Cl), the CMB and galaxy survey data (gal). Here γ determines the late-time growth of cosmic structure, and w should be interpreted purely as a modification to the ΛCDM expansion model (but not directly to the growth). Subscripts 'WM' and '*Pl*' denote the use of WMAP or *Planck*+WP data in combination with ACT and SPT. Note: [a]the combinations with galaxy survey data should be treated with caution due to the caveats noted in the text.

Data	γ	σ_8	w
Cl	0.48 ± 0.19	0.833 ± 0.048	-1
Cl+CMB$_{\rm WM}$	0.56 ± 0.13	0.824 ± 0.037	-1
Cl+CMB$_{\rm WM}$+gal[a]	0.66 ± 0.06	0.802 ± 0.016	-1
Cl+CMB$_{Pl}$	0.58 ± 0.12	0.824 ± 0.037	-1
Cl+CMB$_{Pl}$+gal	0.67 ± 0.06	0.799 ± 0.015	-1
Cl	0.39 ± 0.24	0.850 ± 0.055	-0.90 ± 0.19
Cl+CMB$_{\rm WM}$	0.52 ± 0.14	0.817 ± 0.040	-0.94 ± 0.13
Cl+CMB$_{\rm WM}$+gal	0.60 ± 0.08	0.792 ± 0.020	-0.91 ± 0.08
Cl+CMB$_{Pl}$	0.57 ± 0.14	0.828 ± 0.040	-1.01 ± 0.13
Cl+CMB$_{Pl}$+gal	0.63 ± 0.07	0.799 ± 0.015	-0.96 ± 0.07

data sets have been obtained by, e.g., Nesseris and Perivolaropoulos (2008), Di Porto and Amendola (2008), Samushia et al. (2013); Samushia et al. (2014) and Beutler et al. (2014a).

We follow Rapetti, Blake, et al. (2013), investigating the constraints on γ from our cluster data, the integrated Sachs-Wolfe (ISW) effect on the CMB,[17] and measurements of redshift-space distortions (RSD) and the Alcock-Paczynski (AP) effect from galaxy survey data. In practice, we use CAMB to calculate and tabulate $P(k, z)$ assuming GR, then modify these values from $z = 30$ (well into the matter-dominated regime, where $f \to 1$ independent of γ) onward to be consistent with the growth given by Equation 2.13. This modified power spectrum is then integrated when evaluating the cluster mass function (Equations 2.1–2.2). For details of the calculation of the ISW effect in this model, see Appendix B; as in earlier sections, we use CMB data from ACT, SPT, and either *Planck*+WP or WMAP. The galaxy survey data include results from 6dF (Beutler, Blake, et al. 2012), SDSS (Reid et al. 2012) and the WiggleZ Dark Energy Survey (Blake et al. 2011b). Their likelihood is approximated by a multivariate Gaussian, encoding measurements of $f\sigma_8(z)$ and $F(z) = (1+z)D(z)H(z)/c$ at several redshifts, assuming zero neutrino mass; here D is the angular diameter distance, and c is the speed of light. For consistency, we fix $\sum m_\nu = 0$ in this section for all data sets. Due to the approximate nature of the galaxy survey likelihood used here, compared with the analysis of cluster and CMB data, we urge caution in interpreting the results that combine all three data sets. However, the level of precision that is in principle available from this

[17] Cosmic growth also leaves an imprint at high multipoles through CMB lensing, but currently the CMB constraints on γ primarily come from the ISW effect.

combination (Table 2.1) motivates a more complete analysis of the galaxy survey data, i.e. accounting for all parameter covariances, in future work.

The left panel of Figure 2.1 shows the constraints on γ and σ_8 from clusters, the CMB and galaxy survey data individually. In addition to the parameters shown, we marginalize over the standard set of free parameters of the flat ΛCDM model. In the case of CMB or galaxy survey data alone, there are strong but complementary degeneracies (as discussed by Rapetti, Blake, et al. 2013), whereas the cluster data (with standard priors) constrain the entire model; the marginalized constraints from clusters are $\gamma = 0.48 \pm 0.19$ and $\sigma_8 = 0.83 \pm 0.05$.

All three data sets shown are individually consistent with $\gamma = 0.55$. Their combination has a marginal ($< 2\sigma$) preference for higher values of γ (Table 2.1), though this should be viewed with caution in light of the caveats mentioned above (see also Beutler et al. 2014b). The combination of clusters and the CMB (without galaxy survey data) is fully consistent with GR.

In the right panel of Figure 2.1, we present constraints on models when additional freedom is introduced into the model for the cosmic expansion in the form of the w parameter. In this model, w should not be interpreted as the dark energy equation of state, but simply as a phenomenological departure from the cosmic expansion model given by ΛCDM, in the same way that γ parametrizes departures of the growth history from that given by GR. (In particular, dark energy perturbations associated with values of w different from -1 are not included in the growth equations, which instead depend on γ through Equation 2.13.) The figure shows constraints from clusters alone, and the combination of cluster and CMB data. Here again, the clusters and clusters+CMB data are fully consistent with the standard $w = -1$, $\gamma = 0.55$ model, although the full combination, including the galaxy survey data, exhibits mild ($< 2\sigma$) tension (Table 2.1).

2.5 Discussion

2.5.1 The Role of Follow-up Data

Although a cosmological test can be carried out using only cluster survey data, given a survey of sufficient area and depth (in both mass and redshift), this approach requires relatively strong assumptions regarding the form and scatter of the scaling relations. A straightforward benefit of incorporating additional measurements of masses or mass proxies for even a subset of discovered clusters is that these aspects of the model can be constrained rather than assumed, expanding the scope of cosmological models that can be investigated (e.g. Majumdar and Mohr 2004). In the context of the Dark Energy Survey (DES), Wu, Rozo, and Wechsler (2010) have shown that significant gains in dark energy constraints can be obtained by incorporating X-ray or SZ mass proxy information, for example.

The present work uses three forms of follow-up data (in addition to spectroscopic redshift measurements): weak gravitational lensing observations, X-ray measurements of mass proxies (X-ray luminosity, temperature and gas mass within r_{500}), and X-ray measurements of $f_{\rm gas}$ at r_{2500} for relaxed clusters. To a large extent, the X-ray $f_{\rm gas}$ analysis can be considered independent (Section 2.3.2), providing additional constraints on $\Omega_{\rm m}$ and dark energy parameters. As for the former two types of data, their complementarity goes beyond the fact that X-ray observations are currently more numerous than lensing observations for the clusters in our data set. Namely, as we have emphasized, weak lensing provides nearly unbiased masses on average, but with a significant, irreducible intrinsic scatter on a cluster-by-cluster basis. In contrast, some X-ray (and SZ) mass proxies have a much smaller intrinsic scatter with mass, but the normalization of their scaling relations must be calibrated. The combination of the two types of observations thus provides a robust constraint on the cluster mass scale (from lensing), as well as more precise constraints on the slope and intrinsic scatter of scaling relations (and potentially on the shape of the mass function) than lensing alone can provide.

As we discuss in the next section, significant further improvements in cosmological constraints can be obtained by improving the mass calibration through additional lensing data. Nevertheless, the ability of X-ray and SZ mass proxies to provide more precise mass estimates for individual clusters, and their availability at the highest and lowest redshifts, where lensing observations are very challenging/expensive, underscore their utility for cosmology.

2.5.2 The Benefits of Improved Weak Lensing Data

With relatively modest improvements in lensing systematics (see Applegate, Linden, et al. 2014) and larger samples of clusters with high-quality weak lensing data, constraints on the cluster mass scale at the 5 per cent level are plausible in the near term. Given also a factor of ~ 2 improvement in predictions of the halo mass function (compared with the 10 per cent uncertainty adopted here), doubling of the number of clusters with weak lensing data would then translate to a reduction in the uncertainty on σ_8 (at fixed $\Omega_{\rm m}$) from 4 per cent currently to ~ 2 per cent from clusters alone.[18] At the same time, the new data could provide a ~ 5 per cent precision constraint on $\Omega_{\rm m}$ through the $f_{\rm gas}$ test (Allen, Mantz, et al. 2013; M14), leading to a factor of four improvement in the joint $\Omega_{\rm m}$–σ_8 constraint.

[18]The size of the lensing sample could be straightforwardly increased (approximately doubled) by incorporating data already present in the archives of SuprimeCam and MegaPrime/MegaCam, such as those gathered for the Local Cluster Substructure Survey (Okabe, Takada, et al. 2010; Okabe, Smith, et al. 2013) and the Canadian Cluster Comparison Project (Hoekstra 2007; Hoekstra, Mahdavi, et al. 2012). However, this would require the application of a consistent, rigorously tested reduction and analysis pipeline across the entire data set, and likely the gathering of additional data to ensure that a significant fraction of the clusters are observed in at least five well chosen bands (enabling robust estimates of photometric redshifts for individual lensed galaxies; Applegate, Linden, et al. 2014). The lack of such 5-band observations is currently the most serious limitation to exploiting these archival data.

2.5.3 The Route to Improved Dark Energy Constraints

While the addition of further high-quality weak lensing data for X-ray selected clusters at low-to-intermediate redshifts should lead to significant near-term benefits in the constraints on $\Omega_{\rm m}$ and σ_8, the route to obtaining improved knowledge of gravity from clusters lies primarily in extending the redshift range of the analysis. In this regard, the combination of X-ray and SZ-selected cluster surveys holds significant potential for improvements on modified gravity constraints, which will enable us to move beyond the simple γ-parameterization shown in Figure 2.1. As the field progresses, there will also be a need for increasingly sophisticated theoretical predictions – for example mass functions calibrated to a few per cent precision spanning the full range of interest in mass and redshift, and an appropriate range of baryonic physics, dark energy and fundamental physics models.

2.6 Conclusions

Earlier papers in the WtG series have focussed on providing the most well characterized and unbiased constraints on the absolute cluster mass calibration possible, using measurements of weak gravitational lensing. Here we incorporate those data into a cosmological analysis that uses the number density of massive clusters as a function of time to probe the growth of cosmic structure. In addition to the WtG lensing data, our analysis uses an X-ray selected cluster sample culled from the ROSAT All-Sky Survey, spanning redshifts $0 < z < 0.5$, along with follow-up X-ray data to supply additional mass proxies. We additionally take advantage of cluster gas mass fraction data, which also benefit substantially from the lensing mass calibration, to provide an independent measurement of the cosmic expansion and tight constraints on $\Omega_{\rm m}$, breaking the main degeneracy (with σ_8) present in the analysis of cluster-counts data.

The prospects for further improvements in the constraints on cosmology and fundamental physics from observations of galaxy clusters are substantial. A suite of major new surveys across the electromagnetic spectrum have or will soon come on line (e.g. DES, SPT-3G, Advanced ACT-Pol, eROSITA, LSST, WFIRST-AFTA, *Euclid*). Optimally leveraging the data from these surveys, as well as follow-up facilities, to produce robust cluster catalogs (with well understood purity and completeness), accurate absolute mass calibration (from weak lensing) and sufficient, low-scatter mass proxy information (from X-ray and SZ follow-up) will be critical to obtaining the tightest and most robust constraints possible.

In the near term, the path toward further reducing systematic uncertainties in the absolute mass calibration of low-redshift cluster samples using weak lensing methods seems clear (e.g. Applegate, Linden, et al. 2014), with important work already underway within the Abate et al. (2012) and elsewhere. The most immediate and straightforward aspect of this

would be an expansion of the weak lensing data set to 2–4× more clusters, maintaining comparable data quality to the WtG study. With this, the prospects for, e.g., quickly halving the statistical-plus-systematic uncertainty on σ_8 from clusters are strong. Likewise, for dark energy studies, the prospects for improved constraints by utilizing optimally the full mass and redshift lever arm of new and existing X-ray, optical and SZ-selected cluster samples are excellent.

Acknowledgments

We thank Alastair Edge for sharing his list of likely AGN-dominated BCS and REFLEX clusters, as well as Risa Wechsler and Sam Skillman for insightful discussions. We thank the Dark Cosmology Centre for hosting collaboration meetings during the development of this paper. We also thank the referee for providing prompt, thorough, and very useful comments. Calculations for this work utilized the Coma, Orange and Bullet compute clusters at the SLAC National Accelerator Laboratory, and the HPC facility at the University of Copenhagen. AM was supported by National Science Foundation grants AST-0838187 and AST-1140019. DA acknowledges funding from the German Federal Ministry of Economics and Technology (BMWi) under project 50 OR 1210. S. Adhikari and S. Shandera are supported by the National Aeronautics and Space Administration (NASA) under Grant No. NNX12AC99G issued through the Astrophysics Theory Program. We acknowledge support from the U.S. Department of Energy under contract number DE-AC02-76SF00515; from NASA through Chandra Award Numbers GO8-9118X and TM1-12010X, issued by the Chandra X-ray Observatory Center, which is operated by the Smithsonian Astrophysical Observatory for and on behalf of NASA under contract NAS8-03060; as well as through program HST-AR-12654.01-A, provided by NASA through a grant from the Space Telescope Science Institute, which is operated by the Association of Universities for Research in Astronomy, Inc., under NASA contract NAS 5-26555. The Dark Cosmology Centre is funded by the Danish National Research Foundation.

Based in part on data collected at Subaru Telescope (University of Tokyo) and obtained from the SMOKA, which is operated by the Astronomy Data Center, National Astronomical Observatory of Japan. Based on observations obtained with MegaPrime/MegaCam, a joint project of CFHT and CEA/DAPNIA, at the Canada-France-Hawaii Telescope (CFHT) which is operated by the National Research Council (NRC) of Canada, the Institute National des Sciences de l'Univers of the Centre National de la Recherche Scientifique of France, and the University of Hawaii.

Chapter 3

Cluster abundance as a probe of gravity: chameleon $f(R)$ theories

This chapter contains the following article:

"New constraints on $f(R)$ gravity from clusters of galaxies"

Published in *Phys. Rev. D 92, 044009 (2015).*

Authors:

M. Cataneo, D. Rapetti, F. Schmidt, A. B. Mantz, S. W. Allen, D. E. Applegate, P. L. Kelly, A. von der Linden, R. G. Morris

The abundance of massive galaxy clusters is a powerful probe of departures from General Relativity (GR) on cosmic scales. Despite current stringent constraints placed by stellar and galactic tests, on larger scales alternative theories of gravity such as $f(R)$ can still work as effective theories. Here we present constraints on two popular models of $f(R)$, Hu-Sawicki and "designer", derived from a fully self-consistent analysis of current samples of X-ray selected clusters and accounting for all the covariances between cosmological and astrophysical parameters. Using cluster number counts in combination with recent data from the cosmic microwave background (CMB) and the CMB lensing potential generated by large scale structures, as well as with other cosmological constraints on the background expansion history and its mean matter density, we obtain the upper bounds $\log_{10}|f_{R0}| < -4.79$ and

$\log_{10} B_0 < -3.75$ at the 95.4 per cent confidence level, for the Hu-Sawicki (with $n = 1$) and designer models, respectively. The robustness of our results derives from high quality cluster growth data for the most massive clusters known out to redshifts $z \sim 0.5$, a tight control of systematic uncertainties including an accurate and precise mass calibration from weak gravitational lensing data, and the use of the full shape of the halo mass function over the mass range of our data.

3.1 Introduction

Since the discovery of the late time cosmic acceleration (Perlmutter et al. 1999; Riess et al. 1998) a profusion of theoretical models have been proposed to explain this phenomenon (for recent reviews see Copeland, Sami, and Tsujikawa 2006; Clifton, Ferreira, et al. 2012; Joyce, Jain, et al. 2015). In a nutshell, one can either add a dark fluid with sufficient negative pressure or modify the laws of gravity. Among the alternative theories to General Relativity (GR), $f(R)$ gravity has sparked a lot of interest over the last decade, motivated by its relative simplicity and rich phenomenology (Sotiriou and Faraoni 2010; De Felice and Tsujikawa 2010). In this model, the Einstein-Hilbert action is supplemented by a non-linear function of the Ricci or curvature scalar, R. Conveniently chosen $f(R)$ functions can reproduce the observed accelerated expansion while adding an attractive force of the order of the gravitational interaction. This fifth force is carried by the scalar degree of freedom, dubbed scalaron, $f_R = \mathrm{d}f/\mathrm{d}R$, introduced by the modification of gravity. The range of this new interaction is given by the inverse mass, or equivalently the Compton wavelength of the scalaron, which is directly related to the background amplitude of the scalaron field today, f_{R0}.

In this model, on scales smaller than the Compton wavelength, gravity is enhanced by a factor of 4/3 and structure formation is consequently modified. Above this scale, structures assemble following GR as long as the background Compton wavelength is smaller than the horizon, $\lambda_C \ll H^{-1}$.

Viable $f(R)$ models also present a non-linear mechanism to suppress the modifications of gravity in high-density environments, such as in our Solar System, where GR is known to be a very accurate theory of gravity. This suppression should also be observed within our Galaxy. Theoretical arguments (Hu and Sawicki 2007) supported afterwards by hydrodynamical simulations of galaxy formation and evolution (Fontanot, Puchwein, et al. 2013) require the value of the background field $|f_{R0}|$ to be less than 10^{-6} for this to be the case. Most recently, constraints from distance indicators and dwarf galaxies further reduced this upper limit to $|f_{R0}| \lesssim 4 \times 10^{-7}$ (here and throughout, we state the upper limits at the 95.4 per cent confidence level) (Jain, Vikram, and Sakstein 2013; Vikram, Cabré, et al. 2013). Such small $f(R)$ modifications of gravity cannot leave their imprints on cosmological scales or even on fully non-linear scales such as those within galaxy clusters. Nevertheless, $f(R)$ can serve as a

useful effective theory or working model for tests of gravity on large scales. For this purpose, clusters of galaxies represent a powerful probe of gravity down to scales $\sim$ 1–20 Mpc/h. In particular, it has been shown (Schmidt, Lima, et al. 2009; Lombriser, Koyama, and Li 2014) that the abundance of rare massive halos is substantially enhanced by the presence of a fifth force for $|f_{R0}| > |\Psi| \sim 10^{-6}$–$10^{-5}$, where Ψ is the typical depth of the Newtonian potential for these objects.

In combination with other data sets, Schmidt, Vikhlinin, and Hu 2009 used measurements of the abundance of massive galaxy clusters inferred from X-ray survey data to constrain the Hu-Sawicki model of $f(R)$ gravity (Hu and Sawicki 2007) and obtained the tightest cosmological constraint at the time $|f_{R0}| \lesssim 1.3 \times 10^{-4}$. These authors used a spherical collapse prediction of the number of halos as a function of cosmological parameters, mass and redshift that had previously been validated using N-body simulations (Schmidt, Lima, et al. 2009). We employ this halo mass function (HMF) and extend the approach by including departures from GR as a prefactor to the HMF of Tinker, Kravtsov, et al. (2008), which is based on high resolution GR simulations. This method allows us to efficiently use the full HMF of GR as a baseline, properly accounting for the redshift evolution and covariances of its parameters, as well as other systematic uncertainties (see e.g. Mantz, Allen, Rapetti, and Ebeling 2010). In Schmidt, Vikhlinin, and Hu (2009), the authors mapped modifications of gravity into GR by matching the Sheth-Tormen (ST) HMF (Sheth and Tormen 1999) for $f(R)$ to a Tinker, Kravtsov, et al. (2008) mass function with rescaled σ_8 at a fixed pivot mass. This renormalization was then used to incorporate both CMB and cluster constraints on the growth of structures. These simplifications allowed them to have a limited number of parameters and therefore to be able to perform a maximum likelihood analysis. However, this approach may neglect relevant correlations between astrophysical and cosmological quantities as well as introduce spurious degeneracies between them. Here instead we carry out a Markov Chain Monte Carlo (MCMC) analysis of the full likelihoods of current cluster and CMB data sets, which includes all the covariances between parameters and an advanced treatment of systematic uncertainties and biases. Together with CMB data, and using the full mass and redshift dependence of the HMF, as well as high quality survey (X-ray) and extensive follow-up (X-ray and optical) cluster data, spanning a redshift range $0 < z < 0.5$, we obtain robust and improved constraints on the background scalaron field, $|f_{R0}| < 1.6 \times 10^{-5}$. As in Schmidt, Vikhlinin, and Hu (2009), our results also include constraints from baryon acoustic oscillation (BAO) and type Ia supernova (SNIa) data.

More recently, Dossett, Hu, and Parkinson (2014) and Hu, Raveri, et al. (2015) obtained somewhat tighter upper bounds on $|f_{R0}|$ by comparing the theoretical predictions of the enhanced linear matter power spectrum in $f(R)$ gravity with measurements of the galaxy power spectrum made by the WiggleZ Dark Energy Survey (Drinkwater et al. 2010). As described in those analyses, however, $f(R)$ corrections for the non-linear scales of the matter

power spectrum (see e.g. Li, Hellwing, et al. 2013a) and for the scale-dependence of the halo bias (Parfrey, Hui, and Sheth 2011) were not included. Note that in these as well as in our work, a uniform prior on the logarithm of either the background scalaron field or its Compton wavelength at the present epoch is used in obtaining the main results. We show here that a different choice of prior (e.g. uniform on f_{R0}) can in practice have a non negligible effect on the constraints (see §3.5).

For the "designer" $f(R)$ model, using data from cluster number counts and a uniform prior on the Compton wavelength in Hubble units (B_0), Lombriser, Slosar, et al. (2012) placed an upper limit on this parameter that is equivalent to $|f_{R0}| < 2 \times 10^{-4}$. Unlike previous works, that paper used optically selected clusters from the Sloan Digital Sky Survey (SDSS) data (Koester et al. 2007). Moreover, the modifications of gravity were included in the Tinker, Kravtsov, et al. (2008) HMF (based on GR) through only the calculation of the variance of the linear matter density field. The authors justified this approach by arguing that the data were not sufficiently constraining to enter the regime $|f_{R0}| < 10^{-4}$, where such a HMF is known to no longer be accurate enough.

Secondary anisotropies of the CMB can also be used to measure modifications of gravity. The enhancement in the growth of structure due to $f(R)$ gravity has potentially observable effects on linear scales through the Integrated Sachs-Wolfe (ISW) effect and CMB lensing (Zhang 2006; Song, Peiris, and Hu 2007; Dossett, Hu, and Parkinson 2014). Recent measurements by the *Planck* satellite of the CMB lensing potential generated by large scale structures[1] together with CMB temperature and polarization data place a weak upper bound on $f(R)$ modifications, $|f_{R0}| < 10^{-3}$ (Raveri, Hu, et al. 2014). This additional power is included in our analysis, and for CMB data alone we find consistent results with previous works. Furthermore, combining CMB with cluster data helps break parameter degeneracies and tightens significantly the constraints on the normalization of the matter power spectrum, σ_8. This information is fully accounted for in our results through the multidimensional parameter covariance provided by our joint likelihood analysis.

This paper is organized as follows. In §3.2 we review the phenomenology of $f(R)$ gravity and briefly describe its popular models, Hu-Sawicki (Hu and Sawicki 2007) and designer (Song, Hu, and Sawicki 2007; Pogosian and Silvestri 2008). In §3.3 we discuss the halo mass function employed here. §3.4 contains a description of our cluster data sets, as well as of the other cosmological data sets with which we combine them. Finally, we present our results in §3.5 and conclude in §3.6.

[1] Note that these measurements are statistically independent of those from the temperature power spectrum in that the lensing potential power spectrum is a higher-order correlation function of the CMB temperature maps (see Lewis and Challinor 2006; Das et al. 2011; Engelen et al. 2012; Ade et al. 2014c for details).

3.2 $f(R)$ gravity

In this work we constrain modified gravity theories for which the Einstein-Hilbert action in the Jordan frame includes a general non-linear function of the Ricci scalar, such as

$$S_{EH} = \int \mathrm{d}^4x\sqrt{-g}\left[\frac{R + f(R)}{16\pi G}\right]. \tag{3.1}$$

Here and throughout, we set $c = 1$. GR with a cosmological constant Λ is recovered for $f = -2\Lambda$. This gravity model exhibits an additional attractive force mediated by a new scalar degree of freedom, the scalaron field $f_R \equiv \mathrm{d}f/\mathrm{d}R$. For viable $f(R)$ models (see e.g. Hu and Sawicki 2007; Pogosian and Silvestri 2008), its range is given by the physical Compton wavelength $\lambda_C = (3\,\mathrm{d}f_R/\mathrm{d}R)^{1/2}$. One of the effects of this fifth force is the enhancement of the abundance of massive dark matter halos, as described in §3.3. However, such modifications of gravity are suppressed by the non-linear chameleon effect in high density regions, where the depth of the gravitational potential wells is large compared to the background field, $|\Psi| > |f_R(\bar{R})|$. Note that, throughout the text, overbars denote background quantities.

Previous analytical and numerical works (Noller, Braun-Bates, and Ferreira 2014; Hojjati, Pogosian, Silvestri, et al. 2012; Oyaizu 2008) have shown that for $|f_{R0}| \ll 1$, time derivatives of the scalar field can be neglected compared to spatial derivatives, making the quasi-static approximation (QSA) a fairly accurate description of the modified dynamics on all scales. Relaxing this approximation yields effects of the order λ_C^2/H^{-2}, which could be significant for $|f_{R0}| \sim 1$ at large scales (Hojjati, Pogosian, Silvestri, et al. 2012). However, the ISW effect is the only known observable at (near)-horizon scales, and Hojjati, Pogosian, Silvestri, et al. (2012) showed that it is actually insensitive to large scale corrections associated with the evolution of the scalaron field. Note also that cluster scales are well within the horizon, and hence are not affected by the QSA approximation.

Since $f(R)$ gravity is conformally equivalent to a scalar-tensor theory with constant coupling to the matter fields, whereas electromagnetism is conformally invariant, the geodesics of photons are unchanged by this modification of gravity apart from a conformal rescaling of the gravitational constant by $1 + f_R$ (Bekenstein and Sanders 1994). In other words, given a fixed density field, e.g. a halo of mass M, the resulting lensing potential shows no deviation from that in GR as long as $|f_R| \ll 1$. This argument is particularly important for our observed mass function, since we currently employ a weak gravitational lensing analysis to calibrate our cluster masses. For the field values of interest here ($|f_R| \ll 1$), the assumption of GR in the lensing analysis is conveniently valid for our calculations.

Each $f(R)$ model produces its own evolution of λ_C (Ferraro, Schmidt, and Hu 2011), and the corresponding chameleon screening becomes active at a different redshift and degree of non-linearity, impacting accordingly the growth of structures (cf. He, Li, and Jing 2013; Li,

Hellwing, et al. 2013a; Appleby and Weller 2010). Here we consider two popular forms of $f(R)$, the Hu-Sawicki (HS) (Hu and Sawicki 2007) and "designer" models (Song, Hu, and Sawicki 2007; Pogosian and Silvestri 2008).

3.2.1 Hu-Sawicki model

The HS models have the following functional form

$$f(R) = -2\Lambda \frac{R^n}{R^n + \mu^{2n}}, \tag{3.2}$$

with Λ, μ^2 and n being free parameters. Note that since $R \to 0$ implies $f(R) \to 0$ this model does not strictly contain a cosmological constant. However, in the high-curvature regime, $R \gg \mu^2$, the function above can be approximated as

$$f(R) = -2\Lambda - \frac{f_{R0}}{n} \frac{\bar{R}_0^{n+1}}{R^n}. \tag{3.3}$$

$f_{R0} = -2n\Lambda\mu^{2n}/\bar{R}_0^{n+1}$, which replaces μ^2 as a free parameter of the model, and $\bar{R}_0 \equiv \bar{R}(z=0)$, so that $f_{R0} = f_R(\bar{R}_0)$. Notice that, for $|f_{R0}| \ll 1$, the curvature scales set by $\Lambda \sim \mathcal{O}(\bar{R}_0)$ and μ^2 are very different. This guarantees the validity of the $R \gg \mu^2$ approximation today and in the past.

For this model, deviations from a cosmological constant are of the order of f_{R0}. Consequently, in the limit $|f_{R0}| \ll 10^{-2}$, HS closely mimics the ΛCDM expansion history making these two models practically indistinguishable by geometric tests. However, f_{R0} also affects the formation of cosmic structures. If we fix the scaling index n, geometric probes can constrain Λ, whereas growth tests, such as cluster abundance, can constrain f_{R0}, which controls the strength and range of the force modification. For the HS model, the comoving Compton wavelength takes the form

$$\frac{\lambda_C}{1+z} = \sqrt{3(n+1)|f_{R0}| \frac{\bar{R}_0^{n+1}}{R^{n+2}}}, \tag{3.4}$$

and for a flat ΛCDM background its value today becomes

$$\lambda_{C0} \approx 29.9 \sqrt{\frac{|f_{R0}|}{10^{-4}} \frac{n+1}{4-3\Omega_m}}\ h^{-1}\mathrm{Mpc}, \tag{3.5}$$

where Ω_m denotes the mean density of matter today in units of the critical density. For larger values of n and a fixed f_{R0}, the Compton wavelength shrinks more rapidly when going from $z = 0$ to higher redshifts reducing the amount of time for the modified forces to act on

a given scale, and hence suppressing the enhanced growth compared to smaller n. For this reason, we expect that for larger n, larger f_{R0} will be allowed by the data.

3.2.2 Designer model

Another widely investigated class of $f(R)$ models are the designer models, for which the functional form results from imposing a specific expansion history (see e.g. Pogosian and Silvestri 2008). In this work we restrict ourselves to spatially flat ΛCDM backgrounds. This family of models is commonly parametrized by the dimensionless Compton wavelength squared in Hubble units

$$B_0 \equiv \frac{f_{RR}}{1+f_R} R' \frac{H}{H'}\Big|_{z=0} \approx 2.1\Omega_m^{-0.76}|f_{R0}|, \tag{3.6}$$

with $f_{RR} = \mathrm{d}f_R/\mathrm{d}R$ and $' \equiv \mathrm{d}/\mathrm{d}\ln a$.

Despite the fact that both this and the previous class of models reproduce either exactly or approximately the ΛCDM background, their respective scalaron fields follow different evolutions in time (see e.g. Ferraro, Schmidt, and Hu 2011; Lombriser 2014), and slightly dissimilar modifications of gravity are provided by the two cases. Therefore, one must be careful to compare only constraints from the same class (cf. Ferraro, Schmidt, and Hu 2011; Schmidt, Vikhlinin, and Hu 2009; Lombriser, Slosar, et al. 2012; Appleby and Weller 2010). For $f_{R0} \to 0$ and $B_0 \to 0$, both models reduce to ΛCDM, both in terms of expansion and growth.

3.3 Mass function

A self-consistent and accurate modeling of the mass function of dark matter halos in terms of the $f(R)$ parameters, f_{R0} and n or B_0, as well as the other cosmological parameters is crucial to obtain proper constraints on these parameters. The gold standard for predicting halo mass functions are N-body simulations, which provide the reference values to which semi-analytical predictions (Tinker, Kravtsov, et al. 2008; Sheth and Tormen 1999) are matched. A breakthrough occurred with the first consistent numerical simulations of $f(R)$ gravity (Oyaizu 2008), which have since been followed up with larger and much higher resolution simulations (Zhao, Li, and Koyama 2011; Li, Zhao, Teyssier, et al. 2012; Puchwein, Baldi, and Springel 2013). Unfortunately, these simulations are still very time consuming, and it is not feasible to sample the cosmological parameter space using full simulations. For this reason, it is crucial to resort to physically motivated semi-analytical approaches for the mass function predictions. Schmidt, Lima, et al. (2009) presented a simple approach based on both the spherical collapse approximation and the ST prescription, which they found to

provide a good match to the mass function *enhancement* in $f(R)$ gravity relative to ΛCDM. We will adopt this approach, described in more detail below, to set conservative constraints on $f(R)$ gravity.

The ST description for the comoving number density of halos per logarithmic interval of the virial mass M_v is given by

$$n_{\Delta_v} \equiv \frac{dn}{d\ln M_v} = \frac{\bar{\rho}_m}{M_v}\frac{d\ln\nu}{d\ln M_v}\nu f(\nu). \tag{3.7}$$

$\nu = \delta_c/\sigma(M_v)$ and δ_c are, respectively, the peak height and density thresholds, and

$$\nu f(\nu) = A\sqrt{\frac{2}{\pi}a\nu^2}\left[1+(a\nu^2)^{-p}\right]\exp\left[-a\nu^2/2\right]. \tag{3.8}$$

$\sigma(M)$ is the variance of the linear matter density field convolved with a top hat window function of radius r that encloses a mass $M = 4\pi r^3\bar{\rho}_m/3$ for a given mean background density $\bar{\rho}_m$,

$$\sigma^2(R,z) = \int \frac{d^3k}{(2\pi^3)}|\tilde{W}(kr)|^2 P_L(k,z), \tag{3.9}$$

where $P_L(k,z)$ is the linear power spectrum evolved to redshift z and $\tilde{W}(kr)$ is the Fourier transform of the window function. The normalisation constant is chosen such that $\int d\nu f(\nu) = 1$. For ΛCDM, values of the ST mass function parameters of $p = 0.3$, $a = 0.75$, and $\delta_c = 1.673$ (corresponding to $\Omega_m = 0.24$) have previously been shown to match simulations at the 10–20% level (Schmidt, Lima, et al. 2009). The virial mass is defined as the mass enclosed at the virial radius r_v, such that the average enclosed density is Δ_v times the critical density of the Universe, ρ_c. Equivalently, it is possible to use $\bar{\rho}_m$ rather than ρ_c as a reference value, with the corresponding transformation between both cases given by $\bar{\Delta}_v = \Delta_v/\Omega_m(z)$. The virial mass can then be mapped into any other overdensity Δ assuming a Navarro-Frenk-White (NFW) halo mass profile with virial concentration c_v and using the procedure outlined in Hu and Kravtsov 2003. As shown in Schmidt, Lima, et al. (2009); Lombriser, Koyama, Zhao, et al. (2012); Zhao, Li, and Koyama (2011), within r_v the profiles of dark matter halos in $f(R)$ do not present any significant deviation from those found in GR simulations, and therefore here we can neglect $f(R)$ effects in the mass rescaling. In addition, the exact value of the mass concentration has a negligible effect on our results as long as $c_{200} \gtrsim 3$. For this work we fix $c_{200} = 4$, as appropriate for the mass range of our data (see Mantz et al. 2015 for more details).

Our mass function calculation follows the approach adopted in Shandera, Mantz, et al. (2013). Deviations from GR are contained in a pre-factor given by the ratio of the ST mass

function in $f(R)$ to that in GR

$$n_\Delta = \left(\frac{n_\Delta^{f(R)}}{n_\Delta^{\rm GR}} \bigg|_{\rm ST} \right) n_\Delta|_{\rm Tinker}, \tag{3.10}$$

with

$$n_\Delta|_{\rm Tinker} = \frac{\bar{\rho}_m}{M} \frac{d\ln\sigma^{-1}}{d\ln M} f(\sigma, z), \tag{3.11}$$

and $f(\sigma, z)$ being the parametrization proposed and fitted to GR simulations by Tinker, Kravtsov, et al. (2008). The latter includes the explicit redshift dependence of the parameters and the covariance between them, as implemented in Mantz, Allen, Rapetti, and Ebeling (2010); Mantz et al. (2015), accounting for systematic uncertainties (such as the effects of baryons[2], non-universality, etc.). Also, as explained in Tinker, Kravtsov, et al. (2008), the evolution in redshift of the mass function parameters is increasingly relevant for large overdensities (smaller radii). To attenuate this effect, we choose to work at a relatively large radius by setting $\Delta = 300\Omega_m(z)$. In Eq. (3.10), both the linear variance, $\sigma(M)$, and the spherical collapse parameters are calculated using the corresponding theory of gravity, either GR or $f(R)$. For δ_c, we adopt the following fitting formula (Nakamura and Suto 1997)

$$\delta_c(\Omega_m, z) = \mathcal{A}\left(1 - \mathcal{B}\log_{10}\left[1 + \frac{\Omega_m^{-1} - 1}{(1+z)^3}\right]\right), \tag{3.12}$$

with $\mathcal{A} = 1.6865$ and $\mathcal{B} = 0.0123$ for GR, and $\mathcal{A} = 1.7063$ and $\mathcal{B} = 0.0136$ for $f(R)$. The latter values were calculated assuming a spherical perturbation smaller than the local Compton wavelength and forces enhanced by 4/3 everywhere and for all epochs, and therefore are independent of the particular choice of $f(R)$ model. Using N-body simulations, Schmidt, Lima, et al. (2009) showed that in the large-field regime ($|f_{R0}| \gtrsim 10^{-5}$) these values provide an underestimate of the effect on the mass function, and will thus yield conservative upper limits on $|f_{R0}|$.[3] In addition, in order to model the GR limit we set $n_{\rm ST}^{f(R)}/n_{\rm ST}^{\rm GR}$ to 1 whenever

[2]Using hydrodynamical simulations Arnold, Puchwein, and Springel (2014) showed that there is a bias between masses obtained using dynamical methods and those from lensing techniques, confirming the predictions of Schmidt (2010). As described in the main text, we account for this effect by calibrating our X-ray mass estimates with weak lensing data. In addition, the pre-factor in Eq. 3.10 could also be sensitive to the inclusion of baryonic physics into the calculation of the $f(R)$ HMF, for which only dark matter (DM) predictions currently exist. Puchwein, Baldi, and Springel (2013), however, estimated the impact of baryons on the matter power spectrum using hydrodynamical simulations. From their results one can show that, for scales $k \lesssim 10\,h/\mathrm{Mpc}$, $P^{f(R)}_{\rm DM+baryons}/P^{GR}_{\rm DM+baryons} \approx P^{f(R)}_{\rm DM}/P^{GR}_{\rm DM}$ demonstrating that the effects of baryons are similar for $f(R)$ and GR, and therefore negligible for their ratio (see also Hammami, Llinares, et al. 2015). The pre-factor of Eq. 3.10 should thus not be significantly affected by the presence of baryons.

[3]Even though this HMF was originally calibrated for the HS model with $n = 1$, Ferraro, Schmidt, and Hu (2011) showed that for the regimes of interest here, large-field (linear) and transition, this HMF can also be safely used for other values of n, and by extension for the designer model by correspondingly adjusting only the linear term $\sigma(M, z)$. The results on the matter power spectrum for the HS and designer models from He, Li, and Jing (2013) give also additional support to the latter conclusion.

this ratio becomes smaller than 1. Effectively, this approximation introduces a screening mechanism that is much more efficient than the one predicted by simulations, allowing larger values of f_{R0} to be consistent with the data. A less conservative approach would be to model the chameleon mechanism, which would change the predictions for the mass function when $|f_{R0}| \lesssim 10^{-5}$. Note, however, that entering this regime without properly validating the modeling of the chameleon suppression with simulations might result in spuriously tight constraints. We leave the accurate modeling of the mass function in this regime for future work (Cataneo et al., in preparation). This will then allow us to explore the rest of the parameter space currently available to clusters, and to cosmological data by extension. See also Lombriser, Koyama, and Li (2014); Li and Hu (2011) for recent approaches to modeling the chameleon mechanism.

Lastly, note that, to calculate $\Delta_v^{f(R)}$, we use the fitting formula valid for flat ΛCDM (Bryan and Norman 1998)

$$\Delta_v^{\mathrm{GR}}(\Omega_{mz}) = 18\pi^2 - 82(1-\Omega_{mz}) - 39(1-\Omega_{mz})^2, \tag{3.13}$$

with $\Omega_{mz} \equiv \Omega_m(z)$, and fix the ratio $\Delta_v^{f(R)}/\Delta_v^{\mathrm{GR}}$ to 74/94 (Schmidt, Lima, et al. 2009). We have checked that this scaling is a good approximation (better than 2 per cent) for a range of $0.1 < \Omega_m < 0.6$, which is much wider than the constraints on this quantity set by our cluster data alone (see Mantz et al. 2015), and for a redshift range of $0 < z < 0.7$, which extends beyond that of our cluster growth data.

3.4 Data

3.4.1 Cluster data

For the cluster growth analysis we employ the *ROSAT* Brightest Cluster Sample [BCS; $z < 0.3$ and $F_X(0.1\text{–}2.4\,\mathrm{keV}) > 5 \times 10^{-12}\ \mathrm{erg\,s^{-1}\,cm^{-2}}$] (Ebeling, Edge, Bohringer, et al. 1998), the *ROSAT*-ESO Flux Limited X-ray sample [REFLEX; $z < 0.3$ and $F_X(0.1\text{–}2.4\,\mathrm{keV}) > 3 \times 10^{-12}$ $\mathrm{erg\,s^{-1}\,cm^{-2}}$] (Boehringer et al. 2004), and the Bright sample of the Massive Cluster Survey [Bright MACS; $0.3 < z < 0.5$ and $F_X(0.1\text{–}2.4\,\mathrm{keV}) > 2 \times 10^{-12}\ \mathrm{erg\,s^{-1}\,cm^{-2}}$] (Ebeling, Edge, Mantz, et al. 2010). In order to reduce systematic uncertainties, a few detections later found to have their X-ray emission dominated by point sources (active galactic nuclei) rather than the intracluster medium have been removed, and higher flux limits have been applied to avoid incompleteness when selecting clusters from BCS (cf. Mantz, Allen, Rapetti, and Ebeling 2010; Mantz et al. 2015). Overall, the sample contains a total of 224 clusters. For 94 of these clusters X-ray luminosities and gas masses from *ROSAT* and/or *Chandra* data (see Mantz, Allen, Ebeling, et al. 2010 for details) were used to constrain cluster scaling relations and

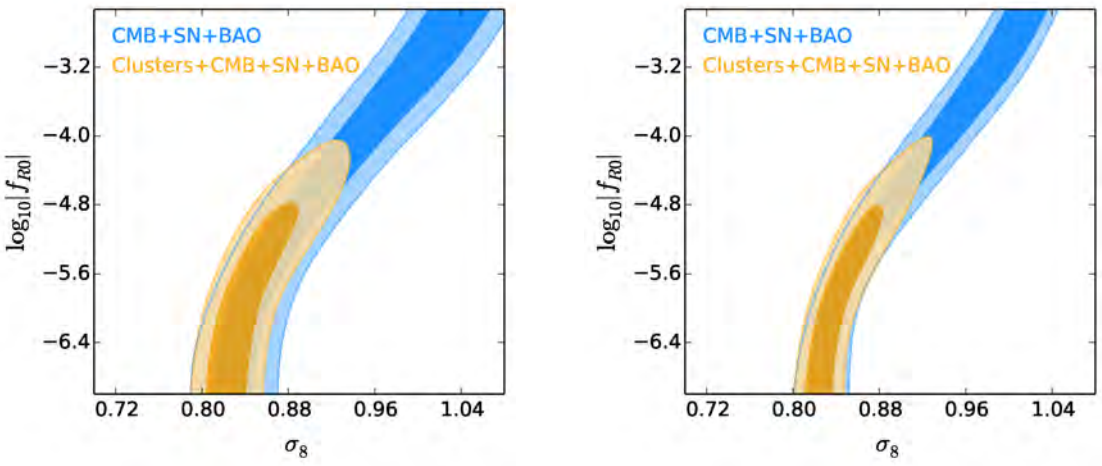

Fig. 3.1 Constraints on the HS model with $n = 1$. Dark and light shadings indicate the 68.3 and 95.4 per cent confidence regions (accounting for systematic uncertainties) from the following data sets: the CMB combined with SNIa+BAO (blue), and the combination of all these with clusters (gold). In the left panel, we use WMAP+ACT+SPT as CMB data, and *Planck*+WP+lensing+ACT+SPT in the right panel.

take full advantage of the mass information available for individual clusters (Mantz et al. 2015).

For the calculation of the absolute cluster mass scale we use state-of-the-art weak gravitational lensing measurements for 50 massive clusters (see Mantz et al. 2015; Linden et al. 2014b; Kelly et al. 2014; Applegate, Linden, et al. 2014 for details). As discussed above, since for the relevant field regime the lensing mass in $f(R)$ is the same as in GR up to currently undetectable effects of order f_{R0}, we do not need to apply any correction on the mass function due to the effect of the fifth force on the mass estimates (Schmidt 2010).

We also employ X-ray measurements of the gas mass fraction, $f_{\rm gas}$, in a shell of 0.8 to 1.2 times the radius corresponding to a critical overdensity $\Delta = 2500$ for a sample of the hottest, most X-ray luminous and dynamically relaxed galaxy clusters (Mantz et al. 2014). These data add constraining power on the background expansion model, and on Ω_m, which helps break the degeneracy of the normalisation of the matter power spectrum $\sigma_8 \equiv \sigma(r = 8h^{-1}\mathrm{Mpc}, z = 0)$ with this parameter. In this experiment, cluster masses are also calibrated using weak lensing data, in order to constrain instrumental (calibration) and astrophysical (bias due to the assumption of hydrostatic equilibrium) systematics.

As shown in Schmidt (2010), we could also employ our measurements of the ratio between lensing and X-ray mass estimates to constrain f_{R0}. In our current analysis, this signal would be completely degenerate with our instrumental and astrophysical uncertainties, and from our present estimates of these systematics, we would have little constraining power on f_{R0}. However, this is a promising new avenue for the near future.

3.4.2 CMB data

For the analyses including CMB data, we use measurements from either the *Wilkinson Microwave Anisotropy Probe* (WMAP 9-year release; Bennett et al. 2013; Hinshaw et al. 2013) or the *Planck* satellite (year-1 release plus WMAP polarization data, hereafter denoted as *Planck*+WP; Ade et al. 2014a). We also use data from the gravitational lensing potential generated by large scale structures, as measured by the *Planck* Collaboration (Ade et al. 2014c). We refer to the combination of these with *Planck*+WP power spectrum data as *Planck*+WP+lensing. Our two complete sets of CMB data also include high multipole measurements from the Acatama Cosmology Telescope (ACT; Das et al. 2014) and the South Pole Telescope (SPT; Keisler et al. 2011; Reichardt et al. 2012; Story et al. 2013).

When using CMB data, we also fit for the cosmic baryon and dark matter densities, $\Omega_b h^2$ and $\Omega_c h^2$; the optical depth to reionization, τ; the amplitude and spectral index of the scalar density perturbations, A_s and n_s; and the characteristic angular scale of the acoustic peaks, θ (which effectively determines H_0). We also marginalize over the set of nuisance parameters associated with each CMB data set, accounting for the thermal Sunyaev-Zel'dovich effect and unresolved foregrounds.

3.4.3 Additional data sets

Certain parameter degeneracies relevant at late times, like the one between f_{R0} and Ω_m, can be helped by including additional cosmological distance probes, such as those using SNIa and BAO data. We use the Union 2.1 compilation of SNIa (Suzuki et al. 2012), and BAO data from a combination of measurements from the 6-degree Field Galaxy Survey (6dF; $z = 0.106$; Beutler et al. 2011), the Sloan Digital Sky Survey (SDSS; $z = 0.35$ and $z = 0.57$; Padmanabhan, Xu, et al. 2012; Anderson et al. 2014b), and the WiggleZ Dark Energy Survey ($z = 0.44, 0.6$ and 0.73; Blake et al. 2011a). Note, however, that including these additional data sets affects our results only when we use WMAP+ACT+SPT as a CMB data set. In this case, we find that the addition of SNIa+BAO data helps in breaking the degeneracy with Ω_m and improves our constraints on f_{R0} or B_0. If instead of WMAP we use *Planck*+WP, the impact of adding SNIa+BAO data is negligible (see section 3.5).

3.5 Results

We obtain the posterior probability distribution functions (pdf) of our parameters using the MCMC engine COSMOMC[4] (Lewis and Bridle 2002) (October 2013 version), but modified to include two additional likelihood modules, one for $f_{\rm gas}$ data[5] and the other for cluster growth

[4] http://cosmologist.info/cosmomc/
[5] http://www.slac.stanford.edu/~amantz/work/fgas14/

data (Mantz et al. 2015). Hereafter we will refer both of them together as cluster data. To calculate the evolution of the cosmic mean background density and its linear perturbations we use MGCAMB[6] (Zhao, Pogosian, et al. 2009; Hojjati, Pogosian, and Zhao 2011), which is an extension of the Boltzmann code CAMB[7] (Lewis, Challinor, and Lasenby 2000) that includes modified gravity models. We have also implemented the HS model[8] into MGCAMB, and a few corresponding modifications to facilitate the calculations of secondary anisotropies of the CMB generated by the modified growth of structure.

Throughout our analysis, we assume the minimal value of the species-summed neutrino mass allowed by neutrino oscillation measurements in the normal hierarchy, $\sum m_\nu = 0.056$ eV, and the standard effective number of relativistic species, $N_{\rm eff} = 3.046$. Massive neutrinos suppress structure formation on scales smaller than the free streaming scale, and this effect can counteract the enhancement introduced by $f(R)$ modifications of gravity, allowing larger f_{R0} values currently excluded (Baldi, Villaescusa-Navarro, et al. 2014; Motohashi, Starobinsky, and Yokoyama 2013). In order to use cluster data to test $f(R)$ models while also allowing $\sum m_\nu$ and $N_{\rm eff}$ to be free parameters would require an accurate HMF validated by simulations that incorporates simultaneously both extensions of ΛCDM. Note, though, that the minimal neutrino mass adopted in the present work is too small to significantly alter our HMF.

For the present-day amplitudes of the scalaron field in each modified gravity model, we employ the following uniform priors: $\log_{10} B_0 \in [-10, 0.5]$ and $\log_{10} |f_{R0}| \in [-10, -2.523]$. Since from theory we have no information on the order of magnitude of the modification (see also Cortês, Liddle, and Parkinson 2015; Dossett, Hu, and Parkinson 2014), we use logarithmic priors, which weight all scales equally. Note, however, that GR ($B_0 = 0$ or $f_{R0} = 0$) is in practice unreachable in log space, and therefore the results for $\log_{10} B_0$ or $\log_{10} |f_{R0}|$ will be dependent on the lower bound of the prior. Using the combination *Planck*+WP+lensing+SNIa+BAO, for the "designer" model we have explicitly checked the dependence of the marginalized pdf on the lower bound of the log-prior for two different values, $[-10, 0.5]$ and $[-7, 0.5]$. The resulting upper limits on $\log_{10} B_0$ show a difference of about 10 per cent. We have also run MCMC chains with uniform priors on B_0 showing that, as expected, in these cases we obtain upper limits that are about an order of magnitude larger than those for the log-priors[9]. It is therefore important to fully state the priors used in the

[6] http://www.sfu.ca/~aha25/MGCAMB.html
[7] http://camb.info
[8] http://icosmology.info/HuSawicki.html
[9] Intuitively, this can be understood by applying a change of variable to convert the linear to the logarithmic pdf (or vice versa). Going from f_{R0} (B_0) to $\log_{10} |f_{R0}|$ ($\log_{10} B_0$) exponentially suppresses the probability for small parameter values due to the Jacobian of the transformation. If one uses directly a log-prior all scales will contribute to the pdf correspondingly lowering the upper limit. One can also directly convert the MCMC scalaron amplitude values from linear to log, accounting for the Jacobian of the transformation. The pdf obtained from the resulting chains will be approximately equivalent to that calculated from chains using a log-prior with a lower bound determined by matching the two pdfs. Note that this bound will be related to the tail of the linear run, which is characterized by the constraining power of the data.

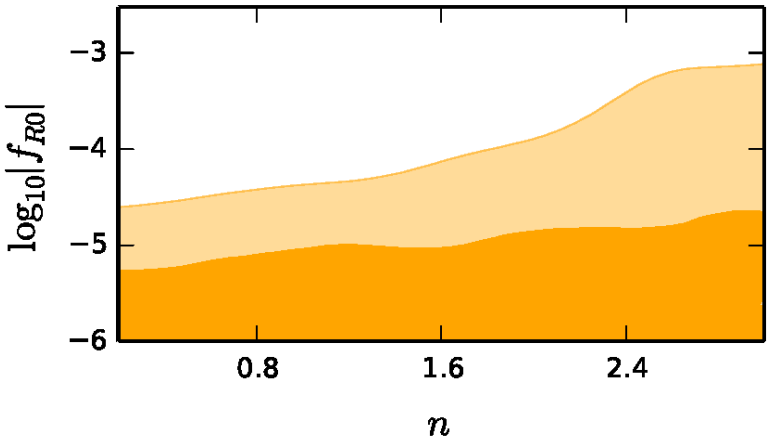

Fig. 3.2 Constraints on the HS model with varying n. Dark and light shadings indicate the 68.3 and 95.4 per cent confidence regions (accounting for systematic uncertainties) from the combination of clusters, CMB (*Planck*+WP+lensing+ACT+SPT) and SNIa+BAO.

analysis in order to allow others to properly compare results. For the HS model with $n = 1$, fig. 3.1 shows the joint constraints on f_{R0} and σ_8 from the CMB (blue contours; including also SNIa and BAO) and from these plus clusters (gold contours). For large values of f_{R0}, CMB data present a clear degeneracy between f_{R0} and σ_8. For $|f_{R0}| \lesssim 10^{-6}$ we recover as expected the same values of σ_8 as those obtained for GR. This is because in this regime the variance of the linear matter fluctuations on a scale of $8h^{-1}$Mpc becomes insensitive to the modifications of gravity.

Given the use of clusters and the CMB, the addition of SNIa and BAO data impacts on our results mainly by constraining Ω_m. When we use clusters plus *Planck*+WP+lensing+ACT+SPT, the impact of including SNIa+BAO data is negligible since the combined Ω_m constraints are essentially unchanged. However, for the combination of clusters with WMAP+ACT+SPT, the inclusion of SNIa+BAO data sets shifts the constraints on Ω_m to higher values providing similar results to those obtained from the combination with *Planck* data.

Cluster data provides strong measurements on the growth of structure at late times when the modifications of gravity are relevant. The main contribution of the CMB to the combined results is to tighten the constraints on matter power spectrum parameters such as A_s and Ω_m, which consequently allow clusters to break the degeneracy between f_{R0} and σ_8 by constraining the latter, and thus providing a tight upper limit on the scalaron amplitude. This is clear in figs. 3.1 and 3.3 by comparing the constraints without and with clusters (blue and gold contours, respectively). Using WMAP+ACT+SPT as the CMB data set, we obtain $\log_{10}|f_{R0}| < -4.73$, and using *Planck*+WP+lensing+ACT+SPT we have $\log_{10}|f_{R0}| < -4.79$ (see also Table 3.1). The CMB constraints on the left panel of fig. 3.1 correspond to WMAP+ACT+SPT data, and those on the right panel to *Planck*+WP+lensing+ACT+SPT

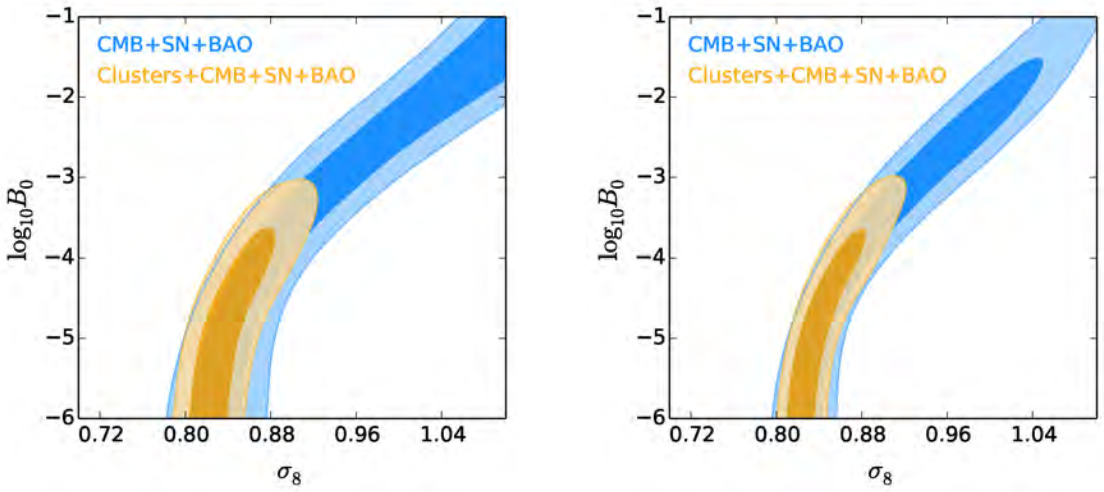

Fig. 3.3 Constraints on the designer model. Dark and light shadings indicate the 68.3 and 95.4 per cent confidence regions (accounting for systematic uncertainties) from the following data sets: clusters (purple), the CMB plus SNIa+BAO (blue), and the combination of all these (gold). In the left panel, we use WMAP+ACT+SPT as CMB data, and *Planck*+WP+lensing+ACT+SPT in the right panel.

data. The higher precision of the measurements from *Planck* improves the constraints on many of the non-gravity specific cosmological parameters and ultimately on σ_8, as shown by comparing these two panels. As pointed out in Dossett, Hu, and Parkinson (2014), without the lensing potential data, large f_{R0} values are preferred due to lower power in the low multipoles and higher lensing signal in the high multipoles of the *Planck* temperature power spectrum. The addition of the lensing potential data, which probes scales in the range $10^{-2} < k < 10^{-1}\,h/\mathrm{Mpc}$ at $z \sim 2$, disfavors large values of f_{R0}, while keeping the constraints on the other cosmological parameters essentially unchanged.

We have also run a more general analysis for the HS model including n as an additional free parameter with a uniform prior of $0.2 \leq n \leq 3$. As expected and shown in fig. 3.2, for increasing n the constraints on f_{R0} become weaker due to a growth of structure that is asymptotically closer to GR. Nonetheless, our results indicate a greater constraining power from the current data than the conservative projections in Ferraro, Schmidt, and Hu (2011).

For the designer model we find similar results. Fig. 3.3 shows that the combination of cluster and CMB data, either from WMAP+ACT+SPT (left panel) or from *Planck*+WP+lensing+ACT+SPT (right panel), constrains the background Compton wavelength to a few tens of megaparsecs ($\log_{10} B_0 < -3.75$ and $\log_{10} B_0 < -3.68$, respectively). As shown before (Dossett, Hu, and Parkinson 2014), we also find that adding the CMB lensing potential data to the combination of *Planck*+WP+ACT+SPT places a mild upper limit on B_0 (see e.g. the right panel of fig. 3.3). However, for the HS model the same data combination does not provide an upper limit on $|f_{R0}|$ at the value that one would expect from naively using eq. 6 to convert the

Table 3.1 Marginalized 95.4 per cent upper limits on $f(R)$ parameters for the two models discussed in the text, Hu-Sawicki (HS) and designer. We add the combination ACT+SPT+SNIa+BAO to all data sets below.

Data	HS model		Designer model
	$\log_{10}\lvert f_{R0}\rvert$	n	$\log_{10} B_0$
Clusters+WMAP	-4.73	1	-3.75
Clusters+*Planck*+WP+lensing	-4.79	1	-3.68
Clusters+*Planck*+WP+lensing	-3.95	$0.2 \leq n \leq 3$	

limit obtained on B_0 for the designer model. This is due to the different evolution of the Compton wavelength in the two models.

Table 3.1 summarizes the upper limits on f_{R0} and B_0[10] for the combinations of data sets used in this work, which are compatible with those obtained combining CMB and matter power spectrum measurements (Dossett, Hu, and Parkinson 2014; Hu, Raveri, et al. 2015). These limits are arguably the most robust to date using the abundance of galaxy clusters and unlike previous work (Schmidt, Vikhlinin, and Hu 2009; Lombriser, Slosar, et al. 2012) push the constraints into the transition regime where the most massive halos are screened.

3.6 Conclusions

We have performed a full, self-consistent joint MCMC likelihood analysis for two $f(R)$ models, Hu-Sawicki (HS) and "designer". These two models mimic either closely or exactly the expansion history of ΛCDM, but deviate with respect to its growth history. Our results are driven by the combination of galaxy cluster and CMB data, to which we also add other data sets. The abundance of massive galaxy clusters is a powerful cosmological probe of gravity on scales that are inaccessible to local and astrophysical tests of gravity, and its sensitivity derives from the steepness of the high mass tail of the halo mass function. The CMB data provide tight measurements on the matter power spectrum at high redshifts that together with those from the cluster data at low redshifts allow us to break key degeneracies and constrain $f(R)$ modifications on the growth rate at late times.

In the context of $f(R)$ gravity, departures from GR are sourced by an additional scalar degree of freedom responsible for an effective fifth force that enhances the growth of structures for scales smaller than its Compton wavelength. As a result, the abundance of massive

[10]Because their growth histories are similar, although not identical, note that the constraints on HS models with n=1 and designer models are comparable. An approximate conversion between f_{R0} and B_0 can be achieved using Eq. 3.6.

halos increases for amplitudes of the background scalar field $|f_{R0}| \gtrsim 10^{-6}$; below this value, the chameleon screening mechanism leads to a negligible modification of the abundance of massive clusters.

We use constraints on the expansion and growth histories from cluster abundance data, and on the expansion history from $f_{\rm gas}$ data. For the latter, it is interesting to note that a comparison between the dynamical masses derived from X-ray data and the weak lensing mass calibration (Schmidt 2010) could also be included in the $f(R)$ analysis to add constraining power in the large-field regime, and to possibly help breaking parameter degeneracies. In particular, while massive neutrinos can partially counteract the effects of $f(R)$ gravity on the abundance of galaxy clusters, these will not lead to a mismatch between their lensing and X-ray masses. This promising measurement is currently limited by instrumental and astrophysical uncertainties in the determination of our X-ray masses. In order to make this option viable, we will therefore need to reduce these systematic uncertainties by e.g. using new X-ray line emission data from the upcoming *Astro-H* mission to measure residual bulk motions. Additional lensing data will then ensure us sufficient constraining power on $f(R)$.

From the combination of cluster and CMB data, either from *Planck*+WP (or WMAP) plus ACT+SPT, and including also SNIa+BAO data, we obtain tight upper bounds $\log_{10}|f_{R0}| < -4.79$ (or -4.73) for the HS model (with $n = 1$) and $\log_{10}|B_0| < -3.68$ (or -3.75) for the designer model. Our results are obtained using high quality cluster growth data up to $z \sim 0.5$, a tight control of systematic uncertainties, a robust mass calibration from weak lensing data, and the full shape of the halo mass function for the mass range of our data. Including CMB data is essential to significantly tighten the constraints on cosmological parameters such as A_s and Ω_m, which then enables clusters to break a remaining key degeneracy between σ_8 and f_{R0} (B_0). SNIa and BAO data are only relevant when WMAP+ACT+SPT is used as a CMB data set. In this case, the addition of the SNIa+BAO data provides similar constraints on Ω_m, and consequently on f_{R0}, to those obtained with the combination that instead of WMAP has *Planck* data.

For the near future, further progress using current cluster data is within reach. Primarily, this will require an accurate modeling of the Chameleon screening mechanism in high density environments as a function of standard cosmological and model parameters, halo mass, and redshift. Testing the resulting theoretical prediction for the HMF against cosmological simulations for different cosmologies will be crucial to assess the accuracy of this result (Cataneo et al., in preparation).

A self-consistent implementation of the non-linear Chameleon suppression of $f(R)$ into our cluster likelihood analysis should reduce the current upper limits by about another order of magnitude, below which data limited to relatively low redshift massive galaxy clusters cannot distinguish between GR and $f(R)$ gravity.

Ongoing and planned surveys will also be able to improve further $f(R)$ constraints. The Dark Energy Survey (Abbott et al. 2005), Euclid (Laureijs et al. 2011) and the Large Synoptic Survey Telescope (Ivezic, Tyson, et al. 2008) in the optical, the eROSITA all-sky survey (Merloni et al. 2012) in the X-ray, and Sunyaev-Zel'dovich effect surveys (such those from *Planck* Ade et al. 2014e, the South Pole Telescope Bleem et al. 2015, and the Atacama Cosmology Telescope Hasselfield et al. 2013) in the mm/submm will substantially expand both the mass and redshift range of cluster samples, including identifying the most massive clusters up to $z \sim 2$. This will allow us to probe all the relevant evolution of the Compton wavelength and extend the measured mass function to masses where departures from GR are significant in the regime $|f_{R0}| \lesssim 10^{-6}$ due to the inefficiency of the chameleon screening mechanism.

Acknowledgments

MC thanks A. Agnello, N. C. Amorisco, M. Barnabè, C. Grillo and R. Wojtak for fruitful discussions on the effects of prior probability distributions. The computational analysis was performed using the High Performance Computing (HPC) facility at the University of Copenhagen, and the Gardar supercomputer of the Nordic HPC project. The Dark Cosmology Centre (DARK) is funded by the Danish National Research Foundation. ABM was supported by the National Science Foundation under grant AST-1140019.

Chapter 4

Halo mass function in $f(R)$ gravity

This chapter contains the following manuscript:

"Cluster abundance in chameleon $f(R)$ gravity I: toward an accurate halo mass function prediction"

Submitted to the *J. Cosmology Astropart. Phys.*; *arXiv* preprints: 1607.08788

Authors:

M. Cataneo, D. Rapetti, L. Lombriser, B. Li

We refine the mass and environment dependent spherical collapse model of chameleon $f(R)$ gravity by calibrating a phenomenological correction inspired by the parameterized post-Friedmann framework against high-resolution N-body simulations. We employ our method to predict the corresponding modified halo mass function, and provide fitting formulas to calculate the fractional enhancement of the $f(R)$ halo abundance with respect to that of General Relativity (GR) within a precision of $\lesssim 5\%$ from the results obtained in the simulations. Similar accuracy can be achieved for the full $f(R)$ mass function on the condition that the modeling of the reference GR abundance of halos is accurate at the percent level. We use our fits to forecast constraints on the additional scalar degree of freedom of the theory, finding that upper bounds competitive with current Solar System tests are within reach of cluster number count analyses from ongoing and upcoming surveys at much larger

scales. Importantly, the flexibility of our method allows also for this to be applied to other scalar-tensor theories characterized by a mass and environment dependent spherical collapse.

4.1 Introduction

The abundance of galaxy clusters depends on the growth rate of cosmic structures as well as on the expansion history of the universe. This makes it a powerful probe of cosmology as a function of redshift, and particularly suited to investigate the nature of dark energy and deviations from General Relativity (GR) (Albrecht et al. 2006; Rapetti, Allen, et al. 2010). Current and upcoming galaxy cluster surveys, such as the Dark Energy Survey (DES) (Abbott et al. 2005), the extended Roentgen Survey with an Imaging Telescope Array (eROSITA) (Merloni et al. 2012), the South Pole Telescope Third-Generation survey (SPT-3G) (Benson et al. 2014), the Large Synoptic Survey Telescope (LSST) (Abell et al. 2009) and *Euclid* (Laureijs et al. 2011), will detect an unprecedented number of these objects covering two orders of magnitude in mass ($M \sim 10^{13.5} - 10^{15.5}\, M_\odot/h$) for redshifts $z \lesssim 2$, with accurate calibration of the mass-observable relations down to a few percent. In order to take full advantage of this wealth of data, numerical and theoretical predictions of the mass distribution of virialized structures (also known as halo mass function) must reach a similar level of precision. Extensive effort has gone into modeling and calibrating this fully nonlinear observable in the standard cosmological constant plus Cold Dark Matter (ΛCDM) paradigm (e.g. Maggiore and Riotto 2010a; Maggiore and Riotto 2010b; Corasaniti and Achitouv 2011a; Corasaniti and Achitouv 2011b; Sheth and Tormen 1999; Jenkins, Frenk, et al. 2001; Tinker, Kravtsov, et al. 2008; Tinker, Robertson, et al. 2010; Crocce, Fosalba, et al. 2010; Manera, Sheth, and Scoccimarro 2010; Warren, Abazajian, et al. 2006; Reed, Smith, et al. 2013; Lukic, Heitmann, et al. 2007; Watson, Iliev, et al. 2013; Despali, Giocoli, et al. 2016; Bocquet, Saro, et al. 2016), and some work in this direction has been carried out for alternative dark energy models and gravity theories (e.g. Barreira, Li, et al. 2013a; Barreira, Li, Baugh, et al. 2013; Barreira, Li, et al. 2014; Bhattacharya, Heitmann, et al. 2011; Cui, Baldi, and Borgani 2012; Brax and Valageas 2012; Schmidt, Lima, et al. 2009; Li and Hu 2011; Lombriser, Li, et al. 2013; Lombriser, Koyama, and Li 2014; Kopp, Appleby, et al. 2013; Achitouv, Baldi, et al. 2016).

In this paper, we focus on the class of scalar-tensor theories known as $f(R)$ gravity (for reviews see e.g. Sotiriou and Faraoni 2010; De Felice and Tsujikawa 2010), where the standard Einstein-Hilbert action is replaced by a general nonlinear function of the Ricci scalar R. The function $f(R)$ can be adjusted to mimic the ΛCDM expansion history, which in turn limits deviations from the standard model only to the growth of structure on both linear and nonlinear scales due to the fifth force mediated by the new scalar degree of freedom, known as *scalaron* (Starobinsky 1980; Oyaizu 2008; Li, Zhao, Teyssier, et al. 2012; Llinares and

Mota 2013; Puchwein, Baldi, and Springel 2013; Pogosian and Silvestri 2008). Constraints from local experiments (Will 2006) are only consistent with functional forms that display the so-called *chameleon* screening mechanism (Khoury and Weltman 2004a). This ensures that force modifications are suppressed and GR is recovered for structures with deep potential wells, as the Solar System and the Galaxy (Hu and Sawicki 2007; Brax, Bruck, Davis, and Shaw 2008). However, the same coupling between the scalaron and the standard matter fields responsible for the chameleon mechanism may lead to catastrophic particle production in the early universe prior to Big Bang Nucleosynthesis (BBN), which can only be alleviated through fine tuning of the scalaron initial conditions (Erickcek, Barnaby, et al. 2013; Erickcek, Barnaby, et al. 2014). In addition, the scalaron amplitude has been strongly constrained on small scales and late times using unscreened local dwarf galaxies, with allowed values in the range $|f_{R0}| \lesssim 10^{-7}$ at 95.4% confidence level (Jain, Vikram, and Sakstein 2013; Vikram, Cabré, et al. 2013). It is also worth noting that this relatively recent technique would still greatly benefit from further investigation on various relevant astrophysical systematic uncertainties. All in all, these results further support the observation that $f(R)$ theories are unlikely candidates for a fundamental theory of gravity. Nevertheless, they can still be regarded as effective theories at low redshifts and on cosmological scales, with measurable deviations from GR predictions of the large scale structure.

The first studies designed to test $f(R)$ gravity with cluster number counts constrained the allowed region of parameter space to $|f_{R0}| \lesssim 10^{-4}$ at 95.4% confidence level (Schmidt, Vikhlinin, and Hu 2009; Lombriser, Slosar, et al. 2012). More recently, from the abundance of X-ray selected massive galaxy clusters and utilizing the conservative halo mass function (HMF) predictions of Schmidt, Lima, et al. (2009), Cataneo, Rapetti, et al. (2015) improved this upper bound by an order of magnitude. Upon accurate modeling of the nonlinear chameleon mechanism, and employing the same cluster abundance data, weak lensing mass calibration and cluster analysis (Mantz et al. 2015) this constraint could be further reduced by about a factor of two. An even more interesting prospect comes from including lower mass objects ($M \sim 10^{13.5}\, M_\odot/h$) at low redshift ($z \sim 0.1$) along with an improved mass calibration down to 5%, which could further strengthen the upper limit to $|f_{R0}| \lesssim 10^{-6}$. Thus, cluster count constraints have the potential to be competitive with those set by astrophysical and local tests of gravity but on much larger scales (Lombriser, Schmidt, et al. 2012; Joyce, Jain, et al. 2015).

To this end, we present a phenomenological modification of the spherical collapse model of Lombriser, Li, et al. (2013), which we calibrate against high-resolution N-body simulations to predict the relative abundance of halos in $f(R)$ gravity with respect to GR within a 5% precision (see Li and Hu 2011; Kopp, Appleby, et al. 2013; Achitouv, Baldi, et al. 2016 for alternative approaches; for recent applications of the theoretical mass function presented in Kopp, Appleby, et al. 2013; Achitouv, Baldi, et al. 2016 see Peirone, Raveri, et al. 2016;

Liu et al. 2016). This is the first in a series of two papers dedicated to accurately modeling, robustly analyzing and tightly constraining chameleon $f(R)$ gravity from the abundance of massive clusters. While here we develop an accurate model of the $f(R)$ mass function, observational constraints will be presented in the second paper of the series. In Sec. 4.2 we review the main aspects of $f(R)$ gravity including the chameleon screening. Sec. 4.3 summarizes the spherical collapse approach of Lombriser, Li, et al. (2013) and introduces our new parametrization to correct for residual inaccuracies in that model. The dark matter only cosmological simulations that we use to calibrate the new model are described in Sec. 4.4, and we present our halo mass function predictions in Sec. 4.5. We conclude in Sec. 4.6 with an outlook on possible extensions and applications of our results.

4.2 Chameleon $f(R)$ gravity

The $f(R)$ gravity model is a simple extension of GR, in which the Einstein-Hilbert action in the Jordan frame is generalized to include an arbitrary nonlinear function of the scalar curvature R,

$$S = \frac{1}{2\kappa^2}\int \mathrm{d}^4x\sqrt{-g}\,[R + f(R)] + S_\mathrm{m}\,[\psi_\mathrm{m}; g_{\mu\nu}]\,. \tag{4.1}$$

Here $\kappa^2 \equiv 8\pi G$, S_m is the action of the ordinary matter fields ψ_m, g is the determinant of the metric tensor $g_{\mu\nu}$, and throughout $c = \hbar = 1$. Obviously, GR with a cosmological constant is restored for $f = -2\Lambda$. In metric $f(R)$ gravity, the modified Einstein field equations can be derived by varying the action in Eq. (4.1) with respect to $g_{\mu\nu}$. In particular, in a matter dominated universe with a flat, spatially homogeneous and isotropic cosmological background, the Friedmann equation reads

$$H^2 + \frac{1}{6}f - \frac{\ddot{a}}{a}f_R + H\dot{f}_R = \frac{\kappa^2}{3}\bar{\rho}_\mathrm{m}, \tag{4.2}$$

and the Ricci scalar

$$\bar{R} = 6\left(\frac{\ddot{a}}{a} + H^2\right), \tag{4.3}$$

where overdots denote differentiation with respect to cosmic time, $a(t)$ is the scale factor, $H \equiv \dot{a}/a$ is the Hubble parameter and $\bar{\rho}_\mathrm{m}$ indicates the background density of matter. Overbars represent background quantities everywhere in the text. In Eq. (4.2) $f_R \equiv \mathrm{d}f/\mathrm{d}R$ is the new scalar degree of freedom of the theory, commonly known as scalaron. Following Pogosian and Silvestri (2008), Eqs. (4.2)-(4.3) can be combined to define the effective density

$$\rho_\mathrm{eff} \equiv \frac{1}{\kappa^2}\left[\frac{1}{2}(f_R R - f) - 3H^2 f_R - 3H\dot{f}_R\right], \tag{4.4}$$

which together with the continuity equation

$$\dot{\rho}_{\rm eff} + 3H\rho_{\rm eff}(1 + w_{\rm eff}) = 0 \tag{4.5}$$

gives the equation of state for the effective fluid

$$w_{\rm eff} \equiv \frac{P_{\rm eff}}{\rho_{\rm eff}} = -\frac{1}{3} - \frac{2}{3}\frac{H^2 f_R - H\dot{f}_R - \frac{1}{2}\ddot{f}_R - \frac{1}{6}f}{\frac{1}{6}f_R R - H^2 f_R - H\dot{f}_R - \frac{1}{6}f}. \tag{4.6}$$

Although our screening refinement method presented in Sec. 4.3.2 is applicable to any viable $f(R)$ or generalized chameleon model (Hu and Sawicki 2007; Pogosian and Silvestri 2008; Khoury and Weltman 2004b; Khoury and Weltman 2004a; Brax, Bruck, Davis, Khoury, et al. 2004; Brax, Davis, and Li 2012), in the rest of this work we shall use the popular Hu-Sawicki functional form (Hu and Sawicki 2007)

$$f(R) = -2\Lambda\frac{R^n}{R^n + \mu^{2n}}, \tag{4.7}$$

where $\Lambda > 0$, μ^2 and $n > 0$ are free parameters. Upon defining $f_{R0} \equiv -2n\Lambda\mu^{2n}/\bar{R}_0^{n+1}$ and $\bar{R}_0 \equiv \bar{R}(z = 0)$, in the high-curvature regime, $R \gg \mu^2$, Eq. (4.7) simplifies to

$$f(R) = -2\kappa^2\bar{\rho}_\Lambda - \frac{f_{R0}}{n}\frac{\bar{R}_0^{n+1}}{R^n}, \tag{4.8}$$

with $\Lambda = \kappa^2\bar{\rho}_\Lambda$. For $|f_{R0}| \ll 1$ this approximation is valid at all redshifts $z \geqslant 0$ owing to the very different curvature values set by $\Lambda \sim \mathcal{O}(\bar{R}_0)$ and μ^2. For this model, Hu and Sawicki (2007) showed that Eq. (4.6) presents $\mathcal{O}(|f_{R0}|)$ deviations from a cosmological constant. Considering that the abundance of galaxy clusters currently provides an upper bound of $|f_{R0}| \lesssim 10^{-5}$ (Cataneo, Rapetti, et al. 2015), and that upcoming improvements could potentially bring this down to $|f_{R0}| \sim 10^{-6}$, we restrict our predictions to the range $10^{-6} \leqslant |f_{R0}| \leqslant 10^{-4}$. In this regime the background evolution closely mimics ΛCDM, and we can safely adopt $w_{\rm eff} = -1$.

The trace of the modified Einstein field equations gives the Klein-Gordon equation for the scalaron

$$\Box f_R = \frac{\partial V_{\rm eff}}{\partial f_R}, \tag{4.9}$$

with the effective potential

$$\frac{\partial V_{\rm eff}}{\partial f_R} = \frac{1}{3}\left(R - f_R R + 2f - \kappa^2\rho_{\rm m}\right). \tag{4.10}$$

Interestingly, $V_{\rm eff}$ depends on the matter density $\rho_{\rm m}$, and for viable $f(R)$ models it presents a minimum at the GR expectation of $R = \kappa^2(\rho_{\rm m} + 4\bar{\rho}_\Lambda)$. Limiting our analysis to this class

of models, for which $|f_R| \ll 1$ at all redshifts and $|f/R| \ll 1$ in the early universe (Hu and Sawicki 2007; Pogosian and Silvestri 2008), in the quasi static approximation (Noller, Braun-Bates, and Ferreira 2014; Hojjati, Pogosian, Silvestri, et al. 2012; Oyaizu 2008) Eq. (4.9) reduces to the Poisson-type equation

$$\nabla^2 \delta f_R = \frac{a^2}{3}\left[\delta R(f_R) - \kappa^2 \delta\rho_{\rm m}\right], \tag{4.11}$$

where coordinates are comoving and fluctuations are obtained removing the background, i.e. $\delta f_R = f_R(R) - f_R(\bar{R})$, $\delta R = R - \bar{R}$, and $\delta\rho_{\rm m} = \rho_{\rm m} - \bar{\rho}_{\rm m}$. We also define the potential Ψ as the time-time metric perturbation $2\Psi \equiv \delta g_{00}/g_{00}$ in the longitudinal gauge. The evolution of Ψ is coupled to the matter density and curvature fluctuations through the modified Poisson equation

$$\nabla^2 \Psi = \frac{2\kappa^2}{3} a^2 \delta\rho_{\rm m} - \frac{a^2}{6}\delta R(f_R). \tag{4.12}$$

The system of Eqs. (4.11)-(4.12) controls the growth of structure, with modifications with respect to GR sourced by how differently curvature responds to matter due to the nonlinear term $\delta R(f_R)$. This effectively corresponds to an additional fifth force with a range given by the inverse mass of the scalaron, as we shall show in the next section.

4.2.1 Large- and small-field regimes

For viable $f(R)$ models, we can approximate the mass of the scalar field as

$$m_{f_R}^2 = \frac{\partial^2 V_{\rm eff}}{\partial f_R^2} \approx \frac{1}{3 f_{RR}} \equiv \left(\frac{2\pi}{\lambda_{\rm C}}\right)^2, \tag{4.13}$$

where we also introduce the Compton wavelength $\lambda_{\rm C}$. The latter defines how far the field can propagate from the source. To gain valuable insight into the solutions to Eqs. (4.11)-(4.12), we use a spherically symmetric top-hat overdensity embedded in the cosmological background with constant radius $r_{\rm th}$ and mass $M = 4\pi r_{\rm th}^3 \delta\rho_{\rm m}/3$. Following Hu and Sawicki (2007), we also define the effective mass

$$M_{\rm eff} \equiv 4\pi \int_0^{r_{\rm th}} (\delta\rho_{\rm m} - \delta R/\kappa^2) r^2 {\rm d}r, \tag{4.14}$$

where r denotes the physical distance from the center of the overdensity. By inspection of Eq. (4.11), $M_{\rm eff}$ can be interpreted as the mass sourcing the exterior scalar field fluctuations responsible for the fifth force.

For a given overdensity, two limiting cases bracket the family of interior solutions for the scalar field: (i) the low-curvature solution, for $\delta R \ll \kappa^2 \delta\rho_{\rm m}$; and (ii) the high-curvature solution, for $\delta R \approx \kappa^2 \delta\rho_{\rm m}$. A necessary condition for (ii) is that the density must change

on scales much longer than the local Compton wavelength implied by the high-curvature solution (Hu and Sawicki 2007). For our top-hat profile, this condition is always violated at the boundary with the cosmological background, consequently part of the exterior must be at low curvature. In addition, Birkhoff's theorem no longer applies (see e.g. Martino, Stabenau, and Sheth 2009) and the exterior low-curvature solution can enter the overdensity, even if the condition above is satisfied. The thickness of this region inside the overdensity depends upon the size of the overdensity itself, its density contrast and the amplitude of the cosmological scalar field. Therefore, the field does not always locally minimize the potential, rather it minimizes the total energy of the system which also includes the gradient kinetic energy associated with the field profile.

In terms of Eq. (4.14), if the entire overdensity is in the low-curvature regime, then $M_{\rm eff} \approx M$. The opposite is true if the high-curvature solution holds everywhere within the overdensity except close to the boundary, i.e. only a thin shell of mass $M_{\rm eff} \ll M$ contributes to the field gradients outside the overdensity. Applying Gauss's theorem to Eq. (4.11) and using the definition of Eq. (4.14), we can write an implicit solution for the field fluctuations at $r_{\rm th}$ (Hu and Sawicki 2007)

$$\delta f_R(r_{\rm th}) = \frac{2}{3}\frac{\kappa^2}{8\pi}\frac{M_{\rm eff}}{r_{\rm th}}. \tag{4.15}$$

Hence, the low-curvature solution provides the upper bound

$$\delta f_R(r_{\rm th}) \leqslant \frac{2}{3}|\Psi_{\rm N}|, \tag{4.16}$$

where $|\Psi_{\rm N}| = \kappa^2 M/8\pi r_{\rm th}$ defines the Newtonian potential at the surface of the sphere. This gives us a method to predict qualitatively the interior field profile for an isolated object and at a fixed background value. In fact, since $\delta f_R \lesssim |\bar{f}_R|$ we have that

$$\begin{aligned} |\bar{f}_R| \gg |\Psi_{\rm N}| &\implies \delta R \ll \kappa^2 \delta\rho_{\rm m}, \\ |\bar{f}_R| \ll |\Psi_{\rm N}| &\implies \delta R \approx \kappa^2 \delta\rho_{\rm m}, \end{aligned} \tag{4.17}$$

which we shall refer to as *large-field regime* and *small-field regime* respectively. The mechanism responsible for recovering the high-curvature solution in the small-field regime is called *chameleon screening* (Khoury and Weltman 2004a).

First, let us consider the case of a background scalar field $|\bar{f}_R| \gg |\Psi_{\rm N}| \sim 10^{-5}$, where $\Psi_{\rm N}$ now refers to the typical depth of the Newtonian potential for galaxy clusters, which are the objects that we are interested in here. In this scenario field fluctuations are relatively small and curvature fluctuations can be linearized as (Chiba, Smith, and Erickcek 2007)

$$\delta R \approx \left.\frac{\partial R}{\partial f_R}\right|_{\bar{R}} \delta f_R = 3\bar{m}^2_{f_R}\delta f_R. \tag{4.18}$$

The combination of Eq. (4.11) and Eq. (4.12), together with the approximation of Eq. (4.18), gives the following solution for the potential in Fourier space

$$k^2\Psi(\mathbf{k}) = -\frac{\kappa^2}{2}\left(1+\frac{1}{3}\frac{k^2}{k^2+\bar{m}_{f_R}^2 a^2}\right)a^2\delta\rho_{\rm m}(\mathbf{k}). \tag{4.19}$$

On scales $k \gg \bar{m}_{f_R}a$ gravitational forces exhibit 1/3 enhancements compared to GR. In this limit, the nature of the additional interaction becomes even clearer for a point-mass with density $\delta\rho_{\rm m}(r) = M\delta_D(r)/2\pi r^2$, where M is the mass, $\delta_D(r)$ denotes a Dirac delta function, and r is expressed in physical coordinates. This system is equivalent to that of a top-hat overdensity of constant radius $r_{\rm th}$, for distances $r > r_{\rm th}$. For this particular case, Eq. (4.19) in real space takes the form

$$\Psi(r) = -\frac{\kappa^2}{8\pi}\frac{M}{r} - \frac{\kappa^2}{24\pi}\frac{M}{r}e^{-\bar{m}_{f_R}(r-r_{\rm th})}, \tag{4.20}$$

where the first term is the standard Newtonian potential and the second term represents a Yukawa-like potential with range defined by the background scalaron mass (Hu and Sawicki 2007). Plugging Eq. (4.20) into Eq. (4.12), and using Eq. (4.18) gives the exterior solution for the scalar field

$$\delta f_R(r) = \frac{\kappa^2}{12\pi}\frac{M}{r}e^{-\bar{m}_{f_R}(r-r_{\rm th})} \quad \text{for } r > r_{\rm th}. \tag{4.21}$$

The interior solution for the field is obtained from Eq. (4.11) noticing that curvature fluctuations can be neglected inside the overdensity ($\delta R \ll \kappa^2\delta\rho_{\rm m}$). In addition, we require the interior and exterior solutions to match at $r = r_{\rm th}$, as well as $\mathrm{d}f_R/\mathrm{d}r = 0$ at $r = 0$ to avoid divergences. With these boundary conditions the solution to Eq. (4.11) is

$$\delta f_R(r) = \frac{\kappa^2}{8\pi}\frac{M}{r_{\rm th}}\left(1-\frac{1}{3}\frac{r^2}{r_{\rm th}^2}\right) \quad \text{for } r < r_{\rm th}. \tag{4.22}$$

Both Eq. (4.21) and Eq. (4.22) are the Jordan frame equivalent of Eqs. (29) and (30) in Khoury and Weltman (2004a).

In the small-field regime, $|\bar{f}_R| \ll |\Psi_{\rm N}| \sim 10^{-5}$, and the scalaron is close to the minimum of the effective potential everywhere inside the overdensity except for a negligible thin-shell at the boundary. This case is characterized by curvature perturbations approaching the GR limit $\delta R = \kappa^2\delta\rho_{\rm m}$, implying small field gradients, $|\nabla^2\delta f_R| \ll \kappa^2\delta\rho_{\rm m}$, that highly suppress force modifications. Hence, the interior solution for the scalar field will be

$$f_{R,\rm in} \approx f_R^{min} \equiv f_{R0}\left[\frac{\bar{R}_0}{\kappa^2(\rho_{\rm m}+4\bar{\rho}_\Lambda)}\right]^{n+1}, \tag{4.23}$$

which gives $|f_R| \ll |f_{R0}|$ for $\rho_\mathrm{m} \gg \bar{\rho}_\mathrm{m}$. Outside the overdensity the field moves towards the cosmological background with gradients negligible compared to the standard gravitational acceleration. In this regime, Eq. (4.12) simply becomes the usual Poisson equation, and Eq. (4.20) retains only the standard Newtonian contribution.

For $|\bar{f}_R| \sim |\Psi_\mathrm{N}| \sim 10^{-5}$, the exterior high-curvature solution can penetrate within the overdensity for a depth $\Delta r \lesssim r_\mathrm{th}$, effectively screening the interior and recovering GR at radii $r < r_\mathrm{th} - \Delta r$. In the next section, we shall estimate the thickness of this shell for our spherical top-hat overdensity with a method that includes the large- and small-field regimes as limiting cases, for $\Delta r \gtrsim r_\mathrm{th}$ and $\Delta r \ll r_\mathrm{th}$ respectively.

4.2.2 Intermediate regime

In this section we follow the treatment presented in Khoury and Weltman (2004a) for the estimation of the radial profile of a chameleon field ϕ in a compact object of radius r_th with constant matter density ρ_in embedded in a background of homogenous density ρ_out. Using the conformal equivalence between $f(R)$ gravity and scalar-tensor theories (see e.g. Pogosian and Silvestri 2008), Lombriser, Li, et al. (2013) derive the thinkness of the shell required for the transition between the exterior and the interior fields both minimizing the effective potential of Eq. (4.10). Denoting these two values $f_{R,\mathrm{out}}$ and $f_{R,\mathrm{in}}$ respectively, the extent of this region within the spherical top-hat overdensity is well approximated in the thin-shell regime $\Delta r/r_\mathrm{th} \ll 1$ by

$$\frac{\Delta r}{r_\mathrm{th}} \approx \frac{3}{\kappa^2 \rho_\mathrm{in}} \frac{f_{R,\mathrm{in}} - f_{R,\mathrm{out}}}{r_\mathrm{th}^2}, \tag{4.24}$$

where we also assumed $r_\mathrm{th} \ll \bar{\lambda}_\mathrm{C}$. For a flat ΛCDM background, the interior and exterior values of the scalar fields minimizing $V_\mathrm{eff}(f_R)$ are obtained directly from Eq. (4.23) as

$$f_{R,\mathrm{in/out}} \approx f_{R0} \left[\frac{1 + 4\frac{\Omega_\Lambda}{\Omega_\mathrm{m}}}{\tilde{\rho}_\mathrm{in/out} a^{-3} + 4\frac{\Omega_\Lambda}{\Omega_\mathrm{m}}} \right]^{n+1}, \tag{4.25}$$

where $\tilde{\rho}_\mathrm{in/out} \equiv \rho_\mathrm{m,in/out}(a=1)/\bar{\rho}_\mathrm{m}(a=1)$, Ω_m is the mean matter density today in units of the critical density $\bar{\rho}_\mathrm{cr}(a=1)$, and $\Omega_\Lambda = 1 - \Omega_\mathrm{m}$. Combining Eqs. (4.24) and (4.25) we obtain the thickness of the thin-shell in terms of the background cosmology and the physical properties of the overdensity

$$\frac{\Delta r}{r_\mathrm{th}} \approx \frac{|f_{R0}| a^3}{\Omega_\mathrm{m} \tilde{\rho}_\mathrm{in} (H_0 r_\mathrm{th})^2} \left[\left(\frac{1 + 4\frac{\Omega_\mathrm{m}}{\Omega_\Lambda}}{\tilde{\rho}_\mathrm{out} a^{-3} + 4\frac{\Omega_\mathrm{m}}{\Omega_\Lambda}} \right)^{n+1} - \left(\frac{1 + 4\frac{\Omega_\mathrm{m}}{\Omega_\Lambda}}{\tilde{\rho}_\mathrm{in} a^{-3} + 4\frac{\Omega_\mathrm{m}}{\Omega_\Lambda}} \right)^{n+1} \right], \tag{4.26}$$

where H_0 denotes the present-day Hubble constant. Throughout, we will also use the equivalent dimensionless quantity $h = H_0/100$ km/s/Mpc.

In the thin-shell limit, the approximate interior solution for the scalaron is

$$f_R(r) \approx \begin{cases} f_{R,\mathrm{in}} & r < r_0, \\ f_{R,\mathrm{in}} - \dfrac{\kappa^2}{9}\rho_{\mathrm{in}}\left(\dfrac{r^2}{2} + \dfrac{r_0^3}{r} - \dfrac{3}{2}r_0^2\right) & r_0 \le r \le r_{\mathrm{th}}, \end{cases} \tag{4.27}$$

with $r_0 = r_{\mathrm{th}} - \Delta r$. Therefore, the magnitude of the additional fifth force F for a unit mass at the surface of the overdensity is given by (Lombriser, Li, et al. 2013; Khoury and Weltman 2004a)

$$F = \frac{1}{2}\nabla f_R\big|_{r_{\mathrm{th}}} \approx \frac{1}{3}F_N\left[3\frac{\Delta r}{r_{\mathrm{th}}} - 3\left(\frac{\Delta r}{r_{\mathrm{th}}}\right)^2 + \left(\frac{\Delta r}{r_{\mathrm{th}}}\right)^3\right], \tag{4.28}$$

where $F_N = GM/r_{\mathrm{th}}^2$ is the Newtonian force. Although Eq. (4.28) is strictly valid only in the thin-shell limit, we extend it to include also the thick-shell regime, where $\Delta r/r_{\mathrm{th}} \gtrsim 1$ and $F = F_N/3$, by defining the ratio

$$\mathcal{F} \equiv \frac{F}{F_N} = \frac{1}{3}\min\left(3\frac{\Delta r}{r_{\mathrm{th}}} - 3\left(\frac{\Delta r}{r_{\mathrm{th}}}\right)^2 + \left(\frac{\Delta r}{r_{\mathrm{th}}}\right)^3, 1\right), \tag{4.29}$$

which provides an interpolation between the small-field regime $\mathcal{F} = 0$ and the large-field regime $\mathcal{F} = 1/3$.

Spherical collapse dynamics in $f(R)$ gravity is complicated by a breakdown of Birkhoff's theorem, inducing shell crossing where the low-curvature exterior solution enters the overdensity. In general, departures from GR lead to the dependence of structure formation on the environment, the halo substructure and the initial density profile (Martino, Stabenau, and Sheth 2009; Borisov, Jain, and Zhang 2012; Kopp, Appleby, et al. 2013; Li and Hu 2011; Li and Efstathiou 2012; Lombriser, Li, et al. 2013). Nevertheless, we adopt a simplified approach built on the assumption that the initial density profile also evolves as a spherical top-hat. In Secs. 4.3.1 and 4.3.2 we will explain our method to fully account for nonlinear structure formation in $f(R)$ gravity within the spherical top-hat scenario, which also corrects for the inaccuracy of Eq. (4.29) in the thick-shell regime.

4.3 Spherical collapse in chameleon $f(R)$ gravity

In Sec. 4.3.1 we first briefly summarize the spherical collapse model for $f(R)$ gravity presented in Li and Efstathiou (2012); Lam and Li (2012); Lombriser, Li, et al. (2013); Lombriser, Koyama, and Li (2014), and subsequently in Sec. 4.3.2 we implement a novel correction into this formalism to account for the departures between the calculations in this simplified picture and those in fully non-linear cosmological N-body simulations.

4.3.1 Mass and environment dependent spherical collapse

We adopt the spherical collapse model to describe halo formation in $f(R)$ gravity by approximating overdensities with spherically symmetric top hats that we evolve with the nonlinear continuity and Euler equations from an initial time to that of their collapse. The chameleon screening effect can be incorporated in the spherical collapse calculation following Li and Efstathiou (2012) (cf. Borisov, Jain, and Zhang 2012) by accounting for the mass and environment dependent gravitational force modification using the thin-shell thickness estimator of Khoury and Weltman (2004a) described in Sec. 4.2.2. Further developments on the chameleon spherical collapse model and its applications to $f(R)$ gravity, the halo mass function, and the halo model have been developed in Lam and Li (2012); Lombriser, Li, et al. (2013); Lombriser, Koyama, and Li (2014). A review of these applications and a comparison to different approaches in modeling the nonlinear structure of chameleon models can be found in Lombriser 2014.

We define the physical radius of the top-hat overdensity as $\zeta(a)$. At an initial scale factor $a_\mathrm{i} \ll 1$ this is given by $\zeta(a_\mathrm{i}) = a_\mathrm{i} r_\mathrm{th}$, but it deviates from this simple linear relation when $a > a_\mathrm{i}$ due to its nonlinear evolution. More specifically, the equation of motion of the spherical shell is given by (Schmidt, Lima, et al. 2009; Li and Efstathiou 2012; Lombriser, Li, et al. 2013)

$$\frac{\ddot{\zeta}}{\zeta} \simeq -\frac{\kappa^2}{6}\left(\bar{\rho}_\mathrm{m} - 2\bar{\rho}_\Lambda\right) - \frac{\kappa^2}{6}\left(1+\mathcal{F}\right)\delta\rho_\mathrm{m}\,, \tag{4.30}$$

where the gravitational force modification $\mathcal{F}$ is given in Eq. (4.29) and we replace $\Delta r/r_\mathrm{th} \to \Delta\zeta/\zeta$. We define the dimensionless variable $y \equiv \zeta(a)/(a r_\mathrm{th})$, and conservation of mass enclosed in the overdensity, $\bar{\rho}_\mathrm{m} a^3 r_\mathrm{th}^3 = \rho_\mathrm{m}\zeta^3$, yields $\tilde{\rho} = \rho_\mathrm{m}/\bar{\rho}_\mathrm{m} = y^{-3}$. The evolution equation for $y_\mathrm{h} = \tilde{\rho}_\mathrm{in}^{-1/3}$ follows from Eq. (4.30),

$$y_\mathrm{h}'' + \left[2 - \frac{3}{2}\Omega_\mathrm{m}(a)\right] y_\mathrm{h}' + \frac{1}{2}\Omega_\mathrm{m}(a)\left(1+\mathcal{F}\right)\left(y_\mathrm{h}^{-3} - 1\right) y_\mathrm{h} = 0\,, \tag{4.31}$$

where the force enhancement is given by Eqs. (4.29) with

$$\frac{\Delta\zeta}{\zeta} \approx \frac{|f_{R0}|a^{4+3n}}{\Omega_\mathrm{m}(H_0 r_\mathrm{th})^2} y_\mathrm{h}\left[\left(\frac{1+4\frac{\Omega_\Lambda}{\Omega_\mathrm{m}}}{y_\mathrm{env}^{-3}+4\frac{\Omega_\Lambda}{\Omega_\mathrm{m}}a^3}\right)^{n+1} - \left(\frac{1+4\frac{\Omega_\Lambda}{\Omega_\mathrm{m}}}{y_\mathrm{h}^{-3}+4\frac{\Omega_\Lambda}{\Omega_\mathrm{m}}a^3}\right)^{n+1}\right]. \tag{4.32}$$

The environment $y_\mathrm{env} = \tilde{\rho}_\mathrm{out}^{-1/3}$ is assumed to evolve according to ΛCDM with

$$y_\mathrm{env}'' + \left[2 - \frac{3}{2}\Omega_\mathrm{m}(a)\right] y_\mathrm{env}' + \frac{1}{2}\Omega_\mathrm{m}(a)\left(y_\mathrm{env}^{-3} - 1\right) y_\mathrm{env} = 0\,, \tag{4.33}$$

which follows from Eq. (4.30) in the limit $\Delta\zeta/\zeta \to 0$, or equivalently $\mathcal{F} \to 0$. We solve the system of differential equations (4.31) and (4.33) with the initial conditions set in the

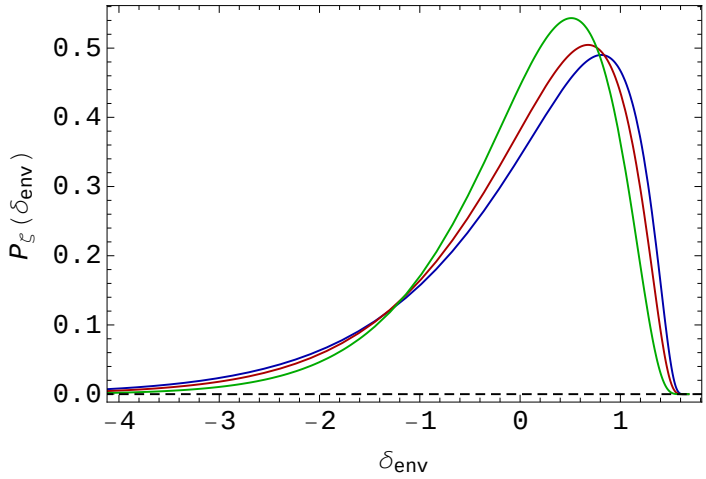

Fig. 4.1 Probability distributions of the Eulerian environment from Eq. 4.36 at three different redshifts, $z = 0$ (blue), $z = 0.2$ (red) and $z = 0.5$ (green). In our spherical collapse calculations, at a given collapsing redshift we select the environmental density at the peak of the corresponding distribution.

matter-dominated regime,

$$y_{\rm h/env,i} = 1 - \frac{\delta_{\rm h/env,i}}{3}\,, \qquad y'_{\rm h/env,i} = -\frac{\delta_{\rm h/env,i}}{3}\,, \tag{4.34}$$

for an initial scale factor $a_{\rm i} \ll 1$. We define the effective linear overdensity

$$\delta_{\rm h/env}(\mathbf{x};\zeta_{\rm h/env}) \equiv \frac{D(a)}{D(a_{\rm i})}\delta_{\rm h/env,i}\,, \tag{4.35}$$

which is extrapolated from the initial overdensity to late times using the linear growth function of ΛCDM, $D(a)$. In particular, we use Eq. (4.35) to define the linear collapse and environmental densities, $\delta_{\rm c}^{f(R)}$ and $\delta_{\rm env}$, respectively. In practice, we evolve Eq. (4.31) from $\delta_{\rm h,i}$ to the scale factor where it produces a singularity, to which we then use Eq. (4.35) to linearly extrapolate $\delta_{\rm h/env,i}$ and define $\delta_{\rm c}^{f(R)}$ and $\delta_{\rm env}$. This effective approach evades complications from the scale-dependent growth in $f(R)$ gravity.

As can be seen from Eq. (4.32), the spherical collapse density, and therefore structure formation in chameleon $f(R)$ gravity, is dependent on both the mass of the halo formed, through $r_{\rm th}$, and its environmental density $\delta_{\rm env}$ or $\delta_{\rm env,i}$. To correctly reproduce the abundance of halos for a given mass measured in N-body simulations and to perform consistent tests of chameleon $f(R)$ gravity against observations, we determine the halo mass function averaged over the different environments. Following Li and Lam (2012); Lombriser, Li, et al. (2013); Lombriser, Koyama, and Li (2014), we define the size of the environment as an Eulerian (physical) radius of $\zeta = 5h^{-1}$ Mpc and approximate the probability distribution of an Eulerian

environmental density $\delta_{\rm env}$ as (Lam and Sheth 2008; Lam and Li 2012)

$$P_\zeta(\delta_{\rm env}) = \frac{\beta^{\varpi/2}}{\sqrt{2\pi}}\left[1+(\varpi-1)\frac{\delta_{\rm env}}{\delta_{\rm c}^\Lambda}\right]\left(1-\frac{\delta_{\rm env}}{\delta_{\rm c}^\Lambda}\right)^{-\varpi/2-1}\exp\left[-\frac{\beta^\varpi}{2}\frac{\delta_{\rm env}^2}{(1-\delta_{\rm env}/\delta_{\rm c}^\Lambda)^\varpi}\right], \quad (4.36)$$

where $\beta = (\zeta/8)^{3/\delta_{\rm c}^\Lambda}/\sigma_8^{2/\varpi}$ with σ_8 being the present-day linear r.m.s. density perturbation in spheres with radius $8h^{-1}$Mpc, $\delta_{\rm c}^\Lambda$ is the linearly extrapolated ΛCDM spherical collapse threshold, and $\varpi = \delta_{\rm c}^\Lambda\gamma$ with

$$\gamma = -\frac{{\rm d}\ln S_\xi}{{\rm d}\ln M_{\rm env}} = \frac{\tilde{n}_{\rm s}+3}{3}. \quad (4.37)$$

We use the Lagrangian (or initial comoving) radius $\xi = 8h^{-1}$ Mpc with $S_\xi = \sigma_8^2$, $\tilde{n}_{\rm s}$ is the slope of the matter power spectrum on large scales at $a_{\rm i} \ll 1$ in the matter era after turn over, and we assume that the environment evolves according to ΛCDM.

The distribution $P_\zeta(\delta_{\rm env})$ is shown in Fig. 4.1 for three different redshifts. We will use the peak of the environmental distribution at a given redshift to approximate the environmentally averaged linear collapse density $\langle\delta_{\rm c}\rangle_{\rm env}$ and with that the observed average halo mass function. More detailed discussions on alternative averaging procedures, comparisons between them, and further details on the role of the environment in chameleon modifications can be found in Li and Lam (2012); Lam and Li (2012); Lombriser, Li, et al. (2013); Lombriser, Koyama, and Li (2014).

4.3.2 Chameleon screening refinement

In Lombriser, Li, et al. (2013); Lombriser, Koyama, and Li (2014); Lombriser (2014) it was shown that at $z = 0$ the spherical collapse model extended to incorporate a dependence on the environment gives a good description of the number density of virialized objects as a function of mass, i.e. of the halo mass function. However, for our purposes this approach is too simplistic, in that as described below it cannot capture in full detail the complex nonlinear dynamics of structure formation in $f(R)$ gravity.

Due to the breakdown of Birkhoff's theorem spherical top-hat overdensities cannot be treated as close FRW universes, since their evolution also depends on the external matter distribution. Because of this, an initially homogeneous spherical overdensity will evolve a profile resulting from the Yukawa-like fifth force in regions where the chameleon mechanism is not in action (Kopp, Appleby, et al. 2013; Borisov, Jain, and Zhang 2012). A possible solution to this problem consists in evolving the full set of field equations for an average initial density profile (Kopp, Appleby, et al. 2013).

On the other hand, the fact that dark matter halos possess higher-density internal substructures increases the chameleon efficiency in suppressing modifications of gravity (Li

and Hu 2011). Moreover, departures from the spherical collapse approximation in $f(R)$ gravity might also impact the growth of nonlinear structures to a greater extent than in GR. In fact, as it was first noticed in Jones-Smith and Ferrer (2012) and further investigated in Burrage, Copeland, and Stevenson (2015), the shape of extended objects affects the chameleon screening reducing its effectiveness with increasing ellipticity. This also introduces "chameleonic" torques that might have a measurable impact on the halo mass accretion history. In addition, Pourhasan, Afshordi, et al. (2011) found that back-reaction effects can boost the chameleon efficiency in minor mergers depending on the mass of the infalling halo.

The complexity of the various physical processes involved, the extent of their individual contributions, as well as their interplay, make this problem amenable to semi-analytical modeling. In this work we opt for a correction of the spherical collapse predictions presented in Sec. 4.3.1 that is inspired by the phenomenological parameterized post-Friedmann (PPF) approach employed in Li and Hu (2011). Here, instead of applying this prescription to the variance of the linear density field while fixing the spherical collapse threshold to the ΛCDM value, we incorporate the PPF modifications through an effective collapse threshold $\delta_{\rm c}^{\rm eff}$, and use the same ΛCDM mass variance $\sigma(M)$ both for GR and $f(R)$ gravity. More specifically, for each background cosmology and collapse redshift $z_{\rm c}$ we define

$$\delta_{\rm c}^{\rm eff}(M, z_{\rm c}) \equiv \epsilon(M, z_{\rm c}|M_{\rm th}^{(1)}, M_{\rm th}^{(2)}, \eta, \vartheta, \chi) \times \delta_{\rm c}^{f(R)}(M, z_{\rm c}, \delta_{\rm env}^{\rm peak}), \tag{4.38}$$

where $\delta_{\rm c}^{f(R)}$ is evaluated following the method outlined in Sec. 4.3.1 at the environmental density where the distribution in Eq. (4.36) peaks, $\delta_{\rm env}^{\rm peak}$. The correction factor is given by

$$\epsilon(M, z_{\rm c}|M_{\rm th}^{(1)}, M_{\rm th}^{(2)}, \eta, \vartheta, \chi) = \frac{1 + (M/M_{\rm th}^{(1)})^{\eta}(\delta_{\rm c}^{\Lambda}/\delta_{\rm c}^{f(R)})^{\chi} + (M/M_{\rm th}^{(2)})^{\vartheta}(\delta_{\rm c}^{f(R)}/\delta_{\rm c}^{\Lambda})}{1 + (M/M_{\rm th}^{(1)})^{\eta} + (M/M_{\rm th}^{(2)})^{\vartheta}}. \tag{4.39}$$

The quantities $M_{\rm th}^{(1)}$, $M_{\rm th}^{(2)}$, η, ϑ and χ are free parameters that we will obtain by fitting our halo mass function model to the halo abundance measured from high-resolution cosmological simulations (see Secs. 4.4 and 4.5). Before this, however, we can simplify the derivation of these parameters on the basis of theoretical and heuristic considerations. Similarly to Li and Hu (2011), we consider $M_{\rm th}^{(1)}$ and $M_{\rm th}^{(2)}$ threshold masses controlling the transition between the $\delta_{\rm c}^{f(R)}$ and $\delta_{\rm c}^{\Lambda}$. As noted in Lombriser (2014), in the original PPF approach (Li and Hu 2011) one can derive the scaling $M_{\rm th} \sim |f_{R0}|^{3/2}$ from Eq. (4.32). Here, we apply this result to our threshold masses, and also include the dependence on $\Omega_{\rm m}$ and n. By interpreting $M_{\rm th}$ as the mass of an isolated halo with an interior scalaron profile approaching the minimum of the effective potential at its center, Eq. (4.32) implies

$$\frac{\Delta\zeta}{\zeta} = 1 \sim \frac{|f_{R0}|}{\Omega_{\rm m} M_{\rm th}^{2/3} \Delta_{\rm vir}^{1/3} (1 + z_{\rm c})^{4+3n}} \left(\frac{1 + 4\frac{\Omega_\Lambda}{\Omega_{\rm m}}}{1 + 4\frac{\Omega_\Lambda}{\Omega_{\rm m}}(1 + z_{\rm c})^{-3}} \right)^{n+1}, \tag{4.40}$$

where we have used $\tilde{\rho}_{\rm in}(z_{\rm c}) \approx \Delta_{\rm vir}(\Omega_{\rm m}, z_{\rm c}) \gg 1$ and $\tilde{\rho}_{\rm out} = 1$, with $\Delta_{\rm vir}$ denoting the virial overdensity in GR as a function of cosmology and collapse redshift. Assuming that we know the threshold mass $\tilde{M}_{\rm th}(\tilde{z}_{\rm c})$ for some particular set of parameters $\{\tilde{\Omega}_{\rm m}, \tilde{f}_{R0}, \tilde{n}\}$ and redshift $\tilde{z}_{\rm c}$, we can then employ Eq. (4.40) to map this mass to any other combination of parameters as

$$\begin{aligned} M_{\rm th} = \quad & \tilde{M}_{\rm th} \quad \left(\frac{|f_{R0}|}{|\tilde{f}_{R0}|}\right)^{3/2} \left(\frac{\tilde{\Omega}_{\rm m}}{\Omega_{\rm m}}\right)^{3/2} \left(\frac{\tilde{\Delta}_{\rm vir}}{\Delta_{\rm vir}}\right)^{1/2} (1+\tilde{z}_{\rm c})^{-\frac{9}{2}(n-\tilde{n})} \\ & \times \quad \frac{\left[1+4\frac{\tilde{\Omega}_\Lambda}{\tilde{\Omega}_{\rm m}}(1+\tilde{z}_{\rm c})^{-3}\right]^{\frac{3}{2}(\tilde{n}+1)}}{\left[1+4\frac{\Omega_\Lambda}{\Omega_{\rm m}}(1+\tilde{z}_{\rm c})^{-3}\right]^{\frac{3}{2}(n+1)}} \frac{\left[1+4\frac{\Omega_\Lambda}{\Omega_{\rm m}}\right]^{\frac{3}{2}(n+1)}}{\left[1+4\frac{\tilde{\Omega}_\Lambda}{\tilde{\Omega}}\right]^{\frac{3}{2}(\tilde{n}+1)}}. \end{aligned} \tag{4.41}$$

Note that Eq. (4.41) simply reduces to $M_{\rm th} \sim |f_{R0}|^{3/2}$ for $\Omega_{\rm m} = \tilde{\Omega}_{\rm m}$ and $n = \tilde{n}$. In this work we use $\tilde{\Omega}_{\rm m} = 0.281$, $|\tilde{f}_{R0}| = 10^{-5}$ and $\tilde{n} = 1$.

We do not impose any sign on η, ϑ, and only require $M_{\rm th}^{(1)}, M_{\rm th}^{(2)} > 0$. Although we expect relatively small corrections to the spherical collapse solution, the domain over which the free parameters can change allows for rather generic deviations. The remaining parameter χ controls how rapidly $\delta_{\rm c}^{\rm eff}$ approaches the ΛCDM threshold at high masses. This depends somewhat on the background scalaron field, and we found that the empirical relation

$$\chi = \frac{1}{2} - \frac{1}{5}\log_{10}\left(\frac{|f_{R0}|}{|\tilde{f}_{R0}|}\right) \tag{4.42}$$

works well for our suites of simulations.

In Fig. 4.2 we compare the spherical collapse predictions of Sec. 4.3.1 (blue lines) with the effective thresholds (red lines) from Eq. (4.38) that we calibrate using the suite A of high-resolution simulations listed in Table 4.1. As we explain in detail in Sec. 4.5, we incorporate Eq. (4.38) into the mass function model that we then fit to the halo abundances obtained from these simulations. For illustrative purposes, the effective thresholds shown in Fig. 4.2 correspond to those for the resulting best-fit values of the parameters in Eq. (4.38). Despite the visible differences, the corrected, effective thresholds remain within a few percent from the original spherical collapse thresholds, which justifies our approach of introducing higher-order corrections. In principle, these effective quantities could be seen as averaged solutions to Eqs. (4.32)-(4.33) over a suitable, yet unknown, environmental density distribution different from that of Eq. (4.36). Here, however, we refrain from giving any profound physical interpretation to such deviations, and remark that they can also be partly attributed to the difference between the virial overdensity $\Delta_{\rm vir}$ (dependent on redshift, mass and cosmology) and the fixed overdensity at which we define dark matter halos in our study (see Sec. 4.5) (Schmidt, Lima, et al. 2009; Despali, Giocoli, et al. 2016). Nevertheless, they hint to the possibility

that the initial density profile, and the geometry and substructure of dark matter halos might leave a mass-dependent imprint on the averaged mass function unaccounted for in the spherical collapse treatment of Lombriser, Li, et al. (2013).

4.4 Simulations

The simulations used to calibrate the theoretical HMFs in this work were run with the ECOSMOG code (Li, Zhao, Teyssier, et al. 2012), which is an extension to the publicly available RAMSES N-body and hydro code (Teyssier 2002) for cosmological simulations in modified gravity theories. The code employs the particle-mesh technique with adaptive mesh refinement to compute the (modified) gravitational force. In short, it starts with what it is called a domain grid which is a regular mesh with $N_{\rm cell}^3 = 1024^3$ cells covering the cubic simulation box of size $L_{\rm box}$ (expressed in units of h^{-1}Mpc). A number of N_p^3 particles are evolved on this mesh from an initial redshift $z_{\rm ini}$. The density field on the mesh is obtained by a cloud-in-cell (CIC) or triangular-shaped cloud (TSC) interpolation to its cells; this is then used to compute the gravitational forces at the cell centres, which are next used to move the particles. To achieve higher force resolution in high-density regions, the code adaptively refines a cell if the effective particle number inside it exceeds some pre-defined criterion $N_{\rm ref}$ – this has proved to be critical to ensure accuracy when solving the modified gravity force, which has a smaller amplitude in these regions due to the chameleon screening. The code is efficiently parallelized using MPI, with domain decomposition achieved through a standard Peano-Hilbert space-filling curve. For more details on the ECOSMOG code please refer to the original code paper for $f(R)$ gravity (Li, Zhao, Teyssier, et al. 2012) and its subsequent extensions to other models (Brax, Davis, et al. 2012; Brax, Davis, et al. 2013; Li, Zhao, and Koyama 2013; Barreira, Li, et al. 2013b; Li, Barreira, et al. 2013).

Two suites of simulations are used in this work. Suite A was run using a flat cosmology with WMAP 9-year best-fit parameters

$$(\Omega_{\rm m}, \Omega_\Lambda, h, n_s, \sigma_8) = (0.281, 0.719, 0.697, 0.971, 0.82)\,, \tag{4.43}$$

where n_s is the scalar spectral index of the primordial power spectrum. We also use suite B (see details in Li, Hellwing, et al. 2013b) with older, WMAP 3-year best-fit parameters

$$(\Omega_{\rm m}, \Omega_\Lambda, h, n_s, \sigma_8) = (0.240, 0.760, 0.730, 0.958, 0.80)\,. \tag{4.44}$$

As described in Sec. 4.5, we use suite A for the actual calibration of the theoretical HMF, and then compare this with simulation results from suite B to test how our fit works for this other cosmology.

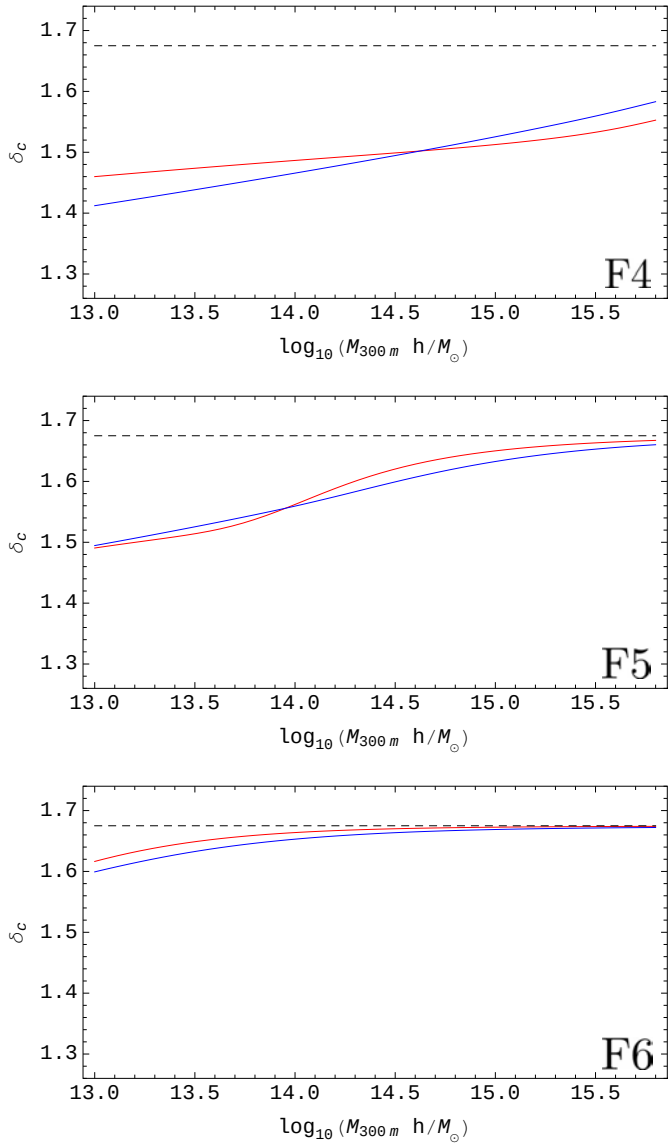

Fig. 4.2 Spherical collapse density thresholds δ_c at $z = 0$ and $\Omega_m = 0.281$ for $|f_{R0}| = 10^{-4}, 10^{-5}, 10^{-6}$ (F4, F5, F6 from top to bottom). In all panels, blue curves are obtained with the method described in Sec. 4.3.1, and red curves correspond to the effective spherical collapse thresholds obtained after we correct them with Eq. (4.39) calibrated with the high-resolution simulations of suite A in Table 4.1. Dashed lines mark the ΛCDM threshold. To avoid confusing notation, we define masses at an overdensity $\Delta = 300$ with respect to the background matter density for both δ_c and $\delta_c^{\rm eff}$. In reality, spherical collapse calculations are only meaningful for $\Delta = \Delta_{\rm vir}$.

Table 4.1 Specifications of the N-body simulations used in this work. $N_{\rm ref}$ – the refinement criterion used in these simulations – is 8.0 for suite A and 9.0 for suite B, and m_p is the simulation particle mass.

Suite	$L_{\rm box}$	N_p^3	density interpolation	force resolution	m_p	realizations
A	$1024h^{-1}$Mpc	1024^3	CIC	$31.2h^{-1}$kpc	$7.8 \times 10^{10}h^{-1}M_\odot$	1
B	$1500h^{-1}$Mpc	1024^3	TSC	$45.8h^{-1}$kpc	$2.1 \times 10^{11}h^{-1}M_\odot$	6

In both suites, we simulated three variants of Hu-Sawicki $f(R)$ gravity with $n = 1$ and different values of f_{R0}: -10^{-6} (hereafter dubbed F6), -10^{-5} (F5) and -10^{-4} (F4). To quantify the modified gravity effects and compare them with our model of the ratio of $f(R)$ to GR, we also run a GR case for each suite. All simulations within a suite or realization started from the same initial redshift $z_{\rm ini} = 49.0$ and were evolved until today ($z = 0$). The initial conditions were generated using the publicly available MPGRAFIC code (Prenet, Pichon, et al. 2008), which employs the standard Zel'dovich approximation to calculate the initial particle displacement and velocity fields. We used the same initial conditions for GR and $f(R)$ simulations within the same suite because at $z = 49$ the effect of this modified gravity model on the particle distributions is negligible. Note that the σ_8 values quoted above are the $z = 0$ linear-theory results for GR (they would be different for different variants of $f(R)$ models), and as such they should be considered as a characterisation of the initial conditions rather than of the large-scale matter clustering today. Further simulation specifications are summarised in Table 4.1.

4.5 Halo mass function

In this section we present our main results on the modeling of the $f(R)$ gravity halo mass function. Compared to previous works, we devote particular care to the mass binning used to derive halo abundances from simulations (see Sec. 4.5.1), as well as to estimate the corresponding uncertainties. We also use our results to forecast approximate constraints from cluster number count data (see Sec. 4.5.3).

4.5.1 Binned mass function from simulations

We identify dark matter halos in our simulations using the ROCKSTAR halo finder (Behroozi, Wechsler, and Wu 2013), which by default obtains spherical overdensity (SO) masses from initial friends-of-friends (FOF) groups neglecting unbound particles. However, masses are defined observationally within spherical apertures of arbitrary size enclosing an overdensity that might not be entirely virialized. Since our goal is to have mass function predictions

calibrated for X-ray, Sunyaev-Zel'dovich (SZ) and optical cluster surveys, we enable ROCKSTAR to calculate strict SO masses including unbound particles, as well as particles that may reside outside of the FOF group associated with the halo. Here, we choose an average overdensity $\Delta = 300$ such that the mass inside a sphere of radius r_Δ is

$$M_{300\mathrm{m}} = \frac{4}{3}\pi r_\Delta^3 \bar{\rho}_\mathrm{m}(z)\Delta. \tag{4.45}$$

Winther et al. (2015) showed that, even for ΛCDM, different modified gravity N-body codes produce mass functions that differ by as much as 10%. It was also noticed that these discrepancies are approximately independent of the particular value of f_{R0}. Thus, taking the ratio of the HMF in $f(R)$ to that in GR reduces this scatter to a more competitive 1-4% (for $z \lesssim 0.5$). In addition, the effects of baryonic physics on the $f(R)$ mass function can be potentially neglected when considering instead the ratio of this HMF to that of GR (Cataneo, Rapetti, et al. 2015; Puchwein, Baldi, and Springel 2013). For this, departures from pure dark matter predictions could be incorporated with the same level of accuracy through a baseline GR mass function calibrated with hydrodynamical simulations (see e.g. Bocquet, Saro, et al. 2016). Initially, one might think that mass function ratios may exhibit larger uncertainties compared to those of the individual mass functions. Nonetheless, halo abundances in GR and $f(R)$ are presumably strongly correlated, and it is reasonable to expect that on average such correlation reduces the errors on the ratios to the level of those on the corresponding mass functions (see Eq. (91) in Brax, Davis, et al. 2012). For these reasons, we consider the HMF ratios

$$\mathcal{R}_i^\mathrm{sim} \equiv \langle \mathcal{R}_i \rangle_\mathrm{JK} = \left\langle \frac{N_{h,i}^{f(R)}}{N_{h,i}^\mathrm{GR}} \right\rangle_\mathrm{JK} \tag{4.46}$$

our fundamental observables from the simulations. In Eq. (4.46) $\langle\cdot\rangle_\mathrm{JK}$ denotes the jackknife average, and $N_{h,i}^{f(R)}$ and $N_{h,i}^\mathrm{GR}$ are the number of halos in the i-th mass bin for $f(R)$ and GR, respectively. Also, we implicitly used the fact that volume and mass bin size are identical for the particular pair of simulations examined. We employ the unbiased jackknife average

$$\langle \mathcal{R}_i \rangle_\mathrm{JK} = N_\mathrm{JK}\overline{\mathcal{R}_i} - (N_\mathrm{JK} - 1)\overline{\mathcal{R}_i^\mathrm{JK}}, \tag{4.47}$$

where N_JK is the number of simulation subvolumes, $\overline{\mathcal{R}_i}$ is the standard sample mean over the N_JK subvolumes, and the resampled jackknife estimates are

$$\overline{\mathcal{R}_i^\mathrm{JK}} = \frac{1}{N_\mathrm{JK}} \sum_{j=1}^{N_\mathrm{JK}} \mathcal{R}_{i,j}^\mathrm{JK}\,, \tag{4.48}$$

with

$$\mathcal{R}_{i,j}^\mathrm{JK} = \frac{1}{N_\mathrm{JK} - 1} \sum_{k \neq j} \mathcal{R}_{i,k}\,. \tag{4.49}$$

For our suite A of simulations in Table 4.1 we divide each box in octants and remove one octant at a time from the full simulation volume to compute Eq. (4.49). We proceed similarly for our suite B, although in this case each jackknife subvolume corresponds to a different realization.

Following Tinker, Kravtsov, et al. (2008), and supported by results in Crocce, Fosalba, et al. (2010); Hoffmann, Bel, and Gaztanaga (2015), we also adopt the jackknife method to estimate the error contributions on Eq. (4.46) from both sample variance and Poisson noise. For each mass bin i we have

$$\sigma_{\mathcal{R},i} = \sqrt{N_{\rm JK} - 1}\, s_{\mathcal{R}^{\rm JK},i}\,, \tag{4.50}$$

where the jackknife sample variance is

$$s^2_{\mathcal{R}^{\rm JK},i} = \overline{(\mathcal{R}_i^{\rm JK})^2} - \left(\overline{\mathcal{R}_i^{\rm JK}}\right)^2. \tag{4.51}$$

On top of this error, we should also include the 1-4% scatter found between N-body codes in Winther et al. (2015), as well as the error introduced by assigning the HMF ratio in each mass bin to the center of the bin (Lukic, Heitmann, et al. 2007). The former is comparable to the error from Eq. (4.50) for masses up to $M \sim 10^{14.5} M_\odot/h$, and dominates over the bin center error in the same range for mass bins $\Delta \log_{10} M = 0.15$. For larger masses the contrary is true. For simplicity, however, we neglect both of these contributions since adding them would not considerably alter our best fits, and a full statistical analysis of the new HMF parameters is not within the scope of this paper. Note also that for the mass range of interest here, 10^{13}–$10^{15.5} M_\odot/h$, we adopt a bin size for which we expect our results of the HMF ratios to be converged within the errors (see e.g. Bhattacharya, Heitmann, et al. 2011; Hoffmann, Bel, and Gaztanaga 2015). Furthermore, previous works showed that in this mass range bins are mostly uncorrelated (Smith and Marian 2011; Hoffmann, Bel, and Gaztanaga 2015), with none or very marginal impact on the best fitting values of the model parameters (Hoffmann, Bel, and Gaztanaga 2015). Hence, in what follows we ignore all covariances between mass bins, the effect of which should be negligible for our results.

Mass function ratios are also suitable to alleviate the consequences of other numerical inaccuracies. Numerical transients related to Zel'dovich initial conditions (1LPT) are responsible for a deficit of massive halos compared to results obtained from second order initial conditions (2LPT) (Crocce, Fosalba, et al. 2010; Reed, Smith, et al. 2013). However, assuming that the same correction applies to the HMF's of both $f(R)$ and GR obtained with 1LPT at $z_{\rm ini} = 49$, for final redshifts in the range $z_{\rm fin} \in [0, 0.5]$ we estimate a conservative average difference between 1LPT and 2LPT HMF ratios of 1%, which is well within our jackknife errors (Taruya 2016). As a final note, Knebe et al. (2013) found a 10% scatter among mass

functions derived using different halo finders. Also in this case, HMF ratios are expected to contain these differences safely within our estimates from Eq. (4.50).

4.5.2 Modeling and fits

We derive our predictions for the ratios of the mass function in $f(R)$ over the mass function in GR from the prescription given by Sheth and Tormen (1999). In this framework, the comoving number density of halos in a logarithmic mass bin around a mass M is

$$n_{\ln M} \equiv \frac{dn}{d\ln M} = \frac{\bar{\rho}_{\rm m}}{M}\frac{d\ln\nu}{d\ln M}\nu f(\nu), \tag{4.52}$$

where $\nu = \delta_{\rm c}/\sigma(M,z)$ is the peak height, with

$$\sigma^2(M,z) = \int \frac{d^3k}{(2\pi^3)}|\tilde{W}_R(k)|^2 P_L(k,z). \tag{4.53}$$

Here, $P_L(k,z)$ is the linear power spectrum[1] at redshift z and $\tilde{W}_R(k)$ is the Fourier transform of the top hat window function of radius R that encloses a mass $M = 4\pi R^3\bar{\rho}_m/3$. We use $\delta_{\rm c} = \delta_{\rm c}^{\Lambda}(z)$ for GR, which we evaluate as Nakamura and Suto 1997

$$\delta_{\rm c}^{\Lambda}(z) \approx \frac{3}{20}(12\pi)^{2/3}\left[1 + 0.0123\log_{10}\Omega_{\rm m}(z)\right], \tag{4.54}$$

and $\delta_{\rm c} = \delta_{\rm c}^{\rm eff}(M,z)$ given in Eq. (4.38) for $f(R)$. The Sheth-Tormen (ST) multiplicity function in Eq. (4.52) is parametrized as

$$\nu f(\nu) = A\sqrt{\frac{2}{\pi}a\nu^2}\left[1 + (a\nu^2)^{-p}\right]\exp\left[-a\nu^2/2\right], \tag{4.55}$$

where (a,p,A) are free parameters defining the high-mass cutoff, the low-mass shape and the normalization of the mass function, respectively. For these, we employ the recent fits from Despali, Giocoli, et al. (2016), where they extended the previous ST fits to be function of a generic overdensity Δ. For easy reference, we report these results here,

$$\begin{aligned} a &= 0.4332x^2 + 0.2263x + 0.7665, \\ p &= -0.1151x^2 + 0.2554x + 0.2488, \\ A &= -0.1362x + 0.3292\,, \end{aligned} \tag{4.56}$$

where $x = \log_{10}[\Delta/\Delta_{\rm vir}(z)]$. In our approach all the modifications of gravity are encoded in $\delta_{\rm c}^{\rm eff}$, thus Eq. (4.56) is used both in GR and $f(R)$, and we approximate the virial overdensity

[1] For the linear calculations of both GR and $f(R)$ we evaluate ΛCDM matter power spectra (see more details later on in the text) using the publicly available code CAMB (Lewis, Challinor, and Lasenby 2000).

as (Bryan and Norman 1998)

$$\Delta_{\rm vir}(z) = \frac{18\pi^2 - 82\left[1-\Omega_{\rm m}(z)\right] - 39\left[1-\Omega_{\rm m}(z)\right]^2}{\Omega_{\rm m}(z)}. \tag{4.57}$$

A similar argument applies to the mass variance of the linear density field. In GR the statistics of collapsed objects at any redshift is fully determined by the initial linear density field

$$\nu_{\rm ini} \equiv \frac{\delta_{\rm i}(z_{\rm c})}{\sigma(M,z_{\rm i})} = \frac{D(z_{\rm c})\delta_{\rm i}(z_{\rm c})}{D(z_{\rm c})\sigma(M,z_{\rm i})} = \frac{\delta_{\rm c}^{\Lambda}(z_{\rm c})}{\sigma(M,z_{\rm c})} = \nu(z_{\rm c}), \tag{4.58}$$

where $\delta_{\rm i}(z_{\rm c})$ represents the density contrast at an initial redshift $z_{\rm i}$ that will eventually produce a halo at a formation time $z_{\rm c}$. Considering that the initial conditions are set such that $\sigma_{f(R)}(M,z_{\rm i}) = \sigma_{\rm GR}(M,z_{\rm i})$ for all scales of interest, then enforcing Eq. (4.58) also in $f(R)$ effectively implies $\sigma_{f(R)}(M,z) = \sigma_{\rm GR}(M,z)$ at all redshifts (Kopp, Appleby, et al. 2013; Lombriser, Li, et al. 2013).

We define our theoretical mass function ratios using Eq. (4.52) together with Eq. (4.55) as

$$\mathcal{R}^{\rm theo}(M) \equiv \frac{n_{\ln M}|_{f(R)}}{n_{\ln M}|_{\rm GR}}, \tag{4.59}$$

which depend on the set of free parameters $M_{\rm th}^{(1)}$, $M_{\rm th}^{(2)}$, η and ϑ introduced in Sec. 4.3.2. For our fitting analysis, we employ the suite A of high-resolution simulations in Table 4.1, and consider each redshift snapshot $z_{\rm c} \in \{0.0, 0.1, 0.2, 0.3, 0.4, 0.5\}$ separately. We obtain the best-fit values by minimizing

$$\chi^2(M_{\rm th}^{(1)}, M_{\rm th}^{(2)}, \eta, \vartheta) = \sum_i \frac{[\mathcal{R}_i^{\rm sim} - \mathcal{R}^{\rm theo}(M_i)]^2}{\sigma_{\mathcal{R},i}^2}, \tag{4.60}$$

where the sum is over mass bins with at least 20 halos to limit the effect of Poisson noise at high masses, and M_i denotes the mass at the bin center. We first fit the F5 simulations to find $\tilde{M}_{\rm th}^{(1)}(z_{\rm c})$ and $\tilde{M}_{\rm th}^{(2)}(z_{\rm c})$, which we then rescale to the other values of f_{R0} using Eq. (4.41). Hence, in the F4 and F6 cases we only fit for η and ϑ. Below, we provide fitting functions for the relevant free parameters entering Eq. (4.39). To achieve enough flexibility without including a large number of terms, for η and ϑ we opted for 2-dimensional surfaces described by cubic polynomials in redshifts with coefficients depending quadratically on $\log_{10}|f_{R0}|$:

$$\begin{aligned}
\tilde{M}_{\rm th}^{(1)}(z) &= 13.8528 - 0.5981z - 2.7073z^2 + 4.1907z^3, \\
\tilde{M}_{\rm th}^{(2)}(z) &= 13.9720 - 0.9003z - 2.9086z^2 + 5.4463z^3, \\
\eta(f_{R0},z) &= \eta_0(f_{R0}) + \eta_1(f_{R0})z + \eta_2(f_{R0})z^2 + \eta_3(f_{R0})z^3, \\
\vartheta(f_{R0},z) &= \vartheta_0(f_{R0}) + \vartheta_1(f_{R0})z + \vartheta_2(f_{R0})z^2 + \vartheta_3(f_{R0})z^3,
\end{aligned} \tag{4.61}$$

where the η_i coefficients are

$$\begin{aligned}
\eta_0(f_{R0}) &= -46.1022 - 18.5382 \log_{10}|f_{R0}| - 1.7648 \left(\log_{10}|f_{R0}|\right)^2 , \\
\eta_1(f_{R0}) &= 6.0520 + 4.8043 \log_{10}|f_{R0}| + 0.7146 \left(\log_{10}|f_{R0}|\right)^2 , \\
\eta_2(f_{R0}) &= -398.9787 - 180.5379 \log_{10}|f_{R0}| - 19.8292 \left(\log_{10}|f_{R0}|\right)^2 , \\
\eta_3(f_{R0}) &= 429.3937 + 201.2807 \log_{10}|f_{R0}| + 22.9045 \left(\log_{10}|f_{R0}|\right)^2 ,
\end{aligned} \tag{4.62}$$

and the ϑ_i coefficients are

$$\begin{aligned}
\vartheta_0(f_{R0}) &= -19.6362 - 8.1120 \log_{10}|f_{R0}| - 0.7744 \left(\log_{10}|f_{R0}|\right)^2 , \\
\vartheta_1(f_{R0}) &= 67.6699 + 25.9151 \log_{10}|f_{R0}| + 2.4720 \left(\log_{10}|f_{R0}|\right)^2 , \\
\vartheta_2(f_{R0}) &= -651.2764 - 274.0971 \log_{10}|f_{R0}| - 28.4491 \left(\log_{10}|f_{R0}|\right)^2 , \\
\vartheta_3(f_{R0}) &= 726.4060 + 311.8720 \log_{10}|f_{R0}| + 33.1439 \left(\log_{10}|f_{R0}|\right)^2 .
\end{aligned} \tag{4.63}$$

Note that all the expressions above are only valid in the redshift range $0 \leqslant z \leqslant 0.5$, for $10^{-6} \leqslant |f_{R0}| \leqslant 10^{-4}$ and $\Delta = 300$.

Based on Eqs. (4.61)-(4.63), the left panel of Fig. 4.3 shows our predictions for the $f(R)$ to GR HMF ratios (lines), and how these compare to the corresponding ratios measured from the simulations in mass bins using Eq. (4.46) (rectangles). Our fits perform very well for the three selected redshifts ($z = 0$, in blue; $z = 0.2$, in red; $z = 0.5$, in green) and for the three representative background field values (F4, F5 and F6), with deviations of $\lesssim 5\%$ from the mean ratios over the entire mass range. Assuming that η and ϑ are slowly varying functions of the cosmological parameters (in particular $\Omega_{\rm m}$), we can also employ Eqs. (4.61)-(4.63) along with Eq. (4.41) to predict the HMF ratios for other background cosmologies. The simulations of suite B in Table 4.1 were run for a sufficiently different background cosmology from the one we used to calibrate our relations (cfr. Eq. (4.43) and Eq. (4.44)) to provide a good test bench in which to assess the validity of these results for other background cosmologies. In the right panel of Fig. 4.3, we illustrate the predictive power of our fits for the F4, F5 and F6 $f(R)$ cosmologies in suite B (top to bottom panels), as well as for snapshots at redshift $z = 0$ (blue), and two other redshifts somewhat different from those in suite A, $z = 0.25$ (red) and $z = 0.44$ (green). Once again, the agreement with simulations is very good for $M \gtrsim 10^{14} M_{\odot}/h$, although discrepancies are visible for smaller masses. Obviously, one possible reason for such behavior is a lack of 'universality' in our fitting parameters, especially for quite distinct cosmologies, such as WMAP3 and WMAP9. However, another plausible explanation is that the lower mass and force resolutions in suite B, together with a different density interpolation method and a less stringent refinement criterion, might affect the low-mass halo abundance in GR and $f(R)$ differently.

Indeed, particle-mesh codes with coarse domain grids suppress the abundance of low-mass halos (O'Shea, Nagamine, et al. 2005; Lukic, Heitmann, et al. 2007). As mentioned in Sec. 4.4, ECOSMOG employs adaptive mesh refinement to improve force resolution, with the refinement criterion being a rather important parameter for the code performance. O'Shea, Nagamine, et al. (2005) recommend a domain grid twice as fine as the mean interparticle spacing, as well as a low refinement threshold to achieve enough force resolution and capture small density peaks at early times. Although the size of our domain grid cells $\Delta_{\rm cell} = L_{\rm box}/N_{\rm cell}$ is equal to or larger than the mean interparticle separation $\Delta_p = L_{\rm box}/N_p$, the low refinement threshold $N_{\rm ref}$ might help to reach an effective domain grid twice as fine as the original one, $\Delta'_{\rm cell} \approx \Delta_{\rm cell}/2$. Lukic, Heitmann, et al. (2007) proposed a criterion for the minimum number of particles required to accurately resolve a halo that at $z = 0$ reads

$$N_p^{\rm halo} \gtrsim 4.2 \left(\frac{\Delta'_{\rm cell}}{\Delta_p}\right)^3 \frac{\Delta}{\Omega_{\rm m}}. \tag{4.64}$$

Recalling that for this work $\Delta = 300$, and using the information in Table 4.1 together with Eqs. (4.43) and (4.44), we have that $M_{\rm halo}^{\rm min} \approx 10^{13.5} M_\odot/h$ and $M_{\rm halo}^{\rm min} \approx 10^{14} M_\odot/h$ for suites A and B respectively. Interestingly, this is consistent with our findings in Fig. 4.3 for the lower-resolution simulations of suite B.

4.5.3 Approximate forecasts

We can now use our fits to make approximate forecasts of the maximum background scalaron field amplitude allowed by cluster abundance data from existing and ongoing surveys. Our fiducial cosmology is ΛCDM in standard GR with the parameters set to the mean values obtained from the full statistical analysis carried out in Cataneo, Rapetti, et al. (2015) for the data combination dubbed there *Clusters+Planck+WP+lensing+ACT+SPT+ SNIa+BAO*, namely

$$(\Omega_{\rm m}, \Omega_\Lambda, h, n_s, \sigma_8) = (0.3, 0.7, 0.683, 0.963, 0.82). \tag{4.65}$$

We opt for a Tinker, Robertson, et al. (2010) fiducial mass function, which we calculate using HMFCALC[2] (Murray, Power, and Robotham 2013) with the model parameters fitted at $\Delta = 300$. Also, for the current purpose we assume that the only observational error is the uncertainty on the weak lensing mass calibration (Sealfon, Verde, and Jimenez 2006; Johnston, Sheldon, et al. 2007; Sheldon et al. 2009; Mandelbaum et al. 2008; Leauthaud et al. 2010; White, Cohn, and Smit 2010; Rozo, Wu, and Schmidt 2011; Applegate, Linden, et al. 2014; Linden et al. 2014a; Applegate et al. 2016) since this is presently the dominant source of error in measurements of the cluster mass function. We then estimate the uncertainty $\epsilon_{\rm MF}$

[2] http://hmf.icrar.org

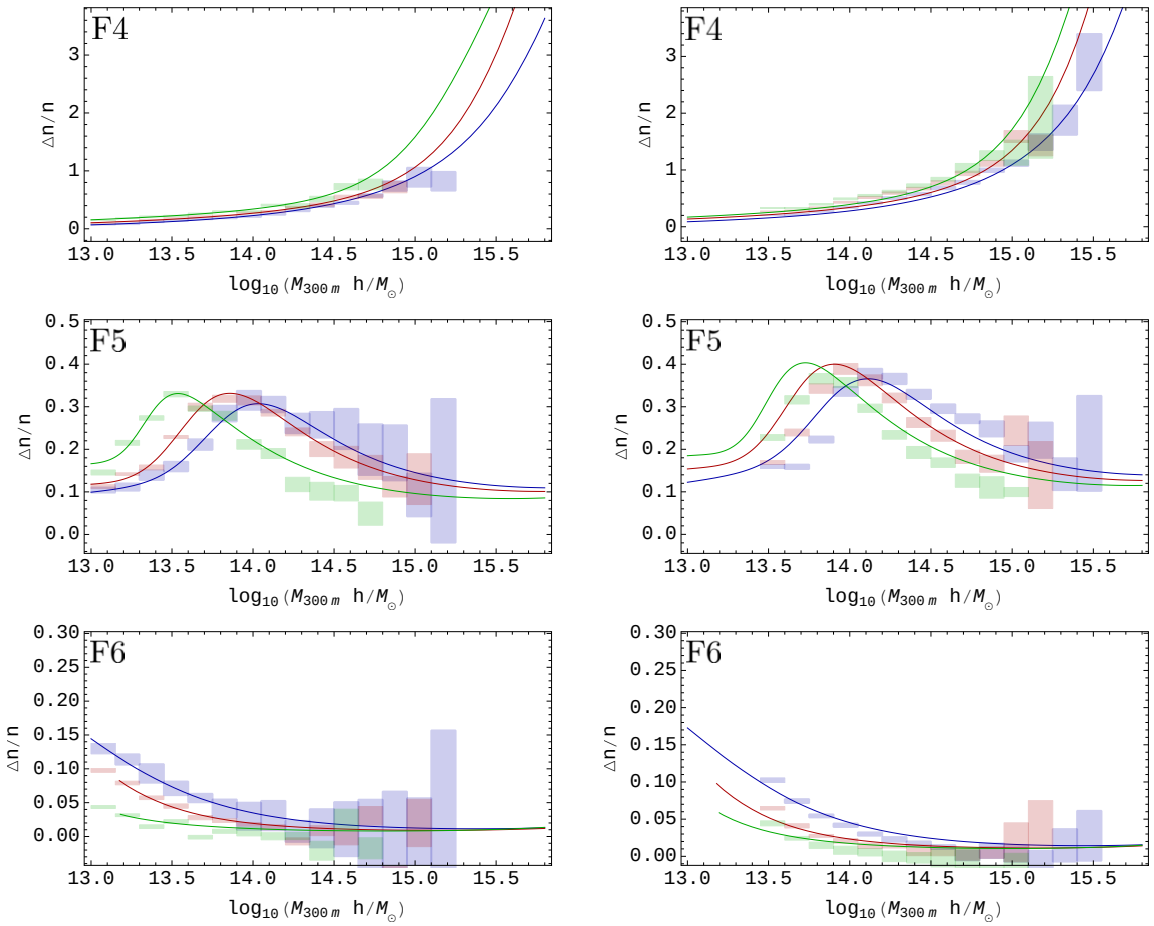

Fig. 4.3 Mass function enhancements in $f(R)$ relative to GR as a function of redshift and background scalaron amplitude (from top to bottom, $|f_{R0}| = 10^{-4}, 10^{-5}, 10^{-6}$). *Left*: comparison between our fits (lines) and halo abundance bins (rectangles) from the high-resolution simulations of suite A, for $z = 0$ (blue), $z = 0.2$ (red) and $z = 0.5$ (green). *Right:* the same as in the left panel but for the lower-resolution simulations of suite B, and for $z = 0$ (blue), $z = 0.25$ (red) and $z = 0.44$ (green). We find our fits to be within 5% precision for $M \gtrsim 10^{14} M_{\odot}/h$ (see also main text for further details).

on the observed cluster number counts by propagating the lensing calibration error $\epsilon_{\rm cal}$ as

$$\epsilon_{\rm MF} = \left| \frac{d \log_{10} n^{\rm Tinker}_{\ln M}}{d \log_{10} M} \right| \epsilon_{\rm cal} \,, \tag{4.66}$$

where $n^{\rm Tinker}_{\ln M}$ represents the fiducial mass function. First, based on results from the Weighing the Giants (WtG) project we consider a mass calibration error of 7% (Applegate, Linden, et al. 2014). This data was used in Cataneo, Rapetti, et al. (2015) together with a conservative mass function model Schmidt, Lima, et al. 2009 to determine the upper bound $|f_{R0}| < 1.62 \times 10^{-5}$ at 95.4% confidence level. The left panel of Fig. 4.4 shows the corresponding mass function model at $z = 0$ for the cosmological parameters given in Eq. (4.65) and this upper limit of $|f_{R0}|$ (dashed red line). The grey shaded area in this panel is the region allowed by the mass calibration uncertainty. Matching simply by visual inspection the expected likelihood of our new model (solid blue line) to that of the previous, conservative model promises a potential improvement over our current constraints of a factor of ~ 2, i.e. $|f_{R0}| \lesssim 8 \times 10^{-6}$. Looking a bit further ahead, the ongoing Dark Energy Survey (DES) (Abbott et al. 2005) should achieve a mass calibration precision of at least 5% in the coming years (Joerg Dietrich, private communication; see also Melchior et al., in prep.) and be able to provide a sample with objects down to masses $\sim 10^{13.5} M_\odot/h$ and redshifts $z \sim 0.1$. The right panel of Fig. 4.4 suggests that with this data we could potentially reduce the current upper limit from Cataneo, Rapetti, et al. (2015) by an order of magnitude, reaching a background Compton wavelength $\lambda_{\rm C} \approx 2\,h^{-1}$ Mpc or equivalently $|f_{R0}| \approx 10^{-6}$. Remarkably, this forecast at cluster scales is competitive with current constraints from local gravity tests. Assuming a galactic Navarro-Frenk-White halo density profile (Navarro, Frenk, and White 1996) embedded in the cosmological background, these tests require an active chameleon screening inside the Galaxy from the center out to the location of our Solar System (Hu and Sawicki 2007; Lombriser, Koyama, and Li 2014) to suppress unobserved modifications above $|f_{R0}| \sim 10^{-6}$.

4.6 Conclusions

The abundance of galaxy clusters is sensitive to the growth of the large scale structure, and as such can effectively test departures from GR on cosmological scales. Upcoming and future cluster surveys will provide exquisite data, requiring accurate percent level theoretical predictions to realize the full potential of these measurements. In this work we have presented a novel semi-analytical approach that combines the advantages of the spherical collapse model of Lombriser, Li, et al. (2013) with the information available in fully nonlinear cosmological simulations. Taking GR as a baseline theory of gravity, we have calibrated mass function ratios in the context of $f(R)$ gravity and obtained fitting functions for our additional parameters able to predict these ratios within a 5% precision for the ranges $10^{13.5} \leqslant M_{\rm 300m}(M_\odot/h)^{-1} \leqslant 10^{15.5}$,

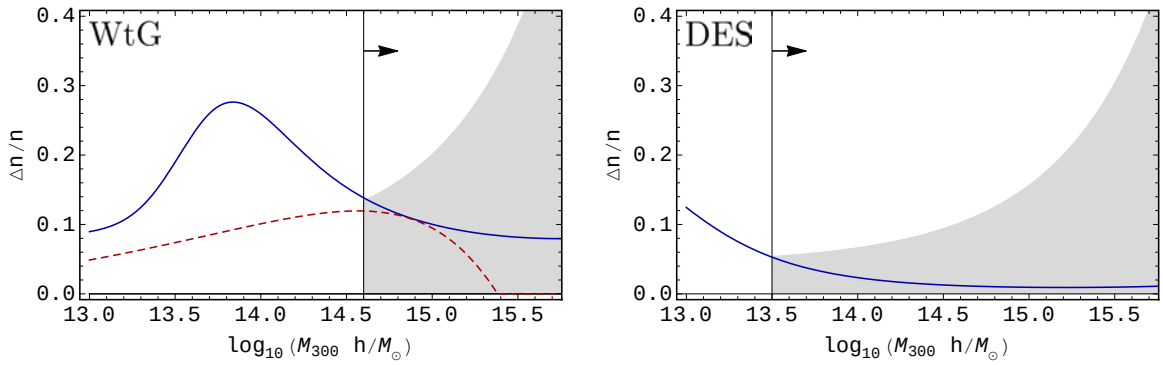

Fig. 4.4 Approximate forecast constraints on the enhancement of the growth of structure due to $f(R)$ gravity from available and forthcoming cluster abundance data. The blue lines are based on our new mass function modeling (see Eqs. (4.38)-(4.39)) and the grey shaded regions on the weak lensing mass calibration uncertainty $\epsilon_{\rm cal}$ for the fiducial ΛCDM cosmology of Eq. (4.65). Vertical lines indicate the lowest cluster mass ends of each data set. *Left:* the dashed red line shows the conservative mass function used in Cataneo et al. (2015) Cataneo, Rapetti, et al. 2015 at $z = 0$ for $|f_{R0}| = 1.62 \times 10^{-5}$, which corresponds to the 95.4% upper limit constraint obtained there. The solid blue line was calculated using the new HMF of this work with $|f_{R0}| = 8 \times 10^{-6}$, which matches the mass calibration $\epsilon_{\rm cal} = 7\%$ from WtG (grey shaded area) and represents a factor of 2 improvement over the current result of the red line using the same data. *Right:* using upcoming DES data down to lower mass objects with a low redshift limit of $z = 0.1$ and $\epsilon_{\rm cal} = 5\%$ (grey shaded area), our new model promises an improvement of the upper bound on $f(R)$ gravity at cluster scales of an order of magnitude, $|f_{R0}| = 10^{-6}$ (blue line).

$10^{-6} \leqslant |f_{R0}| \leqslant 10^{-4}$ and $0 \leqslant z \leqslant 0.5$. This corresponds to about a 50% improvement on the purely spherical collapse results of Lombriser, Li, et al. (2013). A similar level of accuracy can be achieved for the full $f(R)$ mass function on the condition that the modeling of the reference GR halo abundance is accurate at the percent level. Although in Eqs. (4.61)-(4.63) we provide fits only for halo masses defined by mean matter densities of $\bar{\rho} = 300\bar{\rho}_{\rm m}$, our relations can be readily refitted using other mass definitions (e.g. $\bar{\rho} = 500\bar{\rho}_{\rm cr}$) bearing in mind the resolution limitations imposed by Eq. (4.64).

Our method can also be straightforwardly applied to calibrate theoretical mass functions of other scalar-tensor theories characterized by a mass and environment dependent spherical collapse threshold. This is for example the case of the dilaton and symmetron models investigated in Brax, Davis, et al. (2012). Note also that baryonic physics is likely to currently be irrelevant for the HMF ratios (Cataneo, Rapetti, et al. 2015; Puchwein, Baldi, and Springel 2013), and that any departures from DM-only predictions due to baryons could be included through a baseline GR mass function calibrated against hydrodynamical simulations (see e.g. Bocquet, Saro, et al. 2016). Analogous considerations might hold as well for the impact of massive neutrinos on the $f(R)$ to GR halo mass function ratio. It would be interesting to test the performance of our method on cosmological simulations incorporating massive neutrinos in both GR and $f(R)$ (see e.g. Baldi, Villaescusa-Navarro, et al. 2014). If the accuracy of our

predictions remains unchanged when allowing a varying effective sum of the neutrino masses, then it would be sufficient to implement the prescription of Castorina, Sefusatti, et al. (2014) on the baseline GR mass function. Finally, in addition to Poisson noise it will be necessary to account for the uncertainty due to sample variance in order to unbiasedly constrain the low mass end of the HMF with forthcoming cluster number count data (Hu and Kravtsov 2003). For the specific cosmological models of interest, this will require the calculation of the linear bias parameter, which in itself depends on the spherical collapse threshold (Sheth and Tormen 1999; Tinker, Robertson, et al. 2010). For $f(R)$ gravity, we should be able to use our effective linearly extrapolated overdensity (see Eq. (4.38)) to evaluate the linear bias and hence the sample variance contribution (Cataneo et al., in preparation) needed for a series of upcoming key cosmological analyses from ongoing and future cluster surveys.

Acknowledgements

This work used the DiRAC Data Centric system at Durham University, operated by the Institute for Computational Cosmology on behalf of the STFC DiRAC HPC Facility (www.dirac.ac.uk). This equipment was funded by BIS National E-infrastructure capital grant ST/K00042X/1, STFC capital grants ST/H008519/1 and ST/K00087X/1, STFC DiRAC Operations grant ST/K003267/1 and Durham University. DiRAC is part of the National E-Infrastructure. Further numerical computations have been performed with Wolfram *Mathematica*® 9. For part of this work, the Dark Cosmology Centre was funded by the Danish National Research Foundation. DR is supported by a NASA Postdoctoral Program Senior Fellowship at the NASA Ames Research Center, administered by the Universities Space Research Association under contract with NASA. LL is supported by a SNSF Advanced Postdoc.Mobility Fellowship (No. 161058) and the STFC Consolidated Grant for Astronomy and Astrophysics at the University of Edinburgh. BL is supported by STFC Consolidated Grant No. ST/L00075X/1 and No. RF040335.

Chapter 5

Dark matter clustering on mildly nonlinear scales

This chapter contains the following manuscript:

"Efficient exploration of cosmology dependence in the EFT of LSS"

Submitted to the *J. Cosmology Astropart. Phys.*; *arXiv* preprints: 1606.03633

Authors:

M. Cataneo, S. Foreman, L. Senatore

The most effective use of data from current and upcoming large scale structure (LSS) and CMB observations requires the ability to predict the clustering of LSS with very high precision. The Effective Field Theory of Large Scale Structure (EFTofLSS) provides an instrument for performing analytical computations of LSS observables with the required precision in the mildly nonlinear regime. In this paper, we develop efficient implementations of these computations that allow for an exploration of their dependence on cosmological parameters. They are based on two ideas. First, once an observable has been computed with high precision for a reference cosmology, for a new cosmology the same can be easily obtained with comparable precision just by adding the difference in that observable, evaluated with much less precision. Second, most cosmologies of interest are sufficiently close to the *Planck*

best-fit cosmology that observables can be obtained from a Taylor expansion around the reference cosmology. These ideas are implemented for the matter power spectrum at two loops and are released as public codes. When applied to cosmologies that are within 3σ of the *Planck* best-fit model, the first method evaluates the power spectrum in a few minutes on a laptop, with results that have 1% or better precision, while with the Taylor expansion the same quantity is instantly generated with similar precision. The ideas and codes we present may easily be extended for other applications or higher-precision results.

5.1 Introduction

Ongoing and future sky surveys, such as the extended Baryon Oscillation Spectroscopic Survey (eBOSS) (Dawson et al. 2016), the Large Synoptic Survey Telescope (LSST) (Abell et al. 2009), the Dark-Energy Spectroscopic Instrument (DESI) (Levi et al. 2013) and *Euclid* (Refregier, Amara, et al. 2010), as well as current and next generation CMB experiments, such as the South Pole Telescope (SPT) (Ruhl et al. 2004) and the Atacama Cosmology Telescope (ACT) (Thornton et al. 2016), will measure the statistical quantities of the cosmological large-scale structure with percent/sub-percent precision (Percival 2015). One way to compare our predictions to this wealth of data is to evolve structure formation down to highly non-linear scales with large-volume, high-resolution simulations. However, this approach is computationally expensive requiring millions of CPU hours, which makes impractical the investigation of cosmological parameter dependences of survey observables and their covariances.

The reliance on numerical simulation has been largely motivated by the lack of a satisfactory analytic approach. Until recently, analytic techniques were not capable of going beyond tree-level computations in a well-defined fashion, which limited their applicability to very low wavenumbers or motivated the introduction of additional assumptions or approximations with uncontrollable errors. This situation has radically changed in the last few years, with the development of the so-called Effective Field Theory of Cosmological Large Scale Structures (EFTofLSS) (Baumann, Nicolis, et al. 2012; Carrasco, Hertzberg, and Senatore 2012; Porto, Senatore, and Zaldarriaga 2014; Senatore and Zaldarriaga 2015), which has successfully shown its consistency and its capability to predict correlation functions of large scale structure quantities within the mildly non-linear regime (Baumann, Nicolis, et al. 2012; Carrasco, Hertzberg, and Senatore 2012; Carrasco, Foreman, et al. 2014a; Carrasco, Foreman, et al. 2014b; Pajer and Zaldarriaga 2013; Carroll, Leichenauer, and Pollack 2014; Porto, Senatore, and Zaldarriaga 2014; Mercolli and Pajer 2014; Senatore and Zaldarriaga 2015; Angulo, Foreman, et al. 2015; Baldauf, Mercolli, Mirbabayi, et al. 2015; Senatore 2015; Senatore and Zaldarriaga 2014; Lewandowski, Perko, and Senatore 2015; Mirbabayi, Schmidt, and Zaldarriaga 2015; Foreman and Senatore 2016; Angulo, Fasiello, et al. 2015; McQuinn and

White 2016; Assassi, Baumann, Pajer, et al. 2015; Baldauf, Schaan, and Zaldarriaga 2016a; Baldauf, Mirbabayi, et al. 2015; Foreman, Perrier, and Senatore 2016; Baldauf, Mercolli, and Zaldarriaga 2015; Baldauf, Schaan, and Zaldarriaga 2016b; Bertolini, Schutz, Solon, Walsh, et al. 2015; Bertolini, Schutz, Solon, and Zurek 2016). The EFTofLSS has been applied to the description of the dark matter two-point function (Carrasco, Hertzberg, and Senatore 2012; Carrasco, Foreman, et al. 2014b; Senatore and Zaldarriaga 2015; Foreman, Perrier, and Senatore 2016; Baldauf, Mercolli, and Zaldarriaga 2015), three-point function (Angulo, Foreman, et al. 2015; Baldauf, Mercolli, Mirbabayi, et al. 2015), as well as four-point function (which includes the covariance of the power spectrum) (Bertolini, Schutz, Solon, Walsh, et al. 2015; Bertolini, Schutz, Solon, and Zurek 2016). The dark matter momentum power spectrum (Senatore and Zaldarriaga 2015; Baldauf, Mercolli, and Zaldarriaga 2015), displacement field (Baldauf, Mercolli, Mirbabayi, et al. 2015), and vorticity slope (Carrasco, Foreman, et al. 2014b; Hahn, Angulo, and Abel 2015) have also been derived within this framework. Notably, despite the complexity of the physical processes involved on small scales, also the effects of baryons on the power spectrum in the perturbative regime can be naturally incorporated (Lewandowski, Perko, and Senatore 2015). The extension of the EFTofLSS to biased tracers has been carried out in Senatore and Zaldarriaga (2014), and used for the power spectrum and bispectrum in Angulo, Fasiello, et al. (2015). Further applications include redshift space distortions (Senatore and Zaldarriaga 2014; Lewandowski, Senatore, et al. 2015), and the impact of primordial non-Gaussianity on large scale structure observables (Angulo, Fasiello, et al. 2015; Assassi, Baumann, Pajer, et al. 2015; Assassi, Baumann, and Schmidt 2015; Lewandowski, Senatore, et al. 2015).

Several advantages result from this working analytic approach, as for example a simple and intuitive (yet rigorous) understanding of the physics governing the clustering of large scale structures, or the possibility of estimating the errors in our computations. In this work we introduce and implement a suite of computationally efficient algorithms to allow the exploration of a considerable volume of parameter space within the EFTofLSS.

Our idea is rather straightforward, and it is based on combining the analytical insight gained from the EFTofLSS with the fact that, after the *Planck* satellite, our knowledge of the cosmological parameters of our universe is quite accurate, which implies that only small differences among the observables are currently relevant. Suppose we wish to compute the various observables as we change the cosmological parameters with a certain precision. Also, suppose that we have computed these observables for a certain reference cosmology, for example the *Planck* best fit one, with the desired precision. Now, in the EFTofLSS, observables are computed as multi-dimensional convolutions of linear power spectra weighted by some kernels. Therefore, the difference in the computation between two different cosmologies lies just in the difference of the linear power spectra. Therefore, instead of performing these integrations directly for each cosmology, we can simply integrate the difference of the

integrands (we will actually integrate the difference of rescaled integrands, which fits our purpose even better). In this way, the integral that we need to compute is very small, and therefore, in order to obtain a given precision on the final result, it can be computed with a smaller relative precision.

We implement this construction for the two-loop matter power spectrum in Sec. 5.2. With the integration techniques we use in this paper, we find that obtaining this quantity for all cosmologies within the 3σ contour around the *Planck* best fit cosmology with better than 1% accuracy takes a few minutes on a laptop. This makes the cost of computing several cosmologies lighter by about a couple of orders of magnitude [1]. We make this code, `CosmoEFT`, publicly available, together with a C++ implementation of the IR-resummation procedure described in Senatore and Zaldarriaga (2015); Angulo, Foreman, et al. (2015), called `ResumEFT`.

Again, given that we are interested in relatively nearby cosmologies, it appears to be unnecessary to compute correlation functions for each cosmology directly. Instead, it should be enough to compute the Taylor expansion of the relevant quantities, such as the convolution integrals and the counterterms of the EFTofLSS, around the *Planck* cosmology. This can be done by evaluation of a relatively small number of cosmologies to compute the derivatives with respect the cosmological parameters (which is made easier by the use of `CosmoEFT`), so that the correlation functions for all the additional cosmologies can be simply read off the Taylor expansion, with negligible cost in time. We implement this procedure for the two-loop dark matter power spectrum in Sec. 5.3, and we make publicly available a Mathematica notebook, `TaylorEFT`, that allows to read the dark matter power spectrum from the Taylor expansion.

In Sec. 5.4 we perform additional checks on both `TaylorEFT` and the `CosmoEFT` procedures, finding that in general the power spectrum for all cosmologies within the 3σ contour of the *Planck* best fit cosmology can be reproduced within 1% accuracy. Better precision can be achieved by adjusting the precision requirements and the order of the Taylor expansion. We also perform a first, preliminary, exploration of the cosmology dependence of the parameters present in the EFTofLSS which encode the effect of short distance physics at long distances, such as the well-known speed of sound.

5.2 `CosmoEFT`: Efficient exploration of cosmology-dependence in the EFTofLSS

The current state-of-the-art (two-loop) calculation of the matter power spectrum in the EFTofLSS involves five-dimensional loop integrals. Several ways to make the integration more

[1] Using the same idea as presented here, the running time, and the gain, might be even improved by using more sophisticated integration techniques.

efficient have been proposed (Taruya, Bernardeau, et al. 2012; Sherwin and Zaldarriaga 2012; Blas, Garny, and Konstandin 2014; Bertolini, Schutz, Solon, Walsh, et al. 2015; Schmittfull, Vlah, and McDonald 2016; McEwen, Fang, et al. 2016). Given a fixed computational cost for computing the predictions of the EFTofLSS for one cosmology, there remains the question if there is an efficient way to use this result in order not to pay the same price to obtain the result for any cosmology of interest. In Sec. 5.2.1 we present a re-organization of the perturbation theory integrals that greatly reduces the cost of exploring the cosmological parameter space once the result for a given cosmology is known. We give the details of its implementation in Sec. 5.2.2, and evaluate its performance in Sec. 5.2.3. This new method is applied in the publicly available code `CosmoEFT` [2], released with this work.

5.2.1 Integrating differences between cosmologies

After the release of *Planck*'s constraints on cosmological parameters (Ade et al. 2015a), the cosmologies of most interest for future studies will likely be those that have only mild departures from the *Planck* best-fit model. This motivates the following decomposition of the loop integrals we wish to calculate:

$$P_\alpha^{\text{target}}(k) = P_\alpha^{\text{ref}}(k) + \Delta P_\alpha(k) \ , \tag{5.1}$$

where α denotes a particular loop integral, and "target" and "ref" refer to the desired cosmology and a *Planck*-like fiducial ("reference") cosmology respectively. The difference $\Delta P_\alpha(k)$ can trivially be written as the integral of the difference between the reference and target integrands:

$$\Delta P_\alpha(k) \equiv \int \mathrm{d}^3\boldsymbol{q}_1 \dots \mathrm{d}^3\boldsymbol{q}_n \left[P^{\text{target}}_{\alpha,\text{integrand}}(\boldsymbol{k}, \boldsymbol{q}_1, \dots, \boldsymbol{q}_n) - P^{\text{ref}}_{\alpha,\text{integrand}}(\boldsymbol{k}, \boldsymbol{q}_1, \dots, \boldsymbol{q}_n) \right] \ . \tag{5.2}$$

Instead of computing the full P_α^{target} integral separately for each target cosmology, we can precompute P_α^{ref} once, and then only calculate $\Delta P_\alpha(k)$ for each target cosmology. If P_α^{ref} is precomputed with very high precision, then similar precision on the result for P_α^{target} can be achieved with a much lower requirement on the precision of ΔP_α. This incurs a significant reduction of the computational cost of running for several target cosmologies. We stress that this applies independently of the numerical technique used to compute the integrals. We will test our code using the IR-safe MonteCarlo integration of Carrasco, Foreman, et al. (2014a), but our results apply unaltered to any other potentially more efficient integration techniques (Taruya, Bernardeau, et al. 2012; Sherwin and Zaldarriaga 2012; Blas, Garny, and Konstandin 2014; Bertolini, Schutz, Solon, Walsh, et al. 2015; Schmittfull, Vlah, and McDonald 2016; McEwen, Fang, et al. 2016): once the prediction for a reference cosmology

[2] http://web.stanford.edu/~senatore/

has been computed, for the remaining target cosmologies one can directly compute the difference using much lower numerical precision.

One can estimate the relationship between the precision requirements on each term in Eq. (5.1) using basic error propagation. Assuming the numerical integration of $P_\alpha^{\rm ref}$ and $P_\alpha^{\rm target}$ gives uncorrelated errors, we have

$$\sigma_\Delta^2 = \sigma_{\rm ref}^2 + \sigma_{\rm target}^2 \ , \tag{5.3}$$

where $\sigma_{\rm target}$ and $\sigma_{\rm ref}$ are the integration errors of the target and reference cosmology loop integrals, and σ_Δ is the uncertainty in the integration (5.2). Defining the corresponding relative errors

$$\epsilon_{\rm target} \equiv \frac{\sigma_{\rm target}}{|P_\alpha^{\rm target}|} \ , \quad \epsilon_{\rm ref} \equiv \frac{\sigma_{\rm ref}}{|P_\alpha^{\rm ref}|} \ , \quad \epsilon_\Delta \equiv \frac{\sigma_\Delta}{|\Delta P_\alpha|} \ , \tag{5.4}$$

Eq. (5.3) can be rewritten as

$$\epsilon_\Delta = \left|\frac{\Delta P_\alpha}{P_\alpha^{\rm target}}\right|^{-1} \sqrt{\epsilon_{\rm target}^2 + \epsilon_{\rm ref}^2 \left(\frac{P_\alpha^{\rm ref}}{P_\alpha^{\rm target}}\right)^2} \approx \left|\frac{\Delta P_\alpha}{P_\alpha^{\rm target}}\right|^{-1} \epsilon_{\rm target} \ , \tag{5.5}$$

where the approximation is valid because $|P_\alpha^{\rm ref}/P_\alpha^{\rm target}| \sim \mathcal{O}(1)$ and $\epsilon_{\rm target} \gtrsim \epsilon_{\rm ref}$ (in other words, on the target cosmology we will always request at best similar precision to what we have used for the reference cosmology).

At this point, we can further reduce the difference between the target and reference cosmology by taking advantage of the linearity of Eq. (5.2). In fact, we can exactly account for the difference caused by the primordial amplitude of scalar fluctuations A_s with the following modified difference,

$$\Delta\tilde{P}_\alpha(k) \equiv \int {\rm d}^3\boldsymbol{q}_1 \ldots {\rm d}^3\boldsymbol{q}_n \left[P_{\alpha,{\rm integrand}}^{\rm target}(\boldsymbol{k},\boldsymbol{q}_1,\ldots,\boldsymbol{q}_n) - \left(\frac{A_s^{\rm target}}{A_s^{\rm ref}}\right)^{L+1} P_{\alpha,{\rm integrand}}^{\rm ref}(\boldsymbol{k},\boldsymbol{q}_1,\ldots,\boldsymbol{q}_n)\right] , \tag{5.6}$$

for any L-loop integral and adjusting Eq. (5.1) accordingly. Hence, Eq. (5.5) can be rewritten as

$$\epsilon_\Delta \approx \left|\frac{\Delta\tilde{P}_\alpha}{P_\alpha^{\rm target}}\right|^{-1} \epsilon_{\rm target} \ , \tag{5.7}$$

and this equation can then be used to determine the value of ϵ_Δ that will yield a certain desired value for $\epsilon_{\rm target}$.

Given their low dimensionality, one-loop integrals are calculated very efficiently and we can simply replace the k-dependent ratio in Eq. (5.7) with a constant that guarantees sub-percent accuracy over the entire range of scales we are interested in. We find that

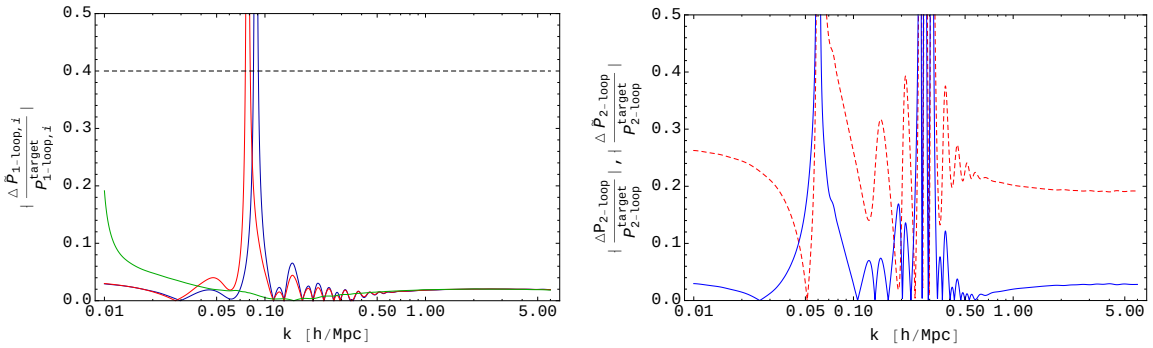

Fig. 5.1 *Left:* The ratio $\Delta\tilde{P}_\alpha(k)/P_\alpha^{\text{target}}$ for the one-loop terms that enter the two-loop EFTofLSS matter power spectrum (see Sec. 5.4 for more details): $P_{\text{1-loop}}$ (*blue*), $P_{\text{1-loop}}^{(c_s)}$ (*red*) and $P_{\text{1-loop}}^{(\text{quad},1)}$ (*green*). $\Delta\tilde{P}_\alpha$ is given by Eq. (5.6) with $L = 1$, and we show results for the `cosmo_5` test cosmology (given in Table 5.1). The black dashed line is the actual k-independent conservative value used in `CosmoEFT` to set the relative precision required for one-loop integrations (see Eq. (5.7)). *Right:* The same ratio for $P_{\text{2-loop}}$, again for the `cosmo_5` cosmology. The dashed red curve uses Eq. (5.2), while the solid blue curve uses the adjusted form, Eq. (5.6), with $P_{\text{2-loop}}^{\text{target/ref}}$ evaluated through direct integration. For general cosmologies, Eq. (5.6) shows a similar improvement over Eq. (5.2) in removing most of the difference associated with the cosmological parameter A_s.

using $\left|\Delta\tilde{P}_{\text{1-loop}}/P_{\text{1-loop}}^{\text{target}}\right| = 0.4$ always overestimates the real ratio (except at zero-crossing); an example of this is shown in the left panel of Fig. 5.1 (We use 0.4 to enable the code to handle cosmologies for which the ratio $\left|\Delta\tilde{P}_{\text{1-loop}}/P_{\text{1-loop}}^{\text{target}}\right|$ will likely be higher than that shown in Fig. 5.1; we have checked that using 0.2 instead of 0.4 does not appreciably affect the code's performance.). When fixing $\epsilon_{\text{target}} = 0.5\%$ and $\left|\Delta\tilde{P}_{\text{1-loop}}/P_{\text{1-loop}}^{\text{target}}\right| = 0.4$, Eq. (5.7) sets $\epsilon_\Delta = 1.25\%$ for all wavenumbers. Due to our overestimation of the true value of $\left|\Delta\tilde{P}_{\text{1-loop}}/P_{\text{1-loop}}^{\text{target}}\right|$, this will result in a target precision even better than 0.5%; in Sec. 5.2.3, we will show this explicitly for several test cosmologies.

A similar procedure works for two-loop integrals, which are, on the other hand, more computationally intensive. The right panel of Fig. 5.1 illustrates the effectiveness of Eq. (5.6) in removing most of the difference associated with the cosmological parameters. This figure also illustrates that, if we can obtain a good estimation for $\Delta\tilde{P}_{\text{2-loop}}/P_{\text{2-loop}}^{\text{target}}$ as a function of k, we can then adjust ϵ_Δ to obtain the same ϵ_{target} at each k, possibly incurring a great reduction of computational expense. Obviously, we cannot use $P_{\text{2-loop}}^{\text{target}}$ to calculate the ratio in Eq. (5.7), since this is the final goal of the computation. However, the main contributor to the difference $\Delta\tilde{P}_{\text{2-loop}}$ is the difference between the linear power spectra that enter into the expressions for $P_{\text{2-loop}}^{\text{target}}$ and $P_{\text{2-loop}}^{\text{ref}}$. These power spectra appear in the integrands of each quantity, but since these integrands will be dominated by the region where all internal momenta are of order k, we can approximate the difference between $P_{\text{2-loop}}^{\text{target}}$ and $P_{\text{2-loop}}^{\text{ref}}$ by replacing each one with the

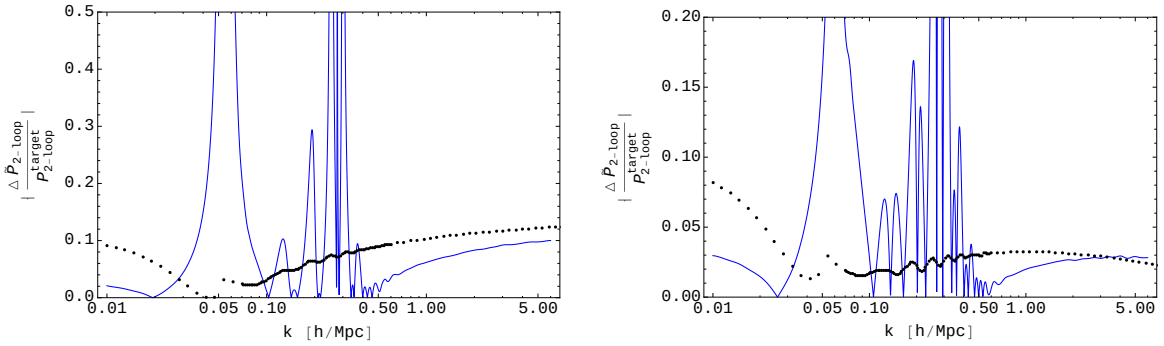

Fig. 5.2 Comparison of estimate (Eq. (5.8), with the modifications described in the main text; *black points*) and exact calculation of $|\Delta\tilde{P}_{\text{2-loop}}/P^{\text{target}}_{\text{2-loop}}|$ (*blue lines*) for two test cosmologies, `cosmo_1` (*left*) and `cosmo_5` (*right*), given in Table 5.1. On average, for $k \gtrsim 0.5\,h\,\text{Mpc}^{-1}$, the estimate slightly over-predicts the exact calculation, but this only means that the precision requested for the integration of $\Delta\tilde{P}_{\text{2-loop}}$ is slightly more conservative than necessary. For lower wavenumbers, the estimate is less precise, but, as we describe in the text, the required precision is also lower. Also, the estimate has the desirable feature of automatically limiting the precision requested close to the zero-crossings of $P^{\text{target}}_{\text{2-loop}}(k)$, by setting a ceiling on the value of $|\Delta\tilde{P}_{\text{2-loop}}/P^{\text{target}}_{\text{2-loop}}|$ in Eq. (5.8).

appropriate power of the linear power spectrum $P_{11}(k)$, obtaining [3]:

$$\left|\frac{\Delta\tilde{P}_{\text{2-loop}}}{P^{\text{target}}_{\text{2-loop}}}\right| \approx \left|1 - \left(\frac{A_s^{\text{target}}}{A_s^{\text{ref}}}\right)^3 \left(\frac{P_{11}^{\text{ref}}(k)}{P_{11}^{\text{target}}(k)}\right)^3\right| . \tag{5.8}$$

However, this estimate makes predictions that are systematically in antiphase with BAO of the exact calculations of $|\Delta\tilde{P}_{\text{2-loop}}/P^{\text{target}}_{\text{2-loop}}|$. Therefore, for $0.05\,h\,\text{Mpc}^{-1} < k < 0.5\,h\,\text{Mpc}^{-1}$ we smooth the estimated adjusted ratios with a top-hat window function,

$$\left|\frac{\Delta\tilde{P}_{\text{2-loop}}(k)}{P^{\text{target}}_{\text{2-loop}}(k)}\right|_{\text{smooth}} = \frac{1}{\Delta k}\int_{k-\Delta k/2}^{k+\Delta k/2} \left|\frac{\Delta\tilde{P}_{\text{2-loop}}(k')}{P^{\text{target}}_{\text{2-loop}}(k')}\right| \mathrm{d}k' , \tag{5.9}$$

where we set the window function width to $\Delta k = 0.1\,h\,\text{Mpc}^{-1}$, roughly equal to twice the BAO period in k-space. The resulting estimate allows us to use Eq. (5.7) to fix ϵ_Δ as a function of k. In Fig. 5.2, we compare this estimate to the exact calculation of $|\Delta\tilde{P}_{\text{2-loop}}/P^{\text{target}}_{\text{2-loop}}|$ in two test cases. The estimate is slightly higher than the exact calculation for $k \gtrsim 0.5\,h\,\text{Mpc}^{-1}$, leading to conservative precision requirements on the integral evaluation. On the other hand, it fails to capture the exact relative ratio for smaller k's. As we shall explain below, this is of marginal concern, since we only aim for global subpercent precision on the final matter power spectrum predictions, and $P_{\text{2-loop}}$ is very small at small wavenumbers. Moreover, to save computational time where $\Delta\tilde{P}_{\text{2-loop}} \approx 0$, we include the additional requirement $\sigma_\Delta = 1.5(\text{Mpc}/h)^3$ for the

[3] For higher loops one can trivially adjust this estimate.

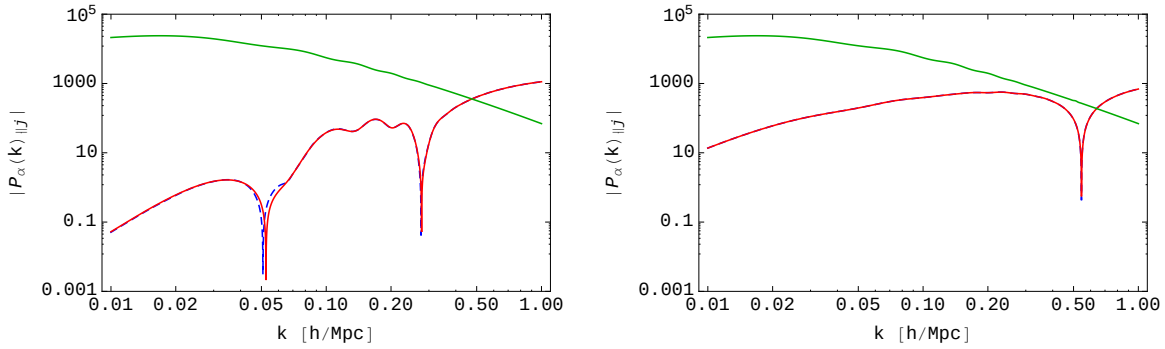

Fig. 5.3 $P_{11}(k)_{\|2}$ (green), $P_{\text{2-loop}}(k)_{\|0}$ from CosmoEFT (dashed blue), and $P_{\text{2-loop}}(k)_{\|0}$ evaluated through full integration (red), all for the cosmo_5 test cosmology (see Table 5.1). We show the IR-resummed version of each term, as indicated by the subscripts. The $P_{\text{2-loop}}$ curves in the left panel are $P_{\text{2-loop}}^{(\text{UV-improved})}$, while the curves in the right panel are $P_{\text{2-loop}}^{(\text{full})}$. The fact that $P_{\text{2-loop}}^{(\text{UV-improved})} \ll P_{11}$ at low k makes the small deviations we observe in the left panel acceptable. On the other hand, $P_{\text{2-loop}}^{(\text{full})}$ amounts to $\sim 1\%$ of P_{11} already at $k \approx 0.05\,h\,\text{Mpc}^{-1}$, leading to more demanding requirements on the precision of $P_{\text{2-loop}}$ if $P_{\text{2-loop}}^{(\text{full})}$ is used.

absolute precision on the two-loop integral derived from Eq. (5.6) (the typical values of $P(k)$ are of order a thousand in this units). This is chosen by the integration routine whenever it turns out to be less stringent than the relative precision ϵ_Δ. Note also that $P_{\text{2-loop}}(k)$ typically possesses two zero crossings, one around $k \sim 0.05\,h\,\text{Mpc}^{-1}$ and a second for $k \sim 0.3\,h\,\text{Mpc}^{-1}$. Around these points, we do not require high precision on the evaluation of $P_{\text{2-loop}}(k)$, and this is also accounted for by our estimates, which automatically impose a ceiling on the value of $|\Delta\tilde{P}_{\text{2-loop}}/P_{\text{2-loop}}^{\text{target}}|$ (and therefore a floor on ϵ_Δ) in the relevant regions.

For the calculations above, as well as within CosmoEFT, we have employed the "UV-improved" version of $P_{\text{2-loop}}$, which is defined by analytically subtracting most of the leading $k^2 P_{11}$ contribution from the full two-loop term, $P_{\text{2-loop}}^{(\text{full})}$ (see details in Foreman, Perrier, and Senatore 2016). The advantage of $P_{\text{2-loop}}^{(\text{UV-improved})}$ over $P_{\text{2-loop}}^{(\text{full})}$ is clear from Fig. 5.3, where the two versions are compared to P_{11} (which is the leading term in the total prediction for the matter power spectrum), and all quantities are shown after resummation following Senatore and Zaldarriaga (2015); Angulo, Foreman, et al. (2015). In particular, the relative error on the EFTofLSS power spectrum prediction coming from the two-loop term is to a good approximation given by the difference between $P_{\text{2-loop}}$ evaluated with Eq. (5.6) and that obtained with the full integration, rescaled by the tree term P_{11}. Therefore, even though using $P_{\text{2-loop}}^{(\text{UV-improved})}$ we cannot achieve $\epsilon_{\text{target}} = 0.5\%$ for $k \lesssim 0.35\,h\,\text{Mpc}^{-1}$, this is more than compensated by its smallness compared to P_{11}. Because of its larger overall amplitude, the same argument does not apply to $P_{\text{2-loop}}^{(\text{full})}$, thus demanding more stringent requirements on its precision. For the sake of completeness, in App. C.0.1 we show how the estimate Eq. (5.8) performs using $P_{\text{2-loop}}^{(\text{full})}$, and in App. C.0.2 we also provide a procedure to more

accurately estimate $|\Delta\tilde{P}_{\text{2-loop}}/P^{\text{target}}_{\text{2-loop}}|$ for this case. For the rest of the paper, $P_{\text{2-loop}}$ will refer to $P^{(\text{UV-improved})}_{\text{2-loop}}$.

As a side remark, target cosmologies that differ from the reference cosmology only for A_s^{target} are readily evaluated in `CosmoEFT` by multiplying the reference loop integrals by a suitable factor $(A_s^{\text{target}}/A_s^{\text{ref}})^{L+1}$.

5.2.2 Details of implementation

Inputs

The `CosmoEFT` code implements the idea we have presented in Sec. 5.2.1. To evaluate the integrals, we use a modification of the Copter library (Carlson, White, and Padmanabhan 2009) that implements the IR-safe integrands from Carrasco, Foreman, et al. (2014a) and computes the loop integrals using Monte Carlo integration routines from the CUBA library (Hahn 2005). Needless to say, the evaluation of the integrals can be performed using some of the alternative techniques presented in, e.g. Taruya, Bernardeau, et al. (2012); Sherwin and Zaldarriaga (2012); Blas, Garny, and Konstandin (2014); Bertolini, Schutz, Solon, Walsh, et al. (2015); Schmittfull, Vlah, and McDonald (2016); McEwen, Fang, et al. (2016). While this might affect the evaluation time of a single integral, it will not affect the relative gain in computational cost that we obtain in computing a target cosmology with our method rather than with a direct computation [4]. We define target cosmologies by means of the following vector of five cosmological parameters:

$$\boldsymbol{\theta} \equiv \{\omega_b, \omega_c, \ln(10^{10} A_s), n_s, h\} \ , \tag{5.10}$$

with all other cosmological parameters fixed to the reference cosmology, for which we use the current best-fit *Planck* parameters (Ade et al. 2015a)[5]. The reference values of the five parameters listed in Eq. (5.10) are shown in the first row of Table 5.1.

`CosmoEFT` reads an initialization file with the following variables that specify the input cosmology:

```
h = 0.6727 #Hubble parameter H_0/(100 km/s/Mpc)
Tcmb = 2.7255 #CMB temperature today
n = 0.9645 #primordial spectral index
Omega_m = 0.313905 #total matter density
Omega_b = 0.0491685 #baryon matter density
sigma8 = 0.843107 #power spectrum normalization
tkfile = ./input/tk_planck_2015.dat #path to transfer function file
```

[4] Apart for adjustment due to how, in the various methods, the numerical error scales with the number of evaluations. Such an adjustment can be trivially performed.

[5] Extension to additional cosmological parameters is relatively straightforward.

```
outdir = ./output/ #output directory
```

(Note that the code takes $\Omega_{\rm m} \equiv (\omega_b + \omega_c)/h^2$ and $\Omega_b \equiv \omega_b/h^2$ instead of ω_c and ω_b as inputs, as well as σ_8 in place of A_s.) The transfer function can be calculated using a Boltzmann code such as `CAMB` [6] or `CLASS` [7], and must be evaluated up to $k \sim 10\,h\,\mathrm{Mpc}^{-1}$. Together with the cosmological parameters listed above, it is then used to compute the linear power spectrum that is employed in subsequent one- and two-loop integrations. In addition, the code reads in the EFTofLSS loop integrals for the reference cosmology, which have been precomputed with precision $\epsilon_{\rm ref} = 0.1\%$ by direct integration. By default, the required precision on the target cosmology is hard-coded and fixed to $\epsilon_{\rm target} = 0.5\%$ for all loop integrals ($\epsilon_{\rm target}$ is named `epsrelTar` in the code). For the one-loop terms, using Eq. (5.7) with the adjusted ratios set to 0.4 (see Fig. 5.1), we require a precision on the difference integral Eq. (5.6) of $\epsilon_\Delta = 1.25\%$, independent of wavenumber and cosmology.

Outputs

`CosmoEFT` outputs two text files, `pk.dat` and `pXloop.dat`, containing the linear power spectrum (P_{11}) and the loop integrals ($P_{\text{1-loop}}$, $P^{(c_{\rm s})}_{\text{1-loop}}$, $P_{\text{2-loop}}$, $P^{(\text{quad},1)}_{\text{1-loop}}$) respectively, all evaluated at $z = 0$ for the specific input cosmology. Wavenumbers are sampled sparsely in the ranges $0.01\,h\,\mathrm{Mpc}^{-1} \leqslant k \leqslant 0.06\,h\,\mathrm{Mpc}^{-1}$ and $0.6\,h\,\mathrm{Mpc}^{-1} \leqslant k \lesssim 10\,h\,\mathrm{Mpc}^{-1}$, whereas we choose a denser sampling in between to accurately follow the BAO. In total, we sample each loop integral at 126 points (shown, for example, by the black points in Fig. 5.2).

The output files from `CosmoEFT`, along with $\Omega_{\rm m}$ and desired redshift, are then used as input for the IR-resummation code `ResumEFT` [8], also released with this work. `ResumEFT` implements the IR-resummation technique developed in Senatore and Zaldarriaga (2015); Angulo, Foreman, et al. (2015) to incorporate the effect of large-scale displacements in the EFTofLSS. Its output consists of a text file including all resummed EFTofLSS terms relevant for the evaluation of the matter power spectrum at tree, one- and two-loop levels. `ResumEFT` makes use of the `FFTLog` algorithm, as described in Hamilton (2000).

5.2.3 Tests and performance

We now proceed to evaluate the performance of `CosmoEFT` by comparing the code's output for various loop integrals to the results of the full integration (*i.e.* without the reference-target split described in Sec. 5.2.1). We quantify the deviation of each test cosmology from the

[6] http://camb.info
[7] http://class-code.net
[8] http://web.stanford.edu/~senatore/

Table 5.1 Cosmological parameters for the reference and test cosmologies employed in this work. Next to each test cosmology, we specify the number of sigmas away from the reference cosmology, as dictated by Eq. (5.11).

Cosmology	ω_b	ω_c	$\ln(10^{10}A_s)$	n_s	h
Reference	0.02225	0.1198	3.094	0.9645	0.6727
`cosmo_1` (3σ)	0.02257	0.1183	3.196	0.9645	0.6793
`cosmo_2` (3σ)	0.02257	0.1168	3.026	0.9645	0.6859
`cosmo_3` (3σ)	0.02193	0.1213	2.992	0.9645	0.6661
`cosmo_4` (3σ)	0.02193	0.1228	3.162	0.9645	0.6595
`cosmo_5` (3σ)	0.02241	0.1213	3.026	0.9596	0.6661
`cosmo_6` (3σ)	0.02209	0.1183	3.162	0.9694	0.6793
`cosmo_7` (4σ)	0.02193	0.1183	2.992	0.9645	0.6727
`cosmo_8` (4σ)	0.02177	0.1183	3.128	0.9645	0.6727
`cosmo_9` (5σ)	0.02161	0.1258	2.924	0.9449	0.6463
`cosmo_10` (3σ)	0.02177	0.1243	2.992	0.9498	0.6529
`cosmo_11` (3σ)	0.02273	0.1153	3.196	0.9792	0.6925

reference (*Planck*) cosmology through the following definition: an "$n\sigma$-cosmology" is defined as a point $\boldsymbol{\theta}$ in parameter space separated from the reference cosmology by n standard deviations, accounting for all the covariances between the cosmological parameters. More formally, the point $\boldsymbol{\theta}$ defines an $n\sigma$-cosmology if it is contained in a thin shell around the 5-dimensional hyper-ellipsoid defined by

$$(\boldsymbol{\theta} - \boldsymbol{\theta}^{\rm ref})^{\rm T}\Sigma_5^{-1}(\boldsymbol{\theta} - \boldsymbol{\theta}^{\rm ref}) = \chi^2_5(p) \ . \tag{5.11}$$

Here, Σ_5^{-1} represents the inverse of the 5×5 covariance submatrix obtained by selecting the appropriate rows and columns from the covariance matrix for the combination "TT+TE+EE+lowP" in Ade et al. (2015a), giving a reasonable account for the covariances between our 5 chosen parameters when all others are marginalized over [9]:

$$\Sigma_5 = \begin{pmatrix} 2.56\times10^{-8} & -1.5\times10^{-7} & 1.8\times10^{-6} & 3.99\times10^{-7} & 7.95\times10^{-7} \\ -1.5\times10^{-7} & 2.25\times10^{-6} & -1.72\times10^{-5} & -5.67\times10^{-6} & -9.62\times10^{-6} \\ 1.8\times10^{-6} & -1.72\times10^{-5} & 1.16\times10^{-3} & 6.54\times10^{-5} & 8.08\times10^{-5} \\ 3.99\times10^{-7} & -5.67\times10^{-6} & 6.54\times10^{-5} & 2.4\times10^{-5} & 2.48\times10^{-5} \\ 7.95\times10^{-7} & -9.62\times10^{-6} & 8.08\times10^{-5} & 2.48\times10^{-5} & 4.36\times10^{-5} \end{pmatrix} . \tag{5.13}$$

[9] For easy reference, 1σ marginalized uncertainties on each parameter from Eq. (5.13) are given below:

$$\sigma(\omega_b) = 0.00016, \quad \sigma(\omega_c) = 0.0015, \quad \sigma(\ln[10^{10}A_s]) = 0.034, \quad \sigma(n_s) = 0.0049, \quad \sigma(h) = 0.0066 \ . \tag{5.12}$$

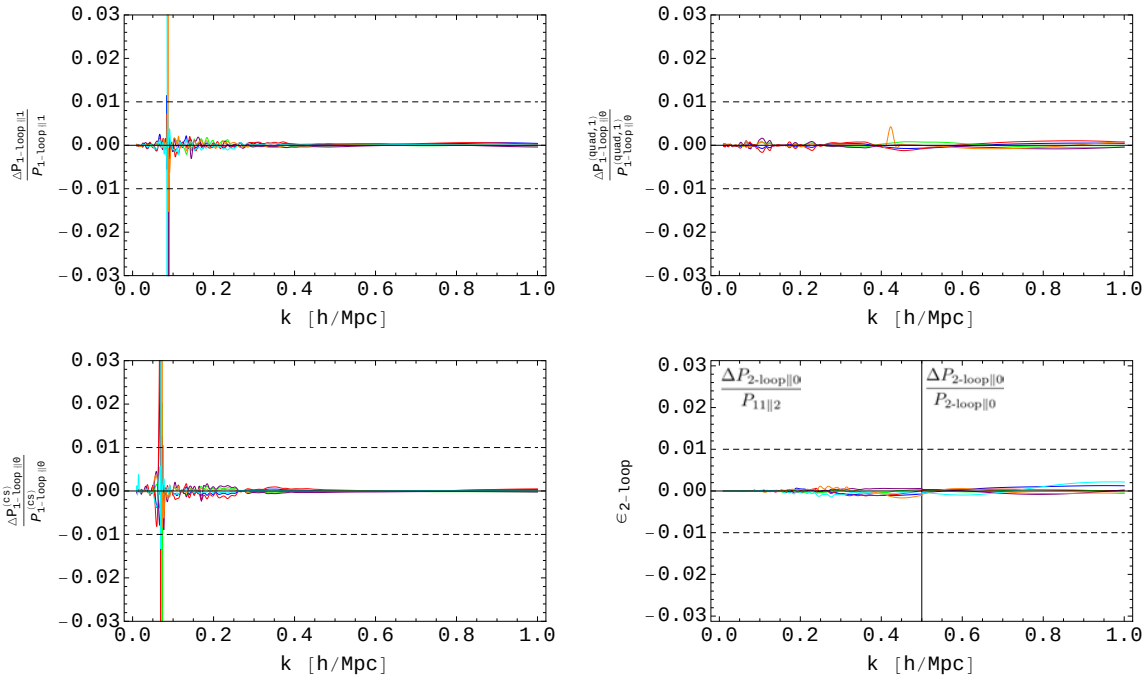

Fig. 5.4 IR-resummed CosmoEFT outputs for our 3σ-cosmologies cosmo_1-6 (in order: blue, red, green, purple, orange, cyan) relative to the direct calculation of the full integrand with precision $\epsilon = 0.1\%$. Here $\epsilon_{\text{target}} = 0.5\%$ for all panels, and spikes are due to zero-crossing. Subscripts $\|0, \|1$ denotes the IR-resummation order as in Senatore and Zaldarriaga 2015. Dashed lines mark 1% departures from direct calculations. For $P_{2\text{-loop}}$ we opt for showing two quantities relevant on two disjoint scale intervals, $k < 0.5\,h\,\text{Mpc}^{-1}$ and $k > 0.5\,h\,\text{Mpc}^{-1}$. $\Delta P_{2\text{-loop}\|0}/P_{11\|2}$ indicates the error on the matter power spectrum predictions, and $\Delta P_{2\text{-loop}\|0}/P_{2\text{-loop}\|0}$ confirms the performance of our estimates for smaller scales.

In Eq. (5.11), $\chi^2_5(p)$ is the quantile function for probability p of the chi-squared distribution with 5 degrees of freedom. Thus, for 3σ, 4σ and 5σ deviations from the reference cosmology $p = 0.997, 0.99993, 0.9999994$, respectively.

In this section, we will examine a number of selected 3σ-cosmologies, given (along with the reference cosmology) in Table 5.1. All cosmologies in this table have $\Omega_k = 0$, $w = -1$, and $k_{\text{pivot}} = 0.05\,\text{Mpc}^{-1}$. Further tests for the 4σ- and 5σ-cosmologies in Table 5.1 are shown in App. D.

We verify the integration prescription described above in Fig. 5.4, where we compare the outputs of CosmoEFT and the direct calculation of P_α^{target} for different integrals entering in the two-loop matter power spectrum prediction. Note that in all cases we have resummed the effect of large-scale displacement fields using ResumEFT. We find that the output for each P_α^{target} is indeed within $\sim$0.5% of the full computation over a wide range of scales, and even better than that for the one-loop integrals. A slight exception is $P_{2\text{-loop}}$. For $P_{2\text{-loop}}$ we divide the range of interest in two subsets, and the separation scale is chosen

around where $P_{\text{2-loop}} \sim P_{11}$ at $z = 0$. As discussed in Sec. 5.2.1, departures from the full integration are much larger than the required precision on scales $k < 0.35\,h\,\text{Mpc}^{-1}$ (they are about 2-3% in this range of k's). However, this error propagates to the final matter power spectrum as the ratio $\Delta P_{\text{2-loop}}/P_{11}$, and Fig. 5.4 shows that this remains within 0.2% for $k < 0.5\,h\,\text{Mpc}^{-1}$ at $z = 0$. Notably, this interval extends with redshift to increasingly smaller scales, in that $P_{\text{2-loop}} \sim D(z)^6$ whereas $P_{11} \sim D(z)^2$, with $D(z)$ denoting the growth factor at redshift z. On scales $k > 0.5\,h\,\text{Mpc}^{-1}$, where our estimate Eq. (5.8) overestimates the exact calculation, differences between `CosmoEFT` and the full integration are well within the requirement $\epsilon_\Delta = 0.5\%$. Of course, overall better precision can be achieved if ϵ_{target} is adjusted to smaller values. However, within `CosmoEFT` special care must be taken to ensure that the variables encoding the maximum number of integral evaluations, i.e. `maxeval` and `maxeval2loop`, are properly set to ensure that the computation is not halted before the desired precision is achieved.

In Table 5.2, we show the computing time required for various evaluations, including the 4σ- and 5σ-cosmologies presented in App. D. The integration strategy outlined in Sec. 5.2.1 reduces the computational cost by about two orders of magnitude compared to a direct computation of P_α^{target} (though the precision requirement on $P_{\text{2-loop}}$ at $k \lesssim 0.5\,h\,\text{Mpc}^{-1}$ is different by a factor of a few in the direct or `CosmoEFT` computations).

The main interest for us in this paper is to make the exploration of the various cosmologies much less computationally expensive than the direct computation. Therefore, in the context of this paper, the most important information is the relative gain with respect to the direct computation. However, one should keep in mind that both the time for obtaining the reference cosmology, as well as the running time of `CosmoEFT`, can be scaled down, probably in an obvious way, by implementing better integration techniques for the perturbation theory expressions, such as those proposed in Taruya, Bernardeau, et al. (2012); Sherwin and Zaldarriaga (2012); Blas, Garny, and Konstandin (2014); Bertolini, Schutz, Solon, Walsh, et al. (2015); Schmittfull, Vlah, and McDonald (2016); McEwen, Fang, et al. (2016). Furthermore, further improvements in the actual running time (wall time) can be achieved with multi-cored processors. In fact, thanks to the high degree of parallelism of the integration routines, we have verified that wall time scales down approximately as the effective number of cores. `CosmoEFT` can greatly benefit from recent advances in CPU technology, with improvements on running times that can be up to three times faster than ours.

5.3 `TaylorEFT`: Taylor expansion of the loop integrals

With the latest *Planck* data release our knowledge of the cosmological parameters in flat ΛCDM cosmologies has reached percent precision (Ade et al. 2015a). In light of this advance, along with the fact that these constraints will only improve if they are combined with

Table 5.2 Computational performance of CosmoEFT for our test cosmologies. CPU time is the amount of time used by all CPUs when executing the code, while wall time is the actual running time of the code (using a quad-core processor with hyper-threading). CPU times for the direct calculation of loop integrals correspond to a precision of $\epsilon = 0.5\%$, and are to a large extent independent of the input cosmology. The "speed-up factor" is just the ratio of the CosmoEFT and direct CPU times.

Cosmology	CPU time direct[a]	CPU time CosmoEFT[b]	Speed-up factor	Wall time[b]
cosmo_1	48 hours	28 min	103	3.6 min
cosmo_2		43 min	67	5.6 min
cosmo_3		15 min	192	2.1 min
cosmo_4		58 min	50	7.7 min
cosmo_5		7 min	411	53 sec
cosmo_6		8 min	360	1.1 min
cosmo_7		10 min	288	1.4 min
cosmo_8		10 min	288	1.5 min
cosmo_9		37 min	78	5.2 min
cosmo_10		29 min	99	3.8 min
cosmo_11		65 min	44	8.6 min

[a] Running on Quad-Core AMD Opteron™Processor 2376, 2.3 GHz. The actual CPU-time on this CPU is 58 hours, although to match the Quad-Core Intel Core™i7 performance we multiply this time by a correction factor of 0.82.
[b] Running on Quad-Core Intel Core™i7, 2.4 GHz.

information from late-time cosmological probes, it seems reasonable to restrict the EFTofLSS predictions to a sufficiently large region around our *Planck*-like reference cosmology. This problem naturally lends itself to a Taylor expansion approach, where each loop integral is represented by a Taylor series up to quadratic order (or higher if necessary) in the deviation of the cosmological parameters from those of the reference cosmology. Such an approach eliminates the need to perform direct integrations to obtain the results of the loop integrals, provided that we are only concerned with cosmologies sufficiently close to the reference one, after the few cosmologies that are needed to construct the Taylor expansion have been evaluated.

5.3.1 Details of implementation

We implement this approach as follows. For each loop integral P_α we can write

$$P_\alpha(k) \approx P_\alpha(k)|_{\boldsymbol{\theta}^{\rm ref}} + \sum_i \Delta\theta_i \left.\frac{\partial P_\alpha(k)}{\partial\theta_i}\right|_{\boldsymbol{\theta}=\boldsymbol{\theta}^{\rm ref}} + \frac{1}{2}\sum_{i,j}\Delta\theta_i\Delta\theta_j \left.\frac{\partial^2 P_\alpha(k)}{\partial\theta_i\,\partial\theta_j}\right|_{\boldsymbol{\theta}=\boldsymbol{\theta}^{\rm ref}}, \tag{5.14}$$

where $\Delta\theta_i \equiv \theta_i - \theta_i^{\rm ref}$. The derivatives are evaluated numerically using the compact stencil in Fig. 5.5. Considering a pair of parameters $\{\theta_i, \theta_j\}$, and fixing the remaining ones to their reference values, the derivatives at the reference cosmology are obtained with the following second order central differences:

$$\left.\frac{\partial P_\alpha}{\partial\theta_i}\right|_{\boldsymbol{\theta}^{\rm ref}} \approx \frac{P_\alpha^{i+1,j} - P_\alpha^{i-1,j}}{2\sigma_i}\,, \tag{5.15}$$

$$\left.\frac{\partial P_\alpha}{\partial\theta_j}\right|_{\boldsymbol{\theta}^{\rm ref}} \approx \frac{P_\alpha^{i,j+1} - P_\alpha^{i,j-1}}{2\sigma_j}\,, \tag{5.16}$$

$$\left.\frac{\partial^2 P_\alpha}{\partial\theta_i^2}\right|_{\boldsymbol{\theta}^{\rm ref}} \approx \frac{P_\alpha^{i+1,j} - 2P_\alpha^{i,j} + P_\alpha^{i-1,j}}{\sigma_i^2}\,, \tag{5.17}$$

$$\left.\frac{\partial^2 P_\alpha}{\partial\theta_j^2}\right|_{\boldsymbol{\theta}^{\rm ref}} \approx \frac{P_\alpha^{i,j+1} - 2P_\alpha^{i,j} + P_\alpha^{i,j-1}}{\sigma_j^2}\,, \tag{5.18}$$

$$\left.\frac{\partial^2 P_\alpha}{\partial\theta_i\partial\theta_j}\right|_{\boldsymbol{\theta}^{\rm ref}} \approx \frac{P_\alpha^{i+1,j+1} - P_\alpha^{i+1,j-1} - P_\alpha^{i-1,j+1} + P_\alpha^{i-1,j-1}}{4\sigma_i\sigma_j}\,. \tag{5.19}$$

Here, for the sake of clarity, we have removed the k-dependence of the loop integrals, and have adopted the shorthands $P_\alpha^{i,j} \equiv P_\alpha(\theta_i^{\rm ref}, \theta_j^{\rm ref})$, $P_\alpha^{i+1,j} \equiv P_\alpha(\theta_i^{\rm ref} + \sigma_i, \theta_j^{\rm ref})$, and so forth. Moreover, we have performed the finite differences over the *Planck* uncertainties on each parameter, σ_i, since $\sigma_i/\theta_i^{\rm ref} \lesssim 0.01$. Our loop integrals depend on five cosmological parameters, and so we need 50 cosmologies (excluding the reference one) to evaluate Eqs. (5.15)-(5.19) for all possible combinations. We have done so using a modified version of `CosmoEFT` that evaluates the $P_{\text{2-loop}}^{(\text{full})}$ using $\epsilon_\Delta = 0.5\%$, which for these cosmologies effectively corresponds to

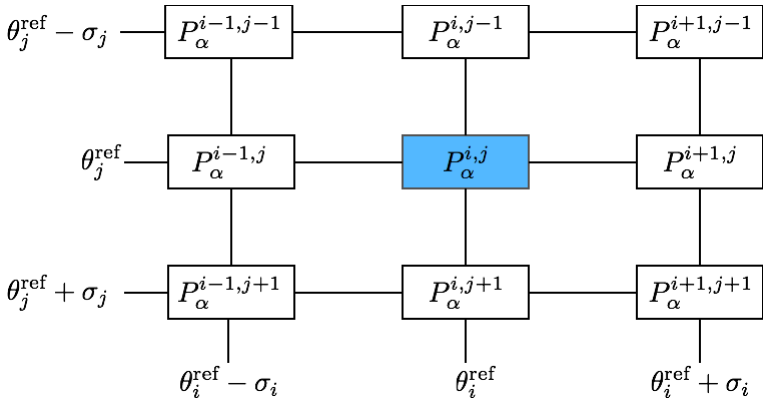

Fig. 5.5 Two-dimensional compact stencil for numerical evaluation of first and second derivatives at $\{\theta_i^{\rm ref}, \theta_j^{\rm ref}\}$. The increments in the two parameters correspond to their *Planck* standard deviations. Loop integrals $P_\alpha^{i,j}$ for the reference cosmology (blue box) are calculated through direct integration with 0.1% precision. The k-dependence has been omitted for clarity.

setting $\epsilon_{\rm target} \approx \epsilon_{\rm ref}$ (see Sec. 5.2), which is important to have sufficient control over numerical errors in the derivatives (we could have alternatively directly used $P_{\text{2-loop}}$, but for the current level of precision $P_{\text{2-loop}}^{\rm (full)}$ was enough.). Note that departures from the reference cosmology along some directions in parameter space can be rather small, so much so that they are dominated by integration errors. In these cases, derivatives can be neglected, and their values are fixed to zero in the expansion in Eq. (5.14).

The Taylor expansion scheme described above allows one to obtain the loop integrals in just a few seconds on a laptop, using a Mathematica script, `TaylorEFT`[10], that we have developed. We store all derivatives in text files within subdirectories organized by loop integral: `fd_<`θ_i`>_<loop>.dat`, for first derivatives, `sd_<`θ_i`>_<loop>.dat`, for pure second derivatives, and `smd_<`θ_i`>_<`θ_j`>_<loop>.dat`, for mixed second derivatives. Derivatives are loaded with the dedicated `Load[]` module in the main `TaylorEFT` script. After specifying a redshift `z0` and the cosmological parameters defining `Cosmology`, the module `CalculateLoops[Cosmology]` reads off the necessary loop expressions using Eq. (5.14) at $z = 0$. `TaylorEFT` also calls `ResumEFT` after the EFT integrals have been obtained, applying the IR-resummation scheme described in Senatore and Zaldarriaga (2015); Angulo, Foreman, et al. (2015) at the chosen redshift `z0`. We shall describe in Sec. 5.4 how this wrapper can be used to directly obtain tree, one- and two-loop matter power spectrum predictions within the EFTofLSS.

5.3.2 Tests

Fig. 5.6 shows how well the resummed EFT loop integrals at $z = 0$ are approximated by the Taylor expansion (5.14) for some of the 3σ-cosmologies from Table 5.1. Clearly, one-loop

[10] http://web.stanford.edu/~senatore/

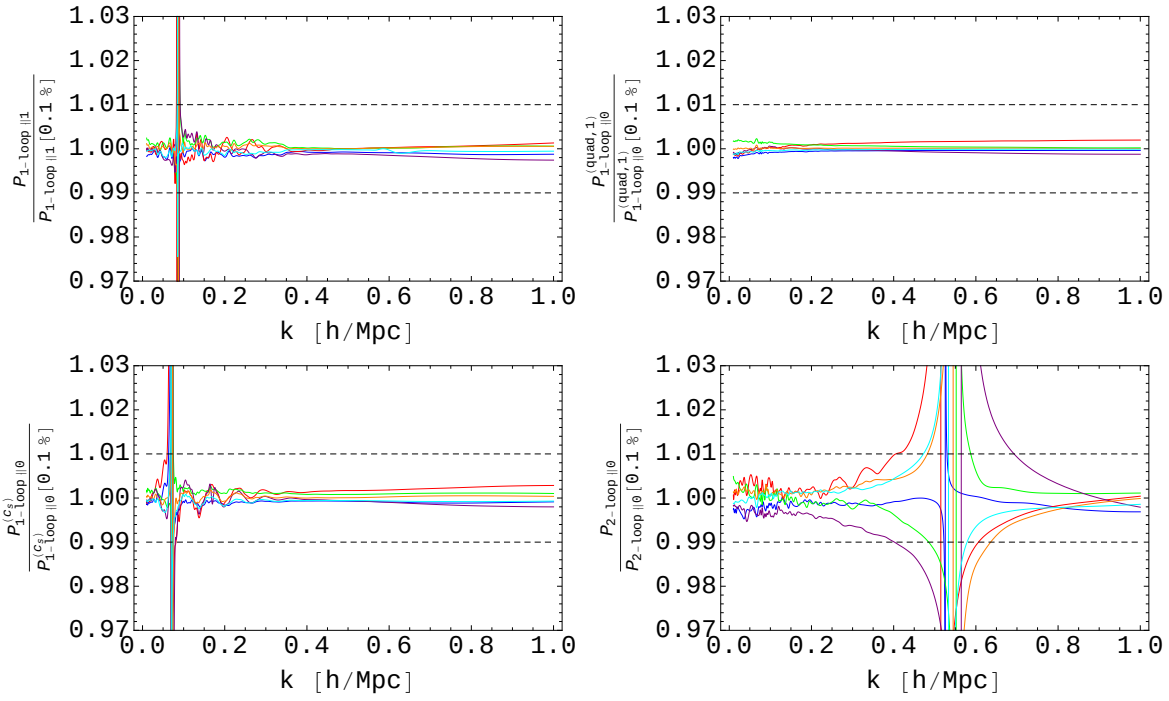

Fig. 5.6 IR-resummed `TaylorEFT` outputs for our 3σ-cosmologies `cosmo_1-6` (in order: blue, red, green, purple, orange, cyan) relative to the direct calculation of the full integrand with precision $\epsilon = 0.1\%$. Spikes are due to zero-crossing and subscripts $\|0, \|1$ denotes the IR-resummation order as in Senatore and Zaldarriaga (2015). Dashed lines mark 1% departures from direct calculations.

integrals reach sub-percent precision over the entire range of scales. $P_{\text{2-loop}}$ exhibits somewhat larger deviations compared to `CosmoEFT` outputs, although still inside the 1% region for a wide range of wavenumbers. In Sec. 5.4, we include two additional cosmologies (`cosmo_10` and `cosmo_11`) to quantify the limits of this implementation. We anticipate here that in order to obtain $P_{\text{EFT-2-loop}}$ within 1% of `FrankenEmu`'s nonlinear $P(k)$ (Heitmann, Lawrence, et al. 2014) [11], each cosmological parameter cannot deviate from its reference value by more than 3σ, i.e. $|\Delta\theta_i| \leqslant 3\sigma$ for any i. In other words, `TaylorEFT` is accurate to within 1% only for cosmologies in a $\sim 3\sigma$ neighborhood of our reference cosmology[12]. Obviously, it is possible that by increasing the order of the Taylor expansion, `TaylorEFT` can be made sufficiently accurate to a larger number of σ's, something that could be straightforwardly implemented.

With this tool at hand, we are now ready to explore the cosmology dependence of the EFTofLSS parameters that incorporate the physics on nonlinear scales.

5.4 The two-loop power spectrum

The two-loop IR-resummed matter power spectrum in the EFTofLSS is given by

$$\begin{aligned} P_{\text{EFT-2-loop}}(k,z) = {} & P_{11}(k,z)_{\|2} + P_{\text{1-loop}}(k,z)_{\|1} - 2(2\pi)c_{s(1)}^2 \left(\frac{k^2}{k_{\text{NL}}^2} P_{11}(k,z)\right)_{\|1} \\ & + P_{\text{2-loop}}(k,z)_{\|0} - 2(2\pi)c_{s(2)}^2 \left(\frac{k^2}{k_{\text{NL}}^2} P_{11}(k,z)\right)_{\|0} \\ & + (2\pi)c_{s(1)}^2 P_{\text{1-loop}}^{(c_s)}(k,z)_{\|0} + (2\pi)^2 \left(c_{s(1)}^2\right)^2 \left(1 + \frac{\zeta + \frac{5}{2}}{2\left(\zeta + \frac{5}{4}\right)}\right) \left(\frac{k^4}{k_{\text{NL}}^4} P_{11}(k,z)\right)_{\|0} \\ & + (2\pi)c_1 P_{\text{1-loop}}^{(\text{quad},1)}(k,z)_{\|0} + 2(2\pi)^2 c_4 \left(\frac{k^4}{k_{\text{NL}}^4} P_{11}(k,z)\right)_{\|0} . \end{aligned} \tag{5.20}$$

Here, each term is resummed applying the formalism developed in Senatore and Zaldarriaga (2015); Angulo, Foreman, et al. (2015) and subscripts follow their notation. For a detailed derivation of Eq. (5.20) see Foreman, Perrier, and Senatore (2016); Carrasco, Foreman, et al. (2014b); Carrasco, Foreman, et al. (2014a); Angulo, Foreman, et al. (2015). We also fix $\zeta = 3$ according to the discussion presented in Foreman and Senatore (2016). Similarly to Foreman, Perrier, and Senatore (2016), in this work we express the EFTofLSS parameters $c_{s(1)}^2$, c_1 in units of $(k_{\text{NL}}/2\,h\text{Mpc}^{-1})^2$ and c_4 in units of $(k_{\text{NL}}/2\,h\text{Mpc}^{-1})^4$, and determine $c_{s(2)}^2$ by matching the one-loop and two-loop EFTofLSS matter power spectrum at the renormalization scale $k_{\text{ren}} = 0.02\,h\,\text{Mpc}^{-1}$. We evaluate P_{11} with the Boltzmann code `CLASS` (Blas, Lesgourgues, and Tram 2011), which within `TaylorEFT` runs through

[11] http://www.hep.anl.gov/cosmology/CosmicEmu/emu.html

[12] This approximately translates to a range in σ_8 of $0.78 \leqslant \sigma_8 \leqslant 0.90$ (see Fig. 5.7).

the designated module `CallCLASS[...]`. In Eq. (5.20) we left implicit both the cosmology dependence and the redshift evolution of the parameters incorporating the nonlinear physics. Below, we investigate these features using `TaylorEFT` in a neighborhood of our reference cosmology, i.e. for cosmologies with $|\Delta\theta_i| \leqslant 3\sigma_i$, where σ_i is the square root of the diagonal element $\Sigma_{5,ii}$ of the covariance matrix in Eq. (5.13).

5.4.1 Cosmology dependence of EFT parameters

Since the cosmology-dependence of the EFTofLSS parameters is not predicted by the theory, we opt once again for a Taylor expansion approach that can capture the cosmology-dependence for relatively small deviations around our reference cosmology. This requires us to find the derivatives of the EFTofLSS parameters with respect to different cosmological parameters. We do so by fitting Eq. (5.20) to `FrankenEmu` output power spectra for an ensemble of cosmologies (the details of the fits are described below), and then finding the required derivatives by fitting the Taylor expansion formula to the ensemble of fitted EFT parameters. The ensemble of cosmologies is composed of points $\boldsymbol{\theta}$ in the parameter space associated with the nodes of a 5-dimensional cubic lattice centered at our reference cosmology, with lattice spacing σ_i in each direction. (We also apply the additional constraint that $|\Delta\theta_i| \leqslant 3\sigma_i$.)

By testing Taylor expansions evaluated at different orders, we find that the following form of the expansion (up to third order in all cosmological parameters, plus up to fourth order in σ_8, due to its strong effect on the EFT parameters) is sufficient to guarantee 1% precision on the final prediction for the power spectrum:

$$c_X(\boldsymbol{\theta}, z) \approx c_X|_{\boldsymbol{\theta}^{\rm ref}} + \sum_i \Delta\theta_i \left.\frac{\partial c_X}{\partial\theta_i}\right|_{\boldsymbol{\theta}=\boldsymbol{\theta}^{\rm ref}} + \frac{1}{2}\sum_{i,j}\Delta\theta_i\Delta\theta_j \left.\frac{\partial^2 c_X}{\partial\theta_i\,\partial\theta_j}\right|_{\boldsymbol{\theta}=\boldsymbol{\theta}^{\rm ref}} + \frac{1}{6}\sum_{i,j,k}\Delta\theta_i\Delta\theta_j\Delta\theta_k \left.\frac{\partial^3 c_X}{\partial\theta_i\,\partial\theta_j\,\partial\theta_k}\right|_{\boldsymbol{\theta}=\boldsymbol{\theta}^{\rm ref}} + \frac{1}{24}(\Delta\sigma_8)^4 \left.\frac{\partial^4 c_X}{\partial\sigma_8^4}\right|_{\boldsymbol{\theta}=\boldsymbol{\theta}^{\rm ref}}, \quad (5.21)$$

where c_X is a placeholder for $c^2_{s(1)}$, c_1 or c_4. Note that we find it more convenient to use σ_8 in place of A_s in this expansion.

We now describe the details of the fits that are used to fix the derivatives in Eq. (5.21). At all redshifts listed in Tab. 5.3, for each cosmology in our catalogue we extract the EFTofLSS parameters by fitting Eq. (5.20) to the nonlinear matter power spectrum output of `FrankenEmu` up to a maximum scale $k_{\rm fit}$ (also listed in Tab. 5.3) determined with the method discussed in Foreman, Perrier, and Senatore (2016). In particular, we derive the best fits and covariances for these parameters by minimizing the chi-square function

$$\chi^2(\mathbf{c}) = \sum_i \left[\frac{P_{\rm NL}(k_i) - P_{\text{EFT-2-loop}}(k_i, \mathbf{c})}{\sigma_P(k_i)}\right]^2, \quad (5.22)$$

Table 5.3 Redshifts and corresponding maximum wavenumbers used in the fits of Eq. (5.21) to the emulator power spectra. We neglect any potential variation of $k_{\rm fit}$ with cosmology (expected to be small), and for each redshift we adopt the values obtained in Foreman, Perrier, and Senatore (2016).

z	$k_{\rm fit}$ $[h\,{\rm Mpc}^{-1}]$
0	0.33
0.05	0.34
0.11	0.36
0.25	0.38
0.38	0.42
0.5	0.46
0.66	0.52
0.85	0.52
1	0.52

where we have explicitly included the dependence of the EFTofLSS predictions on the parameter vector $\mathbf{c} = (c^2_{s(1)}, c_1, c_4)$, and where $P_{\rm NL}(k)$ is the emulator nonlinear power spectrum for which we assume 1% uncorrelated gaussian errors, i.e. $\sigma_P(k_i) = 0.01 \times P_{\rm NL}(k_i)$ (Heitmann, Lawrence, et al. 2014). To find the best-fit $\mathbf{c}_{(0)}$ we resort to the Levenberg-Marquardt method (see e.g. Press, Teukolsky, et al. 2007), which approximates Eq. (5.22) with a quadratic form, such that around the best fit one has

$$\Delta\chi^2 \equiv \chi^2 - \chi^2_{\rm min} \approx \delta\mathbf{c} \cdot \mathcal{C}^{-1} \cdot \delta\mathbf{c}, \tag{5.23}$$

with $\mathcal{C}$ denoting the covariance matrix of the EFTofLSS parameters, and $\delta\mathbf{c} \equiv \mathbf{c} - \mathbf{c}_{(0)}$. We have validated the accuracy of this simplified approach for a sample cosmology by comparing with a full likelihood analysis (taking $-2\ln\mathcal{L} \equiv \chi^2$).

For all redshifts in Tab. 5.3, we then fit Eq. (5.21) to the corresponding parameter extracted with the method outlined above. Coefficients at redshifts different than those listed in Tab. 5.3 are evaluated through interpolation. We have implemented Eq. (5.21) in `TaylorEFT` for $0 \leqslant z \leqslant 1$, and the user can call it through the `EFTParamsFit[...]` module.

After fixing the Taylor coefficients in this way, Eq. (5.21) reproduces the values of $c^2_{s(1)}$, c_1, and c_4 obtained from the exact fits to within 3% for all test cosmologies, well within the marginalized uncertainties on the exact fits: on average, ∼10% for $c^2_{s(1)}$, ∼40% for c_1, and ∼20% for c_4 (see Fig. 5.7). However, these marginalized uncertainties do not tell the whole story: it is important to account for the correlations between the EFTofLSS parameters in an assessment of Eq. (5.21). Using `CosmoEFT` to evaluate the loop integrals in Eq. (5.20), we estimate the correlation matrices (which are mostly cosmology-independent) at $z = 0$ and

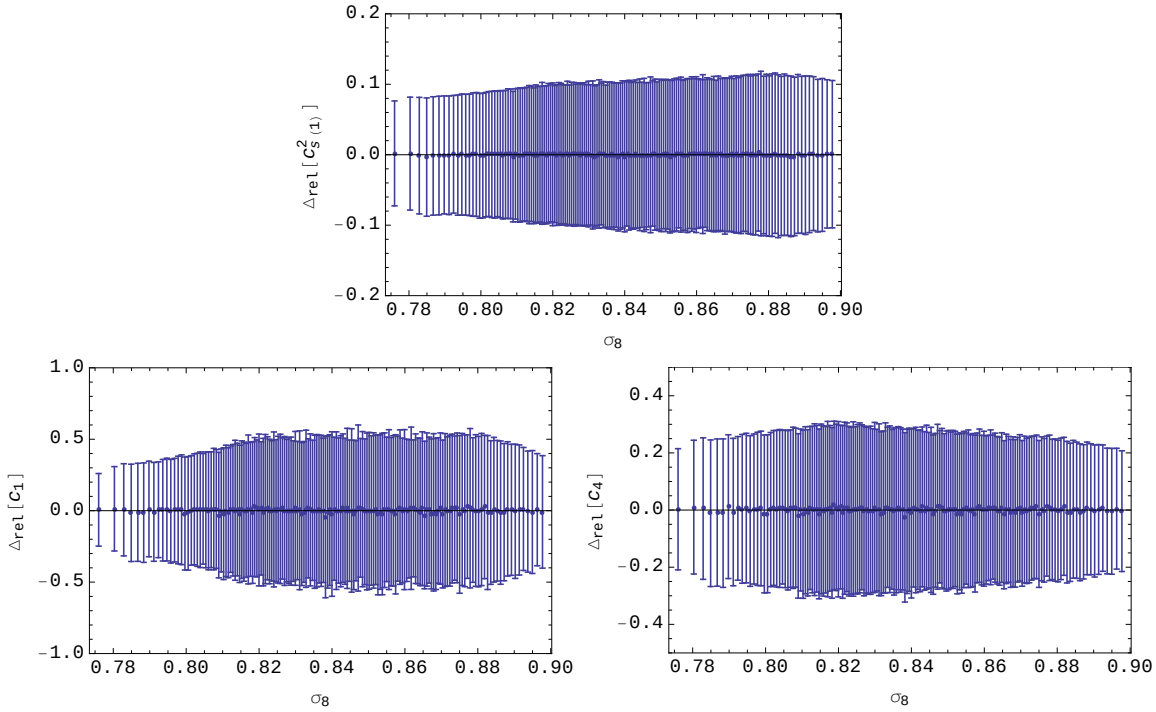

Fig. 5.7 Relative difference between the actual fit matching `TaylorEFT` to `FrankenEmu` and the expansion Eq. (5.21) for the EFTofLSS parameters at $z = 0$ as a function of σ_8. For clarity, each data point represents the average over 100 cosmologies sorted by σ_8, and each of them individually with cosmological parameters satisfying $|\Delta\theta_i| \leqslant 3\sigma_i$. We also average the marginalized errors assuming them independent. So the error from the mismatch between the parameters obtained directly from `TaylorEFT` and from using (5.21) is much smaller than the uncertainty from the fit the the numerical data.

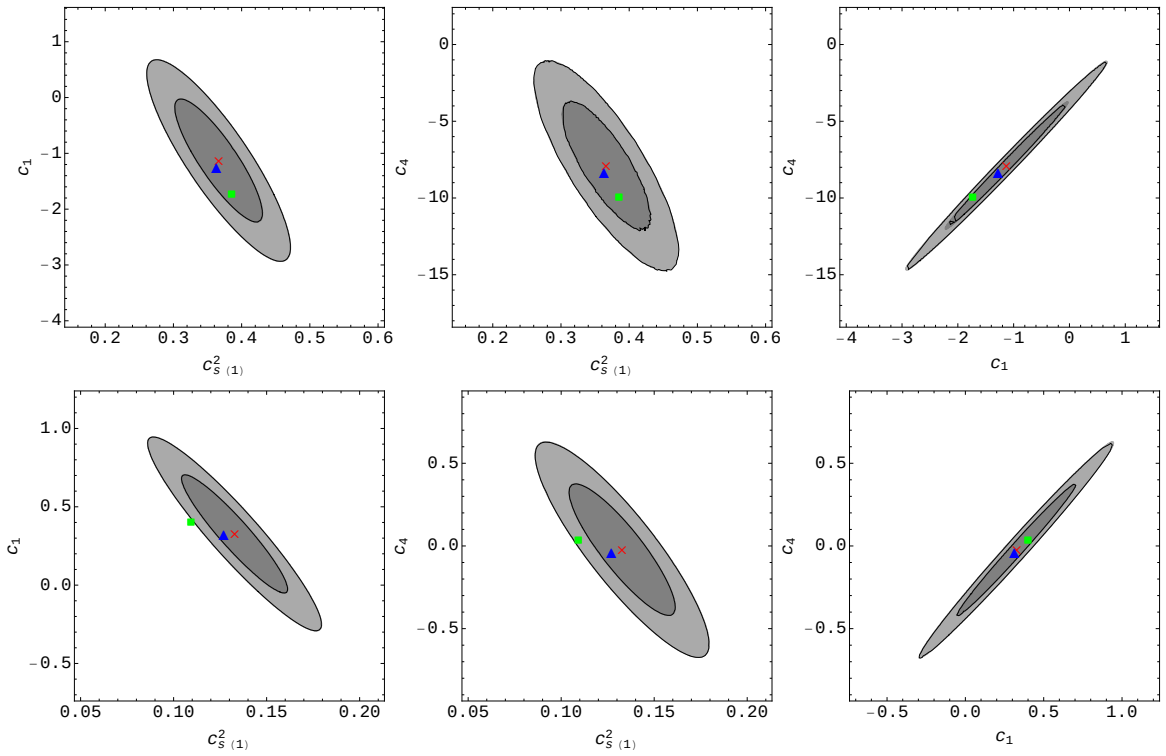

Fig. 5.8 Levenberg-Marquardt 68.3% (dark shadings) and 95.4% (light shadings) confidence regions for `cosmo_10` EFTofLSS parameters at $z = 0$ (top panels) and $z = 0.93$ (bottom panels). Also shown are the best fit values using `CosmoEFT` (red crosses) or `TaylorEFT` loop integrals (blue triangles), and the values given by Eq. (5.21) (green squares). Black contours are derived from a full χ^2 analysis. We find that the differences between direct fits using `CosmoEFT` or `TaylorEFT` output are much smaller than the differences from using Eq. (5.21), which can be as large as $\sim 2\sigma$ for interpolated redshifts.

$z = 0.93$ to be

$$\varrho^{(0)} = \begin{array}{c} \\ c_{s(1)}^2 \\ c_1 \\ c_4 \end{array} \begin{array}{c} \begin{array}{ccc} c_{s(1)}^2 & c_1 & c_4 \end{array} \\ \begin{pmatrix} 1 & -0.86 & -0.80 \\ -0.86 & 1 & 0.99 \\ -0.80 & 0.99 & 1 \end{pmatrix} \end{array}, \quad \varrho^{(0.93)} = \begin{array}{c} \\ c_{s(1)}^2 \\ c_1 \\ c_4 \end{array} \begin{array}{c} \begin{array}{ccc} c_{s(1)}^2 & c_1 & c_4 \end{array} \\ \begin{pmatrix} 1 & -0.94 & -0.88 \\ -0.94 & 1 & 0.99 \\ -0.88 & 0.99 & 1 \end{pmatrix} \end{array}, \tag{5.24}$$

where we have used the relation $\varrho_{ij} = \mathcal{C}_{ij}/\sigma_i\sigma_j$. Evidently, the EFTofLSS parameters display substantial degeneracies, that evolve only mildly with redshift. As discussed in Foreman, Perrier, and Senatore 2016, this degeneracy can be expected based on theory grounds.

In principle, there could be three sources of error in the parameter values, each of which should be compared to the confidence regions defined by the the full covariance matrix: (i) remainders in the Taylor expansion for $P_\alpha(k)$ in Eq. (5.14), (ii) residuals around the Taylor expansion for the EFT parameters in Eq. (5.21), and (iii) redshift interpolation errors in its coefficients. We have performed this comparison for a cosmology from our catalogue

(`cosmo_10`) that maximally departs from our reference cosmology, i.e. $|\Delta\theta_i| = 3\sigma_i$. Explicitly, we computed its parameters using three different methods: fitting Eq. (5.20) to `FrankenEmu` using either `CosmoEFT` or `TaylorEFT` loop integrals, or directly using Eq. (5.21). Fig. 5.8 plots the values obtained from each method along with the Levenberg-Marquardt 68.3% and 95.4% confidence regions (grey shading) and the regions from the full likelihood analysis (black lines).

Differences between `CosmoEFT` and `TaylorEFT` best fitting values in this figure are due solely to (i), while differences between the `CosmoEFT` best fits and values from Eq. (5.21) in the top panels of this figure are caused by both (i) and (ii). These differences are all negligible compared to the size of the 1σ confidence region. However, point (iii) can induce a sizable bias in the value of one or more of the c_X parameters, as shown in the bottom panels of Fig. 5.8 for $c^2_{s(1)}$ ([13]), which is an interpolated redshift. (Of course, by increasing the precision of the numerical data, the number of redshifts, and the order of the Taylor expansion, one expects this offset to be decreased). In Sec. 5.4.2, we will investigate the impact of this bias on the performance of $P_{\text{EFT-2-loop}}$ when compared to simulation data.

Before comparing with simulations, however, let us use Eq. (5.21) to investigate the behavior of the EFT parameters as a function of redshift and cosmology, keeping in mind the possible bias in c_X at interpolated redshifts. For this, we select the cosmologies corresponding to the maximum degeneracy axis of the ellipsoid Eq. (5.11) with $p = 0.997$. This way, all cosmological parameters vary simultaneously and monotonically, making it easier to see their impact on the EFTofLSS parameters. Furthermore, we condense the information about cosmologies in the two derived parameters, Ω_{m} and σ_8, which allows us to easily present how $c^2_{s(1)}$, c_1 and c_4 change with cosmology. This cosmology dependence is shown in Fig. 5.9, at redshifts $z = 0$, $z = 0.11$, and $z = 0.5$. As already discussed in Foreman, Perrier, and Senatore (2016) for the cosmology used for the Dark Sky suite of simulations (Skillman, Warren, et al. 2014), the absolute values of both $c^2_{s(1)}$ and c_4 monotonically decrease with redshift, while c_1 changes sign, reaches a maximum positive value and eventually approaches zero. Our new analysis suggests that the rapidity of these changes and the specific behavior of c_1 indeed depend on cosmology. `CosmoEFT` will enable much more detailed studies of this cosmology-dependence to be carried out in future work.

Fig. 5.10 provides a more detailed picture of the redshift dependence of $c^2_{s(1)}$ for all 3σ cosmologies from Table 5.1. We find that for $z \leq 1$, $c^2_{s(1)}(z)$ scales roughly like $D(z)^p$, with p ranging between 1.5 and 3 (the grey band in Fig. 5.10). As discussed in Foreman, Perrier, and Senatore (2016), a sum of two power-laws of the growth factor should in principle provide a better (and more physically motivated) description of this time dependence, but we do

[13] Note that for contour plots of parameter constraints we adopt the common definitions for the 68.3% and 95.4% confidence regions derived from the χ^2 distribution with two degrees of freedom as the surfaces enclosed by the boundaries $\Delta\chi^2 = 2.30$ and $\Delta\chi^2 = 6.17$, respectively.

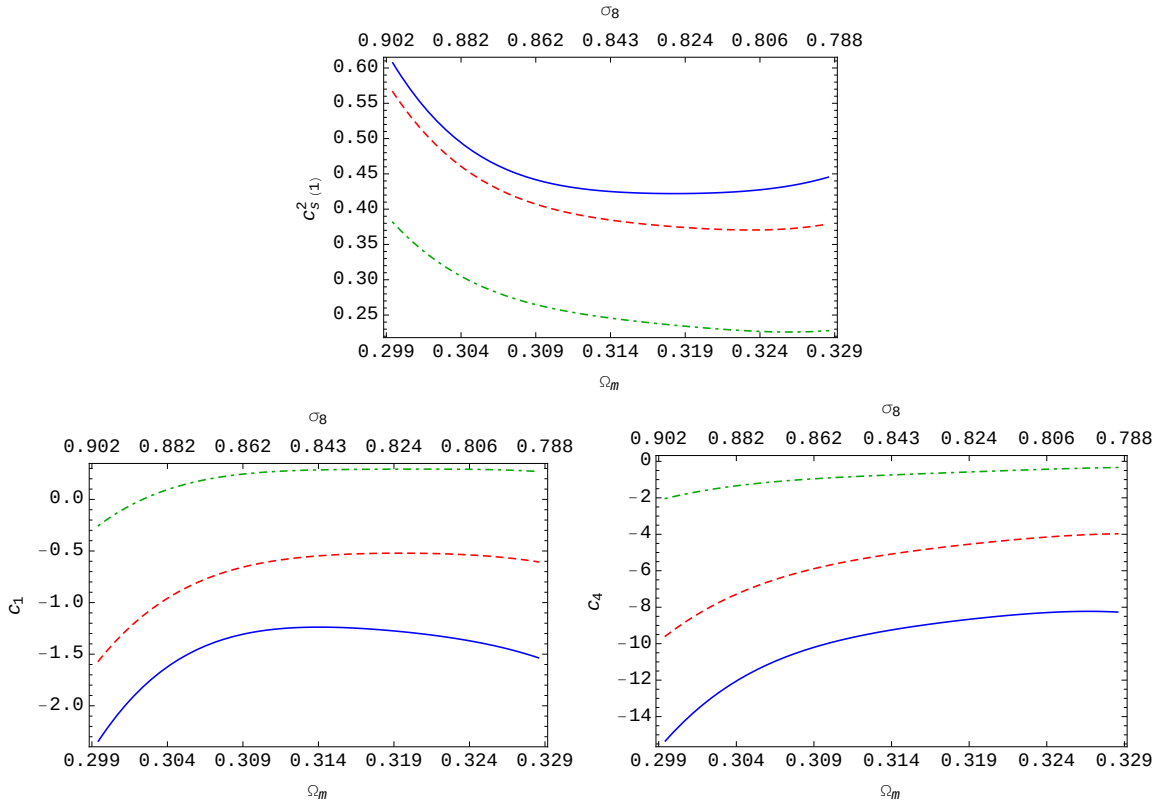

Fig. 5.9 Cosmology dependence of the EFTofLSS parameters at $z = 0$ (solid blue), $z = 0.11$ (dashed red) and $z = 0.5$ (dash-dotted green). We show cosmologies that lie on the maximum degeneracy axis of the ellipsoid Eq. (5.11), up to the edge of the $p = 0.997$ region. In each panel, for a given cosmology we put the corresponding $\Omega_{\rm m}$ on the bottom x-axis and σ_8 on the top x-axis. Note that absolute values of $c^2_{s(1)}$ and c_4 monotonically decrease with redshift regardless the cosmology, whereas c_1 changes sign at different redshifts for different cosmologies. The considerable relative variation of the cosmological parameters is mainly driven by the large uncertainty with which σ_8 is known.

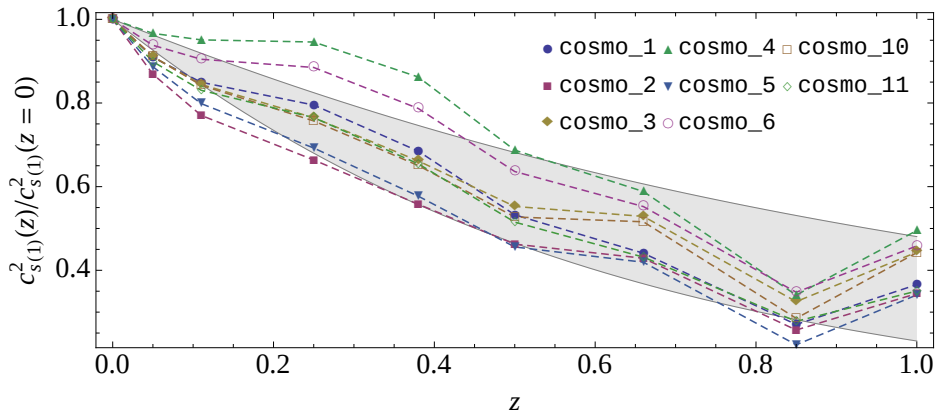

Fig. 5.10 Redshift dependence of $c^2_{s(1)}$ for all 3σ-cosmologies from Table 5.1. Each curve can be roughly approximated by a power-law in the growth factor $D(z)$; for illustration, the grey band spans the range from $D(z)^{1.5}$ to $D(z)^3$.

not perform such fits here because the precision of our $c^2_{s(1)}$ measurements is limited by the precision of the emulator used for these measurements. This is because a measurement of $c^2_{s(1)}$ is essentially a measurement of the coefficient of the $k^2 P_{11}(k)$ term in Eq. (5.20), and a 1% error on the total power spectrum translates into a much larger error on this coefficient ($\gtrsim 10\%$ when fitting up to the $k_{\rm max}$ we use in this work, as shown in Fig. 5.7).

5.4.2 Comparisons with simulation data

Emulator

For all of our 3σ-cosmologies in Tab. 5.1, we compare $P_{\text{EFT-2-loop}}$ to the `FrankenEmu` nonlinear power spectrum to quantify the errors introduced by the Taylor expansion of both the loop integrals and the EFTofLSS parameters discussed above. First, Fig. 5.11 compares the emulator output to the prediction from Eq. (5.20), using `CosmoEFT` to compute the loop integrals. The left panel uses values for $c^2_{s(1)}$, c_1 and c_4 that were fit to emulator output using Eq. (5.20) with `CosmoEFT` computations, while the right panel instead uses values for $c^2_{s(1)}$, c_1 and c_4 that were obtained from fits that use `TaylorEFT` to compute the loop integrals (but not using the Taylor expansion for the parameters (5.21)). Notably, EFTofLSS parameters extracted by means of Taylor expanded loop integrals are sufficiently close to their fiducial values obtained from `CosmoEFT` computations that the EFTofLSS power spectrum predictions are accurate within 1% even for `cosmo_10-11` ($|\Delta\theta_i| = 3\sigma_i$), at redshifts up to $z \sim 1$. The fits in Fig. 5.11 use wavenumbers up to $k_{\rm fit} = 0.44\,h\,\text{Mpc}^{-1}$ at $z = 0.44$ and $k_{\rm fit} = 0.52\,h\,\text{Mpc}^{-1}$ at $z = 0.93$. One should be careful in using the two-loop power spectrum results from the EFTofLSS at wavenumbers greater than roughly $k \sim 0.25 h\text{Mpc}^{-1}$ at $z = 0$, and at higher wavenumbers at higher redshifts, because the theoretical errors become sizable at those scales

(more details in Foreman, Perrier, and Senatore 2016; Baldauf, Mercolli, and Zaldarriaga 2015).

In Fig. 5.12, we assess the performance of our Taylor expansion for the EFTofLSS parameters, given in Eq. (5.21). The left panel shows the relative differences between the emulator and the EFTofLSS two-loop power spectra constructed with the Taylor expanded loop integrals and using Eq. (5.21) for the EFT parameters. The impact of the combination of loop integrals and c_X errors on $P_{\text{EFT-2-loop}}$ is small enough that the EFTofLSS predictions lie within 1% up to $k \sim k_{\text{fit}}$. However, using Eq. (5.21) for the parameters but the `CosmoEFT` loop integrals in Eq. (5.20) does not perform as well (see right panel of Fig. 5.12). This comes from the fact that the Taylor expansion of the EFTofLSS parameters has been calibrated using `TaylorEFT`, and this calibration acts to partly absorb the differences between the `TaylorEFT` and `CosmoEFT` computations of the loop integrals. Clearly, it makes more sense to use the expanded c_X in the situation where the loop integrals are obtained from `TaylorEFT` [14].

Finally, we stress that it is expected that by increasing the order of the Taylor expansion both for the power spectra and for the coefficients, it should be possible to increase the accuracy of the procedure to the level of the accuracy of `CosmoEFT`. Of course the precision of the coefficients is limited by the precision of the numerical data we use to extract them. For this first release of the code, we stopped the Taylor expansion at the order given by (5.14) and (5.21) [15].

Full N-body

Finally, it is useful to quantify the effect of uncertainties in the nonlinear data (such as sample variance of the power spectrum measurements, or possible systematic errors in the emulator we have used for our main results) on the values of the c_X parameters, and on the power spectrum predictions that make use of those values. To do so, we employ high-precision data from a dark matter-only N-body cosmological simulation, and compare the results to those obtained from `FrankenEmu`. For this, we use the publicly-available redshift-zero matter power spectrum extracted from the `ds14_a` box of the Dark Sky simulation suite [16], with $L_{\text{box}} = 8h\,\text{Gpc}^{-1}$, $N_{\text{part}} = 10240^3$, and cosmological parameters $\boldsymbol{\theta}_{DS} = \{0.02214, 0.11754, 3.08518, 0.96764, 0.68806\}$. In Fig. 5.13 we compare the constraints

[14] Although this is not the recommended procedure, if one desires to do so, the expanded c_X can still be used to make predictions within 2% of the emulator power spectrum if the `CosmoEFT` loop integrals are used.

[15] The reason why we can stop at second order in the Taylor expansion of $P(k)$ while we go somewhere between third and fourth order in the Taylor expansion of the EFT parameters, c_X's, is simply due to the fact that when we use the Taylor expansion of $P(k)$, we let the EFT parameters be determined by the fit to the data, which allows for a partial compensation of the error in the $P(k)$ Taylor expansion. Instead, when we directly use the EFT parameters from the Taylor expansion, there is nothing left to compensate for the residual errors. This is why we go to higher order in these. Of course, intermediate procedures where one goes to cubic order both in c_X and $P(k)$ could be allowed, at the cost of running more reference cosmologies (with possibly higher precision requirements).

[16] http://darksky.slac.stanford.edu

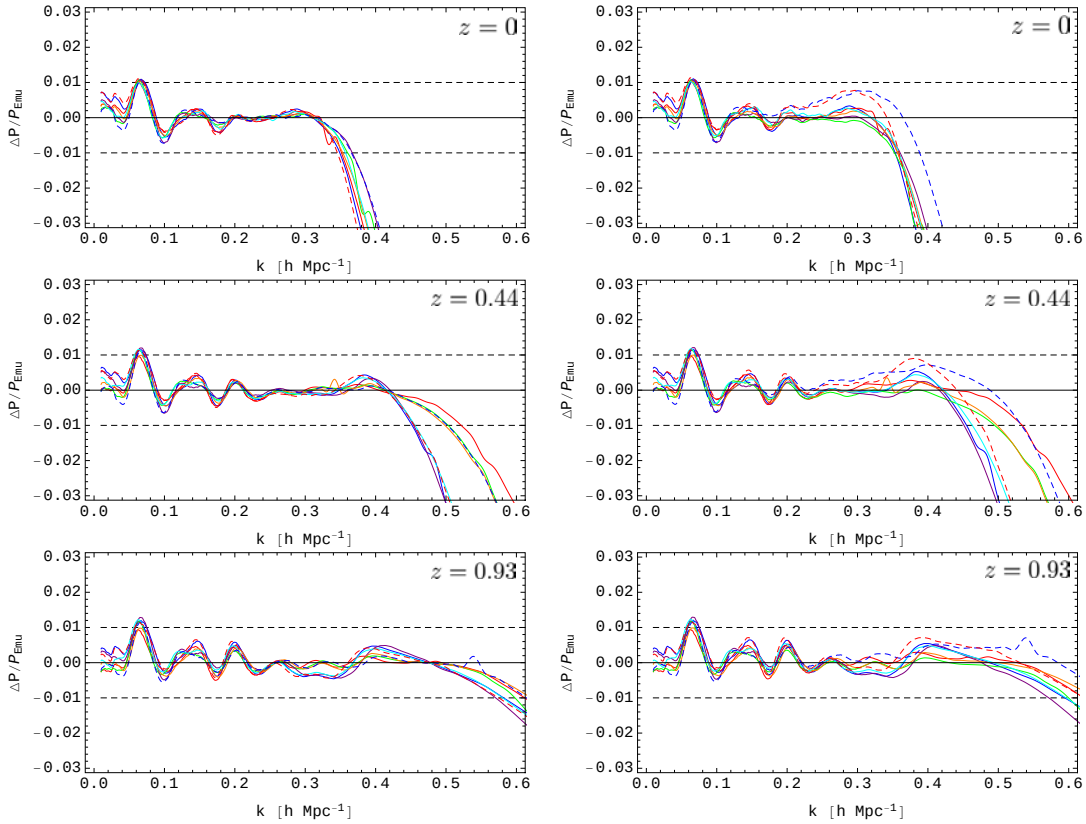

Fig. 5.11 Redshift evolution of the EFTofLSS matter power spectrum predictions compared to `FrankenEmu` outputs for all of our 3σ-cosmologies, `cosmo_1-6` (in order: blue, red, green, purple, orange, cyan) and `cosmo_10-11` (dashed blue and dashed red, respectively). Horizontal dashed lines delimit 1% departures from the emulator power spectra. *Left*: `CosmoEFT` loop integrals are used to build both the EFTofLSS power spectra and to determine the best fit EFT parameters. This column shows the excellent performance of `CosmoEFT`. *Right*: predictions are constructed from `CosmoEFT` loop integrals and use best-fit EFT parameter c_X values obtained with `TaylorEFT` integrals (but not using the Taylor expansion for the parameters (5.21)). This procedure gives a sense of how the two approximations for the loop integrals affects the fitted values of the EFT parameters, and how these values affect the overall power spectrum prediction. For cosmologies with $|\Delta\theta_i| \leq 3\sigma_i$, the overall power spectrum is accurate to within 1% regardless of which loop integrals are used to determine the EFT parameters.

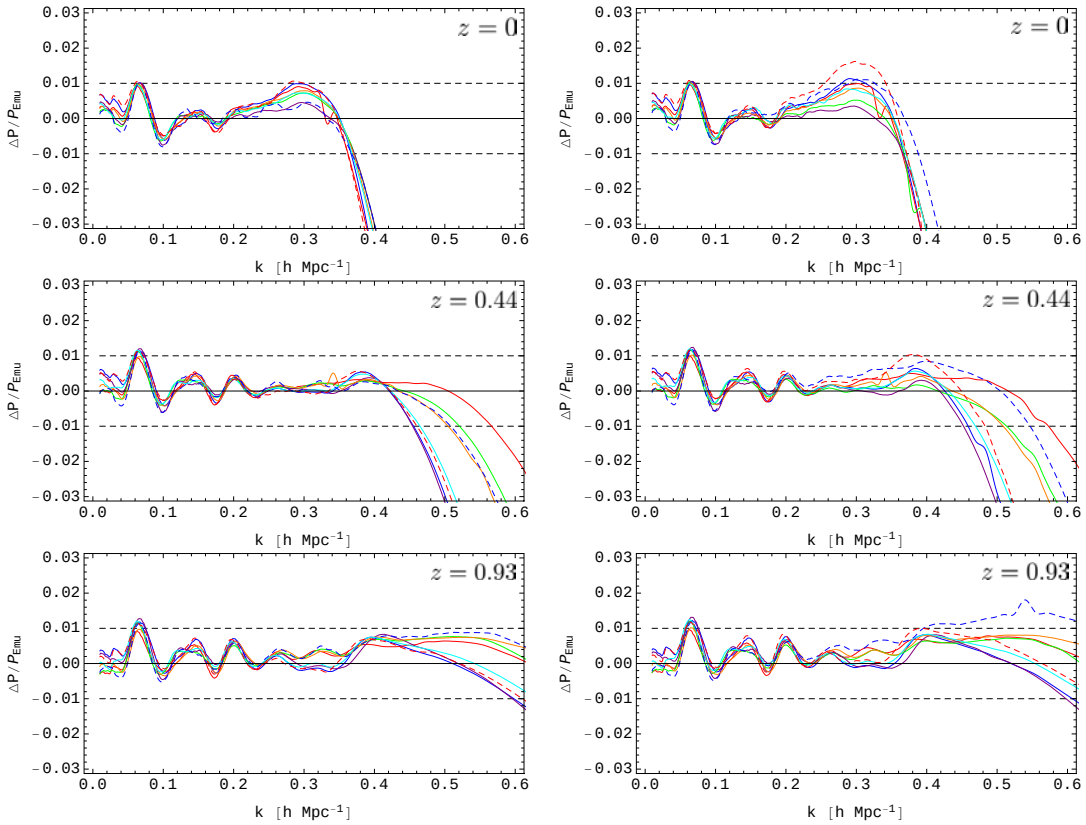

Fig. 5.12 Redshift evolution of the EFTofLSS matter power spectrum predictions compared to `FrankenEmu` outputs for all of our 3σ-cosmologies, `cosmo_1-6` (in order: blue, red, green, purple, orange, cyan) and `cosmo_10-11` (dashed blue and dashed red, respectively). Horizontal dashed lines delimit 1% departures from the emulator power spectra. In both columns, the EFT parameter values are estimated using Eq. (5.21). *Left*: `TaylorEFT` is used to compute the loop integrals. This column shows the excellent performance of `TaylorEFT` combined with the predictions from (5.21). *Right*: `CosmoEFT` is used to compute the loop integrals. This procedure is clearly not the optimal one, but it gives a sense of how the parameters of the EFTofLSS obtained from (5.21) differ from those obtained from a direct fit.

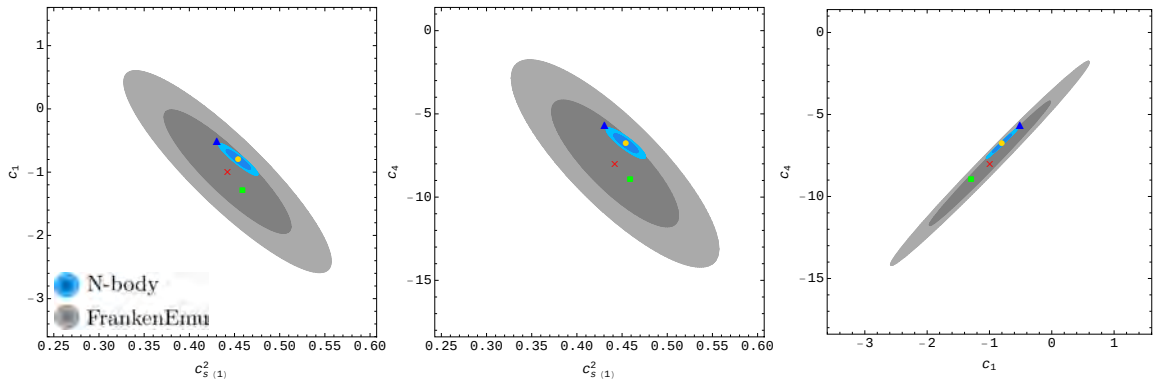

Fig. 5.13 For the Dark Sky cosmology at $z = 0$ (see main text), constraints on the EFTofLSS parameters from emulator data (gray shading) and from `ds14_a` cosmological simulation (blue shading). Dark and light shading respectively indicate the 68.3 and 95.4% confidence regions. Best fits obtained with `CosmoEFT` loop integrals are shown as red crosses for the emulator data and in golden circles for the simulations. Blue triangles represent best fits to the simulations derived with `TaylorEFT` loop integrals, and green squares correspond to the Taylor-expanded coefficients predictions Eq. (5.21).

on the EFTofLSS parameters obtained from fits to `FrankenEmu` with 1% error bars (gray shading) to those from `ds14_a` (blue shading), where the loop integrals have been evaluated with `CosmoEFT`. Note that for these simulations, sample variance at $k_{\rm fit} = 0.33\,h{\rm Mpc}^{-1}$ amounts to $\sim$ 0.1-0.2%. Also in this case $\epsilon_{\rm target} = 0.5\%$ along with $\sigma_\Delta = 1.5({\rm Mpc}/h)^3$ is enough to ensure two-loop matter power spectrum predictions fall within $\sim 0.1\%$ of the data. In fact, for all of the one-loop integrals we have $\Delta P_{\text{1-loop}}/P_{11} \ll 0.1\%$, and the leading source of error is $\Delta P_{\text{2-loop}}/P_{11} \lesssim 0.1\%$ (see Sec. 5.2). Apart from tightening the allowed region of parameter space and consistently shifting the best-fit values of the c_X parameters (golden circles), the parameters extracted directly from the simulation power spectrum display slightly stronger degeneracies, as evident upon inspection of the following correlation matrices:

$$\varrho_{\rm sim} = \begin{array}{c} \\ c^2_{s(1)} \\ c_1 \\ c_4 \end{array} \begin{array}{c} \begin{array}{ccc} c^2_{s(1)} & c_1 & c_4 \end{array} \\ \begin{pmatrix} 1 & -0.94 & -0.89 \\ -0.94 & 1 & 0.99 \\ -0.89 & 0.99 & 1 \end{pmatrix} \end{array}, \quad \varrho_{\rm emu} = \begin{array}{c} \\ c^2_{s(1)} \\ c_1 \\ c_4 \end{array} \begin{array}{c} \begin{array}{ccc} c^2_{s(1)} & c_1 & c_4 \end{array} \\ \begin{pmatrix} 1 & -0.89 & -0.82 \\ -0.89 & 1 & 0.99 \\ -0.82 & 0.99 & 1 \end{pmatrix} \end{array}. \tag{5.25}$$

We also plot the `TaylorEFT` best fit (blue triangles) resulting from the fit to the simulations and the c_X predictions based on Eq. (5.21) (green squares). Not surprisingly, the Taylor expansion of the loop integrals around our reference cosmology is good enough: the c_X's are indeed shifted only mildly along the degeneracy direction. Likewise, our Taylor expanded c_X's lie along the degeneracy direction of the emulator data, which have been used to calibrate that very relation.

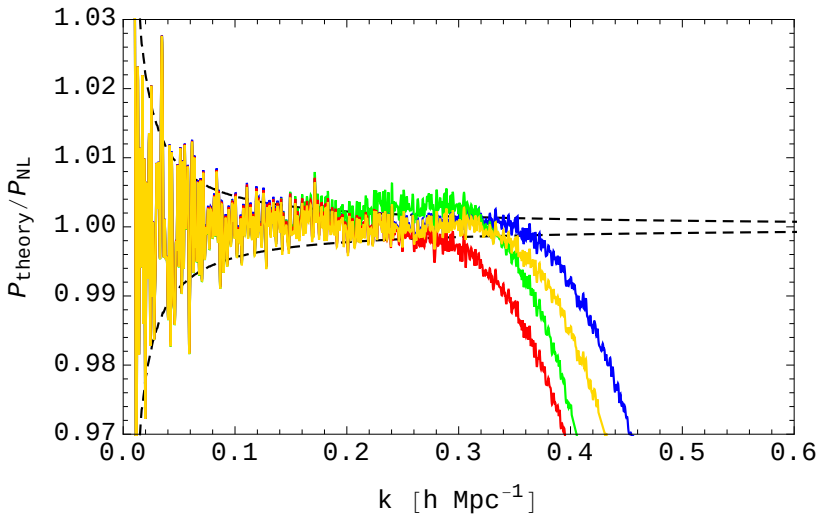

Fig. 5.14 Comparison of two-loop EFTofLSS predictions based on `CosmoEFT` outputs and nonlinear power spectrum measured from the `ds14_a` Dark Sky simulation (see main text). The color coding denotes different values for the EFT parameters: best fit to `ds14_a` power spectrum itself, using `CosmoEFT` loop integrals (gold); best fit to `ds14_a` power spectrum itself, using `TaylorEFT` loop integrals (blue); best fit to `FrankenEmu` output for Dark Sky cosmology (red); and estimated parameter values from Eq. (5.21) (green). Dashed lines delimit sample variance uncertainties in the simulation.

We show how the different values for the EFT parameters impact the EFTofLSS predictions in Fig. 5.14. We compare $P_{\text{EFT-2-loop}}$ to the Dark Sky power spectrum adopting the same color coding as in Fig. 5.13 except that `CosmoEFT` integrals are used everywhere. As already shown in Foreman, Perrier, and Senatore (2016), the direct fit to simulations produces predictions that lie within the sample variance fluctuations of the data up to $k \sim 0.34\,h\,\text{Mpc}^{-1}$, and our reference `CosmoEFT` best fit (in gold) provides a similar match to the data. However, in all the other cases deviations beyond sample variance for $k < k_{\text{fit}}$ are the result of various inaccuracies: interpolation errors in the emulator (in red), residuals in the Taylor expanded loop integrals (in blue), and a combination of these two with other errors described above for the c_X predictions (in green), which obviously cannot perform better than the red curve. In spite of this, each set of parameters corresponds to a power spectrum as close to the best answer as allowed by the method employed: at 1% level for `FrankenEmu` and `TaylorEFT`, and within 2% using the predicted c_X values.

Let us add two additional simple comments. In principle one could ignore simulations and match the parameters of the EFT directly to observational data (where `CosmoEFT` and `TaylorEFT` will still be valuable to obtain the functional form of the various correlation functions). Until now, large uncertainties in observational data have hindered the pursuit of this direction. Nevertheless, this might change with planned all-sky lensing surveys, whose much smaller statistical uncertainties (and better control of systematics) could potentially have

enough power to constrain the c_X's at a level comparable with simulations. Of course, this will require the addition of the description of baryonic effects, as recently done in Lewandowski, Perko, and Senatore (2015); Angulo, Fasiello, et al. (2015), as well as, for galaxies, of biased tracers (Angulo, Fasiello, et al. 2015) [17]. On a different side, it might be interesting to compare the parameters extracted from observations to those obtained from simulations, with the purpose of reducing the parameters that are actually fit to observations, in this way minimizing the loss of information.

5.5 Conclusions

In this work, we have presented a new suite of publicly distributed codes (`CosmoEFT`, `ResumEFT` and `TaylorEFT`) implementing efficient algorithms to evaluate large-scale structure observables in the EFTofLSS framework. These algorithms take advantage of the fact that we are only interested in a neighborhood of cosmological parameter space centered on a "reference" cosmology, which we take to be the best-fit model from *Planck*. The main ideas of each code are as follows:

- Since integration is a linear operation, we can write each loop integral in perturbation theory as a sum of the integral for the reference cosmology and the integral of the *difference* between the integrands for the desired "target" cosmology and the reference cosmology. If the integrals for the reference cosmology have been precomputed with high precision, then the difference integrals can be computed with much lower precision without compromising the precision of the desired result for the target cosmology. This approach has been implemented in `CosmoEFT`. The companion code `ResumEFT` applies the IR-resummation technique of Senatore and Zaldarriaga (2015); Angulo, Foreman, et al. (2015) to the output of `CosmoEFT`.

- In the same spirit, the perturbation theory integrals can be Taylor expanded in the deviation of the cosmological parameters from the reference cosmology, enabling one to simply read off the desired results from the Taylor expansion (provided that the required derivatives have been precomputed). This approach has been implemented in `TaylorEFT`.

As a proof of concept, our codes supply the two-loop IR-resummed predictions from the EFTofLSS for the dark matter power spectrum. These are valid up to mildly nonlinear scales ($k \lesssim 0.3\,h\,\mathrm{Mpc}^{-1}$ at redshift $z = 0$, and increasingly larger wavenumbers for $z > 0$), and for consistency their use should be limited to this regime. Instead, N-body simulations (or

[17] At some higher level of precision, smaller effects might need to be included when studying the determination of these parameters, such as the non-Gaussianity of the covariance matrix and potential degeneracies with cosmological parameters.

emulators) should continue to be employed on nonlinear scales, yet with additional benefits in computational cost from the use of significantly smaller volumes ($L_{\rm box} \sim 100\,h\,{\rm Mpc}^{-1}$).

Our codes are based on ideas that are not specific to the matter power spectrum, and in fact they can be easily applied to other calculations of interest. It will be interesting, and in a sense essential in the light of next generation experiments, to apply these ideas to the computation of higher N-point matter and momentum correlation functions, following Angulo, Foreman, et al. (2015); Baldauf, Mercolli, Mirbabayi, et al. (2015); Senatore and Zaldarriaga (2015); Baldauf, Mercolli, and Zaldarriaga (2015); Bertolini, Schutz, Solon, Walsh, et al. (2015); Bertolini, Schutz, Solon, and Zurek (2016), including the effects of baryons, following Senatore and Zaldarriaga (2014); Angulo, Fasiello, et al. (2015), or the correlation functions for biased tracers, following Senatore and Zaldarriaga (2014); Angulo, Fasiello, et al. (2015), or for the same quantities in redshift space, following Senatore and Zaldarriaga (2014); Lewandowski, Perko, and Senatore (2015). It will also be interesting to see if similar ideas could be implemented in simulations in the same spirit as COLA (Tassev, Zaldarriaga, and Eisenstein 2013; Tassev, Eisenstein, et al. 2015) and in Boltzmann codes such as CMBFAST (Seljak and Zaldarriaga 1996), CAMB (Lewis, Challinor, and Lasenby 2000) and CLASS (Blas, Lesgourgues, and Tram 2011).

Acknowledgements

MC thanks David Rapetti for stimulating discussions. Part of the calculations for this work utilized the Orange and Bullet computer clusters at the SLAC National Accelerator Laboratory. Further numerical computations have been performed with Wolfram *Mathematica*® 9. This work makes use of power spectrum measurements from the Dark Sky suite of simulations, and we thank the Dark Sky team for making those measurements publicly available at http://darksky.slac.stanford.edu. SF is partially supported by the Natural Sciences and Engineering Research Council of Canada. LS is supported by DOE Early Career Award DE-FG02-12ER41854.

References

Abate, Alexandra et al. (2012). "Large Synoptic Survey Telescope: Dark Energy Science Collaboration". In: arXiv: 1211.0310 [astro-ph.CO].

Abbott, T. et al. (2005). "The dark energy survey". In: arXiv: astro-ph/0510346 [astro-ph].

— (2016). "Cosmology from cosmic shear with Dark Energy Survey Science Verification data". In: *Phys. Rev.* D94.2, p. 022001. DOI: 10.1103/PhysRevD.94.022001. arXiv: 1507.05552 [astro-ph.CO].

Abell, Paul A. et al. (2009). "LSST Science Book, Version 2.0". In: arXiv: 0912.0201 [astro-ph.IM].

Abolhasani, Ali Akbar, Mehrdad Mirbabayi, and Enrico Pajer (2016). "Systematic Renormalization of the Effective Theory of Large Scale Structure". In: *JCAP* 1605.05, p. 063. DOI: 10.1088/1475-7516/2016/05/063. arXiv: 1509.07886 [hep-th].

Achitouv, Ixandra, Marco Baldi, et al. (2016). "Imprint of $f(R)$ gravity on nonlinear structure formation". In: *Phys. Rev.* D93.10, p. 103522. DOI: 10.1103/PhysRevD.93.103522. arXiv: 1511.01494 [astro-ph.CO].

Ade, P. A. R. et al. (2014a). "Planck 2013 results. XV. CMB power spectra and likelihood". In: *Astron. Astrophys.* 571, A15. DOI: 10.1051/0004-6361/201321573. arXiv: 1303.5075 [astro-ph.CO].

— (2014b). "Planck 2013 results. XVI. Cosmological parameters". In: *Astron. Astrophys.* 571, A16. DOI: 10.1051/0004-6361/201321591. arXiv: 1303.5076 [astro-ph.CO].

— (2014c). "Planck 2013 results. XVII. Gravitational lensing by large-scale structure". In: *Astron. Astrophys.* 571, A17. DOI: 10.1051/0004-6361/201321543. arXiv: 1303.5077 [astro-ph.CO].

— (2014d). "Planck 2013 results. XX. Cosmology from Sunyaev–Zeldovich cluster counts". In: *Astron. Astrophys.* 571, A20. DOI: 10.1051/0004-6361/201321521. arXiv: 1303.5080 [astro-ph.CO].

— (2014e). "Planck 2013 results. XXIX. The Planck catalogue of Sunyaev-Zeldovich sources". In: *Astron. Astrophys.* 571, A29. DOI: 10.1051/0004-6361/201321523. arXiv: 1303.5089 [astro-ph.CO].

— (2015a). "Planck 2015 results. XIII. Cosmological parameters". In: arXiv: 1502.01589 [astro-ph.CO].

— (2015b). "Planck 2015 results. XV. Gravitational lensing". In: DOI: 10.1051/0004-6361/201525941. arXiv: 1502.01591 [astro-ph.CO].

— (2015c). "Planck 2015 results. XXI. The integrated Sachs-Wolfe effect". In: arXiv: 1502.01595 [astro-ph.CO].

Albrecht, Andreas et al. (2006). "Report of the Dark Energy Task Force". In: arXiv: astro-ph/0609591 [astro-ph].

Allen, S. W., A. C. Fabian, et al. (2003). "Cosmological constraints from the local x-ray luminosity function of the most x-ray luminous galaxy clusters". In: *Mon. Not. Roy. Astron. Soc.* 342, p. 287. DOI: 10.1046/j.1365-8711.2003.06550.x. arXiv: astro-ph/0208394 [astro-ph].

Allen, S. W., A. B. Mantz, et al. (2013). "Measuring cosmic distances with galaxy clusters". In: *Community Summer Study 2013: Snowmass on the Mississippi (CSS2013) Minneapolis, MN, USA, July 29-August 6, 2013*. arXiv: 1307.8152 [astro-ph.CO]. URL: http://www.slac.stanford.edu/econf/C1307292/docs/submittedArxivFiles/1307.8152.pdf.

Allen, S. W., D. A. Rapetti, et al. (2008). "Improved constraints on dark energy from Chandra X-ray observations of the largest relaxed galaxy clusters". In: *Mon. Not. Roy. Astron. Soc.* 383, pp. 879–896. DOI: 10.1111/j.1365-2966.2007.12610.x. arXiv: 0706.0033 [astro-ph].

Allen, S. W., R. W. Schmidt, H. Ebeling, et al. (2004). "Constraints on dark energy from Chandra observations of the largest relaxed galaxy clusters". In: *Mon. Not. Roy. Astron. Soc.* 353, p. 457. DOI: 10.1111/j.1365-2966.2004.08080.x. arXiv: astro-ph/0405340 [astro-ph].

Allen, S. W., R. W. Schmidt, and A. C. Fabian (2002). "Cosmological constraints from the x-ray gas mass fraction in relaxed lensing clusters observed with Chandra". In: *Mon. Not. Roy. Astron. Soc.* 334, p. L11. DOI: 10.1046/j.1365-8711.2002.05601.x. arXiv: astro-ph/0205007 [astro-ph].

Allen, Steven W., August E. Evrard, and Adam B. Mantz (2011). "Cosmological Parameters from Observations of Galaxy Clusters". In: *Ann. Rev. Astron. Astrophys.* 49, pp. 409–470. DOI: 10.1146/annurev-astro-081710-102514. arXiv: 1103.4829 [astro-ph.CO].

Amendola, L. and S. Tsujikawa (June 2010). *Dark Energy*.

Anderson, Lauren et al. (2014a). "The clustering of galaxies in the SDSS-III Baryon Oscillation Spectroscopic Survey: baryon acoustic oscillations in the Data Releases 10 and 11 Galaxy samples". In: *Mon. Not. Roy. Astron. Soc.* 441.1, pp. 24–62. DOI: 10.1093/mnras/stu523. arXiv: 1312.4877 [astro-ph.CO].

— (2014b). "The clustering of galaxies in the SDSS-III Baryon Oscillation Spectroscopic Survey: measuring D_A and H at $z = 0.57$ from the baryon acoustic peak in the Data Release 9 spectroscopic Galaxy sample". In: *Mon. Not. Roy. Astron. Soc.* 439.1, pp. 83–101. DOI: 10.1093/mnras/stt2206. arXiv: 1303.4666 [astro-ph.CO].

Angulo, Raul, Matteo Fasiello, et al. (2015). "On the Statistics of Biased Tracers in the Effective Field Theory of Large Scale Structures". In: *JCAP* 1509, p. 029. DOI: 10.1088/1475-7516/2015/09/029,10.1088/1475-7516/2015/9/029. arXiv: 1503.08826 [astro-ph.CO].

Angulo, Raul, Simon Foreman, et al. (2015). "The One-Loop Matter Bispectrum in the Effective Field Theory of Large Scale Structures". In: *JCAP* 1510, p. 039. DOI: 10.1088/1475-7516/2015/10/039. arXiv: 1406.4143 [astro-ph.CO].

Appleby, Stephen A and Jochen Weller (2010). "Parameterizing scalar-tensor theories for cosmological probes". In: *JCAP* 1012, p. 006. DOI: 10.1088/1475-7516/2010/12/006. arXiv: 1008.2693 [astro-ph.CO].

Applegate, D. E. et al. (2016). "Cosmology and astrophysics from relaxed galaxy clusters – IV. Robustly calibrating hydrostatic masses with weak lensing". In: *Mon. Not. Roy. Astron. Soc.* 457.2, pp. 1522–1534. DOI: 10.1093/mnras/stw005. arXiv: 1509.02162 [astro-ph.CO].

Applegate, Douglas E., Anja von der Linden, et al. (2014). "Weighing the Giants – III. Methods and measurements of accurate galaxy cluster weak-lensing masses". In: *Mon. Not. Roy. Astron. Soc.* 439.1, pp. 48–72. DOI: 10.1093/mnras/stt2129. arXiv: 1208.0605 [astro-ph.CO].

Arnold, Christian, Ewald Puchwein, and Volker Springel (2014). "Scaling relations and mass bias in hydrodynamical $f(R)$ gravity simulations of galaxy clusters". In: *Mon. Not. Roy. Astron. Soc.* 440.1, pp. 833–842. DOI: 10.1093/mnras/stu332. arXiv: 1311.5560 [astro-ph.CO].

Assassi, Valentin, Daniel Baumann, Enrico Pajer, et al. (2015). "Effective theory of large-scale structure with primordial non-Gaussianity". In: *JCAP* 1511, p. 024. DOI: 10.1088/1475-7516/2015/11/024. arXiv: 1505.06668 [astro-ph.CO].

Assassi, Valentin, Daniel Baumann, and Fabian Schmidt (2015). "Galaxy Bias and Primordial Non-Gaussianity". In: *JCAP* 1512.12, p. 043. DOI: 10.1088/1475-7516/2015/12/043. arXiv: 1510.03723 [astro-ph.CO].

Balaguera-Antolinez, A. and Cristiano Porciani (2013). "Counts of galaxy clusters as cosmological probes: the impact of baryonic physics". In: *JCAP* 1304, p. 022. DOI: 10.1088/1475-7516/2013/04/022. arXiv: 1210.4117 [astro-ph.CO].

Baldauf, Tobias, Lorenzo Mercolli, Mehrdad Mirbabayi, et al. (2015). "The Bispectrum in the Effective Field Theory of Large Scale Structure". In: *JCAP* 1505.05, p. 007. DOI: 10.1088/1475-7516/2015/05/007. arXiv: 1406.4135 [astro-ph.CO].

Baldauf, Tobias, Lorenzo Mercolli, and Matias Zaldarriaga (2015). "Effective field theory of large scale structure at two loops: The apparent scale dependence of the speed of sound". In: *Phys. Rev.* D92.12, p. 123007. DOI: 10.1103/PhysRevD.92.123007. arXiv: 1507.02256 [astro-ph.CO].

Baldauf, Tobias, Mehrdad Mirbabayi, et al. (2015). "Equivalence Principle and the Baryon Acoustic Peak". In: *Phys. Rev.* D92.4, p. 043514. DOI: 10.1103/PhysRevD.92.043514. arXiv: 1504.04366 [astro-ph.CO].

Baldauf, Tobias, Emmanuel Schaan, and Matias Zaldarriaga (2016a). "On the reach of perturbative descriptions for dark matter displacement fields". In: *JCAP* 1603.03, p. 017. DOI: 10.1088/1475-7516/2016/03/017. arXiv: 1505.07098 [astro-ph.CO].

— (2016b). "On the reach of perturbative methods for dark matter density fields". In: *JCAP* 1603.03, p. 007. DOI: 10.1088/1475-7516/2016/03/007. arXiv: 1507.02255 [astro-ph.CO].

Baldi, Marco, Francisco Villaescusa-Navarro, et al. (2014). "Cosmic degeneracies – I. Joint N-body simulations of modified gravity and massive neutrinos". In: *Mon. Not. Roy. Astron. Soc.* 440.1, pp. 75–88. DOI: 10.1093/mnras/stu259. arXiv: 1311.2588 [astro-ph.CO].

Bardeen, James M. (1980). "Gauge Invariant Cosmological Perturbations". In: *Phys. Rev.* D22, pp. 1882–1905. DOI: 10.1103/PhysRevD.22.1882.

Barreira, Alexandre, Baojiu Li, Carlton M. Baugh, et al. (2013). "Spherical collapse in Galileon gravity: fifth force solutions, halo mass function and halo bias". In: *JCAP* 1311, p. 056. DOI: 10.1088/1475-7516/2013/11/056. arXiv: 1308.3699 [astro-ph.CO].

Barreira, Alexandre, Baojiu Li, et al. (2013a). "Nonlinear structure formation in the Cubic Galileon gravity model". In: *JCAP* 1310, p. 027. DOI: 10.1088/1475-7516/2013/10/027. arXiv: 1306.3219 [astro-ph.CO].

— (2013b). "Nonlinear structure formation in the cubic Galileon gravity model". In: *JCAP* 10, p. 027. DOI: 10.1088/1475-7516/2013/10/027. arXiv: 1306.3219 [astro-ph.CO].

— (2014). "Nonlinear structure formation in Nonlocal Gravity". In: *JCAP* 1409.09, p. 031. DOI: 10.1088/1475-7516/2014/09/031. arXiv: 1408.1084 [astro-ph.CO].

Bartolo, N., E. Komatsu, et al. (2004). "Non-Gaussianity from inflation: Theory and observations". In: *Phys. Rept.* 402, pp. 103–266. DOI: 10.1016/j.physrep.2004.08.022. arXiv: astro-ph/0406398 [astro-ph].

Battaglia, N., J. R. Bond, et al. (2013). "On the Cluster Physics of Sunyaev-Zel'dovich and X-ray Surveys III. Measurement Biases and Cosmological Evolution of Gas and Stellar Mass Fractions". In: *Astrophys. J.* 777. [Erratum: Astrophys. J.780,189(2014)], p. 123. DOI: 10.1088/0004-637X/780/2/189,10.1088/0004-637X/777/2/123. arXiv: 1209.4082 [astro-ph.CO].

Baumann, Daniel (2011). "Inflation". In: *Physics of the large and the small, TASI 09, proceedings of the Theoretical Advanced Study Institute in Elementary Particle Physics, Boulder, Colorado, USA, 1-26 June 2009*, pp. 523–686. DOI: 10.1142/9789814327183_0010.

arXiv: 0907.5424 [hep-th]. URL: https://inspirehep.net/record/827549/files/arXiv:0907.5424.pdf.

Baumann, Daniel, Alberto Nicolis, et al. (2012). "Cosmological Non-Linearities as an Effective Fluid". In: *JCAP* 1207, p. 051. DOI: 10.1088/1475-7516/2012/07/051. arXiv: 1004.2488 [astro-ph.CO].

Becker, Matthew R. and Andrey V. Kravtsov (2011). "On the Accuracy of Weak Lensing Cluster Mass Reconstructions". In: *Astrophys. J.* 740, p. 25. DOI: 10.1088/0004-637X/740/1/25. arXiv: 1011.1681 [astro-ph.CO].

Behroozi, Peter S., Risa H. Wechsler, and Hao-Yi Wu (2013). "The Rockstar Phase-Space Temporal Halo Finder and the Velocity Offsets of Cluster Cores". In: *Astrophys. J.* 762, p. 109. DOI: 10.1088/0004-637X/762/2/109. arXiv: 1110.4372 [astro-ph.CO].

Bekenstein, Jacob D. and Robert H. Sanders (1994). "Gravitational lenses and unconventional gravity theories". In: *Astrophys. J.* 429, p. 480. DOI: 10.1086/174337. arXiv: astro-ph/9311062 [astro-ph].

Bennett, C. L. et al. (2013). "Nine-Year Wilkinson Microwave Anisotropy Probe (WMAP) Observations: Final Maps and Results". In: *Astrophys. J. Suppl.* 208, p. 20. DOI: 10.1088/0067-0049/208/2/20. arXiv: 1212.5225 [astro-ph.CO].

Benson, B. A. et al. (2013). "Cosmological Constraints from Sunyaev-Zel'dovich-Selected Clusters with X-ray Observations in the First 178 Square Degrees of the South Pole Telescope Survey". In: *Astrophys. J.* 763, p. 147. DOI: 10.1088/0004-637X/763/2/147. arXiv: 1112.5435 [astro-ph.CO].

— (2014). "SPT-3G: A Next-Generation Cosmic Microwave Background Polarization Experiment on the South Pole Telescope". In: *Proc. SPIE Int. Soc. Opt. Eng.* 9153, 91531P. DOI: 10.1117/12.2057305. arXiv: 1407.2973 [astro-ph.IM].

Bergmann, Peter G. (1968). "Comments on the scalar-tensor theory". In: *International Journal of Theoretical Physics* 1.1, pp. 25–36. ISSN: 1572-9575. DOI: 10.1007/BF00668828. URL: http://dx.doi.org/10.1007/BF00668828.

Bernardeau, F., S. Colombi, et al. (2002). "Large scale structure of the universe and cosmological perturbation theory". In: *Phys. Rept.* 367, pp. 1–248. DOI: 10.1016/S0370-1573(02)00135-7. arXiv: astro-ph/0112551 [astro-ph].

Bertolini, Daniele, Katelin Schutz, Mikhail P. Solon, Jonathan R. Walsh, et al. (2015). "Non-Gaussian Covariance of the Matter Power Spectrum in the Effective Field Theory of Large Scale Structure". In: arXiv: 1512.07630 [astro-ph.CO].

Bertolini, Daniele, Katelin Schutz, Mikhail P. Solon, and Kathryn M. Zurek (2016). "The Trispectrum in the Effective Field Theory of Large Scale Structure". In: arXiv: 1604.01770 [astro-ph.CO].

Bertschinger, Edmund (2006). "On the Growth of Perturbations as a Test of Dark Energy". In: *Astrophys. J.* 648, pp. 797–806. DOI: 10.1086/506021. arXiv: astro-ph/0604485 [astro-ph].

Betoule, M. et al. (2014). "Improved cosmological constraints from a joint analysis of the SDSS-II and SNLS supernova samples". In: *Astron. Astrophys.* 568, A22. DOI: 10.1051/0004-6361/201423413. arXiv: 1401.4064 [astro-ph.CO].

Beutler, Florian et al. (2011). "The 6dF Galaxy Survey: Baryon Acoustic Oscillations and the Local Hubble Constant". In: *Mon. Not. Roy. Astron. Soc.* 416, pp. 3017–3032. DOI: 10.1111/j.1365-2966.2011.19250.x. arXiv: 1106.3366 [astro-ph.CO].

— (2014a). "The clustering of galaxies in the SDSS-III Baryon Oscillation Spectroscopic Survey: Signs of neutrino mass in current cosmological datasets". In: *Mon. Not. Roy. Astron. Soc.* 444, p. 3501. DOI: 10.1093/mnras/stu1702. arXiv: 1403.4599 [astro-ph.CO].

— (2014b). "The clustering of galaxies in the SDSS-III Baryon Oscillation Spectroscopic Survey: Testing gravity with redshift-space distortions using the power spectrum multipoles".

In: *Mon. Not. Roy. Astron. Soc.* 443.2, pp. 1065–1089. DOI: 10.1093/mnras/stu1051. arXiv: 1312.4611 [astro-ph.CO].

Beutler, Florian, Chris Blake, et al. (2012). "The 6dF Galaxy Survey: $z \approx 0$ measurement of the growth rate and σ_8". In: *Mon. Not. Roy. Astron. Soc.* 423, pp. 3430–3444. DOI: 10.1111/j.1365-2966.2012.21136.x. arXiv: 1204.4725 [astro-ph.CO].

Bhattacharya, Suman, Katrin Heitmann, et al. (2011). "Mass Function Predictions Beyond LCDM". In: *Astrophys. J.* 732, p. 122. DOI: 10.1088/0004-637X/732/2/122. arXiv: 1005.2239 [astro-ph.CO].

Binney, J. and S. Tremaine (2008). *Galactic Dynamics: Second Edition*. Princeton University Press.

Blake, Chris et al. (2011a). "The WiggleZ Dark Energy Survey: mapping the distance-redshift relation with baryon acoustic oscillations". In: *Mon. Not. Roy. Astron. Soc.* 418, pp. 1707–1724. DOI: 10.1111/j.1365-2966.2011.19592.x. arXiv: 1108.2635 [astro-ph.CO].

— (2011b). "The WiggleZ Dark Energy Survey: measuring the cosmic expansion history using the Alcock-Paczynski test and distant supernovae". In: *Mon. Not. Roy. Astron. Soc.* 418, pp. 1725–1735. DOI: 10.1111/j.1365-2966.2011.19606.x. arXiv: 1108.2637 [astro-ph.CO].

Blake, Chris, J. Berian James, and Gregory B. Poole (2014). "Using the topology of large-scale structure in the WiggleZ Dark Energy Survey as a cosmological standard ruler". In: *Mon. Not. Roy. Astron. Soc.* 437.3, pp. 2488–2506. DOI: 10.1093/mnras/stt2062. arXiv: 1310.6810 [astro-ph.CO].

Blas, Diego, Mathias Garny, and Thomas Konstandin (2014). "Cosmological perturbation theory at three-loop order". In: *JCAP* 1401, p. 010. DOI: 10.1088/1475-7516/2014/01/010. arXiv: 1309.3308 [astro-ph.CO].

Blas, Diego, Julien Lesgourgues, and Thomas Tram (2011). "The Cosmic Linear Anisotropy Solving System (CLASS) II: Approximation schemes". In: *JCAP* 1107, p. 034. DOI: 10.1088/1475-7516/2011/07/034. arXiv: 1104.2933 [astro-ph.CO].

Bleem, L. E. et al. (2015). "Galaxy Clusters Discovered via the Sunyaev-Zel'dovich Effect in the 2500-square-degree SPT-SZ survey". In: *Astrophys. J. Suppl.* 216.2, p. 27. DOI: 10.1088/0067-0049/216/2/27. arXiv: 1409.0850 [astro-ph.CO].

Bocquet, Sebastian, Alex Saro, et al. (2016). "Halo mass function: Baryon impact, fitting formulae and implications for cluster cosmology". In: *Mon. Not. Roy. Astron. Soc.* 456.3, pp. 2361–2373. DOI: 10.1093/mnras/stv2657. arXiv: 1502.07357 [astro-ph.CO].

Boehringer, H. et al. (2004). "The ROSAT-ESO Flux Limited X-ray (REFLEX) Galaxy Cluster Survey. 5. The Cluster catalogue". In: *Astron. Astrophys.* 425, pp. 367–383. DOI: 10.1051/0004-6361:20034484. arXiv: astro-ph/0405546 [astro-ph].

Bond, J. R., S. Cole, et al. (Oct. 1991). "Excursion set mass functions for hierarchical Gaussian fluctuations". In: *ApJ* 379, pp. 440–460. DOI: 10.1086/170520.

Borgani, S., P. Rosati, et al. (2001). "Measuring Ω_m with the rosat deep cluster survey". In: *Astrophys. J.* 561, pp. 13–21. DOI: 10.1086/323214. arXiv: astro-ph/0106428 [astro-ph].

Borisov, Alexander, Bhuvnesh Jain, and Pengjie Zhang (2012). "Spherical Collapse in f(R) Gravity". In: *Phys. Rev.* D85, p. 063518. DOI: 10.1103/PhysRevD.85.063518. arXiv: 1102.4839 [astro-ph.CO].

Brax, Philippe, Carsten van de Bruck, Anne-Christine Davis, Justin Khoury, et al. (2004). "Detecting dark energy in orbit - The Cosmological chameleon". In: *Phys. Rev.* D70, p. 123518. DOI: 10.1103/PhysRevD.70.123518. arXiv: astro-ph/0408415 [astro-ph].

Brax, Philippe, Carsten van de Bruck, Anne-Christine Davis, and Douglas J. Shaw (2008). "f(R) Gravity and Chameleon Theories". In: *Phys. Rev.* D78, p. 104021. DOI: 10.1103/PhysRevD.78.104021. arXiv: 0806.3415 [astro-ph].

Brax, Philippe, Anne-Christine Davis, and Baojiu Li (2012). "Modified Gravity Tomography". In: *Phys. Lett.* B715, pp. 38–43. DOI: 10.1016/j.physletb.2012.08.002. arXiv: 1111.6613 [astro-ph.CO].

Brax, Philippe, Anne-C. Davis, et al. (2012). "Systematic simulations of modified gravity: symmetron and dilaton models". In: *JCAP* 10, p. 002. DOI: 10.1088/1475-7516/2012/10/002. arXiv: 1206.3568 [astro-ph.CO].

— (2013). "Systematic simulations of modified gravity: chameleon models". In: *JCAP* 04, p. 029. DOI: 10.1088/1475-7516/2013/04/029. arXiv: 1303.0007 [astro-ph.CO].

Brax, Philippe and Patrick Valageas (2012). "Structure Formation in Modified Gravity Scenarios". In: *Phys. Rev.* D86, p. 063512. DOI: 10.1103/PhysRevD.86.063512. arXiv: 1205.6583 [astro-ph.CO].

Bryan, G. L. and M. L. Norman (1998). "Statistical properties of x-ray clusters: Analytic and numerical comparisons". In: *Astrophys. J.* 495, p. 80. DOI: 10.1086/305262. arXiv: astro-ph/9710107 [astro-ph].

Burrage, Clare, Edmund J. Copeland, and James Stevenson (2015). "Ellipticity Weakens Chameleon Screening". In: *Phys. Rev.* D91, p. 065030. DOI: 10.1103/PhysRevD.91.065030. arXiv: 1412.6373 [hep-th].

Carlson, Jordan, Martin White, and Nikhil Padmanabhan (2009). "A critical look at cosmological perturbation theory techniques". In: *Phys. Rev.* D80, p. 043531. DOI: 10.1103/PhysRevD.80.043531. arXiv: 0905.0479 [astro-ph.CO].

Carrasco, John Joseph M., Simon Foreman, et al. (2014a). "The 2-loop matter power spectrum and the IR-safe integrand". In: *JCAP* 1407, p. 056. DOI: 10.1088/1475-7516/2014/07/056. arXiv: 1304.4946 [astro-ph.CO].

— (2014b). "The Effective Field Theory of Large Scale Structures at Two Loops". In: *JCAP* 1407, p. 057. DOI: 10.1088/1475-7516/2014/07/057. arXiv: 1310.0464 [astro-ph.CO].

Carrasco, John Joseph M., Mark P. Hertzberg, and Leonardo Senatore (2012). "The Effective Field Theory of Cosmological Large Scale Structures". In: *JHEP* 09, p. 082. DOI: 10.1007/JHEP09(2012)082. arXiv: 1206.2926 [astro-ph.CO].

Carroll, S. M. (2004). *Spacetime and geometry. An introduction to general relativity.*

Carroll, Sean M., Stefan Leichenauer, and Jason Pollack (2014). "Consistent effective theory of long-wavelength cosmological perturbations". In: *Phys. Rev.* D90.2, p. 023518. DOI: 10.1103/PhysRevD.90.023518. arXiv: 1310.2920 [hep-th].

Castorina, Emanuele, Emiliano Sefusatti, et al. (2014). "Cosmology with massive neutrinos II: on the universality of the halo mass function and bias". In: *JCAP* 1402, p. 049. DOI: 10.1088/1475-7516/2014/02/049. arXiv: 1311.1212 [astro-ph.CO].

Cataneo, Matteo, David Rapetti, et al. (2015). "New constraints on $f(R)$ gravity from clusters of galaxies". In: *Phys. Rev.* D92.4, p. 044009. DOI: 10.1103/PhysRevD.92.044009. arXiv: 1412.0133 [astro-ph.CO].

Chiba, Takeshi (2003). "1/R gravity and scalar - tensor gravity". In: *Phys. Lett.* B575, pp. 1–3. DOI: 10.1016/j.physletb.2003.09.033. arXiv: astro-ph/0307338 [astro-ph].

Chiba, Takeshi, Tristan L. Smith, and Adrienne L. Erickcek (2007). "Solar System constraints to general f(R) gravity". In: *Phys. Rev.* D75, p. 124014. DOI: 10.1103/PhysRevD.75.124014. arXiv: astro-ph/0611867 [astro-ph].

Clifton, Timothy, Pedro G. Ferreira, et al. (2012). "Modified Gravity and Cosmology". In: *Phys. Rept.* 513, pp. 1–189. DOI: 10.1016/j.physrep.2012.01.001. arXiv: 1106.2476 [astro-ph.CO].

Conley, A. et al. (2011). "Supernova Constraints and Systematic Uncertainties from the First 3 Years of the Supernova Legacy Survey". In: *Astrophys. J. Suppl.* 192, p. 1. DOI: 10.1088/0067-0049/192/1/1. arXiv: 1104.1443 [astro-ph.CO].

Cooke, Ryan, Max Pettini, et al. (2014). "Precision measures of the primordial abundance of deuterium". In: *Astrophys. J.* 781.1, p. 31. DOI: 10.1088/0004-637X/781/1/31. arXiv: 1308.3240 [astro-ph.CO].

Copeland, Edmund J., M. Sami, and Shinji Tsujikawa (2006). "Dynamics of dark energy". In: *Int. J. Mod. Phys.* D15, pp. 1753–1936. DOI: 10.1142/S021827180600942X. arXiv: hep-th/0603057 [hep-th].

Corasaniti, P. S. and I. Achitouv (2011a). "Excursion Set Halo Mass Function and Bias in a Stochastic Barrier Model of Ellipsoidal Collapse". In: *Phys. Rev.* D84, p. 023009. DOI: 10.1103/PhysRevD.84.023009. arXiv: 1107.1251 [astro-ph.CO].

— (2011b). "Toward a Universal Formulation of the Halo Mass Function". In: *Phys. Rev. Lett.* 106, p. 241302. DOI: 10.1103/PhysRevLett.106.241302. arXiv: 1012.3468 [astro-ph.CO].

Cortês, Marina, Andrew R. Liddle, and David Parkinson (2015). "Tensors, BICEP2 results, prior dependence, and dust". In: *Phys. Rev.* D92.6, p. 063511. DOI: 10.1103/PhysRevD.92.063511. arXiv: 1409.6530 [astro-ph.CO].

Crocce, Martin, Pablo Fosalba, et al. (2010). "Simulating the Universe with MICE: The abundance of massive clusters". In: *Mon. Not. Roy. Astron. Soc.* 403, pp. 1353–1367. DOI: 10.1111/j.1365-2966.2009.16194.x. arXiv: 0907.0019 [astro-ph.CO].

Cui, Weiguang, Marco Baldi, and Stefano Borgani (2012). "The halo mass function in interacting Dark Energy models". In: *Mon. Not. Roy. Astron. Soc.* 424, p. 993. DOI: 10.1111/j.1365-2966.2012.21267.x. arXiv: 1201.3568 [astro-ph.CO].

Cui, Weiguang, Stefano Borgani, et al. (2012). "The effects of baryons on the halo mass function". In: *Mon. Not. Roy. Astron. Soc.* 423, p. 2279. DOI: 10.1111/j.1365-2966.2012.21037.x. arXiv: 1111.3066 [astro-ph.CO].

Dahle, Hakon (2006). "The Cluster Mass Function from Weak Gravitational Lensing". In: *Astrophys. J.* 653, pp. 954–962. DOI: 10.1086/508654. arXiv: astro-ph/0608480 [astro-ph].

Damour, T., F. Piazza, and G. Veneziano (2002a). "Runaway dilaton and equivalence principle violations". In: *Phys. Rev. Lett.* 89, 081601. DOI: 10.1103/PhysRevLett.89.081601. arXiv: gr-qc/0204094.

— (2002b). "Violations of the equivalence principle in a dilaton-runaway scenario". In: *Phys. Rev. D* 66, 046007. DOI: 10.1103/PhysRevD.66.046007. arXiv: hep-th/0205111.

Damour, T. and A. M. Polyakov (1994). "The String dilaton and a least coupling principle". In: *Nucl. Phys. B* 423, pp. 532–558. DOI: 10.1016/0550-3213(94)90143-0. arXiv: hep-th/9401069 [hep-th].

Das, Sudeep et al. (2011). "Detection of the Power Spectrum of Cosmic Microwave Background Lensing by the Atacama Cosmology Telescope". In: *Phys. Rev. Lett.* 107, p. 021301. DOI: 10.1103/PhysRevLett.107.021301. arXiv: 1103.2124 [astro-ph.CO].

— (2014). "The Atacama Cosmology Telescope: temperature and gravitational lensing power spectrum measurements from three seasons of data". In: *JCAP* 1404, p. 014. DOI: 10.1088/1475-7516/2014/04/014. arXiv: 1301.1037 [astro-ph.CO].

Dawson, Kyle S. et al. (2016). "The SDSS-IV extended Baryon Oscillation Spectroscopic Survey: Overview and Early Data". In: *Astron. J.* 151, p. 44. DOI: 10.3847/0004-6256/151/2/44. arXiv: 1508.04473 [astro-ph.CO].

De Felice, Antonio and Shinji Tsujikawa (2010). "$f(R)$ theories". In: *Living Rev. Rel.* 13, p. 3. DOI: 10.12942/lrr-2010-3. arXiv: 1002.4928 [gr-qc].

Despali, Giulia, Carlo Giocoli, et al. (2016). "The universality of the virial halo mass function and models for non-universality of other halo definitions". In: *Mon. Not. Roy. Astron. Soc.* 456.3, pp. 2486–2504. DOI: 10.1093/mnras/stv2842. arXiv: 1507.05627 [astro-ph.CO].

Di Porto, Cinzia and Luca Amendola (2008). "Observational constraints on the linear fluctuation growth rate". In: *Phys. Rev.* D77, p. 083508. DOI: 10.1103/PhysRevD.77.083508. arXiv: 0707.2686 [astro-ph].

Dicke, R. H. (Mar. 1962). "Mach's Principle and Invariance under Transformation of Units". In: *Phys. Rev.* 125 (6), pp. 2163–2167. DOI: 10.1103/PhysRev.125.2163. URL: http://link.aps.org/doi/10.1103/PhysRev.125.2163.

Dodelson, Scott (2003). *Modern Cosmology*. Amsterdam: Academic Press. ISBN: 9780122191411. URL: http://www.slac.stanford.edu/spires/find/books/www?cl=QB981:D62:2003.

Donahue, Megan and G. Mark Voit (1999). "Omega-matter from the temperature-redshift distribution of emss clusters of galaxies". In: *Astrophys. J.* 523, p. L137. DOI: 10.1086/312272. arXiv: astro-ph/9907333 [astro-ph].

Dossett, Jason, Bin Hu, and David Parkinson (2014). "Constraining models of $f(R)$ gravity with Planck and WiggleZ power spectrum data". In: *JCAP* 1403, p. 046. DOI: 10.1088/1475-7516/2014/03/046. arXiv: 1401.3980 [astro-ph.CO].

Drinkwater, Michael J. et al. (2010). "The WiggleZ Dark Energy Survey: Survey Design and First Data Release". In: *Mon. Not. Roy. Astron. Soc.* 401, pp. 1429–1452. DOI: 10.1111/j.1365-2966.2009.15754.x. arXiv: 0911.4246 [astro-ph.CO].

Ebeling, H., A. C. Edge, H. Bohringer, et al. (1998). "The ROSAT Brightest Cluster Sample (BCS) - I. The compilation of the sample and the cluster log N-log S distribution". In: *Mon. Not. Roy. Astron. Soc.* 301, pp. 881–914. DOI: 10.1046/j.1365-8711.1998.01949.x. arXiv: astro-ph/9812394 [astro-ph].

Ebeling, H., A. C. Edge, A. Mantz, et al. (2010). "The X-ray brightest clusters of galaxies from the Massive Cluster Survey". In: *Mon. Not. Roy. Astron. Soc.* 407, p. 83. DOI: 10.1111/j.1365-2966.2010.16920.x. arXiv: 1004.4683 [astro-ph.CO].

Einstein, A. (1916). "Die Grundlage der allgemeinen Relativitätstheorie". In: *Annalen der Physik* 354, pp. 769–822. DOI: 10.1002/andp.19163540702.

Eisenstein, Daniel J. et al. (2005). "Detection of the baryon acoustic peak in the large-scale correlation function of SDSS luminous red galaxies". In: *Astrophys. J.* 633, pp. 560–574. DOI: 10.1086/466512. arXiv: astro-ph/0501171 [astro-ph].

Eke, Vincent R., Shaun Cole, et al. (1998). "Measuring omega(0) using cluster evolution". In: *Mon. Not. Roy. Astron. Soc.* 298, p. 1145. DOI: 10.1046/j.1365-8711.1998.01713.x. arXiv: astro-ph/9802350 [astro-ph].

Ellis, R. S. (Feb. 2010). "Gravitational lensing: a unique probe of dark matter and dark energy". In: *Philosophical Transactions of the Royal Society of London Series A* 368, pp. 967–987. DOI: 10.1098/rsta.2009.0209.

Engelen, A. van et al. (2012). "A measurement of gravitational lensing of the microwave background using South Pole Telescope data". In: *Astrophys. J.* 756, p. 142. DOI: 10.1088/0004-637X/756/2/142. arXiv: 1202.0546 [astro-ph.CO].

Erickcek, Adrienne L., Neil Barnaby, et al. (2013). "Catastrophic Consequences of Kicking the Chameleon". In: *Phys. Rev. Lett.* 110, p. 171101. DOI: 10.1103/PhysRevLett.110.171101. arXiv: 1304.0009 [astro-ph.CO].

— (2014). "Chameleons in the Early Universe: Kicks, Rebounds, and Particle Production". In: *Phys. Rev.* D89.8, p. 084074. DOI: 10.1103/PhysRevD.89.084074. arXiv: 1310.5149 [astro-ph.CO].

Ettori, S., A. Morandi, et al. (2009). "The cluster gas mass fraction as a cosmological probe: a revised study". In: *Astron. Astrophys.* 501, pp. 61–73. DOI: 10.1051/0004-6361/200810878. arXiv: 0904.2740 [astro-ph.CO].

Ettori, S., P. Tozzi, and P. Rosati (2003). "Constraining the cosmological parameters with the gas mass fraction in local and z > 0.7 galaxy clusters". In: *Astron. Astrophys.* 398, pp. 879–890. DOI: 10.1051/0004-6361:20021706. arXiv: astro-ph/0211335 [astro-ph].

Ferraro, Simone, Fabian Schmidt, and Wayne Hu (2011). "Cluster Abundance in $f(R)$ Gravity Models". In: *Phys. Rev.* D83, p. 063503. DOI: 10.1103/PhysRevD.83.063503. arXiv: 1011.0992 [astro-ph.CO].

Flanagan, Eanna E. (2004). "The Conformal frame freedom in theories of gravitation". In: *Class. Quant. Grav.* 21, p. 3817. DOI: 10.1088/0264-9381/21/15/N02. arXiv: gr-qc/0403063 [gr-qc].

Fontanot, Fabio, Ewald Puchwein, et al. (2013). "Semi-analytic galaxy formation in $f(R)$ gravity cosmologies". In: *Mon. Not. Roy. Astron. Soc.* 436, p. 2672. DOI: 10.1093/mnras/stt1763. arXiv: 1307.5065 [astro-ph.CO].

Foreman, S., H. Perrier, and L. Senatore (2016). "Precision Comparison of the Power Spectrum in the EFTofLSS with Simulations". In: *JCAP* 1605, 027, p. 027. DOI: 10.1088/1475-7516/2016/05/027. arXiv: 1507.05326.

Foreman, Simon and Leonardo Senatore (2016). "The EFT of Large Scale Structures at' All Redshifts: Analytical Predictions for Lensing". In: *JCAP* 1604, p. 033. DOI: 10.1088/1475-7516/2016/04/033. arXiv: 1503.01775 [astro-ph.CO].

Frieman, Joshua, Michael Turner, and Dragan Huterer (2008). "Dark Energy and the Accelerating Universe". In: *Ann. Rev. Astron. Astrophys.* 46, pp. 385–432. DOI: 10.1146/annurev.astro.46.060407.145243. arXiv: 0803.0982 [astro-ph].

Hahn, Oliver, Raul E. Angulo, and Tom Abel (2015). "The Properties of Cosmic Velocity Fields". In: *Mon. Not. Roy. Astron. Soc.* 454.4, pp. 3920–3937. DOI: 10.1093/mnras/stv2179. arXiv: 1404.2280 [astro-ph.CO].

Hahn, T. (2005). "CUBA: A Library for multidimensional numerical integration". In: *Comput. Phys. Commun.* 168, pp. 78–95. DOI: 10.1016/j.cpc.2005.01.010. arXiv: hep-ph/0404043 [hep-ph].

Hamilton, A. J. S. (2000). "Uncorrelated modes of the nonlinear power spectrum". In: *Mon. Not. Roy. Astron. Soc.* 312, pp. 257–284. DOI: 10.1046/j.1365-8711.2000.03071.x. arXiv: astro-ph/9905191 [astro-ph].

Hammami, Amir, Claudio Llinares, et al. (2015). "Hydrodynamic Effects in the Symmetron and $f(R)$-gravity Models". In: *Mon. Not. Roy. Astron. Soc.* 449.4, pp. 3635–3644. DOI: 10.1093/mnras/stv529. arXiv: 1503.02004 [astro-ph.CO].

Hasselfield, Matthew et al. (2013). "The Atacama Cosmology Telescope: Sunyaev-Zel'dovich selected galaxyclusters at 148 GHz from three seasons of data". In: *JCAP* 1307, p. 008. DOI: 10.1088/1475-7516/2013/07/008. arXiv: 1301.0816 [astro-ph.CO].

He, Jian-hua, Baojiu Li, and Y. P. Jing (2013). "Revisiting the matter power spectra in $f(R)$ gravity". In: *Phys. Rev.* D88.10, p. 103507. DOI: 10.1103/PhysRevD.88.103507. arXiv: 1305.7333 [astro-ph.CO].

Heitmann, Katrin, Earl Lawrence, et al. (2014). "The Coyote Universe Extended: Precision Emulation of the Matter Power Spectrum". In: *Astrophys. J.* 780, p. 111. DOI: 10.1088/0004-637X/780/1/111. arXiv: 1304.7849 [astro-ph.CO].

Henry, J. Patrick (2000). "Measuring cosmological parameters from the evolution of cluster X-ray temperatures". In: *Astrophys. J.* 534, pp. 565–580. DOI: 10.1086/308783. arXiv: astro-ph/0002365 [astro-ph].

— (2004). "X-ray temperatures for the EMSS high redshift cluster sample: Constraints on cosmology and the dark energy equation of state". In: *Astrophys. J.* 609, pp. 603–616. DOI: 10.1086/421336. arXiv: astro-ph/0404142 [astro-ph].

Henry, J. Patrick, August E. Evrard, et al. (2009). "The X-ray Cluster Normalization of the Matter Power Spectrum". In: *Astrophys. J.* 691, pp. 1307–1321. DOI: 10.1088/0004-637X/691/2/1307. arXiv: 0809.3832 [astro-ph].

Hinshaw, G. et al. (2013). "Nine-Year Wilkinson Microwave Anisotropy Probe (WMAP) Observations: Cosmological Parameter Results". In: *Astrophys. J. Suppl.* 208, p. 19. DOI: 10.1088/0067-0049/208/2/19. arXiv: 1212.5226 [astro-ph.CO].

Hoekstra, Henk (2007). "Comparison of weak lensing masses and X-ray properties of galaxy clusters". In: *Mon. Not. Roy. Astron. Soc.* 379, pp. 317–330. DOI: 10.1111/j.1365-2966.2007.11951.x. arXiv: 0705.0358 [astro-ph].

Hoekstra, Henk, Andisheh Mahdavi, et al. (2012). "The Canadian Cluster Comparison Project: weak lensing masses and SZ scaling relations". In: *Mon. Not. Roy. Astron. Soc.* 427, p. 1298. DOI: 10.1111/j.1365-2966.2012.22072.x. arXiv: 1208.0606 [astro-ph.CO].

Hoffmann, Kai, Julien Bel, and Enrique Gaztanaga (2015). "Comparing halo bias from abundance and clustering". In: *Mon. Not. Roy. Astron. Soc.* 450.2, pp. 1674–1692. DOI: 10.1093/mnras/stv702. arXiv: 1503.00313 [astro-ph.CO].

Hojjati, Alireza, Levon Pogosian, Alessandra Silvestri, et al. (2012). "Practical solutions for perturbed $f(R)$ gravity". In: *Phys. Rev.* D86, p. 123503. DOI: 10.1103/PhysRevD.86.123503. arXiv: 1210.6880 [astro-ph.CO].

Hojjati, Alireza, Levon Pogosian, and Gong-Bo Zhao (2011). "Testing gravity with CAMB and CosmoMC". In: *JCAP* 1108, p. 005. DOI: 10.1088/1475-7516/2011/08/005. arXiv: 1106.4543 [astro-ph.CO].

Hu, Bin, Marco Raveri, et al. (2015). "Exploring massive neutrinos in dark cosmologies with EFTCAMB/ EFTCosmoMC". In: *Phys. Rev.* D91.6, p. 063524. DOI: 10.1103/PhysRevD.91.063524. arXiv: 1410.5807 [astro-ph.CO].

Hu, Wayne (2004). "Covariant linear perturbation formalism". In: *Astroparticle physics and cosmology. Proceedings: Summer School, Trieste, Italy, Jun 17-Jul 5 2002.* arXiv: astro-ph/0402060 [astro-ph].

Hu, Wayne and Scott Dodelson (2002). "Cosmic microwave background anisotropies". In: *Ann. Rev. Astron. Astrophys.* 40, pp. 171–216. DOI: 10.1146/annurev.astro.40.060401.093926. arXiv: astro-ph/0110414 [astro-ph].

Hu, Wayne and Andrey V. Kravtsov (2003). "Sample variance considerations for cluster surveys". In: *Astrophys. J.* 584, pp. 702–715. DOI: 10.1086/345846. arXiv: astro-ph/0203169 [astro-ph].

Hu, Wayne and Ignacy Sawicki (2007). "Models of $f(R)$ Cosmic Acceleration that Evade Solar-System Tests". In: *Phys. Rev.* D76, p. 064004. DOI: 10.1103/PhysRevD.76.064004. arXiv: 0705.1158 [astro-ph].

Hubble, E. (Mar. 1929). "A Relation between Distance and Radial Velocity among Extra-Galactic Nebulae". In: *Proceedings of the National Academy of Science* 15, pp. 168–173. DOI: 10.1073/pnas.15.3.168.

Ivezic, Z., J. A. Tyson, et al. (2008). "LSST: from Science Drivers to Reference Design and Anticipated Data Products". In: arXiv: 0805.2366 [astro-ph].

Jain, Bhuvnesh, Vinu Vikram, and Jeremy Sakstein (2013). "Astrophysical Tests of Modified Gravity: Constraints from Distance Indicators in the Nearby Universe". In: *Astrophys. J.* 779, p. 39. DOI: 10.1088/0004-637X/779/1/39. arXiv: 1204.6044 [astro-ph.CO].

Jenkins, A., C. S. Frenk, et al. (2001). "The Mass function of dark matter halos". In: *Mon. Not. Roy. Astron. Soc.* 321, p. 372. DOI: 10.1046/j.1365-8711.2001.04029.x. arXiv: astro-ph/0005260 [astro-ph].

Johnston, David E., Erin S. Sheldon, et al. (2007). "Cross-correlation lensing: Determining galaxy and cluster mass profiles from statistical weak lensing measurements". In: *Astrophys. J.* 656, pp. 27–41. DOI: 10.1086/510060. arXiv: astro-ph/0507467 [astro-ph].

Jones-Smith, Katherine and Francesc Ferrer (2012). "Detecting Chameleon Dark Energy via Electrostatic Analogy". In: *Phys. Rev. Lett.* 108, p. 221101. DOI: 10.1103/PhysRevLett.108.221101. arXiv: 1105.6085 [astro-ph.CO].

Joyce, Austin, Bhuvnesh Jain, et al. (2015). "Beyond the Cosmological Standard Model". In: *Phys. Rept.* 568, pp. 1–98. DOI: 10.1016/j.physrep.2014.12.002. arXiv: 1407.0059 [astro-ph.CO].

Kazin, Eyal A. et al. (2014). "The WiggleZ Dark Energy Survey: improved distance measurements to $z = 1$ with reconstruction of the baryonic acoustic feature". In: *Mon. Not. Roy. Astron. Soc.* 441.4, pp. 3524–3542. DOI: 10.1093/mnras/stu778. arXiv: 1401.0358 [astro-ph.CO].

Keisler, R. et al. (2011). "A Measurement of the Damping Tail of the Cosmic Microwave Background Power Spectrum with the South Pole Telescope". In: *Astrophys. J.* 743, p. 28. DOI: 10.1088/0004-637X/743/1/28. arXiv: 1105.3182 [astro-ph.CO].

Kelly, Patrick L. et al. (2014). "Weighing the Giants – II. Improved calibration of photometry from stellar colours and accurate photometric redshifts". In: *Mon. Not. Roy. Astron. Soc.* 439.1, pp. 28–47. DOI: 10.1093/mnras/stt1946. arXiv: 1208.0602 [astro-ph.CO].

Khoury, Justin and Amanda Weltman (2004a). "Chameleon cosmology". In: *Phys. Rev.* D69, p. 044026. DOI: 10.1103/PhysRevD.69.044026. arXiv: astro-ph/0309411 [astro-ph].

— (2004b). "Chameleon fields: Awaiting surprises for tests of gravity in space". In: *Phys. Rev. Lett.* 93, p. 171104. DOI: 10.1103/PhysRevLett.93.171104. arXiv: astro-ph/0309300 [astro-ph].

Kilbinger, Martin et al. (2013). "CFHTLenS: Combined probe cosmological model comparison using 2D weak gravitational lensing". In: *Mon. Not. Roy. Astron. Soc.* 430, pp. 2200–2220. DOI: 10.1093/mnras/stt041. arXiv: 1212.3338 [astro-ph.CO].

Knebe, Alexander et al. (2013). "Structure Finding in Cosmological Simulations: The State of Affairs". In: *Mon. Not. Roy. Astron. Soc.* 435, p. 1618. DOI: 10.1093/mnras/stt1403. arXiv: 1304.0585 [astro-ph.CO].

Knobel, Christian (2012). "An introduction into the theory of cosmological structure formation". In: arXiv: 1208.5931 [astro-ph.CO].

Koester, Benjamin et al. (2007). "A MaxBCG Catalog of 13,823 Galaxy Clusters from the Sloan Digital Sky Survey". In: *Astrophys. J.* 660, pp. 239–255. DOI: 10.1086/509599. arXiv: astro-ph/0701265 [astro-ph].

Komatsu, E. et al. (2011). "Seven-Year Wilkinson Microwave Anisotropy Probe (WMAP) Observations: Cosmological Interpretation". In: *Astrophys. J. Suppl.* 192, p. 18. DOI: 10.1088/0067-0049/192/2/18. arXiv: 1001.4538 [astro-ph.CO].

Kopp, Michael, Stephen A. Appleby, et al. (2013). "Spherical collapse and halo mass function in $f(R)$ theories". In: *Phys. Rev.* D88.8, p. 084015. DOI: 10.1103/PhysRevD.88.084015. arXiv: 1306.3233 [astro-ph.CO].

Krauss, L. M. and B. Chaboyer (Jan. 2003). "Age Estimates of Globular Clusters in the Milky Way: Constraints on Cosmology". In: *Science* 299, pp. 65–70. DOI: 10.1126/science.1075631.

Lahav, Ofer, Per B. Lilje, et al. (1991). "Dynamical effects of the cosmological constant". In: *Mon. Not. Roy. Astron. Soc.* 251, pp. 128–136.

Lam, T. Y. and R. K. Sheth (2008). "Perturbation theory and excursion set estimates of the probability distribution function of dark matter, and a method for reconstructing the initial distribution function". In: *Mon. Not. Roy. Astron. Soc.* 386, p. 407. DOI: 10.1111/j.1365-2966.2008.13038.x. arXiv: 0711.5029 [astro-ph].

Lam, Tsz Yan and Baojiu Li (2012). "Excursion set theory for modified gravity: correlated steps, mass functions and halo bias". In: *Mon. Not. Roy. Astron. Soc.* 426, pp. 3260–3270. DOI: 10.1111/j.1365-2966.2012.21746.x. arXiv: 1205.0059 [astro-ph.CO].

Landau, L. D. and E. M. Lifshitz (1959). *Fluid mechanics*.

Laureijs, R. et al. (2011). "Euclid Definition Study Report". In: arXiv: 1110.3193 [astro-ph.CO].

Leauthaud, A. et al. (2010). "A Weak Lensing Study of X-ray Groups in the COSMOS survey: Form and Evolution of the Mass-Luminosity Relation". In: *Astrophys. J.* 709, pp. 97–114. DOI: 10.1088/0004-637X/709/1/97. arXiv: 0910.5219 [astro-ph.CO].

Levi, Michael et al. (2013). "The DESI Experiment, a whitepaper for Snowmass 2013". In: arXiv: 1308.0847 [astro-ph.CO].

Lewandowski, Matthew, Ashley Perko, and Leonardo Senatore (2015). "Analytic Prediction of Baryonic Effects from the EFT of Large Scale Structures". In: *JCAP* 1505, p. 019. DOI: 10.1088/1475-7516/2015/05/019. arXiv: 1412.5049 [astro-ph.CO].

Lewandowski, Matthew, Leonardo Senatore, et al. (2015). "On the EFT of Large Scale Structures in Redshift Space". In: arXiv: 1512.06831 [astro-ph.CO].

Lewis, Antony and Sarah Bridle (2002). "Cosmological parameters from CMB and other data: A Monte Carlo approach". In: *Phys. Rev.* D66, p. 103511. DOI: 10.1103/PhysRevD.66.103511. arXiv: astro-ph/0205436 [astro-ph].

Lewis, Antony and Anthony Challinor (2006). "Weak gravitational lensing of the cmb". In: *Phys. Rept.* 429, pp. 1–65. DOI: 10.1016/j.physrep.2006.03.002. arXiv: astro-ph/0601594 [astro-ph].

Lewis, Antony, Anthony Challinor, and Anthony Lasenby (2000). "Efficient computation of CMB anisotropies in closed FRW models". In: *Astrophys. J.* 538, pp. 473–476. DOI: 10.1086/309179. arXiv: astro-ph/9911177 [astro-ph].

Li, Baojiu, Alexandre Barreira, et al. (2013). "simulating the quartic Galileon gravity model on adaptively refined meshes". In: *JCAP* 11, p. 012. DOI: 10.1088/1475-7516/2013/11/012. arXiv: 1308.3491 [astro-ph.CO].

Li, Baojiu and George Efstathiou (2012). "An Extended Excursion Set Approach to Structure Formation in Chameleon Models". In: *Mon. Not. Roy. Astron. Soc.* 421, p. 1431. DOI: 10.1111/j.1365-2966.2011.20404.x. arXiv: 1110.6440 [astro-ph.CO].

Li, Baojiu, Wojciech A. Hellwing, et al. (2013a). "The nonlinear matter and velocity power spectra in $f(R)$ gravity". In: *Mon. Not. Roy. Astron. Soc.* 428, pp. 743–755. DOI: 10.1093/mnras/sts072. arXiv: 1206.4317 [astro-ph.CO].

— (2013b). "The nonlinear matter and velocity power spectra in f(R) gravity". In: *MNRAS* 428, p. 743. DOI: 10.1093/mnras/sts072. arXiv: astro-ph/1206.4317 [astro-ph].

Li, Baojiu and Tsz Yan Lam (2012). "Excursion set theory for modified gravity: Eulerian versus Lagrangian environments". In: *Mon. Not. Roy. Astron. Soc.* 425, p. 730. DOI: 10.1111/j.1365-2966.2012.21592.x. arXiv: 1205.0058 [astro-ph.CO].

Li, Baojiu, Gong-Bo Zhao, and Kazuya Koyama (2013). "Exploring Vainshtein mechanism on adaptively refined meshes". In: *JCAP* 1305, p. 023. DOI: 10.1088/1475-7516/2013/05/023. arXiv: 1303.0008 [astro-ph.CO].

Li, Baojiu, Gong-Bo Zhao, Romain Teyssier, et al. (2012). "ECOSMOG: An Efficient Code for Simulating Modified Gravity". In: *JCAP* 1201, p. 051. DOI: 10.1088/1475-7516/2012/01/051. arXiv: 1110.1379 [astro-ph.CO].

Li, Yin and Wayne Hu (2011). "Chameleon Halo Modeling in $f(R)$ Gravity". In: *Phys. Rev.* D84, p. 084033. DOI: 10.1103/PhysRevD.84.084033. arXiv: 1107.5120 [astro-ph.CO].

Linden, Anja von der et al. (2014a). "Robust Weak-lensing Mass Calibration of Planck Galaxy Clusters". In: *Mon. Not. Roy. Astron. Soc.* 443.3, pp. 1973–1978. DOI: 10.1093/mnras/stu1423. arXiv: 1402.2670 [astro-ph.CO].

— (2014b). "Weighing the Giants – I. Weak-lensing masses for 51 massive galaxy clusters: project overview, data analysis methods and cluster images". In: *Mon. Not. Roy. Astron. Soc.* 439.1, pp. 2–27. DOI: 10.1093/mnras/stt1945. arXiv: 1208.0597 [astro-ph.CO].

Linder, Eric V. (2005). "Cosmic growth history and expansion history". In: *Phys. Rev.* D72, p. 043529. DOI: 10.1103/PhysRevD.72.043529. arXiv: astro-ph/0507263 [astro-ph].

Liu, Xiangkun et al. (2016). "Constraining $f(R)$ Gravity Theory Using CFHTLenS Weak Lensing Peak Statistics". In: *Phys. Rev. Lett.* 117.5, p. 051101. DOI: 10.1103/PhysRevLett.117.051101. arXiv: 1607.00184 [astro-ph.CO].

Llinares, Claudio and David Mota (2013). "Releasing scalar fields: cosmological simulations of scalar-tensor theories for gravity beyond the static approximation". In: *Phys. Rev. Lett.* 110.16, p. 161101. DOI: 10.1103/PhysRevLett.110.161101. arXiv: 1302.1774 [astro-ph.CO].

Lombriser, Lucas (2014). "Constraining chameleon models with cosmology". In: *Annalen Phys.* 526, pp. 259–282. DOI: 10.1002/andp.201400058. arXiv: 1403.4268 [astro-ph.CO].

Lombriser, Lucas, Kazuya Koyama, and Baojiu Li (2014). "Halo modelling in chameleon theories". In: *JCAP* 1403, p. 021. DOI: 10.1088/1475-7516/2014/03/021. arXiv: 1312.1292 [astro-ph.CO].

Lombriser, Lucas, Kazuya Koyama, Gong-Bo Zhao, et al. (2012). "Chameleon $f(R)$ gravity in the virialized cluster". In: *Phys. Rev.* D85, p. 124054. DOI: 10.1103/PhysRevD.85.124054. arXiv: 1203.5125 [astro-ph.CO].

Lombriser, Lucas, Baojiu Li, et al. (2013). "Modeling halo mass functions in chameleon f(R) gravity". In: *Phys. Rev.* D87.12, p. 123511. DOI: 10.1103/PhysRevD.87.123511. arXiv: 1304.6395 [astro-ph.CO].

Lombriser, Lucas, Fabian Schmidt, et al. (2012). "Cluster Density Profiles as a Test of Modified Gravity". In: *Phys. Rev.* D85, p. 102001. DOI: 10.1103/PhysRevD.85.102001. arXiv: 1111.2020 [astro-ph.CO].

Lombriser, Lucas, Anze Slosar, et al. (2012). "Constraints on $f(R)$ gravity from probing the large-scale structure". In: *Phys. Rev.* D85, p. 124038. DOI: 10.1103/PhysRevD.85.124038. arXiv: 1003.3009 [astro-ph.CO].

Lovelock, D. (Mar. 1971). "The Einstein Tensor and Its Generalizations". In: *Journal of Mathematical Physics* 12, pp. 498–501. DOI: 10.1063/1.1665613.

— (June 1972). "The Four-Dimensionality of Space and the Einstein Tensor". In: *Journal of Mathematical Physics* 13, pp. 874–876. DOI: 10.1063/1.1666069.

Lukic, Zarija, Katrin Heitmann, et al. (2007). "The Halo Mass Function: High Redshift Evolution and Universality". In: *Astrophys. J.* 671, pp. 1160–1181. DOI: 10.1086/523083. arXiv: astro-ph/0702360 [ASTRO-PH].

Ma, Chung-Pei and Edmund Bertschinger (1995). "Cosmological perturbation theory in the synchronous and conformal Newtonian gauges". In: *Astrophys. J.* 455, pp. 7–25. DOI: 10.1086/176550. arXiv: astro-ph/9506072 [astro-ph].

Maeda, K.-I. (1988). "On time variation of fundamental constants in superstring theories". In: *Mod. Phys. Lett. A* 3, pp. 243–249. DOI: 10.1142/S0217732388000295.

Maggiore, Michele and Antonio Riotto (2010a). "The Halo Mass Function from Excursion Set Theory. I. Gaussian fluctuations with non-Markovian dependence on the smoothing scale". In: *Astrophys. J.* 711, pp. 907–927. DOI: 10.1088/0004-637X/711/2/907. arXiv: 0903.1249 [astro-ph.CO].

— (2010b). "The Halo mass function from excursion set theory. II. The diffusing barrier". In: *Astrophys. J.* 717, pp. 515–525. DOI: 10.1088/0004-637X/717/1/515. arXiv: 0903.1250 [astro-ph.CO].

Majumdar, Subhabrata and Joseph J. Mohr (2004). "Self calibration in cluster studies of dark energy: Combining the cluster redshift distribution, the power spectrum and mass measurements". In: *Astrophys. J.* 613, pp. 41–50. DOI: 10.1086/422829. arXiv: astro-ph/0305341 [astro-ph].

Mandelbaum, R. et al. (2008). "Precision photometric redshift calibration for galaxy-galaxy weak lensing". In: *Mon. Not. Roy. Astron. Soc.* 386, pp. 781–806. DOI: 10.1111/j.1365-2966.2008.12947.x. arXiv: 0709.1692 [astro-ph].

Manera, Marc, Ravi K Sheth, and Roman Scoccimarro (2010). "Large scale bias and the inaccuracy of the peak-background split". In: *Mon. Not. Roy. Astron. Soc.* 402, p. 589. DOI: 10.1111/j.1365-2966.2009.15921.x. arXiv: 0906.1314 [astro-ph.CO].

Mantz, A. B. et al. (2014). "Cosmology and astrophysics from relaxed galaxy clusters – II. Cosmological constraints". In: *Mon. Not. Roy. Astron. Soc.* 440.3, pp. 2077–2098. DOI: 10.1093/mnras/stu368. arXiv: 1402.6212 [astro-ph.CO].

Mantz, A., S. W. Allen, et al. (2008). "New constraints on dark energy from the observed growth of the most X-ray luminous galaxy clusters". In: *Mon. Not. Roy. Astron. Soc.* 387, pp. 1179–1192. DOI: 10.1111/j.1365-2966.2008.13311.x. arXiv: 0709.4294 [astro-ph].

Mantz, Adam B. et al. (2015). "Weighing the giants – IV. Cosmology and neutrino mass". In: *Mon. Not. Roy. Astron. Soc.* 446, pp. 2205–2225. DOI: 10.1093/mnras/stu2096. arXiv: 1407.4516 [astro-ph.CO].

Mantz, Adam B., Steven W. Allen, et al. (2016). "Weighing the Giants V: Galaxy Cluster Scaling Relations". In: arXiv: 1606.03407 [astro-ph.CO].

Mantz, Adam, Steven W. Allen, Harald Ebeling, et al. (2010). "The Observed Growth of Massive Galaxy Clusters II: X-ray Scaling Relations". In: *Mon. Not. Roy. Astron. Soc.* 406, pp. 1773–1795. DOI: 10.1111/j.1365-2966.2010.16993.x. arXiv: 0909.3099 [astro-ph.CO].

Mantz, Adam, Steven W. Allen, and David Rapetti (2010). "The Observed Growth of Massive Galaxy Clusters IV: Robust Constraints on Neutrino Properties". In: *Mon. Not. Roy. Astron. Soc.* 406, pp. 1805–1814. DOI: 10.1111/j.1365-2966.2010.16794.x. arXiv: 0911.1788 [astro-ph.CO].

Mantz, Adam, Steven W. Allen, David Rapetti, and Harald Ebeling (2010). "The Observed Growth of Massive Galaxy Clusters I: Statistical Methods and Cosmological Constraints". In: *Mon. Not. Roy. Astron. Soc.* 406, pp. 1759–1772. DOI: 10.1111/j.1365-2966.2010.16992.x. arXiv: 0909.3098 [astro-ph.CO].

Martino, Matthew C., Hans F. Stabenau, and Ravi K. Sheth (2009). "Spherical Collapse and Modified Gravity". In: *Phys. Rev.* D79, p. 084013. DOI: 10.1103/PhysRevD.79.084013. arXiv: 0812.0200 [astro-ph].

McEwen, Joseph E., Xiao Fang, et al. (2016). "FAST-PT: a novel algorithm to calculate convolution integrals in cosmological perturbation theory". In: arXiv: 1603.04826 [astro-ph.CO].

McQuinn, Matthew and Martin White (2016). "Cosmological perturbation theory in 1+1 dimensions". In: *JCAP* 1601.01, p. 043. DOI: 10.1088/1475-7516/2016/01/043. arXiv: 1502.07389 [astro-ph.CO].

Mercolli, Lorenzo and Enrico Pajer (2014). "On the velocity in the Effective Field Theory of Large Scale Structures". In: *JCAP* 1403, p. 006. DOI: 10.1088/1475-7516/2014/03/006. arXiv: 1307.3220 [astro-ph.CO].

Merloni, A. et al. (2012). "eROSITA Science Book: Mapping the Structure of the Energetic Universe". In: arXiv: 1209.3114 [astro-ph.HE].

Mirbabayi, Mehrdad, Fabian Schmidt, and Matias Zaldarriaga (2015). "Biased Tracers and Time Evolution". In: *JCAP* 1507.07, p. 030. DOI: 10.1088/1475-7516/2015/07/030. arXiv: 1412.5169 [astro-ph.CO].

Mo, H., F. C. van den Bosch, and S. White (May 2010). *Galaxy Formation and Evolution.*

Motohashi, Hayato, Alexei A. Starobinsky, and Jun'ichi Yokoyama (2013). "Cosmology Based on $f(R)$ Gravity Admits 1 eV Sterile Neutrinos". In: *Phys. Rev. Lett.* 110.12, p. 121302. DOI: 10.1103/PhysRevLett.110.121302. arXiv: 1203.6828 [astro-ph.CO].

Mukhanov, Viatcheslav F., H. A. Feldman, and Robert H. Brandenberger (1992). "Theory of cosmological perturbations. Part 1. Classical perturbations. Part 2. Quantum theory of perturbations. Part 3. Extensions". In: *Phys. Rept.* 215, pp. 203–333. DOI: 10.1016/0370-1573(92)90044-Z.

Munshi, D., P. Valageas, et al. (2008). "Cosmology with Weak Lensing Surveys". In: *Phys. Rept.* 462, pp. 67–121. DOI: 10.1016/j.physrep.2008.02.003. arXiv: astro-ph/0612667 [astro-ph].

Murray, Steven, Chris Power, and Aaron Robotham (2013). "HMFcalc: An Online Tool for Calculating Dark Matter Halo Mass Functions". In: arXiv: 1306.6721 [astro-ph.CO].

Nakamura, Takahiro T. and Yasushi Suto (1997). "Strong gravitational lensing and velocity function as tools to probe cosmological parameters: Current constraints and future predictions". In: *Prog. Theor. Phys.* 97, pp. 49–81. DOI: 10.1143/PTP.97.49. arXiv: astro-ph/9612074 [astro-ph].

Navarro, Julio F., Carlos S. Frenk, and Simon D. M. White (1996). "The Structure of cold dark matter halos". In: *Astrophys. J.* 462, pp. 563–575. DOI: 10.1086/177173. arXiv: astro-ph/9508025 [astro-ph].

— (1997). "A Universal density profile from hierarchical clustering". In: *Astrophys. J.* 490, pp. 493–508. DOI: 10.1086/304888. arXiv: astro-ph/9611107 [astro-ph].

Nesseris, S. and Leandros Perivolaropoulos (2008). "Testing Lambda CDM with the Growth Function delta(a): Current Constraints". In: *Phys. Rev.* D77, p. 023504. DOI: 10.1103/PhysRevD.77.023504. arXiv: 0710.1092 [astro-ph].

Neto, Angelo F., Liang Gao, et al. (2007). "The statistics of lambda CDM Halo Concentrations". In: *Mon. Not. Roy. Astron. Soc.* 381, pp. 1450–1462. DOI: 10.1111/j.1365-2966.2007.12381.x. arXiv: 0706.2919 [astro-ph].

Noller, Johannes, Francesca von Braun-Bates, and Pedro G. Ferreira (2014). "Relativistic scalar fields and the quasistatic approximation in theories of modified gravity". In: *Phys. Rev.* D89.2, p. 023521. DOI: 10.1103/PhysRevD.89.023521. arXiv: 1310.3266 [astro-ph.CO].

Nordtvedt Jr., K. (Sept. 1970). "Post-Newtonian Metric for a General Class of Scalar-Tensor Gravitational Theories and Observational Consequences." In: *ApJ* 161, p. 1059. DOI: 10.1086/150607.

Nunez, Alvaro and Slava Solganik (2004). "The Content of f(R) gravity". In: arXiv: hep-th/0403159 [hep-th].

Okabe, Nobuhiro, Graham P. Smith, et al. (2013). "LoCuSS: The Mass Density Profile of Massive Galaxy Clusters at z=0.2". In: *Astrophys. J.* 769, p. L35. DOI: 10.1088/2041-8205/769/2/L35. arXiv: 1302.2728 [astro-ph.CO].

Okabe, Nobuhiro, Masahiro Takada, et al. (2010). "LoCuSS: Subaru Weak Lensing Study of 30 Galaxy Clusters". In: *Publ. Astron. Soc. Jap.* 62, pp. 811–870. DOI: 10.1093/pasj/62.3.811. arXiv: 0903.1103 [astro-ph.CO].

O'Shea, Brian W., Kentaro Nagamine, et al. (2005). "Comparing AMR and SPH cosmological simulations: 1. Dark matter and adiabatic simulations". In: *Astrophys. J. Suppl.* 160, pp. 1–27. DOI: 10.1086/432645. arXiv: astro-ph/0312651 [astro-ph].

Oyaizu, Hiroaki (2008). "Non-linear evolution of $f(R)$ cosmologies I: methodology". In: *Phys. Rev.* D78, p. 123523. DOI: 10.1103/PhysRevD.78.123523. arXiv: 0807.2449 [astro-ph].

Padilla, Antonio (2015). "Lectures on the Cosmological Constant Problem". In: arXiv: 1502.05296 [hep-th].

Padmanabhan, Nikhil, Xiaoying Xu, et al. (2012). "A 2 per cent distance to z=0.35 by reconstructing baryon acoustic oscillations - I. Methods and application to the Sloan Digital Sky Survey". In: *Mon. Not. Roy. Astron. Soc.* 427.3, pp. 2132–2145. DOI: 10.1111/j.1365-2966.2012.21888.x. arXiv: 1202.0090 [astro-ph.CO].

Pajer, Enrico and Matias Zaldarriaga (2013). "On the Renormalization of the Effective Field Theory of Large Scale Structures". In: *JCAP* 1308, p. 037. DOI: 10.1088/1475-7516/2013/08/037. arXiv: 1301.7182 [astro-ph.CO].

Parfrey, Kyle, Lam Hui, and Ravi K. Sheth (2011). "Scale-dependent halo bias from scale-dependent growth". In: *Phys. Rev.* D83, p. 063511. DOI: 10.1103/PhysRevD.83.063511. arXiv: 1012.1335 [astro-ph.CO].

Peiris, H. V. et al. (2003). "First year Wilkinson Microwave Anisotropy Probe (WMAP) observations: Implications for inflation". In: *Astrophys. J. Suppl.* 148, pp. 213–231. DOI: 10.1086/377228. arXiv: astro-ph/0302225 [astro-ph].

Peirone, Simone, Marco Raveri, et al. (2016). "Constraining f(R) Gravity with Planck Sunyaev-Zel'dovich Clusters". In: arXiv: 1607.07863 [astro-ph.CO].

Pen, Ue-Li (1997). "The Universal deceleration and angular diameter distances to clusters of galaxies". In: *New Astron.* 2, pp. 309–317. DOI: 10.1016/S1384-1076(97)00021-3. arXiv: astro-ph/9610090 [astro-ph].

Percival, Will J. (2015). "Large Scale Structure Observations". In: *Proceedings, International School of Physics 'Enrico Fermi': New Horizons for Observational Cosmology.* Vol. 186. [,317(2015)], pp. 101–135. DOI: 10.1093/acprof:oso/9780198728856.003.0007,10.3254/978-

1-61499-476-3-101. arXiv: 1312.5490 [astro-ph.CO]. URL: http://inspirehep.net/record/1272804/files/arXiv:1312.5490.pdf.

Perlmutter, S. et al. (1999). "Measurements of Omega and Lambda from 42 high redshift supernovae". In: *Astrophys. J.* 517, pp. 565–586. DOI: 10.1086/307221. arXiv: astro-ph/9812133 [astro-ph].

Pierpaoli, Elena, Stefano Borgani, et al. (2003). "On determining the cluster abundance normalization". In: *Mon. Not. Roy. Astron. Soc.* 342, p. 163. DOI: 10.1046/j.1365-8711.2003.06525.x. arXiv: astro-ph/0210567 [astro-ph].

Pillepich, Annalisa, Cristiano Porciani, and Oliver Hahn (2010). "Universal halo mass function and scale-dependent bias from N-body simulations with non-Gaussian initial conditions". In: *Mon. Not. Roy. Astron. Soc.* 402, pp. 191–206. DOI: 10.1111/j.1365-2966.2009.15914.x. arXiv: 0811.4176 [astro-ph].

Planelles, Susana, Stefano Borgani, et al. (2013). "Baryon Census in Hydrodynamical Simulations of Galaxy Clusters". In: *Mon. Not. Roy. Astron. Soc.* 431, p. 1487. DOI: 10.1093/mnras/stt265. arXiv: 1209.5058 [astro-ph.CO].

Pogosian, Levon and Alessandra Silvestri (2008). "The pattern of growth in viable $f(R)$ cosmologies". In: *Phys. Rev.* D77. [Erratum: Phys. Rev.D81,049901(2010)], p. 023503. DOI: 10.1103/PhysRevD.77.023503,10.1103/PhysRevD.81.049901. arXiv: 0709.0296 [astro-ph].

Polarski, David and Radouane Gannouji (2008). "On the growth of linear perturbations". In: *Phys. Lett.* B660, pp. 439–443. DOI: 10.1016/j.physletb.2008.01.032. arXiv: 0710.1510 [astro-ph].

Porto, Rafael A., Leonardo Senatore, and Matias Zaldarriaga (2014). "The Lagrangian-space Effective Field Theory of Large Scale Structures". In: *JCAP* 1405, p. 022. DOI: 10.1088/1475-7516/2014/05/022. arXiv: 1311.2168 [astro-ph.CO].

Pourhasan, R., N. Afshordi, et al. (2011). "Chameleon Gravity, Electrostatics, and Kinematics in the Outer Galaxy". In: *JCAP* 1112, p. 005. DOI: 10.1088/1475-7516/2011/12/005. arXiv: 1109.0538 [astro-ph.CO].

Prenet, S., C. Pichon, et al. (2008). "Initial conditions for large cosmological simulations". In: *ApJS* 178, p. 179. DOI: 10.1086/590370. arXiv: astro-ph/0804.3536 [astro-ph].

Press, William H. and Paul Schechter (1974). "Formation of galaxies and clusters of galaxies by selfsimilar gravitational condensation". In: *Astrophys. J.* 187, pp. 425–438. DOI: 10.1086/152650.

Press, William H., Saul A. Teukolsky, et al. (2007). *Numerical Recipes 3rd Edition: The Art of Scientific Computing*. 3rd ed. New York, NY, USA: Cambridge University Press. ISBN: 0521880688, 9780521880688.

Puchwein, Ewald, Marco Baldi, and Volker Springel (2013). "Modified Gravity-GADGET: A new code for cosmological hydrodynamical simulations of modified gravity models". In: *Mon. Not. Roy. Astron. Soc.* 436, p. 348. DOI: 10.1093/mnras/stt1575. arXiv: 1305.2418 [astro-ph.CO].

Rapetti, David, Steven W. Allen, et al. (2009). "Constraints on modified gravity from the observed X-ray luminosity function of galaxy clusters". In: *Mon. Not. Roy. Astron. Soc.* 400, p. 699. DOI: 10.1111/j.1365-2966.2009.15510.x. arXiv: 0812.2259 [astro-ph].

— (2010). "The Observed Growth of Massive Galaxy Clusters III: Testing General Relativity on Cosmological Scales". In: *Mon. Not. Roy. Astron. Soc.* 406, pp. 1796–1804. DOI: 10.1111/j.1365-2966.2010.16799.x. arXiv: 0911.1787 [astro-ph.CO].

Rapetti, David, Chris Blake, et al. (2013). "A combined measurement of cosmic growth and expansion from clusters of galaxies, the CMB and galaxy clustering". In: *Mon. Not. Roy. Astron. Soc.* 432, p. 973. DOI: 10.1093/mnras/stt514. arXiv: 1205.4679 [astro-ph.CO].

Raveri, Marco, Bin Hu, et al. (2014). "Effective Field Theory of Cosmic Acceleration: constraining dark energy with CMB data". In: *Phys. Rev.* D90.4, p. 043513. DOI: 10.1103/PhysRevD.90.043513. arXiv: 1405.1022 [astro-ph.CO].

Reed, Darren S., Robert E. Smith, et al. (2013). "Toward an accurate mass function for precision cosmology". In: *Mon. Not. Roy. Astron. Soc.* 431, p. 1866. DOI: 10.1093/mnras/stt301. arXiv: 1206.5302 [astro-ph.CO].

Refregier, A., A. Amara, et al. (2010). "Euclid Imaging Consortium Science Book". In: arXiv: 1001.0061 [astro-ph.IM].

Reichardt, C. L. et al. (2012). "A measurement of secondary cosmic microwave background anisotropies with two years of South Pole Telescope observations". In: *Astrophys. J.* 755, p. 70. DOI: 10.1088/0004-637X/755/1/70. arXiv: 1111.0932 [astro-ph.CO].

— (2013). "Galaxy clusters discovered via the Sunyaev-Zel'dovich effect in the first 720 square degrees of the South Pole Telescope survey". In: *Astrophys. J.* 763, p. 127. DOI: 10.1088/0004-637X/763/2/127. arXiv: 1203.5775 [astro-ph.CO].

Reid, Beth A. et al. (2012). "The clustering of galaxies in the SDSS-III Baryon Oscillation Spectroscopic Survey: measurements of the growth of structure and expansion rate at z=0.57 from anisotropic clustering". In: *Mon. Not. Roy. Astron. Soc.* 426, p. 2719. DOI: 10.1111/j.1365-2966.2012.21779.x. arXiv: 1203.6641 [astro-ph.CO].

Reid, Beth A., Licia Verde, et al. (2010). "Robust Neutrino Constraints by Combining Low Redshift Observations with the CMB". In: *JCAP* 1001, p. 003. DOI: 10.1088/1475-7516/2010/01/003. arXiv: 0910.0008 [astro-ph.CO].

Reiprich, Thomas H. and Hans Boehringer (2002). "The Mass function of an X-ray flux-limited sample of galaxy clusters". In: *Astrophys. J.* 567, pp. 716–740. DOI: 10.1086/338753. arXiv: astro-ph/0111285 [astro-ph].

Renaux-Petel, Sébastien (2015). "Primordial non-Gaussianities after Planck 2015: an introductory review". In: *Comptes Rendus Physique* 16, pp. 969–985. DOI: 10.1016/j.crhy.2015.08.003. arXiv: 1508.06740 [astro-ph.CO].

Rest, A. et al. (2014). "Cosmological Constraints from Measurements of Type Ia Supernovae discovered during the first 1.5 yr of the Pan-STARRS1 Survey". In: *Astrophys. J.* 795.1, p. 44. DOI: 10.1088/0004-637X/795/1/44. arXiv: 1310.3828 [astro-ph.CO].

Riess, Adam G. et al. (1998). "Observational evidence from supernovae for an accelerating universe and a cosmological constant". In: *Astron. J.* 116, pp. 1009–1038. DOI: 10.1086/300499. arXiv: astro-ph/9805201 [astro-ph].

Riess, Adam G., Lucas Macri, et al. (2011). "A 3% Solution: Determination of the Hubble Constant with the Hubble Space Telescope and Wide Field Camera 3". In: *Astrophys. J.* 730. [Erratum: Astrophys. J.732,129(2011)], p. 119. DOI: 10.1088/0004-637X/732/2/129, 10.1088/0004-637X/730/2/119. arXiv: 1103.2976 [astro-ph.CO].

Rindler, W. (1977). *Essential relativity. Special, general and cosmological.*

Ross, Ashley J., Lado Samushia, et al. (2015). "The clustering of the SDSS DR7 main Galaxy sample – I. A 4 per cent distance measure at $z = 0.15$". In: *Mon. Not. Roy. Astron. Soc.* 449.1, pp. 835–847. DOI: 10.1093/mnras/stv154. arXiv: 1409.3242 [astro-ph.CO].

Rozo, Eduardo et al. (2010). "Cosmological Constraints from the SDSS maxBCG Cluster Catalog". In: *Astrophys. J.* 708, pp. 645–660. DOI: 10.1088/0004-637X/708/1/645. arXiv: 0902.3702 [astro-ph.CO].

Rozo, Eduardo, Hao-Yi Wu, and Fabian Schmidt (2011). "Stacked Weak Lensing Mass Calibration: Estimators, Systematics, and Impact on Cosmological Parameter Constraints". In: *Astrophys. J.* 735, p. 118. DOI: 10.1088/0004-637X/735/2/118. arXiv: 1009.0756 [astro-ph.CO].

Ruhl, John E. et al. (2004). "The South Pole Telescope". In: *Proc. SPIE Int. Soc. Opt. Eng.* 5498, p. 11. DOI: 10.1117/12.552473. arXiv: astro-ph/0411122 [astro-ph].

Rykoff, E. S. et al. (2014). "redMaPPer I: Algorithm and SDSS DR8 Catalog". In: *Astrophys. J.* 785, p. 104. DOI: 10.1088/0004-637X/785/2/104. arXiv: 1303.3562 [astro-ph.CO].

Samushia, Lado et al. (2013). "The Clustering of Galaxies in the SDSS-III DR9 Baryon Oscillation Spectroscopic Survey: Testing Deviations from Λ and General Relativity using anisotropic clustering of galaxies". In: *Mon. Not. Roy. Astron. Soc.* 429, pp. 1514–1528. DOI: 10.1093/mnras/sts443. arXiv: 1206.5309 [astro-ph.CO].

— (2014). "The clustering of galaxies in the SDSS-III Baryon Oscillation Spectroscopic Survey: measuring growth rate and geometry with anisotropic clustering". In: *Mon. Not. Roy. Astron. Soc.* 439.4, pp. 3504–3519. DOI: 10.1093/mnras/stu197. arXiv: 1312.4899 [astro-ph.CO].

Sasaki, Shin (1996). "A New Method to Estimate Cosmological Parameters Using the Baryon Fraction of Clusters of Galaxies". In: *Publ. Astron. Soc. Jap.* 48, p. L119.

Schmidt, Fabian (2010). "Dynamical Masses in Modified Gravity". In: *Phys. Rev.* D81, p. 103002. DOI: 10.1103/PhysRevD.81.103002. arXiv: 1003.0409 [astro-ph.CO].

Schmidt, Fabian, Marcos Vinicius Lima, et al. (2009). "Non-linear Evolution of $f(R)$ Cosmologies III: Halo Statistics". In: *Phys. Rev.* D79, p. 083518. DOI: 10.1103/PhysRevD.79.083518. arXiv: 0812.0545 [astro-ph].

Schmidt, Fabian, Alexey Vikhlinin, and Wayne Hu (2009). "Cluster Constraints on $f(R)$ Gravity". In: *Phys. Rev.* D80, p. 083505. DOI: 10.1103/PhysRevD.80.083505. arXiv: 0908.2457 [astro-ph.CO].

Schmittfull, Marcel and Zvonimir Vlah (2016). "FFT-PT: Reducing the 2-loop large-scale structure power spectrum to one-dimensional, radial integrals". In: arXiv: 1609.00349 [astro-ph.CO].

Schmittfull, Marcel, Zvonimir Vlah, and Patrick McDonald (2016). "Fast Large Scale Structure Perturbation Theory using 1D FFTs". In: arXiv: 1603.04405 [astro-ph.CO].

Schuecker, Peter, Hans Bohringer, et al. (2003). "The REFLEX galaxy cluster survey VII: Omega-m and sigma-8 from cluster abundance and large scale clustering". In: *Astron. Astrophys.* 398, pp. 867–878. DOI: 10.1051/0004-6361:20021715. arXiv: astro-ph/0208251 [astro-ph].

Scoccimarro, Roman and Joshua Frieman (1996). "Loop corrections in nonlinear cosmological perturbation theory". In: *Astrophys. J. Suppl.* 105, p. 37. DOI: 10.1086/192306. arXiv: astro-ph/9509047 [astro-ph].

Sealfon, Carolyn, Licia Verde, and Raul Jimenez (2006). "Stacking weak lensing signals of sz clusters to constrain cluster physics". In: *Astrophys. J.* 649, pp. 118–128. DOI: 10.1086/505928. arXiv: astro-ph/0601254 [astro-ph].

Sehgal, Neelima et al. (2011). "The Atacama Cosmology Telescope: Cosmology from Galaxy Clusters Detected via the Sunyaev-Zel'dovich Effect". In: *Astrophys. J.* 732, p. 44. DOI: 10.1088/0004-637X/732/1/44. arXiv: 1010.1025 [astro-ph.CO].

Seljak, Uros (2002). "Cluster abundance normalization from observed mass-temperature relation". In: *Mon. Not. Roy. Astron. Soc.* 337, p. 769. DOI: 10.1046/j.1365-8711.2002.05801.x. arXiv: astro-ph/0111362 [astro-ph].

Seljak, Uros and Matias Zaldarriaga (1996). "A Line of sight integration approach to cosmic microwave background anisotropies". In: *Astrophys. J.* 469, pp. 437–444. DOI: 10.1086/177793. arXiv: astro-ph/9603033 [astro-ph].

Senatore, Leonardo (2015). "Bias in the Effective Field Theory of Large Scale Structures". In: *JCAP* 1511.11, p. 007. DOI: 10.1088/1475-7516/2015/11/007. arXiv: 1406.7843 [astro-ph.CO].

Senatore, Leonardo and Matias Zaldarriaga (2014). "Redshift Space Distortions in the Effective Field Theory of Large Scale Structures". In: arXiv: 1409.1225 [astro-ph.CO].

— (2015). "The IR-resummed Effective Field Theory of Large Scale Structures". In: *JCAP* 1502, p. 013. DOI: 10.1088/1475-7516/2015/02/013. arXiv: 1404.5954 [astro-ph.CO].

Shandera, Sarah, Adam Mantz, et al. (2013). "X-ray Cluster Constraints on Non-Gaussianity". In: *JCAP* 1308, p. 004. DOI: 10.1088/1475-7516/2013/08/004. arXiv: 1304.1216 [astro-ph.CO].

Sheldon, Erin S. et al. (2009). "Cross-correlation Weak Lensing of SDSS Galaxy Clusters I: Measurements". In: *Astrophys. J.* 703, pp. 2217–2231. DOI: 10.1088/0004-637X/703/2/2217. arXiv: 0709.1153 [astro-ph].

Sherwin, Blake D. and Matias Zaldarriaga (2012). "The Shift of the Baryon Acoustic Oscillation Scale: A Simple Physical Picture". In: *Phys. Rev.* D85, p. 103523. DOI: 10.1103/PhysRevD.85.103523. arXiv: 1202.3998 [astro-ph.CO].

Sheth, Ravi K., H. J. Mo, and Giuseppe Tormen (2001). "Ellipsoidal collapse and an improved model for the number and spatial distribution of dark matter haloes". In: *Mon. Not. Roy. Astron. Soc.* 323, p. 1. DOI: 10.1046/j.1365-8711.2001.04006.x. arXiv: astro-ph/9907024 [astro-ph].

Sheth, Ravi K. and Giuseppe Tormen (1999). "Large scale bias and the peak background split". In: *Mon. Not. Roy. Astron. Soc.* 308, p. 119. DOI: 10.1046/j.1365-8711.1999.02692.x. arXiv: astro-ph/9901122 [astro-ph].

Silvestri, Alessandra, Levon Pogosian, and Roman V. Buniy (2013). "Practical approach to cosmological perturbations in modified gravity". In: *Phys. Rev.* D87.10, p. 104015. DOI: 10.1103/PhysRevD.87.104015. arXiv: 1302.1193 [astro-ph.CO].

Silvestri, Alessandra and Mark Trodden (2009). "Approaches to Understanding Cosmic Acceleration". In: *Rept. Prog. Phys.* 72, p. 096901. DOI: 10.1088/0034-4885/72/9/096901. arXiv: 0904.0024 [astro-ph.CO].

Skillman, Samuel W., Michael S. Warren, et al. (2014). "Dark Sky Simulations: Early Data Release". In: arXiv: 1407.2600 [astro-ph.CO].

Smith, Robert E. and Laura Marian (2011). "What do cluster counts really tell us about the Universe?" In: *Mon. Not. Roy. Astron. Soc.* 418, p. 729. DOI: 10.1111/j.1365-2966.2011.19525.x. arXiv: 1106.1665 [astro-ph.CO].

Song, Yong-Seon, Wayne Hu, and Ignacy Sawicki (2007). "The Large Scale Structure of $f(R)$ Gravity". In: *Phys. Rev.* D75, p. 044004. DOI: 10.1103/PhysRevD.75.044004. arXiv: astro-ph/0610532 [astro-ph].

Song, Yong-Seon, Hiranya Peiris, and Wayne Hu (2007). "Cosmological Constraints on $f(R)$ Acceleration Models". In: *Phys. Rev.* D76, p. 063517. DOI: 10.1103/PhysRevD.76.063517. arXiv: 0706.2399 [astro-ph].

Sotiriou, Thomas P. (2006). "f(R) gravity and scalar-tensor theory". In: *Class. Quant. Grav.* 23, pp. 5117–5128. DOI: 10.1088/0264-9381/23/17/003. arXiv: gr-qc/0604028 [gr-qc].

Sotiriou, Thomas P. and Valerio Faraoni (2010). "$f(R)$ Theories Of Gravity". In: *Rev. Mod. Phys.* 82, pp. 451–497. DOI: 10.1103/RevModPhys.82.451. arXiv: 0805.1726 [gr-qc].

Stanek, Rebecca, D. Rudd, and A. E. Evrard (2009). "The Effect of Gas Physics on the Halo Mass Function". In: *Mon. Not. Roy. Astron. Soc.* 394, pp. L11–L15. DOI: 10.1111/j.1745-3933.2008.00597.x. arXiv: 0809.2805 [astro-ph].

Starobinsky, A.A. (1980). "A new type of isotropic cosmological models without singularity". In: *Physics Letters B* 91.1, pp. 99–102. ISSN: 0370-2693. DOI: http://dx.doi.org/10.1016/0370-2693(80)90670-X. URL: http://www.sciencedirect.com/science/article/pii/037026938090670X.

Story, K. T. et al. (2013). "A Measurement of the Cosmic Microwave Background Damping Tail from the 2500-square-degree SPT-SZ survey". In: *Astrophys. J.* 779, p. 86. DOI: 10.1088/0004-637X/779/1/86. arXiv: 1210.7231 [astro-ph.CO].

Suzuki, N. et al. (2012). "The Hubble Space Telescope Cluster Supernova Survey: V. Improving the Dark Energy Constraints Above $z > 1$ and Building an Early-Type-Hosted Supernova Sample". In: *Astrophys. J.* 746, p. 85. DOI: 10.1088/0004-637X/746/1/85. arXiv: 1105.3470 [astro-ph.CO].

Taruya, Atsushi (2016). "Constructing perturbation theory kernels for large-scale structure in generalized cosmologies". In: arXiv: 1606.02168 [astro-ph.CO].

Taruya, Atsushi, Francis Bernardeau, et al. (2012). "RegPT: Direct and fast calculation of regularized cosmological power spectrum at two-loop order". In: *Phys. Rev.* D86, p. 103528. DOI: 10.1103/PhysRevD.86.103528. arXiv: 1208.1191 [astro-ph.CO].

Tassev, Svetlin, Daniel J. Eisenstein, et al. (2015). "sCOLA: The N-body COLA Method Extended to the Spatial Domain". In: arXiv: 1502.07751 [astro-ph.CO].

Tassev, Svetlin, Matias Zaldarriaga, and Daniel Eisenstein (2013). "Solving Large Scale Structure in Ten Easy Steps with COLA". In: *JCAP* 1306, p. 036. DOI: 10.1088/1475-7516/2013/06/036. arXiv: 1301.0322 [astro-ph.CO].

Taylor, J. E. (2011). "Dark Matter Halos from the Inside Out". In: *Advances in Astronomy* 2011, 604898, p. 604898. DOI: 10.1155/2011/604898. arXiv: 1008.4103 [astro-ph.CO].

Taylor, T. R. and G. Veneziano (1988). "Dilaton Couplings at Large Distances". In: *Phys. Lett. B* 213, pp. 450–454. DOI: 10.1016/0370-2693(88)91290-7.

Teyssier, Romain (2002). "Cosmological hydrodynamics with adaptive mesh refinement: a new high resolution code called ramses". In: *Astron. Astrophys.* 385, pp. 337–364. DOI: 10.1051/0004-6361:20011817. arXiv: astro-ph/0111367 [astro-ph].

Thornton, R. J. et al. (2016). "The Atacama Cosmology Telescope: The polarization-sensitive ACTPol instrument". In: arXiv: 1605.06569 [astro-ph.IM].

Tinker, Jeremy L., Andrey V. Kravtsov, et al. (2008). "Toward a halo mass function for precision cosmology: The Limits of universality". In: *Astrophys. J.* 688, pp. 709–728. DOI: 10.1086/591439. arXiv: 0803.2706 [astro-ph].

Tinker, Jeremy L., Brant E. Robertson, et al. (2010). "The Large Scale Bias of Dark Matter Halos: Numerical Calibration and Model Tests". In: *Astrophys. J.* 724, pp. 878–886. DOI: 10.1088/0004-637X/724/2/878. arXiv: 1001.3162 [astro-ph.CO].

Truemper, J. (June 1993). "ROSAT - A new look at the X-ray sky". In: *Science* 260, pp. 1769–1771. DOI: 10.1126/science.260.5115.1769.

Viana, Pedro T. P., Robert C. Nichol, and Andrew R. Liddle (2002). "Constraining the matter power spectrum normalization using the SDSS/RASS and reflex cluster surveys". In: *Astrophys. J.* 569, p. L75. DOI: 10.1086/340664. arXiv: astro-ph/0111394 [astro-ph].

Vikhlinin, A. et al. (2009). "Chandra Cluster Cosmology Project III: Cosmological Parameter Constraints". In: *Astrophys. J.* 692, pp. 1060–1074. DOI: 10.1088/0004-637X/692/2/1060. arXiv: 0812.2720 [astro-ph].

Vikhlinin, Alexey et al. (2003). "Cosmological constraints from evolution of cluster baryon mass function at z 0.5". In: *Astrophys. J.* 590, pp. 15–25. DOI: 10.1086/374863. arXiv: astro-ph/0212075 [astro-ph].

Vikram, Vinu, Anna Cabré, et al. (2013). "Astrophysical Tests of Modified Gravity: the Morphology and Kinematics of Dwarf Galaxies". In: *JCAP* 1308, p. 020. DOI: 10.1088/1475-7516/2013/08/020. arXiv: 1303.0295 [astro-ph.CO].

Voevodkin, A. and Alexey Vikhlinin (2004). "Constraining amplitude and slope of the mass fluctuation spectrum using cluster baryon mass function". In: *Astrophys. J.* 601, pp. 610–620. DOI: 10.1086/380818. arXiv: astro-ph/0305549 [astro-ph].

Wagoner, Robert V. (June 1970). "Scalar-Tensor Theory and Gravitational Waves". In: *Phys. Rev. D* 1 (12), pp. 3209–3216. DOI: 10.1103/PhysRevD.1.3209. URL: http://link.aps.org/doi/10.1103/PhysRevD.1.3209.

Wang, Junpu, Lam Hui, and Justin Khoury (2012). "No-Go Theorems for Generalized Chameleon Field Theories". In: *Phys. Rev. Lett.* 109, p. 241301. DOI: 10.1103/PhysRevLett.109.241301. arXiv: 1208.4612 [astro-ph.CO].

Warren, Michael S., Kevork Abazajian, et al. (2006). "Precision determination of the mass function of dark matter halos". In: *Astrophys. J.* 646, pp. 881–885. DOI: 10.1086/504962. arXiv: astro-ph/0506395 [astro-ph].

Watson, William A., Ilian T. Iliev, et al. (2013). "The halo mass function through the cosmic ages". In: *Mon. Not. Roy. Astron. Soc.* 433, p. 1230. DOI: 10.1093/mnras/stt791. arXiv: 1212.0095 [astro-ph.CO].

Weinberg, Steven (1972). *Gravitation and Cosmology*. New York: John Wiley and Sons. ISBN: 0471925675, 9780471925675. URL: http://www-spires.fnal.gov/spires/find/books/www?cl=QC6.W431.

— (1989a). "The Cosmological Constant Problem". In: *Rev. Mod. Phys.* 61, pp. 1–23. DOI: 10.1103/RevModPhys.61.1.

— (Jan. 1989b). "The cosmological constant problem". In: *Rev. Mod. Phys.* 61 (1), pp. 1–23. DOI: 10.1103/RevModPhys.61.1. URL: http://link.aps.org/doi/10.1103/RevModPhys.61.1.

— (2008). *Cosmology*. URL: http://www.oup.com/uk/catalogue/?ci=9780198526827.

Weller, Jochen and A. M. Lewis (2003). "Large scale cosmic microwave background anisotropies and dark energy". In: *Mon. Not. Roy. Astron. Soc.* 346, pp. 987–993. DOI: 10.1111/j.1365-2966.2003.07144.x. arXiv: astro-ph/0307104 [astro-ph].

White, Martin, J. D. Cohn, and Renske Smit (2010). "Cluster Galaxy Dynamics and the Effects of Large Scale Environment". In: *Mon. Not. Roy. Astron. Soc.* 408, p. 1818. DOI: 10.1111/j.1365-2966.2010.17248.x. arXiv: 1005.3022 [astro-ph.CO].

Will, Clifford M. (2006). "The Confrontation between general relativity and experiment". In: *Living Rev. Rel.* 9, p. 3. DOI: 10.12942/lrr-2006-3. arXiv: gr-qc/0510072 [gr-qc].

Winther, Hans A. et al. (2015). "Modified Gravity N-body Code Comparison Project". In: *Mon. Not. Roy. Astron. Soc.* 454.4, pp. 4208–4234. DOI: 10.1093/mnras/stv2253. arXiv: 1506.06384 [astro-ph.CO].

Wright, Candace Oaxaca and Tereasa G. Brainerd (May 2000). "Gravitational Lensing by NFW Halos". In: *Astrophys. J.* 534, pp. 34–40. DOI: 10.1086/308744.

Wu, Hao-Yi, Eduardo Rozo, and Risa H. Wechsler (2010). "Annealing a Follow-up Program: Improvement of the Dark Energy Figure of Merit for Optical Galaxy Cluster Surveys". In: *Astrophys. J.* 713, pp. 1207–1218. DOI: 10.1088/0004-637X/713/2/1207. arXiv: 0907.2690 [astro-ph.CO].

Zhang, Pengjie (2006). "Testing $f(R)$ gravity against the large scale structure of the universe." In: *Phys. Rev.* D73, p. 123504. DOI: 10.1103/PhysRevD.73.123504. arXiv: astro-ph/0511218 [astro-ph].

Zhao, Gong-Bo, Baojiu Li, and Kazuya Koyama (2011). "N-body Simulations for $f(R)$ Gravity using a Self-adaptive Particle-Mesh Code". In: *Phys. Rev.* D83, p. 044007. DOI: 10.1103/PhysRevD.83.044007. arXiv: 1011.1257 [astro-ph.CO].

Zhao, Gong-Bo, Levon Pogosian, et al. (2009). "Searching for modified growth patterns with tomographic surveys". In: *Phys. Rev.* D79, p. 083513. DOI: 10.1103/PhysRevD.79.083513. arXiv: 0809.3791 [astro-ph].

Appendix A

Figures Using *Planck* Data

Figure A.1 shows results equivalent to Figure 2.1, with the substitution of *Planck* 1-year data (plus WMAP polarization; Ade et al. 2014b) for WMAP 9-year data (Hinshaw et al. 2013).

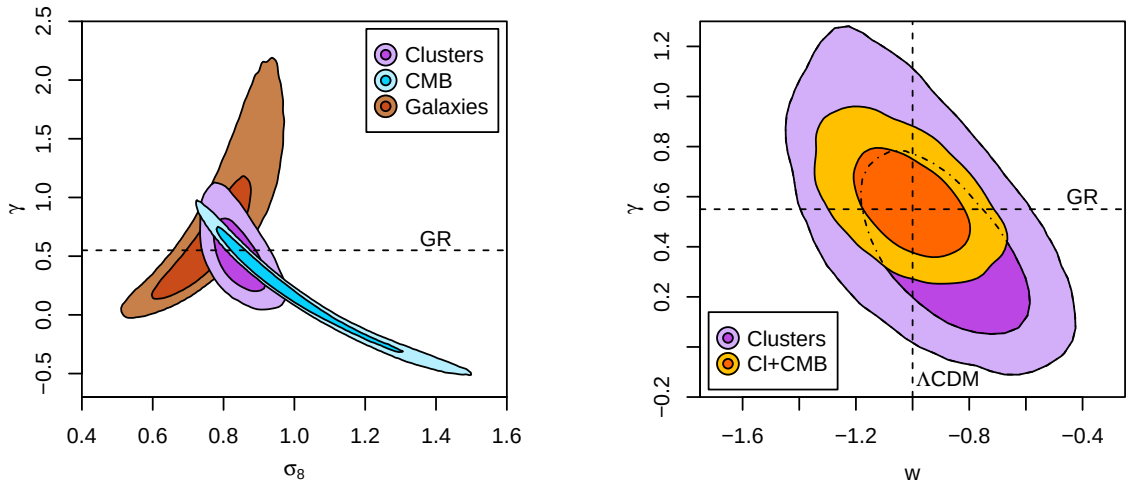

Fig. A.1 Constraints on cosmological models from the cluster data set, CMB data from *Planck*+WP, ACT and SPT (Keisler et al. 2011; Reichardt et al. 2012; Story et al. 2013; Das et al. 2014; Ade et al. 2014b), type Ia supernovae (Suzuki et al. 2012), baryon acoustic oscillations (Beutler et al. 2011; Padmanabhan, Xu, et al. 2012; Anderson et al. 2014b), and their combination. These figures are identical to the equivalent ones in Section 2.4 apart from the substitution of *Planck* 1-year data (plus WMAP polarization) for WMAP 9-year data.

Appendix B

The ISW Effect in Free Growth-Index Models

In our study of the growth index of cosmic structure (Section 2.4.1) we obtain the contribution of the ISW effect to the anisotropy power spectrum of the CMB temperature fluctuations through an integral over time of the variation of the gravitational potential with respect to conformal time, $\dot{\phi}$ (Weller and Lewis 2003). For the latter, we take the derivative of the gauge invariant Poisson equation

$$k^2\phi = -4\pi G a^2 \rho \Delta, \tag{B.1}$$

where $\rho\Delta \equiv \sum_i \rho_i \delta_i + 3\mathcal{H}\sum_i (\rho_i + P_i)\theta_i$, with $\mathcal{H}$ being the Hubble parameter in conformal time, ρ_i and P_i the densities and pressures for each species i, and each of the sums the mass-averaged density contrast, δ_i, and velocity divergence, θ_i, for a given gauge (Bardeen 1980). In synchronous gauge, we have $\rho_{\rm c}\Delta_{\rm c} \equiv \rho_{\rm c}\delta_{\rm c}$, $\rho_{\rm b}\Delta_{\rm b} \equiv \rho_{\rm b}\delta_{\rm b} + 3\mathcal{H}\rho_{\rm b}\theta_{\rm b}k^{-2}$, and $\rho_{\rm r}\Delta_{\rm r} \equiv \rho_{\rm r}\delta_{\rm r} + 4\mathcal{H}\rho_{\rm r}\theta_{\rm r}k^{-2}$ for CDM (c), baryons (b), and radiation (r, including massless neutrinos and photons), respectively (Ma and Bertschinger 1995). Note that after recombination the baryon velocity fluctuations evolve as $\dot{\theta}_{\rm b} = -\mathcal{H}\theta_{\rm b} + c_{\rm s}^2 k^2 \delta_{\rm b}$, where $c_{\rm s}$ is the baryonic sound speed, which after baryon-photon decoupling is rapidly driven to zero by adiabatic cooling. This implies that at late times baryonic perturbations will, like those for CDM, follow mainly metric perturbations, $\dot{\delta}_{\rm b} \approx \dot{\delta}_{\rm c} = -\dot{h}/2$. For radiation, we have $\dot{\delta}_{\rm r} = -4\theta_{\rm r}/3 - 2\dot{h}/3$ and $\dot{\theta}_{\rm r} = k^2(\delta_{\rm r}/4 - \sigma_{\rm r})$, where the anisotropic stress perturbation is defined as $(\rho + P)\sigma \equiv -(\hat{k}_i\hat{k}_j - \delta_{ij}/3)\Sigma_i^j$, with i and j denoting the indexes for the spatial components, and Σ_i^j the shear stress, which is negligible after recombination. Therefore, in the matter-dominated era we have oscillating solutions for both $\delta_{\rm r}$ and $\theta_{\rm r}$, and both terms of $\rho_{\rm r}\Delta_{\rm r}$ (see above) become strongly suppressed by $\rho_{\rm r} \propto a^{-4}$. We finally obtain $k^2\phi \approx -4\pi G a^2 \delta\rho_{\rm m}$, and thus

$$\dot{\phi} \approx 4\pi G(a^2/k^2)\mathcal{H}\delta\rho_{\rm m}\left[1 - \Omega_{\rm m}(a)^{\gamma}\right]. \tag{B.2}$$

More discussion can be found in Rapetti, Allen, et al. (2009); Rapetti, Allen, et al. (2010); Rapetti, Blake, et al. (2013).

Appendix C

Alternative treatments of two-loop terms

C.0.1 Using full version of $P_{\text{2-loop}}$ instead of $P_{\text{2-loop}}^{\text{(UV-improved)}}$

Instead of using the "UV-improved" version of $P_{\text{2-loop}}$, as in Foreman, Perrier, and Senatore (2016) and Sec. 5.2.1, we may instead use the full version of this term, as done in Foreman and Senatore (2016) and earlier works. As we explain below, this form of $P_{\text{2-loop}}$ has the advantage of possessing fewer zero crossings than the UV-improved version. However, it also has the disadvantage that the leading UV contribution to $P_{\text{2-loop}}^{(\text{full})}$, which is absent from $P_{\text{2-loop}}^{(\text{UV-improved})}$, is first numerically computed and then effectively removed by a suitable choice of $c_{s(2)}^2$, whereas $P_{\text{2-loop}}^{(\text{UV-improved})}$ simply does not compute this contribution in the first place.

As with $P_{\text{2-loop}}^{(\text{UV-improved})}$, we use Eq. (5.6) instead of Eq. (5.2) when evaluating the difference between $P_{\text{2-loop}}^{(\text{full})}$ for the target and reference cosmologies, and once again we find that the extra A_s rescaling implemented in Eq. (5.6) is effective in analytically removing much of the difference between the two calculations; this is shown in Fig. C.1. This figure also shows that the ratio $\Delta\tilde{P}_{\text{2-loop}}(k)/P_{\text{2-loop}}^{\text{target}}$ is better behaved than for the $P_{\text{2-loop}}^{(\text{UV-improved})}$, possessing fewer zero-crossings; this will lead to a closer agreement between the exact calculation of the ratio and the estimate described below.

The procedure for estimating $\Delta\tilde{P}_{\text{2-loop}}(k)/P_{\text{2-loop}}^{\text{target}}$ is very similar to what we presented in Sec. 5.2.1. We begin with the same expression used there, repeated below for convenience:

$$\left|\frac{\Delta\tilde{P}_\alpha}{P_\alpha^{\text{target}}}\right| \approx \left|1 - \left(\frac{A_s^{\text{target}}}{A_s^{\text{ref}}}\right)^{L+1} \left(\frac{P_{11}^{\text{ref}}(k)}{P_{11}^{\text{target}}(k)}\right)^{L+1}\right|. \tag{C.1}$$

Recall that in the case of the UV-improved $P_{\text{2-loop}}$, this estimate was motivated by the fact that the integrand of $P_{\text{2-loop}}^{(\text{UV-improved})}$ should be dominated by momenta of order k. In the

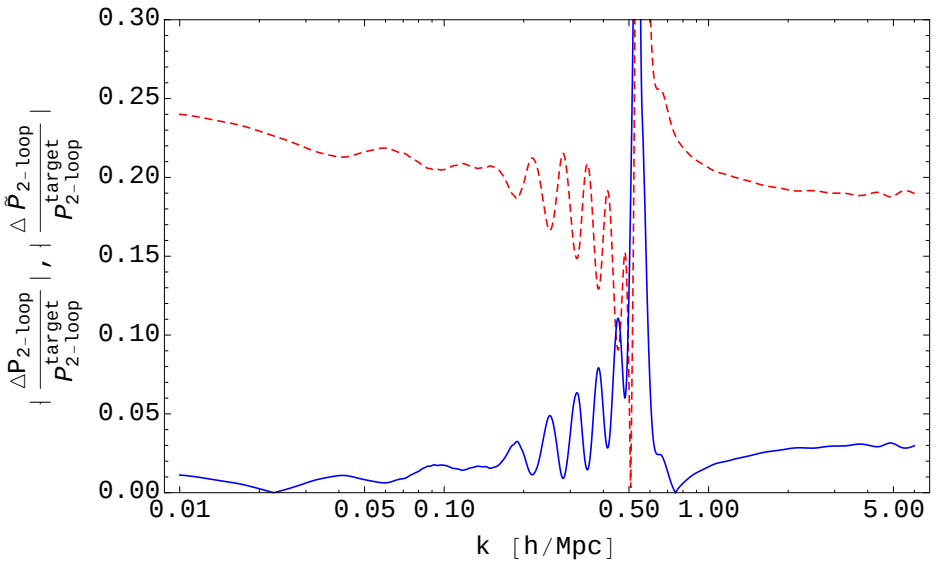

Fig. C.1 For the `cosmo_5` test cosmology, we show $\Delta P_{\text{2-loop}}(k)/P^{\text{target}}_{\text{2-loop}}$ (the red dashed line, evaluated using Eq. (5.2)) and $\Delta\tilde{P}_{\text{2-loop}}(k)/P^{\text{target}}_{\text{2-loop}}$ (the blue solid line, evaluated using Eq. (5.6)), where $P_{\text{2-loop}}$ is the full calculation rather than the "UV-improved" version used in Sec. 5.2.1. As with $P^{\text{(UV-improved)}}_{\text{2-loop}}$, Eq. (5.6) shows a large improvement over Eq. (5.2) in removing most of the difference associated with the cosmological parameter A_s.

non-UV-improved case, this is not necessarily true, as the UV contribution that is now included could cause the integral to be dominated by momenta much larger than k. Despite this concern, the estimate in Eq. (C.1) turns out to predict the desired ratio at a level that is more than adequate for our purposes here.

As before, this estimate on its own is slightly sub-optimal, so we implement the following extra steps:

1. We apply the smoothing given in Eq. (5.9) over the range $0.03\,h\,\text{Mpc}^{-1} < k < 0.5\,h\,\text{Mpc}^{-1}$.

2. Since Eq. (C.1) occasionally under-predicts the exact ratio at low wavenumbers, we multiply the estimate by 2 for $k < 0.6\,h\,\text{Mpc}^{-1}$.

In Fig C.2, we compare this estimate to the exact calculation of $|\Delta\tilde{P}_{\text{2-loop}}/P^{\text{target}}_{\text{2-loop}}|$ in two test cases. The estimate is slightly higher than the exact calculation overall, again leading to slightly more conservative precision requirements on the integral evaluation than strictly necessary. The zero-crossing around $k \sim 0.5\,h\,\text{Mpc}^{-1}$ is also nicely handled by the estimate, which again imposes a ceiling on the value of $|\Delta\tilde{P}_{\text{2-loop}}/P^{\text{target}}_{\text{2-loop}}|$ in the relevant region.

To provide more detailed proof that the estimate described above is suitable for our purposes, in App. C.0.2 we provide a procedure to more accurately estimate $|\Delta\tilde{P}_{\text{2-loop}}/P^{\text{target}}_{\text{2-loop}}|$ for the non-UV-improved case. The resulting runtimes of the `CosmoEFT` code are not significantly

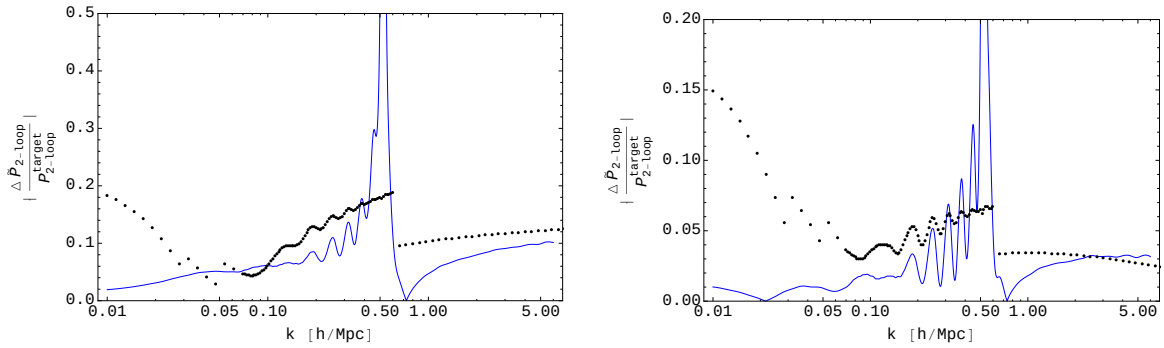

Fig. C.2 Comparison of estimate (Eq. (5.8), with the modifications described in the main text; *black points*) and exact calculation of $|\Delta\tilde{P}_{\text{2-loop}}/P^{\text{target}}_{\text{2-loop}}|$ (*blue lines*) for two test cosmologies, `cosmo_1` (*left*) and `cosmo_5` (*right*), given in Table 5.1. On average, the estimate slightly over-predicts the exact calculation, but this only means that the precision requested for the integration of $\Delta\tilde{P}_{\text{2-loop}}$ is slightly more conservative than necessary. Also, the estimate has the desirable feature of automatically limiting the precision requested close to the zero-crossing of $P^{(\text{full})}_{\text{2-loop}}(k)$, by setting a ceiling on the value of $|\Delta\tilde{P}_{\text{2-loop}}/P^{\text{target}}_{\text{2-loop}}|$ in Eq. (5.8).

different whether we use these more detailed estimates or the estimates presented in this section. Overall, both estimates typically determine ϵ_Δ to be ∼5-10 times larger than ϵ_{target}, clearly a significant improvement over performing an exact calculation using ϵ_{target} at all wavenumbers.

Finally, in Fig. C.3, we compare the exact ($\epsilon_{\text{target}} = 0.1\%$) $P^{(\text{full})}_{\text{2-loop}}$ computation with the computation where ϵ_{target} is set using Eq. (5.7) and the procedure we have just described. Aside from the region close to the zero crossing at $k \sim 0.5\,h\,\text{Mpc}^{-1}$, the faster computation is within ∼0.5% of the more precise computation for at least $k < 1\,h\,\text{Mpc}^{-1}$.

C.0.2 Alternative estimates for determining integration precision for $P_{\text{2-loop}}$

Recall that, in order to set the the integration precision ϵ_Δ used by computations in `CosmoEFT`, we make use of Eq. (5.7), repeated below for convenience:

$$\epsilon_\Delta \approx \left|\frac{\Delta\tilde{P}_\alpha}{P^{\text{target}}_\alpha}\right|^{-1} \epsilon_{\text{target}} \ , \tag{C.2}$$

In the main text of the paper, we use Eq. (5.8) to approximate $|\Delta\tilde{P}_\alpha/P^{\text{target}}_\alpha|$. In this appendix, we describe a more detailed estimate, and compare its performance to that of Eq. (5.8).

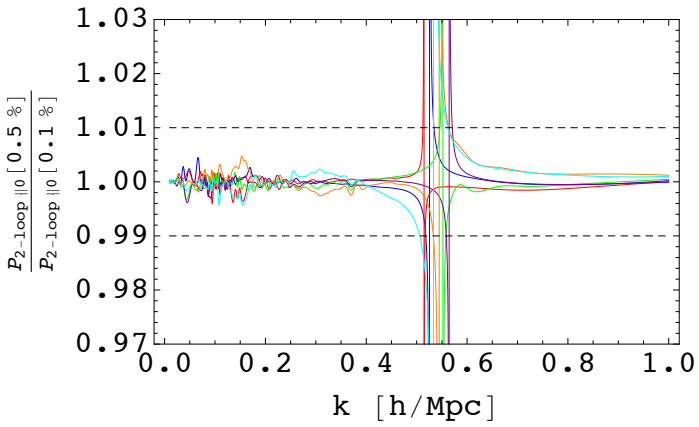

Fig. C.3 For all of the 3σ-cosmologies from Table 5.1, we show $P^{(\text{full})}_{\text{2-loop}}$ evaluated with ϵ_{target} determined using the procedure in App. C.0.1, normalized to $P^{(\text{full})}_{\text{2-loop}}$ computed using $\epsilon_{\text{target}} = 0.1\%$. Aside from the region close to the zero crossing at $k \sim 0.5\,h\,\text{Mpc}^{-1}$, the faster computation is within $\sim$0.5% of the more precise computation over the entire wavenumber range of interest.

In Foreman and Senatore (2016), it was found that $P^{(\text{full})}_{\text{2-loop}}$ is roughly described by the following:

$$P^{(\text{full})}_{\text{2-loop}}(k) \approx \alpha \frac{P^2_{\text{1-loop}}(k)}{P_{11}(k)} + 2(2\pi)c^2_{s(2)}\frac{k^2}{k^2_{\text{NL}}}P_{11}(k)\ . \tag{C.3}$$

As stated in Foreman and Senatore (2016), for $\alpha = 0.3$ the estimate is within a factor of 2 of exact calculation for $k \lesssim 0.7\,h\,\text{Mpc}^{-1}$, with the accuracy increasing at lower k. We have verified that this value of α works well for all of our test cosmologies described below, which suggests α is only weakly dependent on cosmology and can be fixed for our purposes.

Note that, as extensively explained in Carrasco, Foreman, et al. (2014b); Foreman and Senatore (2016), $c^2_{s(2)}$ can be completely determined from theory alone: it will take the form of a function of the free parameters of the EFTofLSS, but determination of this function does not rely on access nonlinear data. However, to make use of the estimate (C.3), we require prior knowledge of $c^2_{s(2)}$ as a function of cosmology. Therefore, our strategy will be to pre-calibrate $c^2_{s(2)}$ by fitting approximate predictions to the output of simulations, and then feed these pre-calibrated values back into the estimates used in the `CosmoEFT` algorithm. Here and throughout, we express $c^2_{s(2)}$ in $(k_{\text{NL}}/2\,h\,\text{Mpc}^{-1})^2$ units.

We model $c^2_{s(2)}$ at $z = 0$ with a Taylor expansion in the five cosmological parameters. Specifically, we use

$$\begin{aligned} c^2_{s(2)}(\boldsymbol{\theta}) = c^2_{s(2)}(\boldsymbol{\theta}^{\text{ref}}) + \sum_i \Delta\theta_i \left.\frac{\partial c^2_{s(2)}(\boldsymbol{\theta})}{\partial\theta_i}\right|_{\boldsymbol{\theta}=\boldsymbol{\theta}^{\text{ref}}} + \frac{1}{2}\sum_{i,j}\Delta\theta_i\Delta\theta_j \left.\frac{\partial^2 c^2_{s(2)}(\boldsymbol{\theta})}{\partial\theta_i\,\partial\theta_j}\right|_{\boldsymbol{\theta}=\boldsymbol{\theta}^{\text{ref}}} \\ + \frac{1}{6}\sum_{i,j,k}\Delta\theta_i\Delta\theta_j\Delta\theta_k \left.\frac{\partial^3 c^2_{s(2)}(\boldsymbol{\theta})}{\partial\theta_i\,\partial\theta_j\,\partial\theta_k}\right|_{\boldsymbol{\theta}=\boldsymbol{\theta}^{\text{ref}}}\ , \end{aligned} \tag{C.4}$$

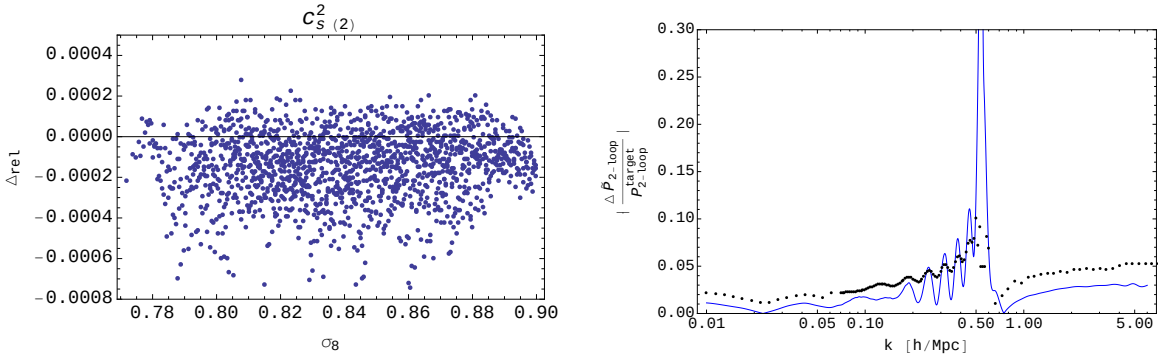

Fig. C.4 *Left:* Relative departure of the estimated $c^2_{s(2)}$ values from the predictions of Eq. (C.4) for a large sample of cosmologies in the 4σ 5-cube centered at our reference cosmology. In all cases, the agreement between the two is excellent (within 0.1%). *Right:* For the `cosmo_5` test cosmology (given in Table 5.1), comparison between the exact adjusted relative ratio (blue) and its estimate (dots) based on Eq. (C.3) together with the $c^2_{s(2)}$ prediction of Eq. (C.4).

where $\Delta\theta_i \equiv \theta_i - \theta_i^{\rm ref}$ and i, j, k run over the 5 parameters in (5.10). We determine the derivatives in Eq. (C.4) by fitting to a large sample of cosmologies whose parameters lie within a 4σ 5-cube centered at our reference cosmology. That is, for each of these cosmologies, we obtain the nonlinear power spectrum from the `FrankenEmu` emulator, calculate the corresponding two-loop EFT prediction using `TaylorEFT` (described in Sec. 5.3), and extract the corresponding value of $c^2_{s(2)}$ by fitting the prediction to the nonlinear spectrum. The values of the derivatives in Eq. (C.4) are obtained by fitting this equation to the resulting $c^2_{s(2)}$ values as a function of $\boldsymbol{\theta}$. The left panel of Fig. C.4 shows that, after fixing the values of the derivatives, the accuracy of Eq. (C.4) is within 0.1% for all these cosmologies.

To compensate for fitting errors and expansion errors in `TaylorEFT`, we add a constant additive shift of 0.01 to the estimation for $\Delta\tilde{P}_\alpha/P_\alpha^{\rm target}$ that follows from Eq. (C.3), clearly visible at low k in the right panel of Fig. C.4. Interestingly enough, Eq. (C.3) can predict the zero-crossing k_c of the adjusted ratio (C.2) fairly well; for all cosmologies of interest, the zero-crossing is in the range $\delta k_c \equiv (0.5, 0.6)\, h\,{\rm Mpc}^{-1}$. We use this, together with our specific k sampling, to place an upper limit on the absolute value of $\Delta\tilde{P}_\alpha/P_\alpha^{\rm target}$ used by the code by imposing that at most six points within δk_c can be above the corresponding threshold. For these wavenumbers, we use an arbitrary small value $r_c = 0.05$ for $\Delta\tilde{P}_\alpha/P_\alpha^{\rm target}$ in Eq. (C.2), effectively reducing integration times by increasing the required relative precision to $\epsilon_\Delta = 10\%$ wherever $\Delta\tilde{P}_{\text{2-loop}}$ is negligible compared to $(A_s^{\rm target}/A_s^{\rm ref})^3 P^{\rm ref}_{\text{2-loop}}$.

As with Eq. (5.8), Eq. (C.3) systematically predicts BAO in antiphase with the exact calculations. Therefore, for $0.055\, h\,{\rm Mpc}^{-1} < k < k_c$ we smooth the estimated adjusted ratios with the top-hat window function from Eq. (5.9). When Eq. (5.9) returns a ratio larger than the upper limit, we replace it by its unsmoothed value. Finally, for $k > 4.4\, h\,{\rm Mpc}^{-1}$, our

Table C.1 Computational performance of `CosmoEFT` for our test cosmologies, when either the estimates from Sec. 5.2.1 (simple estimate – SE) or App. C (detailed estimate – DE) are used to set the integration precision ϵ_Δ. In most cases, the running times are almost identical, indicating that the estimates from Sec. 5.2.1 may be used without a significant loss of computational efficiency.

Cosmology	Wall time (SE)	Wall time (DE)
`cosmo_1`	5.2 min	5.3 min
`cosmo_2`	10.9 min	10.8 min
`cosmo_3`	3.3 min	3.3 min
`cosmo_4`	11 min	7.3 min
`cosmo_5`	1.4 min	1.3 min
`cosmo_6`	2.3 min	1.4 min
`cosmo_7`	2.0 min	1.6 min
`cosmo_8`	1.7 min	1.8 min
`cosmo_9`	14 min	9.0 min
`cosmo_10`	9 min	6 min
`cosmo_11`	15 min	11 min

estimation for $\Delta\tilde{P}_\alpha / P_\alpha^{\text{target}}$ always approaches a constant in the k-range we are interested in, hence for these wavenumbers we simply use its value at $k = 4.4\,h\,\text{Mpc}^{-1}$.

In Table C.1, we compare the wall times for evaluation of each of our 11 test cosmologies using the simpler estimates from the main text or the estimates from this appendix. In most cases, we find comparable performance, while the few larger discrepancies are caused by because the simpler estimates are more conservative in some cases.

Appendix D

`CosmoEFT`: additional checks

In this appendix, we repeat the tests from Sec. 5.2.3 for the 4σ- and 5σ-cosmologies from Table. 5.1. Here, we also use $\epsilon_{\rm target} = 0.5\%$, and first check that the estimates Eq. (5.8) are a good approximation of the two-loop modified ratios in Fig. D.1. In Figs. D.2-D.3 we then compare the resummed `CosmoEFT` calculations with the equivalent outputs obtained through direct integration, verifying that `CosmoEFT` achieves the expected precision.

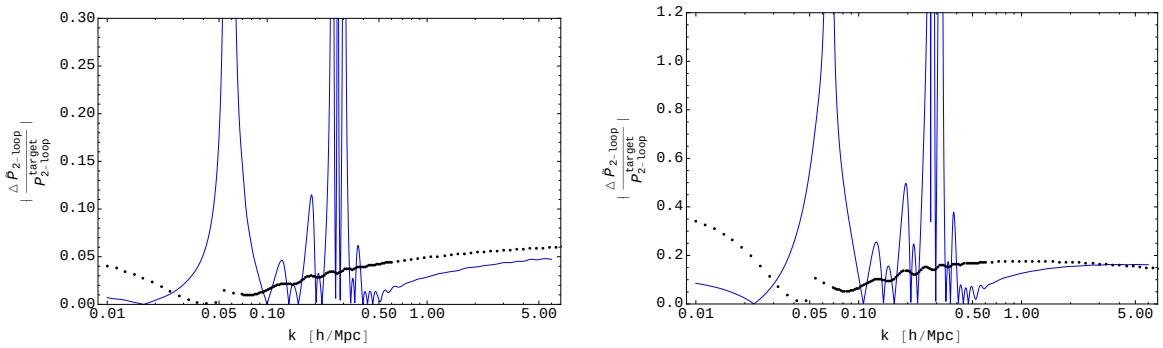

Fig. D.1 Comparison between the exact adjusted relative ratio (blue) and its estimate (dots) based on Eq. (5.8) for `cosmo_8` (left) and `cosmo_9` (right).

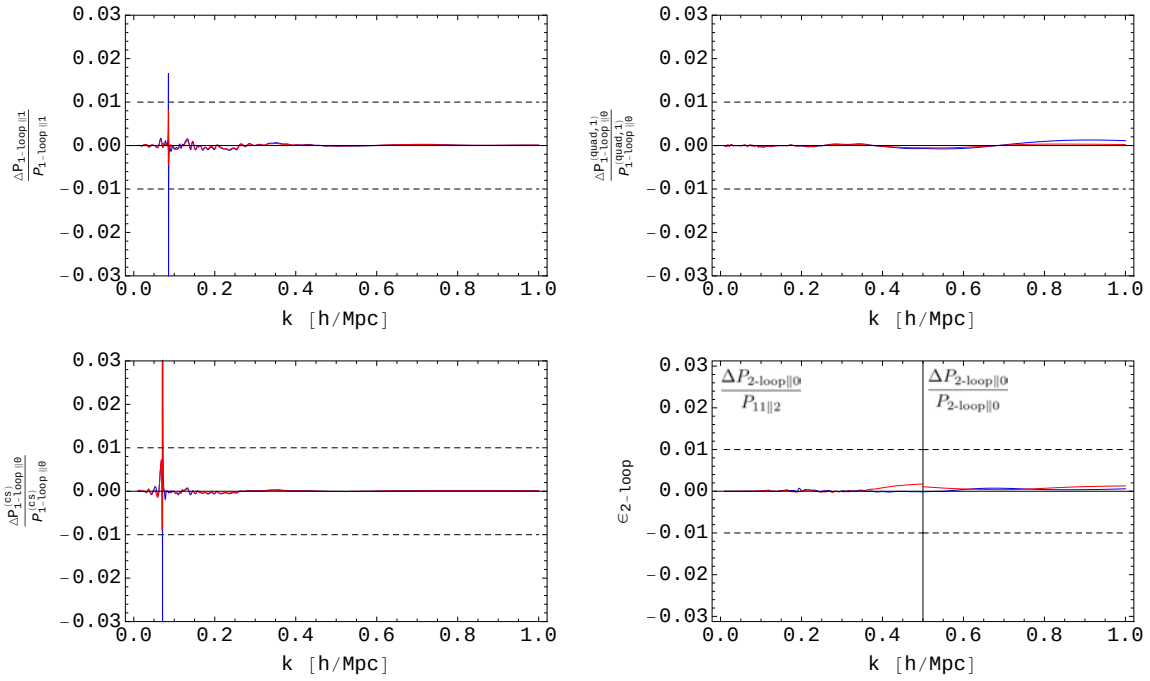

Fig. D.2 Resummed CosmoEFT outputs for our 4σ-cosmologies cosmo_7-8 (blue and red, respectively) relative to the direct calculation of the full integrand with precision $\epsilon = 0.1\%$. We used $\epsilon_{\mathrm{target}} = 0.5\%$, and spikes indicate zero-crossing. Subscripts $\|0, \|1$ denotes the resummation order as in Senatore and Zaldarriaga (2015). Dashed lines mark 1% departures from direct calculations. As in Fig. 5.4, for $P_{2\text{-loop}}$ we show $\Delta P_{2\text{-loop}\|0}/P_{11\|2}$ for $k < 0.5\,h\,\mathrm{Mpc}^{-1}$, which propagates directly to the matter power spectrum predictions, and $\Delta P_{2\text{-loop}\|0}/P_{2\text{-loop}\|0}$ for $k > 0.5\,h\,\mathrm{Mpc}^{-1}$, which proves the goodness of our estimates for smaller scales.

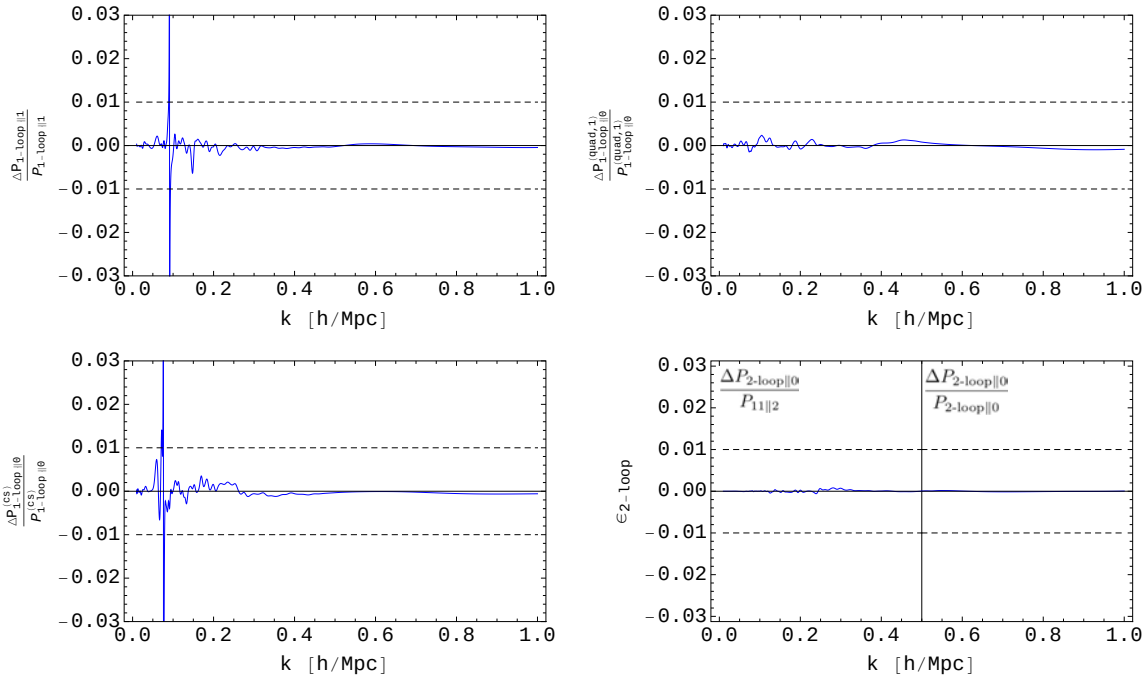

Fig. D.3 Resummed `CosmoEFT` outputs for our 5σ-cosmology `cosmo_9` relative to the direct calculation of the full integrand with precision $\epsilon = 0.1\%$. We used $\epsilon_{\text{target}} = 0.5\%$, and spikes indicate zero-crossing. Subscripts $\|0, \|1$ denotes the resummation order as in Senatore and Zaldarriaga (2015). Dashed lines mark 1% departures from direct calculations. As in Fig. 5.4, for $P_{2\text{-loop}}$ we show $\Delta P_{2\text{-loop}\|0}/P_{11\|2}$ for $k < 0.5\,h\,\text{Mpc}^{-1}$, which propagates directly to the matter power spectrum predictions, and $\Delta P_{2\text{-loop}\|0}/P_{2\text{-loop}\|0}$ for $k > 0.5\,h\,\text{Mpc}^{-1}$, which verifies the performance of our estimates for smaller scales.